Versatile Oligoamide α-helix Mimetic Scaffolds

Valeria Azzarito

Submitted in accordance with the requirements for the degree of

Doctor of Philosophy

University of Leeds

School of Chemistry

April 2014

Intellectual Property and Publication Statements

The candidate confirms that the work submitted is her own, except where work which has formed part of jointly-authored publications has been included. The contribution of the candidate and the other authors to this work has been explicitly indicated below. The candidate confirms that appropriate credit has been given within the thesis where reference has been made to the work of others.

The introduction of section 1.3 and section 1.3.2 Chapter 1 was adapted from a review article published in February 2013: 'Inhibition of alpha-helix mediated protein-protein interactions using designed molecules', V. Azzarito, K. Long, N. S. Murphy and A. J. Wilson, Nat. Chem. 2013, 5, 161–173. The contributions of the authors were as follows: VA (the candidate) wrote the corresponding section of the review and produced the related figures, AJW edited the manuscript into its present form (see attached copy); other authors have equally contributed to the review (on different sections).

The work reported in Chapter 2 formed the basis for a research article published online in December 2011: 'Conformational properties of O-alkylated benzamides', P. Prabhakaran, V. Azzarito, T. Jacobs, M. J. Hardie, C. A. Kilner, T. A. Edwards, S. L. Warriner, A. J. Wilson, Tetrahedron 2012, 68, 4485-4491. The contributions of the authors were as follows: AJW, PP and VA (the candidate) designed the research, VA (the candidate) performed the research on the 2-O-alkylated scaffold and drafted the corresponding section of the manuscript, PP performed the research on the 3-O-alkylated scaffold, MJH, CAK and TJ solved the crystal structures, AJW SLW and TAE edited the manuscript into its present form (see attached copy).

The work reported in Chapter 3 formed the basis for a research article published online in July 2012: '2-O-Alkylated Para-Benzamide α-Helix Mimetics: The Role of Scaffold Curvature', V. Azzarito, P. Prabhakaran, A. I. Bartlett, N. S. Murphy, M. J. Hardie, C. A. Kilner, T. A. Edwards, S. L. Warriner, A. J. Wilson, Org. Biomol. Chem. 2012, 10, 6469-6472. The contributions of the authors were as follows: AJW and VA (the candidate) designed the research, VA (the candidate) performed the research on the 2-O-alkylated scaffold and drafted the corresponding section of the manuscript, PP and NSM performed the research on the 3-O-alkylated scaffold, AIB performed

the biological assay, MJH and CAK solved the crystal structures, AJW SLW and TAE edited the manuscript into its present form (see attached copy).

Acknowledgements

First and foremost, I would like to thank my supervisor, Prof Andy J. Wilson, for the fantastic work we have done together in these three and a half years. Thank you for this extremely stimulating project, for the constant, enthusiastic and never-ending support and, above all, for believing in me in that July 2010 interview and giving me an opportunity that has really changed my life. I would also like to thank my co-supervisor Dr Stuart L. Warriner, for all his invaluable help in every scientific matter, for all the encouragement throughout these years and for the all the attempts to convert me into a 200 km cyclist (one day I will try, I promise).

Thanks to the European Research Council for funding my PhD and to all the people that collaborated to this project: Dr Julie Fisher for her NMR knowledge and for being a great support; Dr Chris J. Empson for his endless patience in helping with the robot; Dr Thomas A. Edwards for trying to teach me how to crystallise proteins; Dr Michaele Hardie for her help with the X-ray; Simon Barrett for never saying 'no' at my next crazy NMR request; Martin Huscroft for all the time spent helping me with the HPLC and all the technical and administrative staff for the assistance during these years.

The biggest and most sincere thank you goes to the Wilson group, past and current members, for being the 'dream-team' to work with. Thanks to Adam, Mazza, Panchami and Maria for the warm welcome when I joined the group; to George P. (my Georgeee boy), for being my strongest support when I was down and for all the Double Muscles gigs; to Kérya and Tasha, my homies, my sisters, thank you for the wonderful time spent together, for all the crazy moments in Pennington street and for gifting me with a friendship that will last forever, no matter where we are. Thanks to Anna, my 'post-Doc mum', for all the help and support and for introducing me to salsa dancing; to Kelly, for your calming influence and for not killing me during the Biotechnology YES competition; to Silvia, for brightening every day with the warmest Spanish smile; to George B, for every and each one of your funny stories and for being always nice with auntie Vale; to Hannah, for helping me while I was in biology and making it a better place to work; to Jenny, for being the star biology post-Doc and for all your yummy cakes; to Alice for being always so sweet; to Jayapal, for being always so happy; to Sarah for the constant support while I was

writing this thesis; to Irene, you wonderful crazy little thing, thank you for providing me with coffee almost every day since your arrival in the group; to Ludwig, for being the fantastic latest acquisition of this wonderful group and having already conquered a place in my heart. I will miss you a lot guys! The most special thanks goes however to my 'PhD soul-mate', Dave. We started this adventure together and nothing would have ever been the same without you! Thank you for every single moment in these three and a half years fit-Welsh. The end has arrived and there will never be enough words to say how much I will miss you.

A number of other people have been of massive support during these years. Firstly (and most importantly), I would like to thank Phil. My love, thank you so much for believing in me as much as you do and for being always at my side, sustaining me and encouraging me at every step. Thanks to Nic for all the moments spent together, all the chats, the gym sessions and the cocktail nights; to James for being a central support during my first year and for all the times you were 'too busy' for a coffee; to Giorgia, for being the wonderful friend you are; to the entirety of 'team Italy', Andrea, Roberta, Carlo, Tatiana and Gabriele, thank you for making me feel always a bit at home; to Diana, Ivona and Kat, thank you for all the funny moments in the Astbury Society and for all the support in this past year; to Charlotte for all our fantastic double dates; to Keeran, for all the nice Fridays together; to Hernan, for being a great friend and for helping me in finding a job; to Antoine and Sam for our super funny quadruple dates; to 'team Winkworth' for being like a second family to me. Thank you all!

Sentiti ringraziamenti vanno ai miei migliori amici in Italia: Ivan, Giovanni, Elisa, Luca, Simona, Rosa, Diletta e Ilaria. Grazie ragazzi per esserci stati in ogni momento, anche se la distanza ci ha forzatamente separati.

I ringraziamenti conclusivi vanno alla mia famiglia. Questa tesi è dedicata a voi, perché senza di voi non avrei mai potuto essere dove sono ed aver raggiunto questo importante traguardo. Alla mia mamma, grazie per aver accettato questa mia difficile scelta che ci ha tenute tanto lontane e per avermi supportata in ogni istante. Alla mia Bizzi adorata, amore mio sei sempre con me, non importa quanto lontane. Alla mia nonna meravigliosa, una presenza costante e mio modello di vita. Al mio papà, perché anche se non potrai mai sapere di questo mio successo, so che saresti stato fiero ed orgoglioso di me. Grazie a tutti.

Abstract

Protein-protein interactions (PPIs) play a pivotal role in mediating a number of biological processes involved in the development of infected or diseased states. Since α-helices constitute the most abundant motif at characterised protein interfaces, α-helix mediated PPIs represent an attractive target for therapeutic intervention and their inhibition with α-helix mimetics has emerged as a powerful strategy. Encouraging results have been obtained through the design of foldamers and proteomimetics and the current state-of-the-art is described in Chapter 1.

The Wilson group is interested in the development of aromatic oligoamide α-helix mimetics. The work presented in this thesis was therefore aimed at developing a better understanding of the conformational properties of this family of proteomimetics through screening against two key oncogenic targets, p53/*h*DM2 and Mcl-1/NOXA B, in order to identify key features required to reproduce the functional role of α-helices and achieve effective inhibition.

A 2-*O*-alkylated oligobenzamide scaffold was designed to determine the effect of non-covalent interactions on the conformational preference and molecular recognition properties of these oligomers. The conformational studies performed on regioisomeric 2-*O* and 3-*O*-alkylated dimers are described in Chapter 2, whilst the biophysical assessment of trimers of both series for p53/*h*DM2 inhibition is reported in Chapter 3.

These studies pointed to a complex interplay of interactions influencing the conformational and protein recognition properties of these mimetics and led to design of a new hybrid α-helix mimetic scaffold. Chapter 4 describes the conformational studies and structure-activity relationship data obtained from biological assays of a 35-membered library built using a robust solid-phase strategy. This scaffold allowed the identification of the first examples of enantioselective recognition of type III mimetics by different proteins and enantiodependent differentiation of mimetics by a protein partner, and represents a potential starting point to elaborate rule based approaches for the design of proteomimetics aimed at effective PPI inhibition.

Table of Contents

List of Tables

List of Figures

List of Schemes

List of Abbreviations

Biology

Bcl-2	B-cell lymphoma 2
Bcl-x_L	Bcl extralarge
Bak	Bcl-2 homologous Antagonist Killer
BID	BH3 Interaction domain Death agonist
BIM	Bcl-2 Interacting Mediator of cell death
CD	Circular Dichroism
Cdc42	Cell division cycle 42
CHR	C-terminal Heptad Repeat domain
CaM	Calmodulin
Dbl	Diffuse B-cell Lymphoma
Dbs	Dbl's big sister
ELISA	Enzyme-Linked Immunosorbent Assay
ERα	Oestrogen Receptor α
ERK	Extracellular signal-Regulated Kinases
FA	Fluorescence Anisotropy
FPA	Fluorescence Polarization Assay
gB	Glycoprotein B
gp41	Glycoprotein 41
*h*DM2	Human Double Minute 2
*h*DMX	Human Double Minute X
HBS	Hydrogen-Bonding Surrogates
HCMV	Human Cytomegalovirus
HEK293	Human Embryonic Kidney 293

HIF-1α	Hypoxia-Inducible Factor 1 alpha
HIV	Human Immunodeficiency virus
IAPP	Islet Amyloid Polypeptide
IC_{50}	Half maximal Inhibitory Concentration
ITC	Isothermal Calorimetry
K_i	Inhibition constant
K_d	Dissociation constant
Mcl-1	Induced Myeloid Leukemia Cell differentiation protein
*m*DM2	Murine Double Minute 2
*m*DMX	Murine Double Minute X
MOMP	Mitochondria Outer Membrane Permeabilisation
MRE	Mean Residual Ellipticity
NK	Neurokinin
p300	E1A binding Protein 300
p53	Tumour protein 53
PPIs	Protein-Protein Interactions
PTHrP	Parathoid Hormone related Protein
PUMA	p53 Upregulated Modulator of Apoptosis
smMLCK	Small muscle Myosin Light Chain Kinase
SOS	Son Of Sevenless guanine nucleotide exchange factor
SPR	Surface Plasmon Resonance
TUNEL	Terminal deoxynucleotidyl transferase dUTP Nick End Labeling
VEGF	Vascular Endothelial Growth Factor
WT	Wild Type

Chemistry

ABA	Amino Benzoic Acid
Bn	Benzyl
*i*Bu	Isobutyl
*i*Pr	Isopropyl
DIPEA	*N*,*N*′-Diisopropylethylamine
DMF	*N*,*N*′-Dimethylformamide
DMSO	Dimethylsulfoxide
Fmoc	Fluorenylmethyloxycarbonyl
FITC	Fluorescein-isothiocyanate
HABA	Hydroxy Amino Benzoic Acid
HATU	(1-[Bis(dimethylamino)methylene]-1H-1,2,3-triazolo [4,5-b]pyridinium 3-oxid hexafluorophosphate
THF	Tetrahydrofuran
TFA	Trifluoroacetic Acid

Other terms

HTS	High throughput screening
HPLC	High performance liquid chromatography
HRMS	High resolution mass spectrometry
LC-MS	Liquid phase Chromatography-Mass spectrometry
MMFFs	Merck Molecular Force Fields
MR	Molar Refraction
NMR	Nuclear Magnetic Resonance
NOESY	Nuclear Overhauser Effect Spectroscopy
QSAR	Quantitative Structure Activity Relationship

RMSD	Root Mean Square Deviation
SAR	Structure-Activity Relationship
SPPS	Solid phase peptide synthesis

Amino acids codes

Amino acid name	Three-letter code	One letter code
Alanine	Ala	A
Arginine	Arg	R
Asparagine	Asn	N
Aspartic acid	Asp	D
Cysteine	Cys	C
Glutamic acid	Glu	E
Glutamine	Gln	Q
Glycine	Gly	G
Histidine	His	H
Isoleucine	Ile	I
Leucine	Leu	L
Lysine	Lys	K
Methionine	Met	M
Ornithine	Orn	O
Phenylalanine	Phe	F
Proline	Pro	P
Serine	Ser	S
Threonine	Thr	T
Tryptophan	Trp	W
Tyrosine	Tyr	Y
Valine	Val	V

Chapter 1

Inhibition of α-helix mediated PPIs using designed molecules

This chapter will discuss the importance of α-helix mediated protein-protein interactions (PPIs) in chemical biology and drug discovery. The current state-of-the-art on designed inhibitors will be reviewed with a focus on the key challenges faced in developing generic approaches for the development of effective inhibitors.

The introduction of section 1.3 and section 1.3.2 contributed to the following review article:

V. Azzarito, K. Long, N. S. Murphy, A. J. Wilson, *Nat. Chem.* **2013**, *5*, 161-173.[1]

1.1 Introduction

Protein-protein interactions (PPIs) play a key role in mediating a number of biological processes often involved in the development of infected or diseased states. Representative processes mediated by PPIs include HIV viral fusion,[2] the apoptosis pathway involving Bcl-2 (B-cell lymphoma 2) family[3] and misfunction of human tumour suppressor p53 due to overexpression of the protein *h*DM2 (Human Double Minute 2).[4] The development of new molecular therapeutics for the inhibition of PPIs therefore represents one of the biggest challenges in chemical biology as it is unclear how to effectively and selectively target these interactions using small molecules.

The design of small competitive inhibitors of PPIs is in fact limited by several factors[5,6,7,8], including:

- the lack of natural ligands in providing direct links that allow generation of new molecules with effective mimicry;
- the large interfacial area of the target proteins;
- noncontiguous binding regions of protein partners.

It is commonly accepted that in order to be a competitive inhibitor, a small molecule must cover 800-1100 $Å^2$ of the protein surface, matching the projection of hydrophobic and charged domains on a flat or slightly convex surface (Figure 1.1).[8, 9]

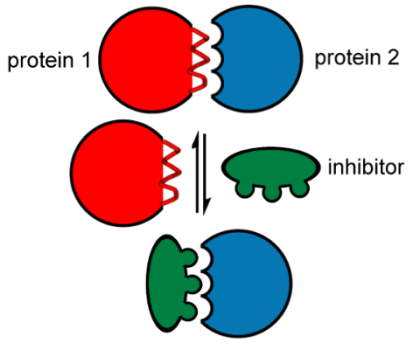

Figure 1.1 Schematic cartoon illustrating recognition and inhibition of PPIs.

These limitating factors contributed to the historical belief that PPIs are 'unligandable' using small molecules.

Traditional drug-discovery approaches have succeeded in finding nanomolar inhibitors designed to specifically target PPIs.[10,11,12,13] This approach has however the disadvantage of lacking generality for the generation of drug candidates.

Despite these challenges, a crucial observation is that PPIs often are driven by interactions of a few residues, known as a 'hot-spots', which constitute the key binding region.[14] This significantly simplifies the design of small molecules able to target PPIs, since critical portions of the target protein may be mimicked with relatively simple scaffolds.

In this context, it has been shown that over 30% of protein secondary structures is α-helical in nature, thus making it the most abundant motif and designating α-helix mediated PPIs as a particularly attractive target in chemical biology.[15]

Typical α-helix structures complete one turn every 3.6 amino acid residues and have a rise of 5.4 Å per turn due to backbone dihedral angles of Ψ = - 41° and Φ = - 62° (Figure 1.2 a-b).[15, 16]

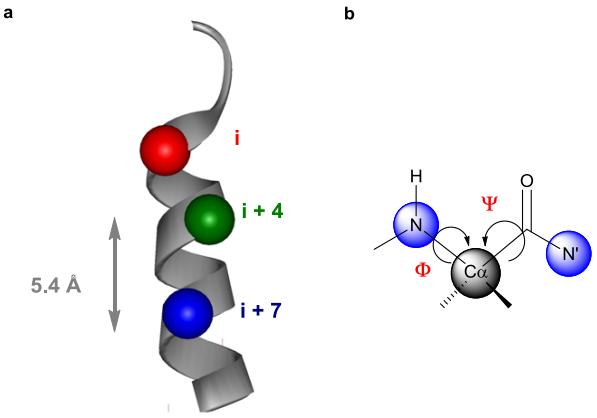

Figure 1.2 Structural features of an α-helix a α-Helix key residues and rise per turn; **b** Dihedral angles definition in the peptide bond.

The hydrogen-bonding network in an α-helical central core stabilises the secondary structure placing amino acid side chains along its surface. Binding with the protein partner occurs through key side-chains generally located along one face of the helix, which correspond to residues at the *i*, *i* + 4(3), *i* + 7(8) and often *i* + 11 positions in the sequence (Figure 1.2 a).[3, 4, 17]

In designing effective inhibitors of this family PPIs, it should be therefore possible to recapitulate the helical core using a rod-shaped object presenting side chains in a spatial orientation comparable to that of the native helix (Figure 1.3).

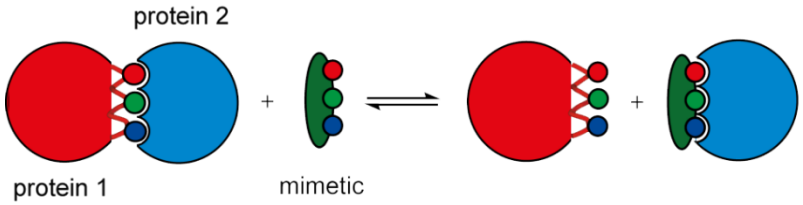

Figure 1.3 Schematic cartoon illustrating the action of a mimetic rod-shaped scaffold as a competitive inhibitor of an α-helix mediated PPI.

Of the many approaches developed over the years, the design of *proteomimetics* (non-peptidic structures that mimic larger areas of the protein surface)[18] and *surface mimetics* (molecules containing recognition domains capable

of binding 'hot-spots' on a protein surface over a sufficiently large surface area) [19] has been particularly encouraging.

1.2 Protein-protein interactions as a therapeutic target

Protein-protein interactions play a central role in a number of essential cellular processes and since it has been estimated that the human interactome includes around 650,000 PPIs,[20] their control and modulation could prove critical for therapeutic intervention.

Among biological processes regulated by α-helix mediated PPIs, the prevention and treatment of cancer has received significant attention. Cancer is a disease in which mutations occur in genes, which regulate cell growth. As a consequence, the transformation of a healthy cell into a cancer cell occurs.[21] Changes in oncogenes, resulting in overexpression or gene products with different properties, promote the development of the malignant phenotype of cancer. Mutations in tumour suppressor genes, which are involved in the inhibition of cell division and survival, can also have consequences. Typically, a single change is insufficient to promote the development of cancer because the body uses safeguard mechanisms, like *apoptosis* (programmed cell death), in response to cellular anomalies.

Because of the key role played in oncogenesis, considerable attention has been devoted to the p53/*h*DM2[4] and Bcl-2 family PPIs,[3] which represent potential targets for chemotherapy and will be discussed in detail in the following sections.

1.2.1 p53/*h*DM2

p53 is a sequence-specific transcriptional activator and the major human tumour-suppressor protein. Its biological roles include apoptosis, inhibition of cell cycle progression and acceleration of DNA repair.[22] In the absence of cellular stress, p53 resides in a biologically latent state. However, in response to a stress-related signal (*e.g.* DNA damage, uncontrolled activation of oncogenes *etc.*), this protein becomes activated and initiates a biological response which either allows DNA repair or starts apoptosis to eliminate the damaged cell from the replicative pool.[4, 22]

*h*DM2 plays a key role in regulating the function and the stability of p53. Structural studies on the *h*DM2 mouse homologue p53/*m*DM2 (Murine Double Minute 2) complex [23,4] revealed that *m*DM2 interacts with a 15 residue α-helical region of p53, in an interface which is almost totally hydrophobic. Alanine-scanning mutational analysis identified three key binding residues, Phe19, Trp23 and Leu26, which are located at the *i*, *i* + 4, *i* + 7 positions of the helix respectively (Figure 1.4).[24]

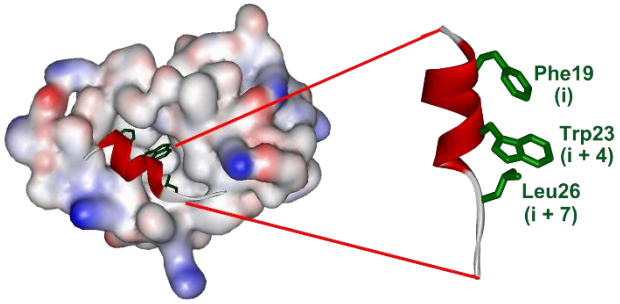

Figure 1.4 p53/*h*DM2 interaction (PDB ID: 1YCR) with the isolated helical segment of the p53 peptide showing the key binding residues.

When the cell is healthy, the p53/*h*DM2 PPI activates a negative feedback loop, which prevents the apoptotic activity of p53. The inactivation of p53 happens through two major mechanisms (Figure 1.5). Firstly, the binding to the *N*-terminal transactivation domain of p53 blocks critical interactions with other proteins necessary for regulation of gene expression, thus interfering with the transcriptional activity of p53. Secondly, *h*DM2 acts as a p53-specific E3 ubiquitin ligase and promotes its rapid degradation by the 26S proteasome, leaving its intracellular concentration low and tightly regulated. Furthermore, because the *h*DM2 gene contains two adjacent p53 binding sites, during its activity as a sequence-specific transcriptional activator, p53 can stimulate the expression of *h*DM2, which in turn results in its inactivation.

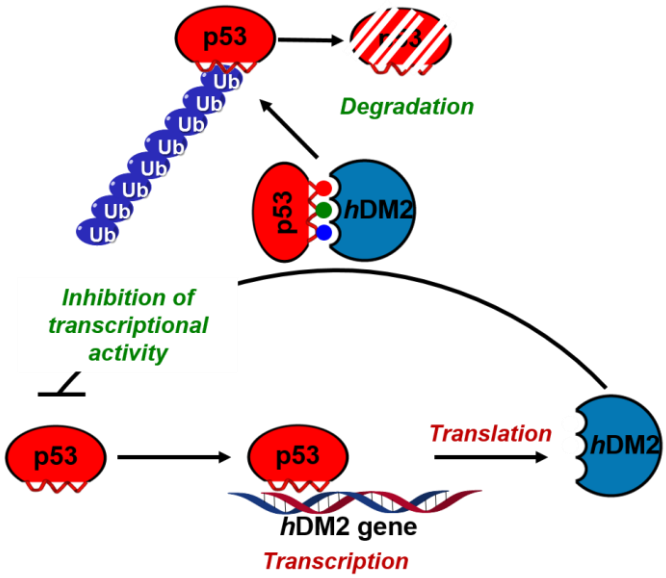

Figure 1.5 p53/*h*DM2 autoregulatory negative feedback loop: physical blockage of p53 upon binding and promotion of its ubiquitination and proteasomal degradation; p53-regulated transcription of the *h*DM2 gene for *h*DM2 expression.

In the presence of a tumour-related signal, however, *h*DM2 is overexpressed, and its elevated levels interfere with the activity of p53, downregulating its apoptotic activity against malignant cells.

For this reason, this PPI is considered an important target in the treatment of cancer development[23] and its inhibition with small molecules has been the object of extensive research in the past decade.

1.2.2 The Bcl-2 family PPIs

Proteins of the Bcl-2 family have a central role in the regulation of apoptosis.[3] They control the mitochondrial outer membrane permeabilisation (MOMP) and contain one or more characteristic domains named 'Bcl-2 homology' (BH) regions.[25, 26] To date, four BH-domains have been identified (BH1-4), which are known to be crucial for biological function. As shown in Table 1.1, proteins of the Bcl-2 family include anti-apoptotic members (*e.g.* Bcl-2, Bcl-x_L (Bcl extralarge) and Mcl-1 (induced myeloid leukemia cell differentiation protein)), which possess all four homology domains; multidomain pro-apoptotic members (*e.g.* Bak- Bcl-2 homologous antagonist killer, Bax- Bcl-2-associated X protein), possessing sequence homology for the BH1, BH2 and BH3 regions, and, finally BH3-only pro-apoptotic

members (*e.g.* NOXA B), which are also referred to as effector proteins or death domains.

Table 1.1 Bcl-2 family members

Anti-apoptotic members	Multidomain Pro-apoptotic members	BH3-only Pro-apoptotic members
Bcl-2	Bak	NOXA B
Bcl-x_L	Bax	BIM
Mcl-1		BID
Bcl-w		BAD
A1		PUMA
		BMF

Structural studies on several Bcl-2 family proteins showed a common overall fold in which the anti-apoptotic proteins have a hydrophobic groove acting as a binding site for α-helical regions on pro-apoptotic proteins.[12] For example, X-ray studies revealed that Bcl-x_L interacts with Bak by binding 16 residues of its helical portion (PDB ID: 1BXL). Alanine-scanning mutational analysis further indicated that the key binding residues (Val574, Leu578, Ile581 and Ile585) are all hydrophobic and are located on the same face of the helix at the *i*, *i* + 4, *i* + 7 and *i* + 11 positions (Figure 1.6).[3]

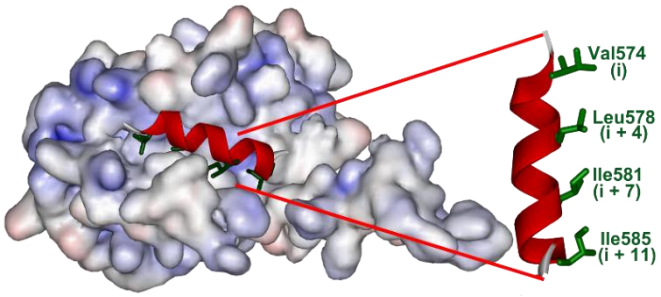

Figure 1.6 Crystal structures of the Bcl xL/Bak interaction (PDB ID: 1BXL) with the isolated helical segment of the Bak peptide showing the key binding residues.

In a similar way, the BH3-only pro-apoptotic protein NOXA B binds Mcl-1 through four key 'hot-spot' residues (Glu74, Leu78, Ile81 and Val85) at the *i*, *i* + 4, *i* + 7 and *i* + 11 positions of the helix (Figure 1.7; PDB ID: 2JM6).[27] The charged Glu74 residues differentiates the interaction from the PPIs of Bcl-x_L. Notably, unlike other BH3-only members such ah BIM (Bcl-2 interacting mediator of cell death) and

BID (BH3 interacting domain death agonist) which recognise different anti-apoptotic Bcl-2 family proteins, NOXA B only binds to Mcl-1[27, 28] (and to a lesser extent A1).[26]

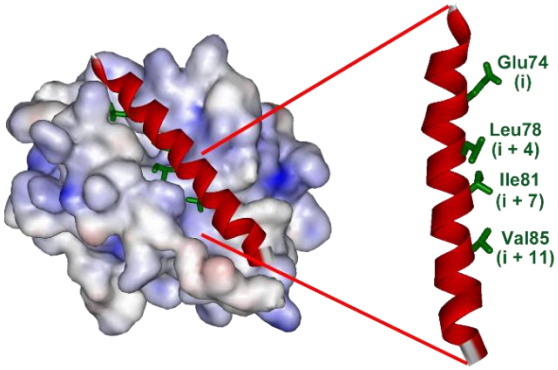

Figure 1.7 Crystal structures of the Mcl-1/NOXA B interaction (PDB ID: 2JM6) with the isolated helical segment of the NOXA B peptide showing the key binding residues.

Under normal circumstances, activating BH3-only pro-apoptotic proteins bind to anti-apoptotic partners. This process allows for multidomain pro-apoptotic proteins to oligomerise in the MOM facilitating ion and cytochrome *c* efflux from mitochondria and thus initiating the caspase cascade responsible for cancer cells death (Figure 1.8 a).

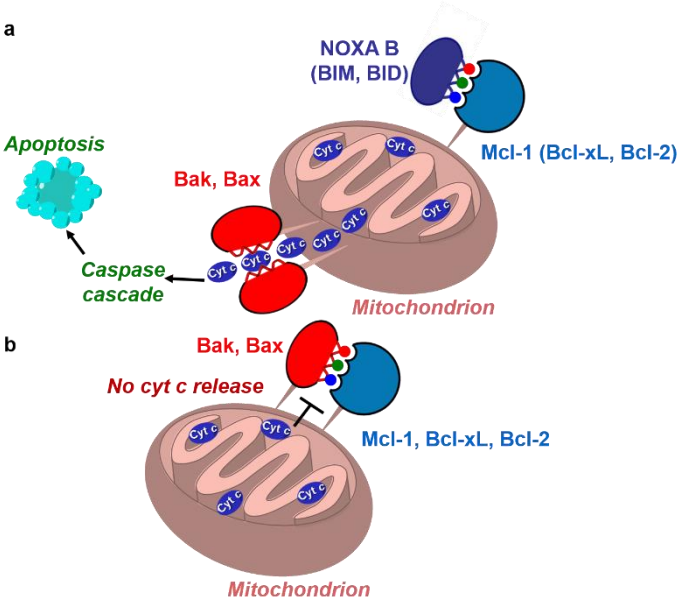

Figure 1.8 Regulation of apoptosis by the Bcl-2 family PPIs a Healthy conditions: BH3-only proteins bind to anti-apoptotic proteins allowing multidomain pro-apoptotic members to oligomerise and activate the caspase cascade necessary for the apoptosis of malignant cells; **b** Stressed conditions: anti-apoptotic proteins are overexpressed and sequester multidomain pro-apoptotic proteins thus causing the survival of cancer cells.

However, upon induction of stress-related signals, anti-apoptotic proteins are overexpressed and sequester Bak-like members, thus inhibiting their activity and misregulating the normal apoptotic process (Figure 1.8 b).

Even though the complete mode-of-action is still unclear, the misregulation of the normal apoptotic loop mediated by Bcl-2 proteins is known to be a major cause of cancer cell survival and chemotherapy resistance. It is therefore clear that the design of small molecule mimetics of the BH3-only members is extremely attractive for the development of anticancer agents.

1.3 α-Helix mimetics: state of the art

Foldamers are sequence-specific oligomers that adopt well-defined three dimensional conformations which reproduce the secondary structural features of proteins, peptides and oligonucleotides. According to Huc[29] the efficacy of a class of foldamers to be used in the design of a specific secondary structure depends on the aptitude to fulfil four main criteria:

- the *predictability* of folding, which is mainly associated with the design of structures that are forced to fold in the desired conformation;
- the *ease of synthesis* and thus *accessibility*; this is one of the most important aspects to consider in generating a proteomimetic and it is the reason why amide bonds are used by many research groups;
- the *stability* of a foldamer conformation since conformational changes may affect the predictability of the folded state;
- the possibility for a foldamer to be *tunable* in order to access different sequences using the same design principles.

Examples of foldamers that meet all the requirements to function as inhibitors of PPIs have been reported in the last few years.[1] According to Ripka[30] three different types of α-helix mimetic foldamers can be considered.

Type I mimetics reproduce the local topography of the helix by matching the peptide backbone (Figure 1.9 a-b).

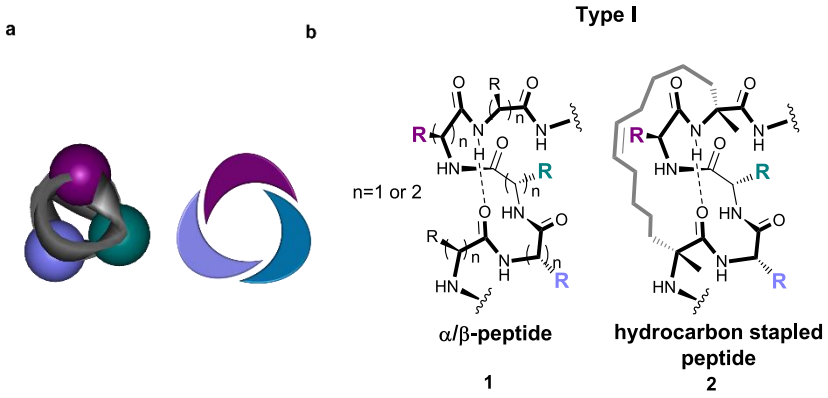

Figure 1.9 Type I α-helix mimetics a Top view of an α-helix (left) with a cartoon representation (right) showing the three recognition faces in purple, dark cyan and violet; **b** Two examples of Type I mimetics: the side-chains are colour coded to identify the recognition face mimicked.

α/β-Peptide foldamers (**1**, Figure 1.9 b) reported by the groups of Gellman[31] and Schepartz[32] and stapled peptides (**2**, Figure 1.9 b) reported by Verdine and co-workers[33] represent examples of type I helix mimetics.

Proteomimetics are considered type III mimetics since they match the topography of the original helix motif by mimicking the spatial orientation of its key residues rather than recapitulating the helical conformation (Figure 1.10 a-b).[18] The terphenyl scaffold (**3**, Figure 1.10 b) introduced by Hamilton's group[18] ten years ago is the first example of a proteomimetic structure in which the side chains reproduce the position of critical residues of an α-helix secondary structure. These two families of mimetics will be reviewed in depth in sections 1.3.1 and 1.3.2.

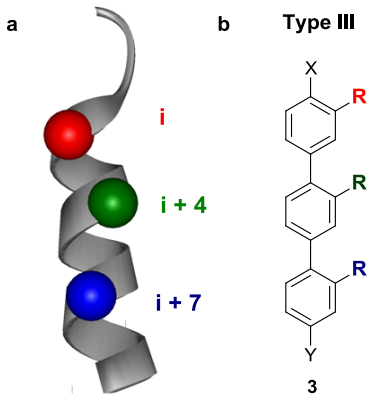

Figure 1.10 Type III α-helix mimetics a Schematic representing an α-helix: 'hot-spot' residues are represented in CPK format and colour coded; **b** Terphenyl template: the side-chains are colour coded to identify the residues mimicked.

Type II mimetics are small non-peptide molecules that bind to a peptide receptor but do not necessarily mimic the original helix structure and serve simply as functional mimetics. Identification of inhibitors in this class using conventional drug-discovery processes has proved difficult, mainly due to the different 'chemical space' occupied by traditional drug molecules. Nonetheless, several examples of potent inhibitors of PPIs identified *via* high throughput screening (HTS) or fragment-base approaches have been reported in recent years. Hoffmann-La Roche first identified a family of tetra-substituted imidazoles (Nutlins) which displayed inhibitory activity against the p53/ *h*DM2 interaction. The most potent derivative, Nutlin-3 (**4**, Figure 1.11 a-b), showed an IC_{50} (half maximal inhibitory concentration) value of 90 nM in an ELISA (Enzyme-linked immunosorbent assay).[10] Nutlin-3 has progressed to clinical trials, although its inability to target the related *h*DMX (human double minute X) interaction may prevent its use as an anticancer therapeutic.

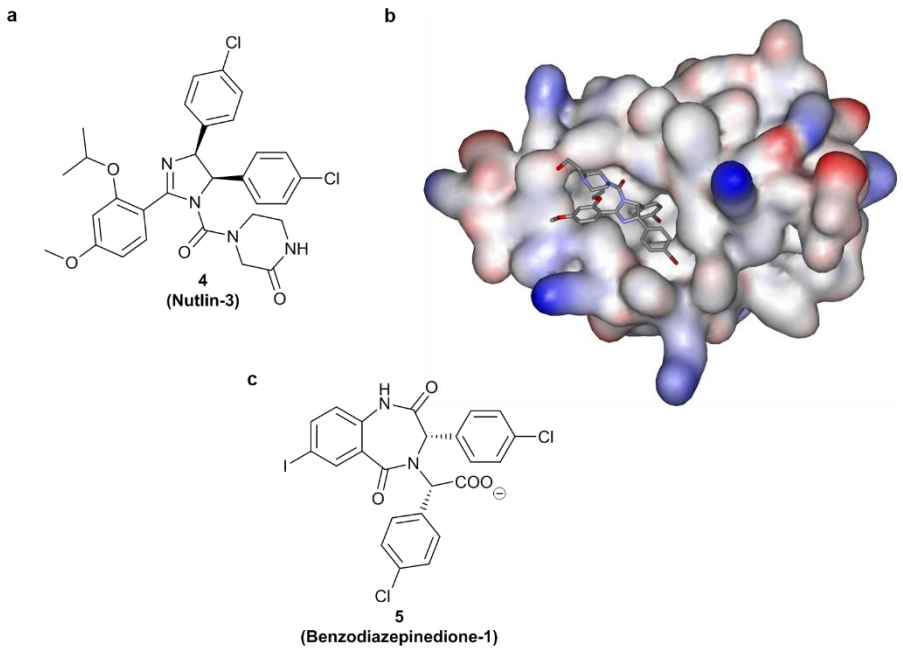

Figure 1.11 Small molecule inhibitors of PPIs identified via HTS **a** Chemical structure of Nutlin-3; **b** X-Ray structure of the Nutlin/*m*DM2 complex (PDB ID: 1RV1) **c** Chemical structure of benzodiazepinedione-1.

In a similar approach, Johnson & Johnson pharmaceuticals[34] identified a benzodiazepinedione family (**5**, Figure 1.11 c) able to disrupt the p53/*m*DM2 PPI with an IC_{50} value of 420 nM.[11]

Abbott Laboratories employed a fragment based SAR (structure-activity relationship) by NMR method in order to generate a library of potential inhibitors of the Bcl-x_L/Bak PPI.[12] Of all the compounds generated, the molecule ABT-737 (**6**, Figure 1.12 a-b) exhibited high affinity for the Bcl-x_L protein in a fluorescence polarisation assay (FPA) with a K_i (inhibition constant) value of 0.6 nM.[13] The major limitation of ABT-737 is the lack of oral bioavailability. A structural study on the key sites along the backbone was therefore performed in order to optimise the pharmacokinetic/pharmacodynamic ratio of the drug and thus improve oral efficacy. The analysis resulted in the identification of ABT-263 (**7**, Figure 1.12 a) as a potent orally bioavailable mimetic, with retention of affinity for Bcl-2 family proteins (K_i < 1 nM) and similar selectivity pattern of ABT-737.[35] Optimised derivatives of this inhibitor have recently been reported and shown to inhibit cell growth in cancer lines with IC_{50} values of 60-90 nM.[36, 37]

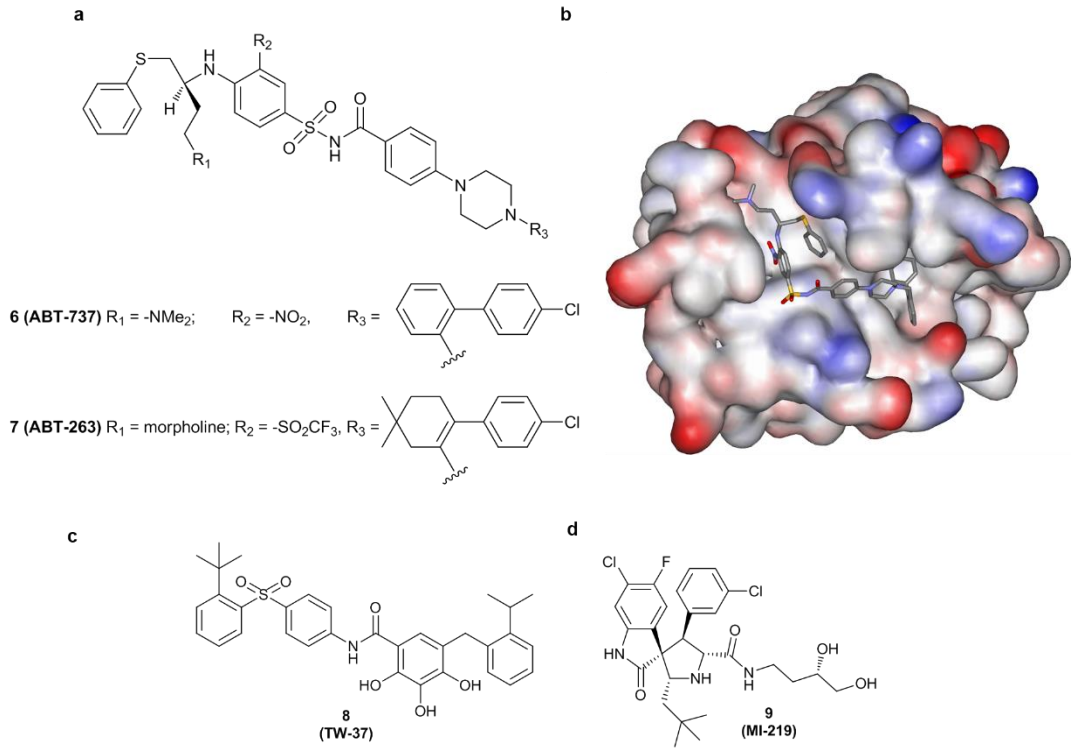

Figure 1.12 Small molecule inhibitors of PPIs identified via structure-based screening **a** Chemical structures of ABT-737 and ABT-263; **b** X-Ray structure of the ABT-737/ Bcl-xL complex (PDB ID: 2YXJ); **c** Chemical structure of TW-37; **d** Chemical structure of MI-219.

Wang and co-workers employed a structure based screening method to design a library of molecules that could target the elongated groove of antiapoptotic proteins

that bind the BH3 domain.[38] Following this strategy, the benzenesulfonyl derivative TW-37 (**8**, Figure 1.12 c) was identified as an effective inhibitor of Bcl-2 family proteins, by impeding cell growth involved in breast, prostate, lymphoma and pancreatic cancer with K_i values in the low micromolar range.[39,40] The group subsequently employed the same approach to target the p53/*m*DM2 PPI. The screening resulted in the design of a new family of spiro-oxindoles and MI-219 (**9**, Figure 1.12 c) was identified as the most potent compound of the series with a K_i value of 5 nM and a 10000-fold selectivity in targeting the *m*DM2 protein over *m*DMX (murine double minute X).[41]

Despite the discovery of potent inhibitors, the use of traditional approaches to identify small mimetics is unfortunately limited by the number of structures present in screening libraries and by the capability of available computer algorithms. These approaches further present the disadvantage of lacking versatility so that the potential to learn general design rules is perhaps less likely. For these reasons, this family of mimetics will not be further discussed.

1.3.1 Type I mimetics

Type I mimetics are short fragments of peptide, which reproduce the local topography of the α-helical motif found at a protein-protein interface. The use of peptides as therapeutics is highly desirable because of their ability to access mimicry of a complex set of functions which cannot be completely reached by a small molecule.[42,43] Peptides are however affected by poor transport properties and they are intrinsically prone to proteolytic degradation, properties that have unfortunately limited their use.[44] To overcome these limitations and improve pharmacokinetics properties, numerous approaches have focused on stabilising the helical backbone through the introduction of covalent or non-covalent constraints. These approaches can be grouped into two general categories: helical foldamers and constrained peptides.

1.3.1.1 Foldamers adopting a helical conformation

Foldamers containing β-aminoacids (**1**) have been extensively exploited during the past decade, since they present improved proteolytic and conformational

stability and a more favorable pharmacodynamic profile than their natural counterparts.[45] In spite of the additional degree of freedom induced by the extra methylene group of β-amino acids,[46] structural studies have shown that suitably substituted or conformationally constrained β-peptides possess a higher propensity to adopt well defined folded states in solution, making it possible to observe a defined structure within relatively short sequences.[31, 47]

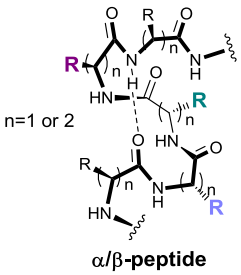

α/β-peptide

1

Seebach[48] first reported the synthesis and complete characterisation of a β-peptide sequence. Circular dichroism (CD) and X-ray analysis showed that these peptides adopt the desired helical conformation due to the favourable H-bond network between the amide proton and the carbonyl moieties.

Gellman and co-workers designed a series of β-peptides to mimic five key residues of the gB (glycoprotein B) heptad repeat involved in the development of human cytomegalovirus (HCMV, alternatively known as herpesvirus-5).[49] Assessment of a small library of compounds provided an inhibitor with an IC_{50} of 30 μM with notably improved activity to their α-peptide analogues.

Further interest has been devoted to β^3 peptides. In this context Schepartz[32] reported a series of 3_{14}-helical β-peptides able to bind the *h*DM2 protein and act as potent inhibitors of the p53/*h*DM2 PPI. The strategy is shown in Figure 1.13 and exploited introduction of non-natural side chains in a β^3-peptide backbone in order to improve the affinity of the molecule for the target protein.

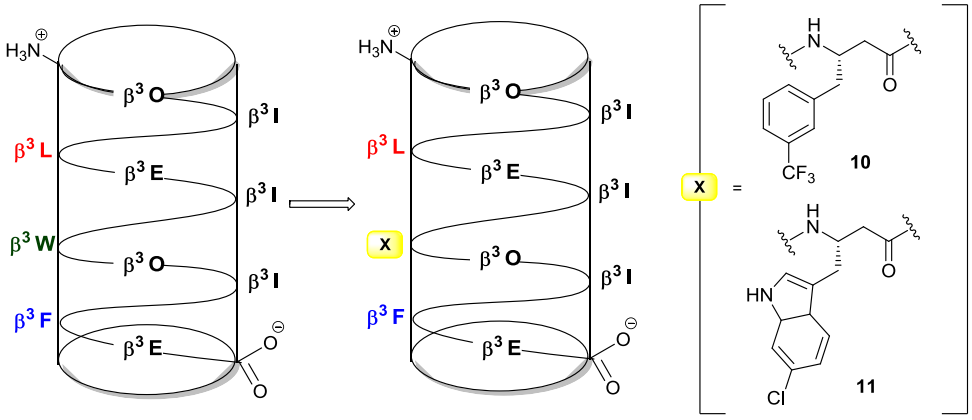

Figure 1.13 Side chains orientation in a β^3-peptide and substitution of a key residue with a non-natural derivative.

A FPA analysis in the presence of a fluorescently labelled p53 resulted in the identification of derivatives **10** and **11** as the best inhibitors of the series. The assay suggested that these molecules interact with *h*DM2 in a very similar way to the native helix, disrupting the protein-protein interaction with IC_{50} values of 15.9 nM and 3.30 nM respectively, probably due to the improved ability of these side chains to fill the hydrophobic pocket of the protein compared to the tryptophan residue of the parent peptide.

The Gellman group also investigated mixed α/β-peptides with the aim of targeting the Bcl-2 family of PPIs. [50,51,52,53,47] Microwave-assisted synthesis *via* sequential coupling reactions led to the identification of the chimeric peptide **12** as a potent inhibitor of the Bcl-x_L/Bak interaction.

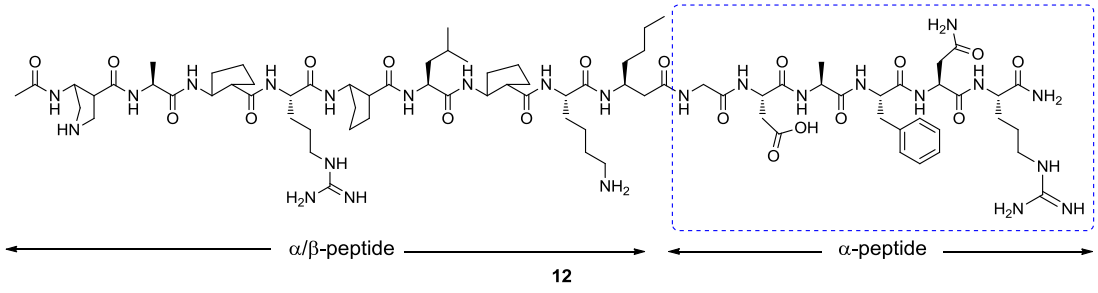

A FP competition assay in the presence of a fluorophore-labelled Bak peptide gave an IC_{50} value of 52 nM. Conservative modification of the C-terminal segment

followed by truncation studies, provided peptide **13**. This analogue showed comparable affinity for Bcl-xL (IC_{50} = 78 nM) with improved proteolytic stability.

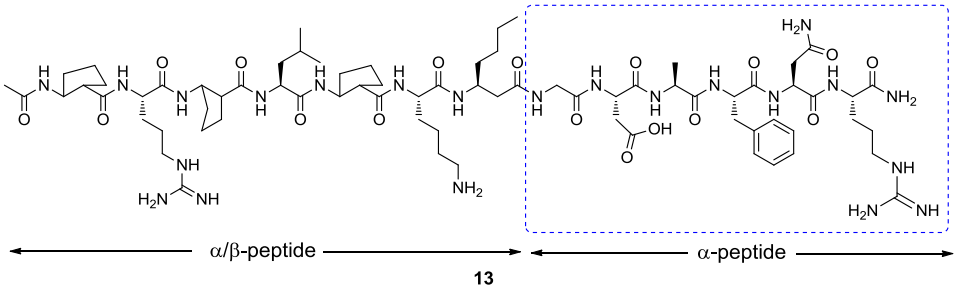

13

Similar approaches were subsequently employed to target the Bcl-x_L/BIM PPI, leading to the identification of weak inhibitors.[50] A crystal structure of the most potent BIM chimeric peptide bound to Bcl-x_L (PDB ID: 3FDM; Figure 1.14 a)[54] highlighted the importance of solvent-exposed residues in inducing the helical conformation (Figure 1.14 b).

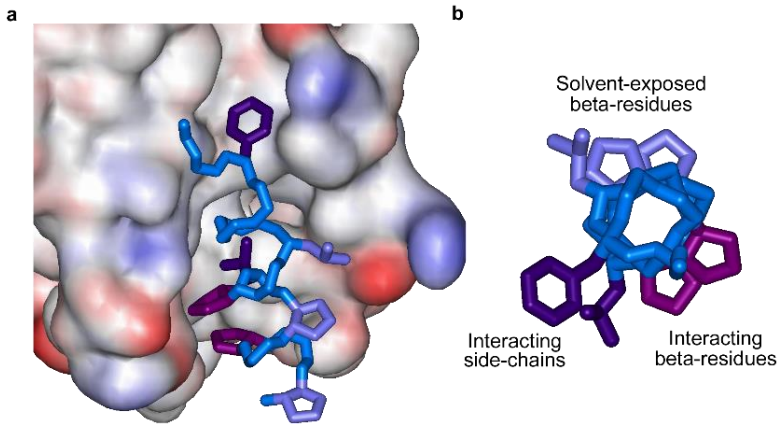

Figure 1.14 BIM chimeric α/β peptide a Chimeric mimetic (α/β +α)-peptide bound to Bcl-xL (PDB ID: 3FDM); **b** Top view of the chimeric mimetic (PDB ID : 3FDM) distinguishing the spatial orientation of interacting α (purple) and β (pink) residues and of solvent exposed β-residues (light purple).

However, the reduced activity of these derivatives suggested that more subtle matching of the α-helix may be necessary to target certain PPIs and that the topographical mimicry of key side-chains along one face of a helical scaffold may not be sufficient to identify potent inhibitors.

The Gellman group therefore employed a sequence-based approach for the design of a PUMA (p53 upregulated modulator of apoptosis) analogue, introducing

β-residues at selected positions within the helix.[55] The study of seven analogues containing an ααβαααβ repeat revealed that the position of the β-residue has a significant effect on the activity and selectivity of these foldamers. A dual peptide inhibitor of Bcl-x_L and Mcl-1 (K_i = 1 nM and 150 nM respectively) was identified.[56] The crystal structure of this PUMA-mimetic bound to Bcl-x_L (PDB ID: 2YJ1; Figure 1.15 a) revealed that in order to achieve tight binding, the helical backbone accommodated the extra methylene unit of the β-residues through expansion of the helix radius. Furthermore, the heptad ααβαααβ repeat gave rise to a more regular helix where all the β-amino acids were aligned along the solvent-exposed face, thus allowing maintenance of the *i*, *i* + 4, *i* + 7 and *i* + 11 interaction pattern of regular α-helices (Figure 1.15 b).

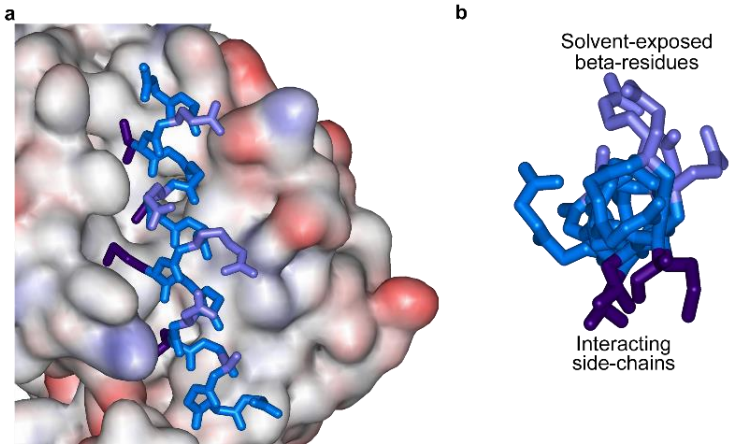

Figure 1.15 PUMA chimeric ααβαααβ peptide a Chimeric mimetic ααβαααβ-peptide bound to Bcl-xL (PDB ID: 2YJ1); **b** Top view of the chimeric mimetic (PDB ID : 2YJ1) distinguishing the spatial orientation of interacting α-residues(purple) and of solvent exposed β-residues (light purple).

Combining the success of the sequence-based approach and the use of β^3 peptides, the Gellman group developed a two-step sequence-based design of an α/β-peptide that prevents the formation of the six-helix bundle of the HIV membrane protein.[57] Firstly, β^3-residues were inserted into the α-sequence of the *C*-terminal heptad repeat domain (CHR) of gp41 (glycoprotein 41) to form ααβααβ repeats. Subsequently, selected β^3-residues were replaced by cyclically constrained β-residues, to overcome the entropy penalty associated with the preorganisation required for more flexible analogues. This approach allowed the identification of a

potent peptide (K_i = 9 nM), with a ~380 fold improvement on the analogous acyclic α/β-peptide (Figure 1.16).[57]

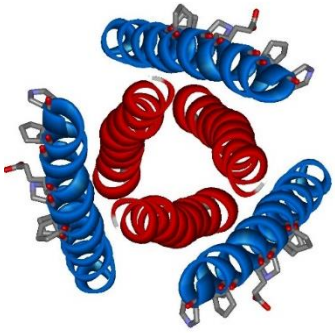

Figure 1.16 Top view of the six-helix bundle formed by the *N*-terminal heptad domain α-peptides (red) and the α/β foldamers (blue) (PDB ID: 3G7A).

1.3.1.2 Covalently constrained peptides

Although peptides are attractive candidates for the disruption of protein-protein interactions, their susceptibility to proteolytic degradation and poor cell penetration properties often affect their efficacy as *in vivo* reagents. In order to overcome these issues, there has been a growing interest in the introduction of covalent linkages between residues close in space that can stabilise the secondary structure, as degradation usually requires the peptide to adopt unstrucrtured conformations.

One of the most remarkable examples is the hydrocarbon stapling demonstrated by Verdine and co-workers.[33] The strategy relies on the introduction of α,α'-disubstituted non-natural amino acids containing olefin-bearing tethers which can undergo ruthenium catalyzed olefin metathesis[58] in order to generate an all-hydrocarbon staple (Scheme 1.1).

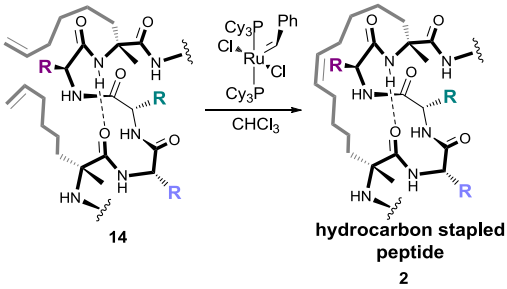

Scheme 1.1 Synthetic strategy for the synthesis of a stapled peptide.

This new hydrocarbon-stapled backbone approach provided a platform for a number of significant studies over the last decade. Following this route, Korsmeyer and co-workers generated a library of hydrocarbon-stapled peptides in order to mimic the BH3 domain of BID. [33] A FPA binding test revealed that one of these derivatives possessed a K_d (dissociation constant) value of 38.8 nM, which represented a six fold enhancement in binding affinity as compared to that of the unmodified BID BH3 peptide (K_d = 269 nM). Furthermore, both *in vitro* and *in vivo* assay showed that this peptide can activate the apoptotic pathway to kill leukaemia cells and inhibit growth of human leukaemia xenografts and this approach has ultimately been patented.[59]

The Walensky group further demonstrated the validity of such an approach and described a series of stapled peptides which act as effective inhibitors of the Mcl-1 protein (PDB ID: 3MK8; Figure 1.17 a).[60] Interestingly, this constrained peptide was not derived from the structure of one of the BH3-only pro-apoptotic partners of Mcl-1, but instead from a peptide derived from Mcl-1 itself.

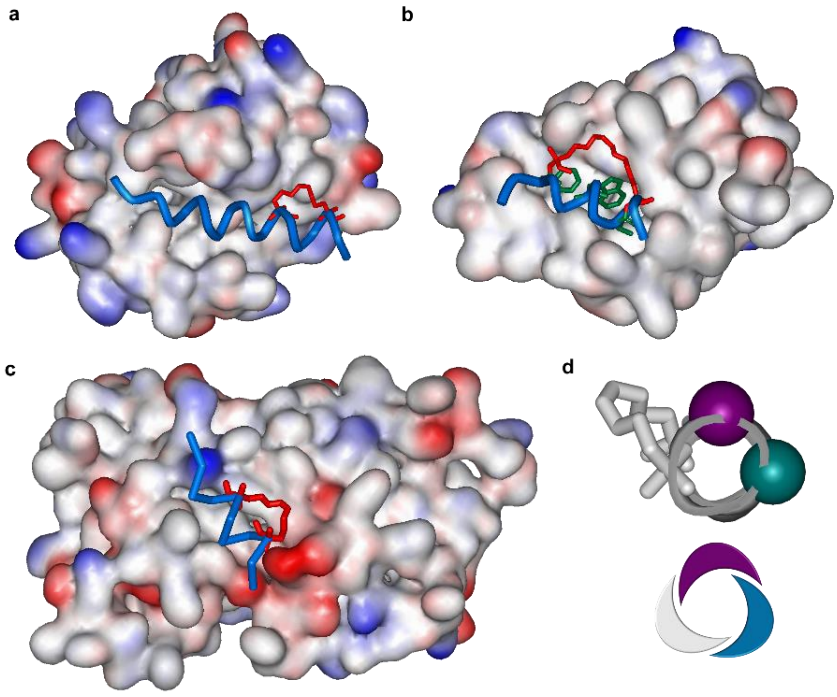

Figure 1.17 Crystal structures of stapled peptides bound to proteins a Mcl-1 and a hydrocarbon-stapled peptide (PDB ID: 3MK8); **b** *h*DM2 and a hydrocarbon-stapled peptide (PDB ID: 3V3B); **c** ERα and a hydrocarbon-stapled peptide (PDB ID: 2YJA); **d** Top view of a stapled α-helix (top) with a cartoon representation (bottom) of the three recognition faces, showing in grey the face affected by the introduction of the covalent constraint.

Dual stapled-peptides inhibitors of *h*DM2 and *h*DMX have also been identified and shown to bind these proteins with nanomolar affinity in a FP assay. [65] The group of Verdine obtained a crystal structure of a stapled-p53 derivative bound to *m*DM2 (PDB ID: 3V3B; Figure 1.17 b),[61] which revealed that the hydrocarbon staple itself can contribute to the binding in the protein cleft. Similar behaviour was also observed in a stapled peptide shown to bind to the oestrogen receptor α (ERα) with a K_d of 674 nM in a Surface Plasmon Resonance (SPR) experiment (PDB ID: 2YJA; Figure 1.17 c).[62] This analysis highlighted that the relationship between structure and properties for these mimetics needs to be carefully considered as the hydrocarbon staple can interfere with one of the helical recognition faces (Figure 1.17 d).

Verdine and co-workers also reported a stapled mimetic of the co-activator peptide MAML 1 and showed its activity as a direct-acting agonist of the oncogenic transcription factor NOTCH 1.[63] This work was particularly noteworthy, as the large interface of transcription factors and the absence of hydrophobic pockets make them extremely difficult targets.

Furthermore, Walensky and co-workers reported a hydrocarbon double-stapled peptide, which was shown to be resistant to protease both *in vitro* and *in vivo* and displayed enhanced inhibitory activity against gp41 assembly.[64]

Finally, the Wilson group recently reported on a BID-like peptide containing an α-alkenyl monosubstituted staple (**15**).[65] The work showed that the removal of the extra methyl substituent did not affect the proteolytic stability and the helicity of this peptide, which retained inhibitory activity against the Bcl-x_L/Bak PPI comparable to its disubstituted analogue (IC_{50} = 0.62 ± 0.02 μM-monosubstituted *vs* 1.15 ± 0.04 μM-disubstituted in a FA-Fluorescence Anisotropy- competition assay).

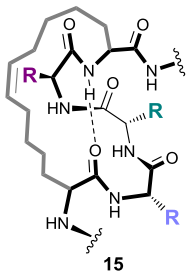

15

The lactam link (**16**, Figure 1.18 a) is one of the most investigated approaches for constraining peptides and was first reported by Rosenblatt *et al.*[66] who stabilised a parathoid hormone related protein (PTHrP) analogue resulting in a 5-10 times potency increase compared to the parent linear peptide.

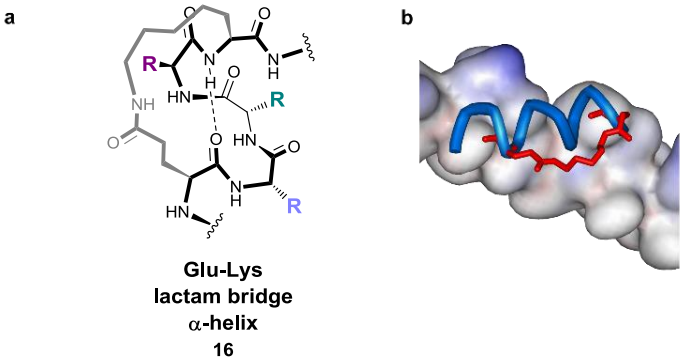

Figure 1.18 Lactam-bridged peptide a Generic structure of a peptide stapled with a Glu-Lys lactam bridge; **b** Crystal structure of gp41 in complex with a lactam-bridged peptide (PDB ID: 1GZL).

Following earlier work from McDowell and co-workers, [67] the Kim group reported on the stabilisation of a 14-residue *C*-terminal peptide of gp41 *via* cross linking two glutamic acid residues at the *i* and *i* + 7 positions with an α,ω-diaminoalkane group. The introduction of this covalent constraint produced a potent inhibitor (IC_{50} = 35 μM, K_d = 1.2 μM) of the interaction with the hydrophobic pocket of HIV-1 gp41 (PDB ID: 1GZL; Figure 1.18 b).[2]

Several other groups have proved the strategy successful. Important examples are the stabilisation of the oestrogen-binding co-activator peptide, reported by Geistlinger and Guy,[68] and a series of papers from Fairlie and co-workers.[69] Following this strategy, this group successfully mimicked the helical epitopes of (i) a quorum sensing pheromone which abolished growth of the bacteria *S. pneumonia* at sub micromolar concentrations, (ii) the F fusion protein of Respiratory Syncytial Virus showing picomolar inhibition of viral fusion, (iii) the RNA-binding viral protein HIV-1 Rev showing nanomolar affinity for the RNA segment Rev Responsive Element and (iv) the human hormone nociceptin, which induced intracellular ERK (extracellular signal-regulated kinases) phosphorylation at picomolar concentrations (the most potent agonist identified to date).[69]

An alternative method for constraining peptides is to stabilise the helical conformation *via* disulfide-linkers (**17**, Figure 1.19 a).

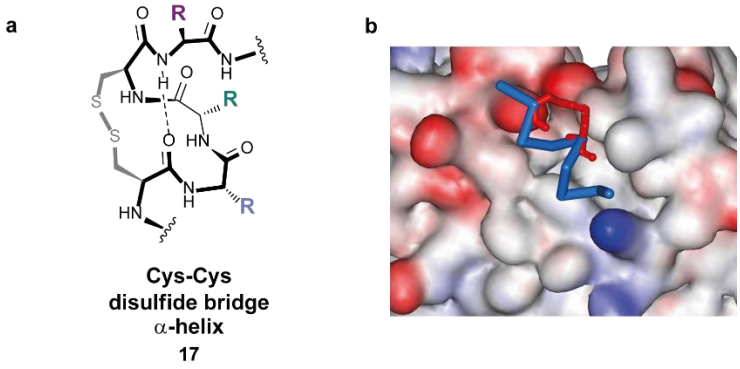

Figure 1.19 Disulfide-bridged peptide a Generic structure of a peptide stapled with a Cys-Cys disulfide bridge; **b** Crystal structure of ERα in complex with a disulfide-bridged peptide (PDB ID: 1PCG).

A remarkable example is a disulfide bridged nonapeptide reported by Spatola and co-workers which was shown to inhibit the ERα/co-activator interaction with an inhibition constant an order of magnitude higher than the lactam bridged analogue (K_i = 25 nM *vs* 220 nM).[70] An X-ray crystal structure of the stapled peptide bound to ERα (PDB ID: 1PCG; Figure 1.19 b) showed that the mimetic adopted a helical conformation. The result was particularly interesting as CD spectra indicated minimal helicity for this peptide in solution, suggesting that conformational changes were induced upon binding.

Arora and co-workers devised an alternative strategy for constraining α-helices using a hydrogen bond surrogate (HBS). The method employs ring-closing metathesis on olefin-bearing residues at the *i* and *i* + 4 positions, resulting in a covalent linkage *in lieu* of a native main-chain hydrogen bond (**18**).[71]

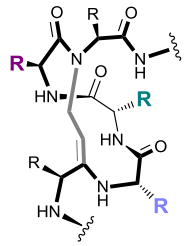

Such a strategy is attractive as it overcomes the limit of side-chain tethers, which block at least one face of the putative helix. Several examples in which this approach has been successfully applied have been reported. A highly helical HBS-peptide of the Bak BH3 α-helix was shown to bind to Bcl-x_L with a dissociation constant value of 69 nM.[72] A HBS-helix derived from the *C*-peptide from gp41, also actively bound to the *N*-terminal hydrophobic pocket thus inhibiting the gp41-mediated cell fusion (IC_{50} value of 43 μM).[73] Similarly, a HBS-helix of the *C*-terminal transactivation domain of HIF-1α (hypoxia-inducible factor 1 alpha) showed a K_d value of 420 nM for binding to p300 (E1A binding protein 300) CH1 domain and down-regulated VEGF (vascular endothelial growth factor) transcription.[74] A cell-permeable synthetic α-helix was also shown to disrupt the interaction between the guanosine-triphosphate-binding protein Ras and the guanine nucleotide exchange factor SOS, downregulating Ras signalling in response to receptor tyrosine kinase activation.[75]

Finally, Alleman and co-workers developed a photocontrolled approach based on the BH3 domain peptides of Bak and BID to target the anti-apoptotic protein Bcl-x_L (Figure 1.20 a-b).[76]

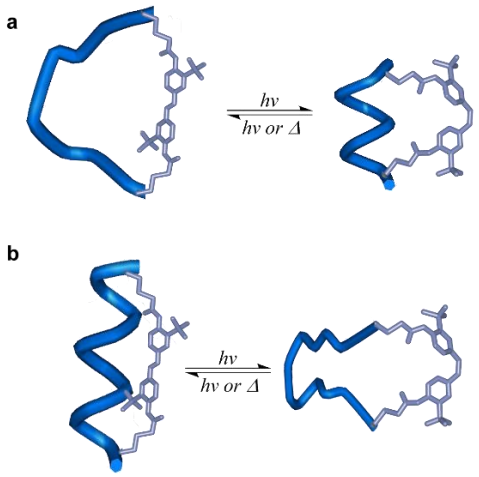

Figure 1.20 Photocontrolled α-helices a Irradiation of peptides containing an azobenzene crosslinker introduced *via i*, *i* + 4 or *i*, *i* + 7 cysteine linkages undergo *trans*/*cis* isomerisation forming a stabilised helix; **b** Irradiation of peptides containing an azobenzene crosslinker introduced *via i*, *i* + 11 cysteine linkages undergo *trans*/*cis* isomerisation destabilising the helical structure.

The strategy was based on the introduction of an azobenzene crosslinker *via* cysteine residues at the *i*, *i* + 4, *i* + 7 or *i* + 11 positions, which undergoes *cis/trans* isomerisation on irradiation thus stabilising or destabilising the helical structure. Bak- and BID-based peptides in their helix-stabilised configurations displayed higher affinities for Bcl-x_L than their destabilised counterparts, with examples of a 200-fold selectivity for binding to Bcl-x_L over *h*DM2.[76]

1.3.2 Type III mimetics

The use of simple synthetic molecules that can mimic the helical secondary structure of proteins is a logical but challenging progression from using type I inhibitors of PPIs. Proteomimetics are considered type III mimetics since they match the topography of the original helix motif by mimicking the spatial orientation of its key residues.[30] The potentially improved synthetic accessibility and enhanced drug-like character of such ligands could have advantages with respect to type I mimetics. Furthermore, template scaffolds could overcome the inherent limitations of type II mimetics in that modular approaches should be transferable to different PPIs simply by matching side-chains to the helical target of interest.

The earliest small molecules designed to mimic the residues of an α-helix involved in PPIs were the trisubstituted indanes (**19**, Figure 1.21 a) reported by Horwell *et al.*[77].

As suggested by molecular modelling calculations, this relatively rigid scaffold allows the three substituents to reproduce the orientation in space of the α-helix side chains at *i* - 1, *i* and *i* + 1 positions. Although the template does not cover a surface area large enough to properly represent an α-helix mimetic, binding assays between NK1, NK2 and NK3 (neurokinin 1, 2 and 3) tachykinin receptors and some derivatives with large hydrophobic side chains like Phe-Phe and Trp-Phe showed micromolar inhibition, thus confirming that non-peptidic small molecules can successfully be used to disrupt PPIs.[77]

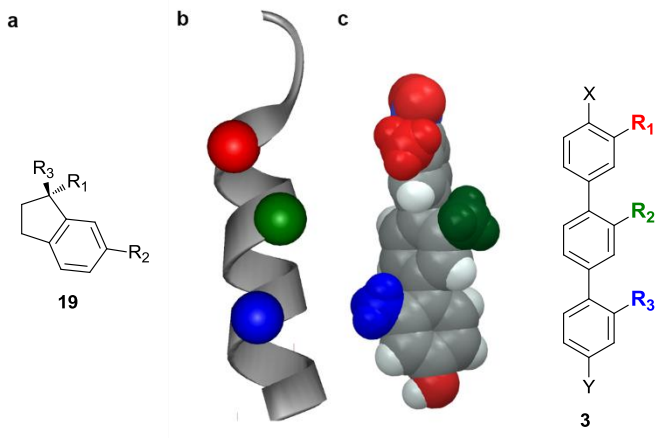

Figure 1.21 Original strategy for the design of type III mimetics a The indane template; **b** Representation of an α-helix highlighting the alignment of the *i*, *i* + 4 and *i* + 7 residues along a single face; **c** Core structure of a 3,2',2"-terphenyl scaffold and X-ray crystal structure in space-filling format; the colour scheme shows the good matching between the projection of the ortho side chains in the proteomimetic and the key residues of the helix.

Following this pioneering work, Hamilton and co-workers identified the first true α-helix mimetic.[18] They reported the synthesis and conformational analysis of a series of trisubstituted 3,2',2"-terphenyl derivatives (**3**, Figure 1.21 c) in which the aryl core assumes a staggered conformation projecting the ortho substituents to mimic the position of the *i*, *i* + 3(4) and *i* + 7 residues of the helix (Figure 1.21 b-c).

The first family of mimetics was designed to target the interaction between calmodulin (CaM) and the α-helical domain of small muscle myosin light chain kinase (smMLCK).[18] Competition assays using the plasma membrane helical peptide C20W which selectively binds to the *C*-terminal domain of CaM, showed that derivative **3a**, which possesses side chains mimicking Trp800, Thr803 and Val807 residues of smMLCK, acts as a potent inhibitor of this PPI (IC_{50} = 9 nM).

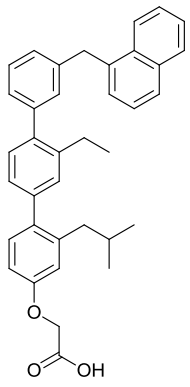

3a

Terphenyl derivatives with side chains that could mimic the key leucine and isoleucine residues were synthesised as structural mimetics of the α-helical heptad sequence of the *C*-terminal domain of gp41. A series of assays showed that mimetic **3b** disrupted the PPI with IC_{50} values in the micromolar range.[78]

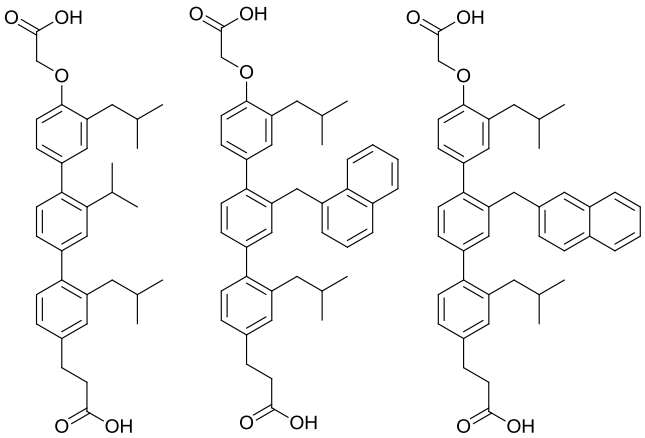

Analogues of **3b** were also tested against the Bcl-x_L/Bak interaction.[79] Hydrophobic side chains were incorporated in the terphenyl mimetics in order to simulate the key binding residues of the Bcl-x_L helix and FP assays confirmed that these molecules can also effectively disrupt this PPI, yielding K_d values in the micromolar range, with derivative **3c** being the strongest inhibitor (K_d = 114 nM). Docking studies further supported the validity of the strategy by showing that the molecule indeed mimicked the central cylindrical core of the native Bcl-x_L helix and interacted with the protein by hydrophobic contacts between the substituents and the protein pocket. The ability of these mimetics to work in intact cells was subsequently demonstrated through inhibition of the BH3-mediated interaction with Bcl-x_L in human embryonic kidney 293 (HEK293) cells treated with the terphenyls.[80]

A vital feature in the design of type III mimetics is the ability to selectively modulate different PPIs. Selective inhibition of the Bcl-x_L/Bak interaction over the p53/*h*DM2 PPI was indeed achieved by a suitable exchange of a methyl-1-naphthyl **3c** for a methyl-2-naphthyl **3d** side chain in the terphenyl sequence.

Despite the potential for an iterative synthetic strategy, this α-helix mimetic family suffers from a relatively high hydrophobicity.[81] Considerable effort has therefore been focused on identification of scaffolds with more versatile syntheses

and properties that are consistent with 'drug-like' molecules.[82,83,84] For instance, Hamilton and co-workers replaced the benzyl core with pyridine (**20**, Figure 1.22 a) although this scaffold suffers from a challenging 15-step synthesis and biological properties have yet to be reported.[85]

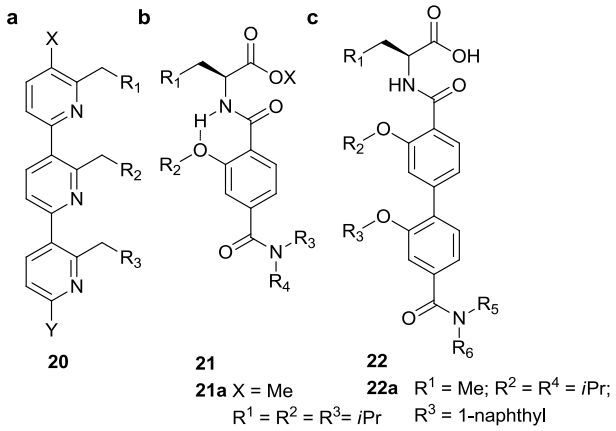

Figure 1.22 Proteomimetic scaffolds with hydrophilic backbones I a Terpyridine-based; **b** Terephthalamide-based; **c** 4,4'-Dicarboxamide-based.

Further notable examples are the terephthalamide (**21**, Figure 1.22 b) and the 4,4'-dicarboxamide (**22**, Figure 1.22 c) templates developed by Hamilton and co-workers, which present increased drug-like character thanks to their improved solubility and retain the advantage of a desirable synthetic route.[86,87]

Notably, the inhibitory activity of the most potent compounds of the series against the Bcl-x_L/Bak interaction was comparable to or lower than the terphenyl derivatives (Figure 1.22 b-c **21a**, K_i = 0.78 μM; **22a**, K_i = 1.8 μM). An interesting observation from these experiments is that mimicking an additional 'hot-spot' residue of the native α-helix in the 4,4'-dicarboxamide scaffold does not always result in an improvement of potency. Although counterintuitive, this result has been confirmed by the biological data obtained for an oligobenzoylurea template developed to access longer mimetics and where every secondary aryl unit is replaced with a more hydrophilic acylurea isostere (**23**, Figure 1.23 a). [88,89] The potential of this scaffold to act as a template for PPI inhibitors was shown through inhibition of the Bcl-x_L/Bak interaction, although these compounds displayed lower inhibitory potency than the terephthalamide and 4,4-dicarboxamide templates, with the most potent derivative (**23a**, Figure 1.23 a) having a K_i value of 2.4 μM.

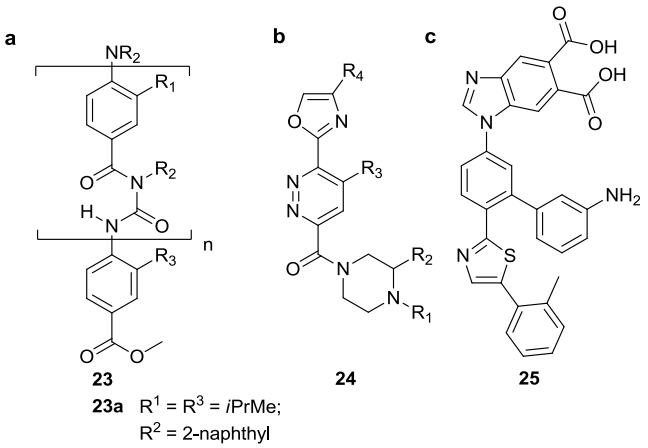

Figure 1.23 Proteomimetic scaffolds with hydrophilic backbones II a Oligourea; **b** Oxazole-pyridazine-piperazine; **c** 5-6-5-Imidazole-phenyl-thiazole.

Rebek *et al.* developed a new oxazole-pyridazine-piperazine mimetic with hydrophobic side chains to reproduce the *i*, *i* + 4 and *i* + 7 residues of the helix (**24**, Figure 1.23 b).[90] The incorporation of more hydrophilic components allowed access to a molecule with both a hydrophobic surface for recognition and a 'wet edge' rich in hydrogen bond donors and acceptors, which enhanced water solubility. Furthermore, the introduction of an oxazole ring helped to increase the rigidity of the α-helix mimetic and thus decrease the loss of entropy upon binding. A small library of compounds yielded Bcl-x_L/Bak inhibitors, although these were less potent than their terphenyl analogues.

A 5-6-5 imidazole-phenyl-thiazole scaffold (**25**, Figure 1.23 c) has also been designed by Hamilton and co-workers in which the terminal positions of the original terphenyl were replaced with more hydrophilic five-membered heterocycles.[91] Derivative **25** was specifically designed to disrupt the PPI between Cdc42 (cell division cycle 42) and Dbs (Dbl's big sister) which regulates cancer cell resistance to cytotoxic therapies and it showed an IC_{50} value of 67.0 μM in a mant-GDP fluorescence assay.

A desirable approach to the identification of potent inhibitors of helix mimetics would be to generate libraries of ligands. The design of helix mimetics that are amenable to library synthesis is therefore gaining attention. Among the synthesis of small molecule inhibitors of PPIs, in the last years a new appealing family has emerged: aromatic oligoamides. What makes this family so appealing is the

accessibility due to the formation of the amide bond and the *predictable folding pattern*, which is predominantly controlled by the conformation of the aryl-NHCO-aryl bond and by the interaction with ortho substituents.[29] Rotations around the NHCO-aryl and CONH-aryl bonds are indeed restricted by a series of hydrogen-bonds and because of conjugation with the aromatic groups.

As shown in Figure 1.24, the preferred *anti* or *syn* conformation of the NHCO-aryl bond can be easily biased by the presence of exo or endocyclic H-bond acceptors/donors.

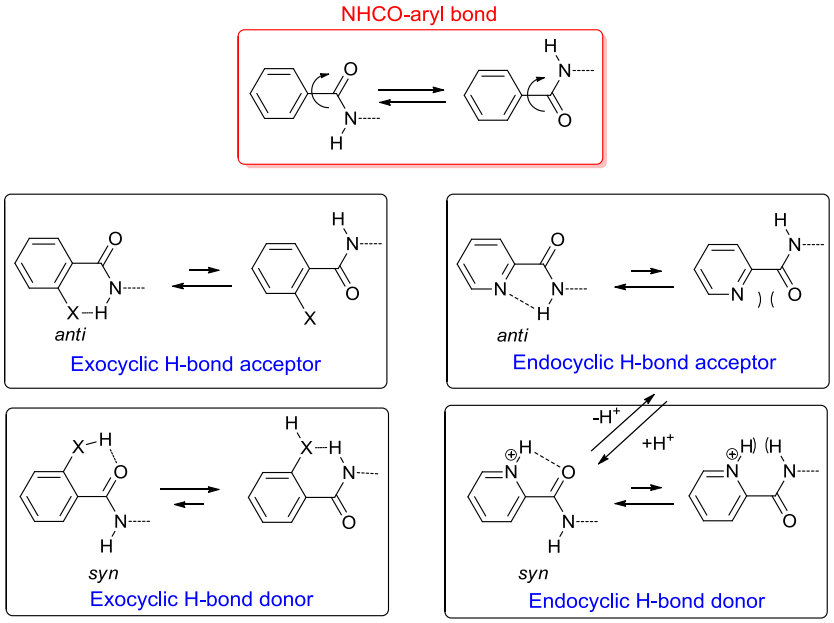

Figure 1.24 Preferred geometry of NHCO-aryl bond.

Similar considerations can thus be made for the geometry of the CONH-aryl bond, as shown in Figure 1.25.

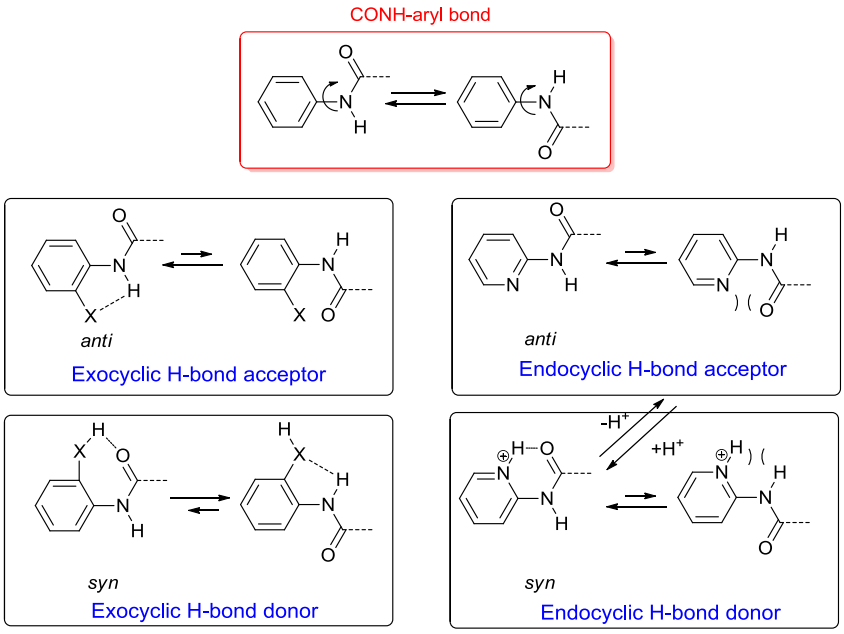

Figure 1.25 Preferred geometry of CONH-aryl bond.

The extent of stabilisation of the folding pattern depends on the H-bonding ability of the two partners and on the repulsive interactions between adjacent groups, but in general, these interactions allow accurate prediction of the conformational preference of the oligoamide.

Huc first reported the synthesis and structural analysis of a family of hydroxyl-substituted oligopyridine dicarboxamide helical foldamers (**26**, Figure 1.26 a).[92] X-Ray diffraction studies supported by NMR analysis showed that derivatives containing benzyloxy, hydroxy and hydroxylate moieties adopt robust helical patterns stabilised by intramolecular hydrogen bonds between the amide protons and the pyridine nitrogens, even in water, thus revealing a strong improvement in stability compared to short α-and β-peptides.

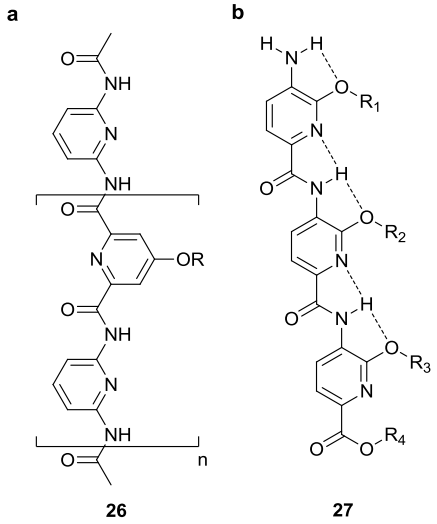

Figure 1.26 Proteomimetic scaffolds amenable to library assembly I a Oligopyridine dicarboxamides; **b** Trispyridylamide-based.

Encouraged by this result, Hamilton and co-workers[93] reported the design and synthesis of a trispyridylamide scaffold (**27**, Figure 1.26 b). Molecular modelling studies, confirmed using X-ray crystallography, showed that this template is almost completely planar. Conformational preference is induced by intramolecular hydrogen-bonds between the NH group of the amides and the ortho alkoxy functionalities, thus projecting the three side-chains on the same face of the molecule and in the same orientation of the *i*, *i* + (3)4 and *i* + 7 residues of an α-helix. Furthermore, X-ray analysis on the tri-isopropyl substituted derivative revealed that the side-chains were tilted at 45°, presumably to optimize the interaction between the lone-pair on the oxygen atom and the amide-NH functionality. The study revealed also that the distances between the amide proton and either the pyridine nitrogen atom (2.1 Å) or the oxygen atom of the alkoxy side-chain (2.2 Å), are consistent with the formation of five membered rings within the structure.

A significant number of derivatives were synthesised and their ability to disrupt the Bcl-x_L/Bak PPI was assessed by FPA which allowed identification of two oligopyridines (**27a**, **27b**) with K_i values of 2.3 and 1.6 μM respectively.[93] Subsequent studies revealed this scaffold to be suitable for modulation of islet amyloid polypeptide (IAPP) aggregation. [94]

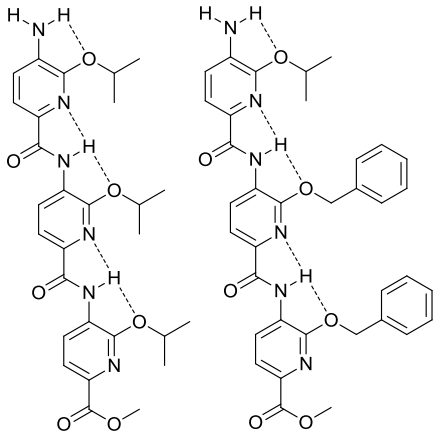

27a **27b**

Although structural rigidity is a pre-requisite of a helix mimetic, a degree of flexibility can help to maximise interactions with the target protein through 'induced-fit'. Several groups developed oligobenzamide mimetics based on Hamilton's original pyridylcarboxamide scaffold in which the pyridyl ring has been replaced by a benzene ring, removing one of the pre-organizing hydrogen-bonding interactions. Structural studies on these derivatives[95] suggested that the backbone curvature can be controlled to match that of target α-helices by using combinations of pyridine and benzene rings in the scaffold. Fletcher and co-workers recently described a series of BH3 mimetics where the distribution of pyridine and benzene rings was selected to control the extent of intramolecular hydrogen bonding and therefore flexibility (**28**, Figure 1.27 a) resulting in nanomolar inhibitors that were also shown to possess activity in cell viability assays.[96] In particular, derivative **28a** (Figure 1.27 a) was recently reported as an inhibitor of the Bcl-xL/Bak and Mcl-1/Bak PPIs, showing IC_{50} values of 395 ± 54 nM and 10.21 ± 0.83 μM respectively in a FPA.[97] The mimetic also induced apoptosis in multiple cancer cell lines, as evidenced by a TUNEL (terminal deoxynucleotidyl transferase dUTP nick end labeling) assay.[97]

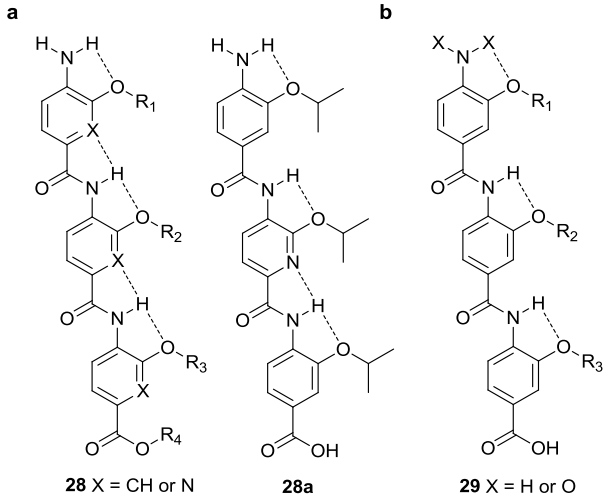

Figure 1.27 Proteomimetic scaffolds amenable to library assembly II a Mixed oligopyridyl-oligobenzamides; **b** 3-*O*-Alkylated oligobenzamides.

The Wilson group also developed a 3-*O*-alkylated oligobenzamide scaffold (**29**, Figure 1.27 b),[98, 99] which is attractive because it retained side-chain flexibility in order to maximise the interactions necessary to have good binding affinity. A library of compounds was designed to target the p53/*h*DM2 PPI and tested in a FA competition assay, which allowed identification of micromolar inhibitors of this interaction, with derivatives **29a** and **29b** showing IC_{50} values of 1.6 and 1.0 μM respectively. The group also reported a microwave-assisted solid-phase strategy which offers a route to a large library of new molecules.[100]

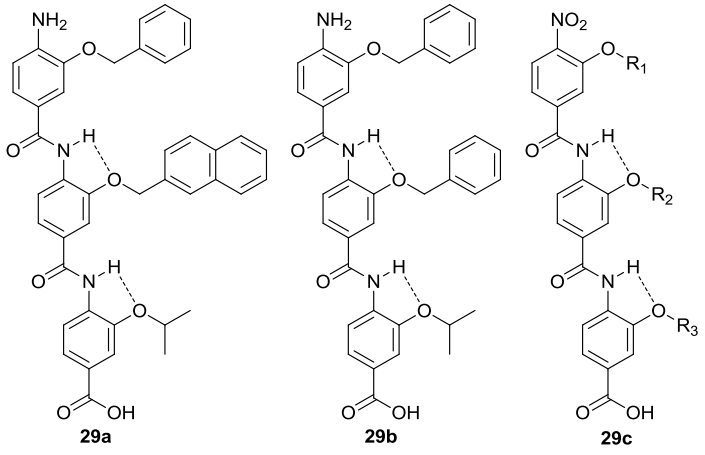

In parallel, Ahn's [101] and Boger's[102] groups synthesised some analogous nitro-acid templates to test their ability to act as PPIs inhibitors (**29c**). In particular, Boger and co-workers prepared a > 8000 member library which was initially tested

against the p53/*h*DM2 PPI, although showing lower potency than their amino-acid counterparts. Subsequently, the same library was tested against the gp41 assembly, allowing the identification of micromolar inhibitors with effective activity in cell-fusion assays (IC_{50} = 5-8 μM).[103]

In an effort to improve the 'drug-like' character of this family of mimetics, the Wilson group recently reported on a 3-*O*-alkylated scaffold functionalised with a PEG (polyethylene glycol) chain (**30**, Figure 1.28 a).[104] This derivative, carrying a 'wet-edge', displayed improved solubility but retained micromolar activity against the p53/*h*DM2 interaction (IC_{50} = 7.54 ± 0.37 μM).

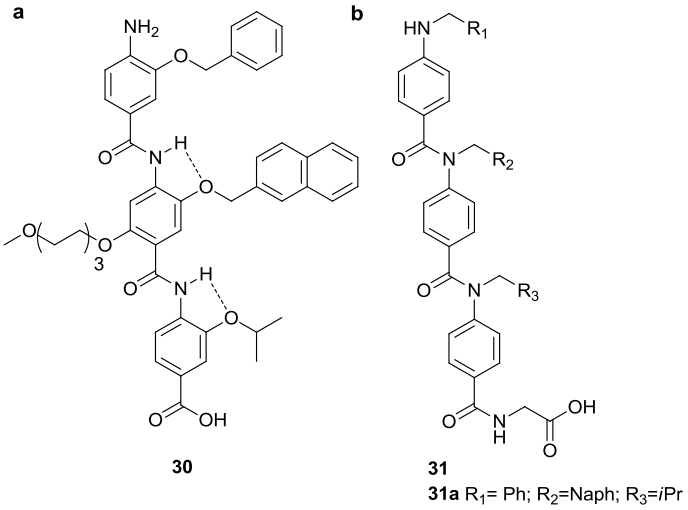

Figure 1.28 Proteomimetic scaffolds amenable to library assembly III **a** PEG-functionalised 3-*O*-alkylated oligobenzamide; **b** *N*-Alkylated oligobenzamides.

The first solid-phase method for synthesis of an α-helix mimetic was also described in 2010 by the Wilson group. The development of such a strategy represented an effective and elegant way to generate molecular diversity *via* accessible modular synthesis amenable to library assembly. *N*-Alkylated oligobenzamides (**31**, Figure 1.28 b) were obtained using this strategy and tested against the p53/*h*DM2 interaction with **31a** being the strongest inhibitor (IC_{50} = 2.8 μM). [105,106]

Oligobenzamides with side chains attached directly to the aromatic rings have been described by the Guy group (**32**, Figure 1.29).[107] A library of 173 compounds targeting the p53/*h*DM2 interaction was developed through structure-based

computational design and synthesised using solution phase parallel chemistry. The most potent inhibitor in this series was compound **32a** with K_i = 12 μM.

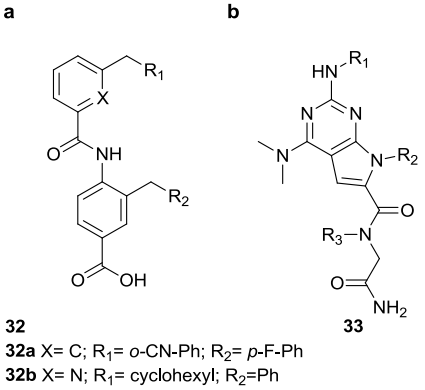

Figure 1.29 Proteomimetic scaffolds amenable to library assembly IV a 3-Alkylated oligobenzamides; **b** Pyrrolopyrimidine-based.

Mixed pyridyl/benzamide dimers with side chains directly attached to the aromatic rings were also investigated by Craik and co-workers as mimetics of an α-helix found at the dimerisation interface of the Kaposi's Sarcoma-Associated Herpesvirus Protease.[108] Screening a library of 182 compounds in a fluorogenic activity assay identified compound **32b** (Figure 1.29 a) as the most potent inhibitor (IC_{50} = 3.1 ± 0.2 μM).

Lim and co-workers developed a new pyrrolopyrimidine-based α-helix mimetic (**33**, Figure 1.29 b).[109] The scaffold possesses the advantages of being rigid and pre-organised whilst also presenting a 'wet-edge' for water solubility. The work is most noteworthy in that a solid-phase strategy was developed which allowed divergent synthesis of a library of 900 members. Assays against the p53/*m*DMX and p53/*m*DM2 PPIs conducted on 90 randomly chosen members of the library identified low micromolar inhibitors. The most potent compounds of the series were also shown to increase p53 levels and activity in cells which was indicative of cell-permeability and release of p53 from its complex with *h*DMX or *h*DM2.

One limiting feature of the α-helix mimetics described so far is that they mimic only one face of the α-helix. Recent developments have been described by the Hamilton group who disclosed a variation on the terphenyl scaffold that mimics an additional residue in the *i* + 3 position by incorporating an indane ring in the central

position of the terphenyl (**34**, Figure 1.30 a).[110] Ahn and co-workers further adapted the *O*-alkylated oligobenzamide scaffold by placing a second alkoxy group on the opposite side of the aromatic ring (**35**, Figure 1.30 c)[111] thus reproducing the *i*, *i* + 2, *i* + 5 and *i* + 7 residues of an α-helix (Figure 1.30 b), whilst the Hamilton group similarly appended an amide side chain.[112]

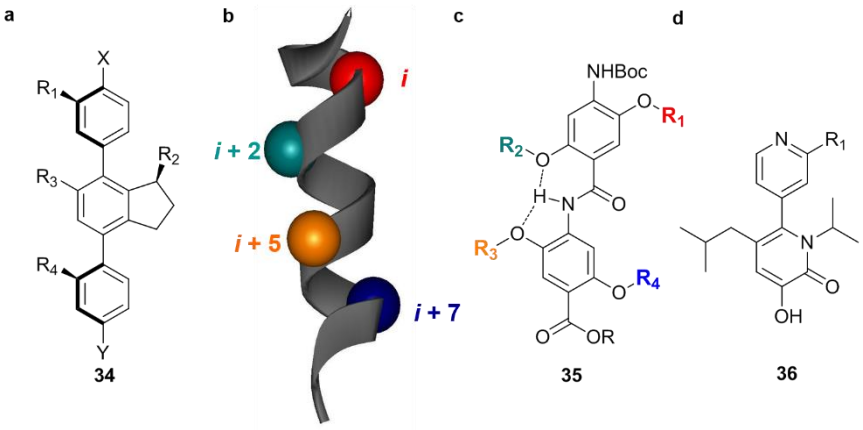

Figure 1.30 Proteomimetics with multifacial mimicry properties a Diphenylindane-based; **b** Representation of an α-helix highlighting the alignment of residues *i*, *i* + 2, *i* + 5 and *i* + 7; **c** Bis-benzamide template; **d** Pyridyl pyridone template.

The Hamilton group also described a pyridyl-pyridone scaffold (**36**, Figure 1.30 d) designed to target the ERα/co-activator interaction.[113] The scaffold mimics more than one helical recognition face by incorporating a leucine surrogate on the pyridone ring to reproduce the *i* + 3 residue of the native helix and hence reproduce the α-helical LXXLL motif of the co-activator proteins. A small series of derivatives gave inhibition constants in the low micromolar range.

Several other examples of potential α-helix mimetics have been reported in the past years. Notable are the oligooxopiperazine scaffold (**37**, Figure 1.31 a) reported by the Arora group,[114] the 1,4-dipiperazino benzene family (**38**, Figure 1.31 b) developed by Konig and co-workers[83], the oligoquinoline template (**39**, Figure 1.31 c) reported by Moreau and co-workers [115] and the 6/6/6/6 *trans*-fused polycyclic ethers family (**40**, Figure 1.31 d) exploited by the Hirama group.[82] No reports on inhibition of PPIs have been described to date for any of these scaffolds.

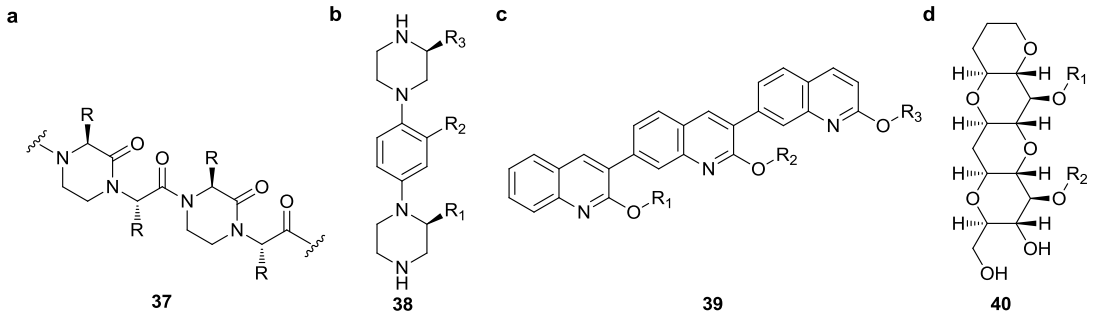

Figure 1.31 Example of Type III mimetics a Oligooxopiperazine scaffold; **b** 1,4-dipiperazino benzene scaffold; **c** Oligoquinoline-based; **d** 6/6/6/6 trans-fused polycyclic ethers.

1.4 Project aims

As this chapter highlights, α-helix mediated PPIs are an important target for therapeutic intervention. Considerable effort has been directed in the past decade towards the design of type I and type III α-helix mimetics, which could overcome the limitations encountered by small molecule inhibitors generated through traditional drug-discovery approaches. In spite of the potential shown by these foldamers, the discovery of mimetics that can target PPIs in a *predictable* manner remains a major challenge.

The Wilson group is interested in the development of aromatic oligoamide proteomimetics. Since conformational diversity plays a key role in modulating protein recognition, this project was aimed at developing a better understanding of the conformational properties of this family of mimetics, in order to identify key features required to reproduce the functional role of α-helices and to achieve specificity and selectivity towards different PPIs. The 3-*O*-alkylated oligobenzamide scaffold, which was shown to act as an effective α-helix mimetic and micromolar inhibitor of the p53/*h*DM2 PPI,[98, 99] constituted the starting point for these studies.

The present work aimed at investigating the effect that non-covalent interactions could have on the conformational preference of aromatic foldamers,[116] and at the generation of libraries of mimetics with diverse side-chains, backbone and polarities for SAR studies.

A new regioisomeric 2-*O*-alkylated oligobenzamide scaffold (Figure 1.32 a, Chapters 2 and 3) was initially designed with the hypothesis that minor variations in the backbone architecture and hydrogen bonding pattern could have an impact on the conformational preference of these oligomers and affect molecular recognition properties. [117,118]

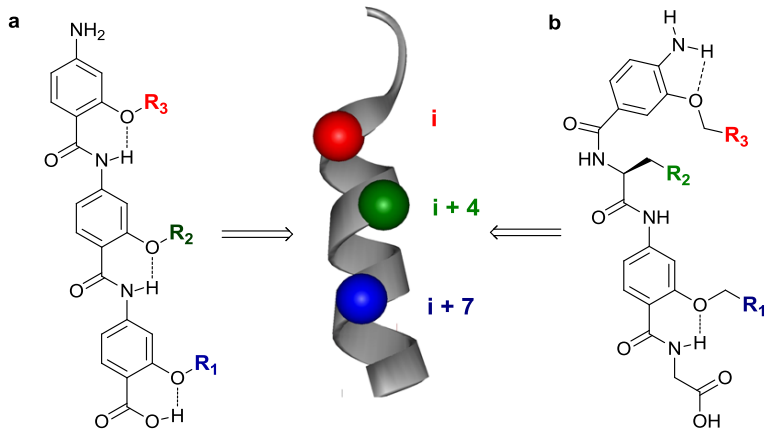

Figure 1.32 Novel aromatic α-helix mimetic foldamers showing mimicry of the 'hot spot' residues of an α-helix (in CPK format and colour coded) a 2-*O*-Alkylated oligobenzamide scaffold; **b** Hybrid benzamide scaffold.

A hybrid benzamide α-helix mimetic was subsequently designed (Figure 1.32 b, Chapter 4), where the structural rigidity of the oligobenzamide backbone was broken through substitution of the middle aryl-unit with an amino acid thus introducing irregularity and different H-bonded conformations. It was envisaged that this strategy would allow the generation of a mimetic with access to a wider conformational space and that the chiral nature of the scaffold would enable studies on the effect of stereocentres in molecular recognition.

The combination of these results could represent a significant starting point to build a rule based approach for the design of effective foldamers targeted to PPI inhibition.

Chapter 2

Conformational properties of 2-*O*-alkylated benzamides

This chapter will discuss the design, synthesis and conformational analyses of 2-*O*-alkylated *p*-benzamide dimers. The study was performed to understand the role played by non-covalent interactions in defining conformational preferences and long range inter/intramolecular order for this class of aromatic foldamers. Comparison with the 3-*O*-alkylated family,[98, 99] both in solid and solution-state, revealed the importance of hydrogen bonding and side-chain packing in determining preferred conformations. Given the potential shown by this class of foldamer to act as α-helix mimetics, the insights offered by these results should be important for inhibitor design.

The work reported in this chapter formed the basis of the following publication:

P. Prabhakaran, **V. Azzarito**, T. Jacobs, M. J. Hardie, C. A. Kilner, T. A. Edwards, S. L. Warriner, A. J. Wilson, *Tetrahedron* **2012**, *68*, 4485-4491.[117]

2.1 Design and synthesis of 2-*O*-alkylated benzamides

The design and synthesis of novel foldamers represents one of the biggest challenges in contemporary chemical biology, since these scaffolds can be tailored as functional architectures to mimic the complexity of natural biopolymers.[1, 119, 120] Non-covalent interactions have been shown to play a key role in determining the preferred architecture adopted by a range of oligomers.[18, 19, 29, 31, 48, 99, 105, 121, 122] Above all, hydrogen bonding has proven to be a significant driving force for conformational preference[12] and the introduction of this structural feature through amide linkages has therefore been extensively exploited in designing new foldamers.[29]

Previous research reported by the Wilson group,[98, 99] together with work carried out in several other groups,[87, 93, 96, 101, 102, 123] has identified 3-*O*-alkylated aromatic oligoamides as a new class of α-helix mimetics (see also Chapter 1).

The 3-*O*-alkylated template enables cyclic five membered [S(5)] intramolecular H-bonding [124, 125] between the oxygen of the alkoxy substituent and the amide protons, which stabilises the structure in a rod-shaped conformation and restricts rotation around the NH-Ar axis (Figure 2.1 a).

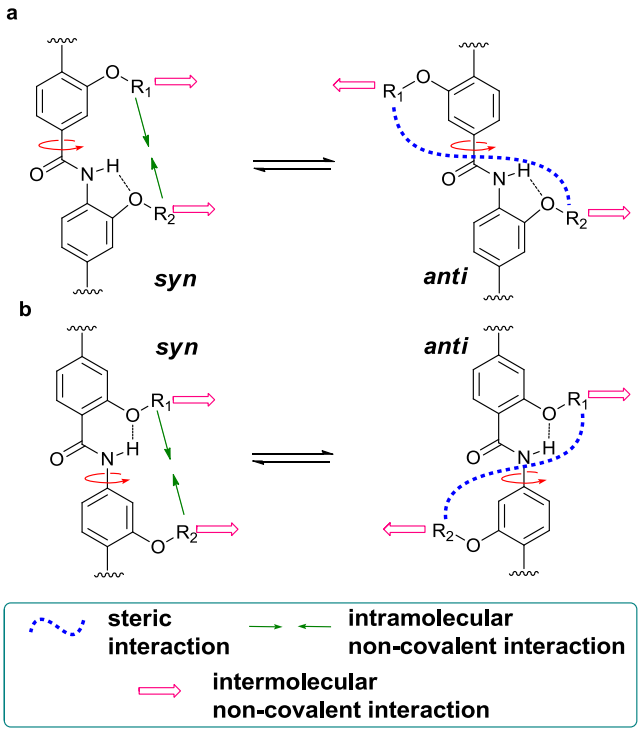

Figure 2.1 Role of non-covalent interactions in defining the conformational properties of aromatic oligoamides a 3-*O*-alkylated benzamides with a S(5) intramolecular H-bond; **b** 2-*O*-alkylated benzamides with a S(6) intramolecular H-bond.

In an effort to rationalise the effect of non-covalent interactions in driving the preferred conformation, a novel 2-*O*-alkylated template was therefore designed with the hypothesis that the introduction of a six-membered [S(6)] intramolecular H-bonded ring would lock the rotation around the Ar-CO axis and change the conformational preference of this scaffold (Figure 2.1 b).

The series was investigated with model dimers as they possess all the key structural features of longer oligomers. Together with the possibility of intramolecular

H-bonding through the linking amide moiety, the two side-chains of the dimer can be oriented on the same (*syn*) or opposite (*anti*) side of the backbone (Figure 2.1 a-b). Since the preferred orientation can be driven by either intra- or intermolecular side-chain/side-chain interactions (green and pink arrows in Figure 2.1), but also by steric effects (blue dashed line in Figure 2.1), structural studies on these derivatives provide insight on the role that such interactions play in defining backbone architecture and molecular packing for this class of foldamers.

2.1.1 Monomer syntheses

Monomers of the 2-*O*-alkylated series were synthesised by adapting the 3-step route previously reported for the 3-*O*-alkylated scaffold (Scheme 2.1).[98]

Esterification of commercially available 2-hydroxy-4-nitro benzoic acid (**41**), followed by an aqueous work-up, gave access to methyl-ester **42** in excellent yield. Subsequent alkylation of the hydroxyl group with the appropriate bromide provided building blocks containing both aliphatic and aromatic side-chains.

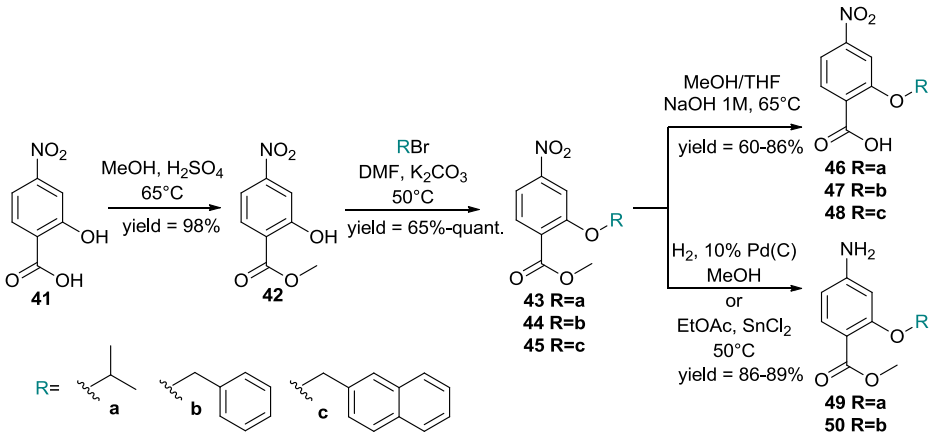

Scheme 2.1 Synthetic route to 2-*O*-alkylated *p*-nitrobenzoic acid and *p*-aminobenzoate monomers.

Reduction of the nitro-group and hydrolysis of the ester moiety were performed on these common building blocks in order to obtain monomers for the synthesis of the dimers.

A simple base-catalysed hydrolysis was used for the synthesis of the 2-alkoxy-4-nitro benzoic acid derivatives (**46**-**48**), which were obtained in good yields after aqueous work-up.

Two different approaches were followed to access the methyl-4-amino-2-alkoxy-benzoate derivatives (**49** and **50**). Palladium-catalysed hydrogenation[126] was used to reduce monomer **49** containing an aliphatic side-chain, however, the ability of the transition-metal-catalysed hydrogenation to cleave benzylic-type moieties made this method unsuitable for the synthesis of amine **50**. Reduction mediated by tin(II)-chloride provided a convenient alternative and led to pure products in good to excellent yields.[127]

2.1.2 Dimer syntheses

2-*O*-Alkylated *p*-benzamide dimers **51**-**53** were obtained following the previously reported chain elongation strategy[98] *via* coupling reactions between 2-alkoxy-4-nitro benzoic acid and methyl-4-amino-2-alkoxy-benzoate monomers (Scheme 2.2).

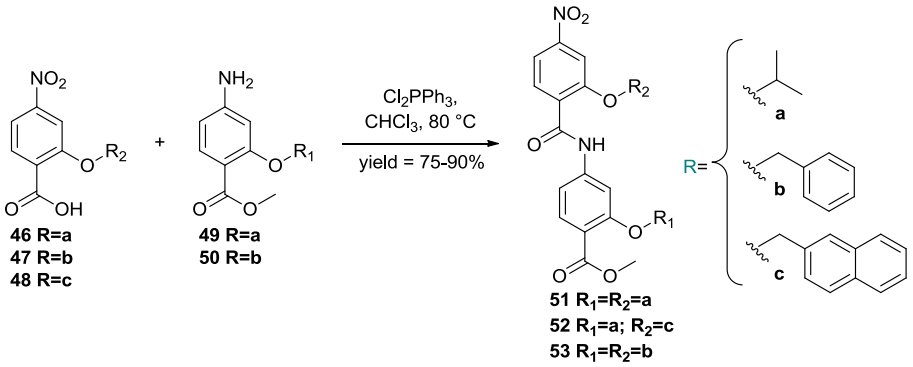

Scheme 2.2 Synthesis of 2-*O*-alkylated *p*-benzamide dimers *via* a chain elongation approach.

The chosen coupling agent was dichloro triphenylphosphorane,[128] which mediates the amide-bond formation through *in situ* pre-activation of the acid moiety as the acid chloride. Purification *via* column chromatography or SAX (strong anion exchange) chromatography led to pure dimers in good to excellent yields.

In order to compare the conformational properties of this new 2-*O*-alkylated scaffold, dimers of the 3-*O*-alkylated series were also synthesised and purified by Dr P. Prabhakaran following a similar route (**54**-**56**, Figure 2.2).

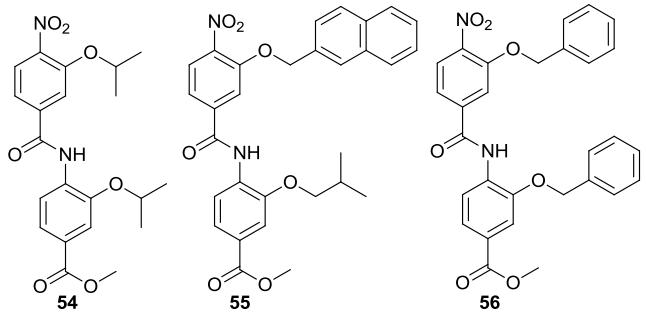

Figure 2.2 3-*O*-alkylated *p*-benzamide dimers employed in conformational studies.

2.2 Solid-state conformational analyses

Single crystals of the 2-*O*-alkylated *p*-benzamide dimers **51** and **52** were grown by the slow evaporation of a chloroform or methanol solution respectively (for further details see Chapter 6). Crystals of the 3-*O*-alkylated *p*-benzamide dimers **54**-**56** suitable for X-ray diffraction were also grown by Dr P. Prabhakaran by either slow evaporation or diffusion methods.

Structural studies were then performed on these molecules to determine how the subtle balance between intra- and intermolecular interactions controls the conformational preference of these derivatives in the solid-state.

2.2.1 Intramolecular non-covalent interactions

The solid-state conformation of these molecules is shown in Figure 2.3 (X-ray structure determination performed by C. A. Kilner and Dr T. Jacobs). The X-ray structures confirmed that both 2-*O*-alkylated dimers **51** and **52** and 3-*O*-alkylated dimers **54**-**56** adopt an extended structure in the solid state. The distances and angles between atoms were also consistent with intramolecular H-bonding between the amide NH and the alkoxy oxygen on the neighbouring side-chain (Figure 2.3).

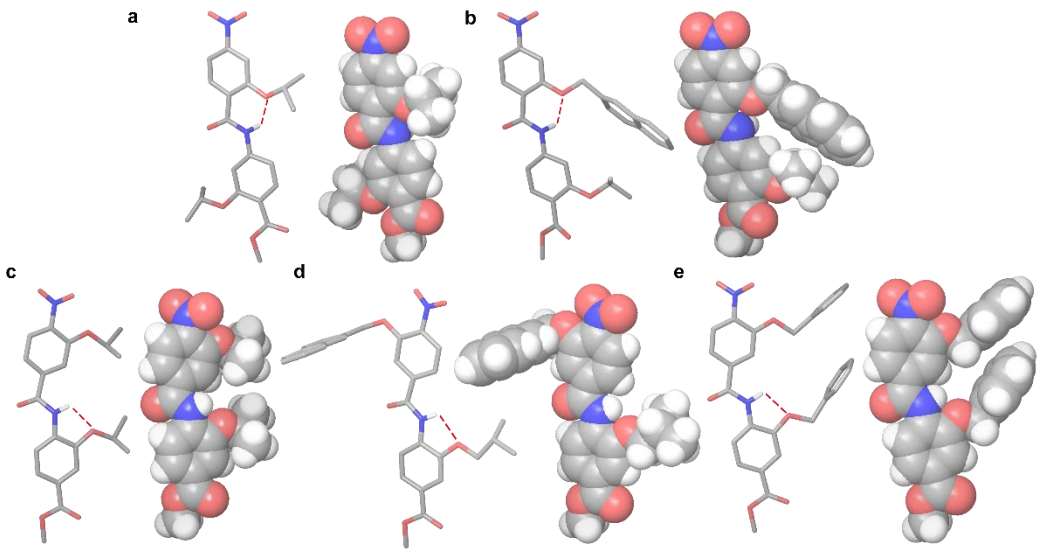

Figure 2.3 Single crystal X-ray structures of *p*-benzamide dimers shown in stick and CPK representation a Crystal structure of **51**; **b** Crystal structure of **52**; **c** Crystal structure of **54**; **d** Crystal structure of **55**; **e** Crystal structure of **56**. [Reprinted from *Tetrahedron*, Vol *68*, P. Prabhakaran, V. Azzarito, T. Jacobs, M. J. Hardie, C. A. Kilner, T. A. Edwards, S. L. Warriner, A. J. Wilson, "Conformational properties of *O*-alkylated benzamides", Pages No. 4485-4491, Copyright (2011), with permission from Elsevier (License number 3327630552830)]

The measured NH···O distances were ~ 1.9-2.0 Å for the 2-*O*-alkylated dimers and ~ 2.1-2.4 Å for the 3-*O*-alkylated dimers, in accordance with the range observed in foldamers constrained with S(6)[129] and S(5)[125] intramolecular H-bonding respectively (Table 2.1).

Table 2.1 Hydrogen bonding parameters observed in the crystal structure of 2-*O*-alkylated dimers 51 and 52 and 3-*O*-alkylated dimers 54, 55 and 56.

Dimer	$d_{NH\cdots O}$	Angle N-H··O	H-bond type
51	1.957 Å	139.55°	S(6)
52	1.961 Å	140.49°	S(6)
54	2.385 Å	96.54°	S(5)
55	2.201 Å	108.73°	S(5)
56	2.138 Å	109.36°	S(5)

In the homofunctionalised 2-*O*-alkylated dimer **51**, the isopropyl groups were oriented on opposite sides of the backbone, in an *anti* conformation (Figure 2.3 a). In contrast, its regioisomeric analogue **54** exposed the isopropyl groups in a *syn* orientation (Figure 2.3 c) and displayed a longer NH···O distance, indicative of a

weaker interaction. In a similar way, the benzyl groups of the homofunctionalised 3-*O*-alkylated dimer **56** were aligned in a *syn* orientation (Figure 2.3 d). Interestingly, a distance of 4.78 Å between the benzyl rings indicated that no π-π stacking was observed between these side-chains (reported π-π distance 3.3-3.8 Å),[130] suggesting that larger or more flexible groups are necessary for intramolecular non-covalent interactions or steric effects to occurr and determine the *syn*/*anti* ratio in these oligomers. This hypothesis was confirmed by the crystal structure of the heterofunctionalised dimers **52** and **55** (Figure 2.3 b and d).

In the 2-*O*-alkylated derivative **52** (Figure 2.3 b), the side-chains adopted a *syn* orientation. A distance of 2.78 Å between the isopropyl group and the 2-(naphthyl)methyl moiety, indicative of a CH-π interaction (reported distance < 3.2 Å),[131, 132] illustrated that sterically larger groups are able to interact with each other. However, analogous groups in the 3-*O*-alkylated dimer **55** (Figure 2.3 d) were oriented in an *anti* conformation. This result on dimer **55**, functionalised with an isobutyl group, was particularly noteworthy as it differed from observations previously reported by Hamilton and co-workers on a series of 3-*O*-*i*Bu functionalised benzamides which were shown to adopt *syn* orientations in the solid-state, apparently due to a strong propensity to interdigitate through side-chain/side-chain interactions.[133]

To gather information on the impact of the intramolecular H-bonds on the conformational properties of these *p*-benzamide derivatives, the curvature of the backbone was investigated. Crystal structures were superimposed using the software Maestro® (Figure 2.4 a-d) pairing 1-C1, 1-C4, 2-C1 and 2-C4 atoms (partial numbering of backbone is shown in Figure 2.4 a, complete numbering is given in section 6.1, Chapter 6).

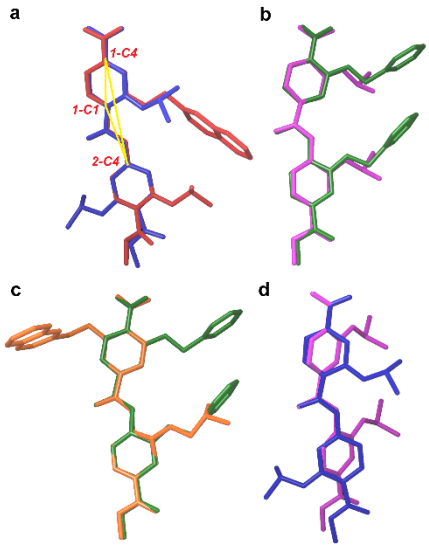

Figure 2.4 Superposition of crystal structures showing backbone orientation and curvature a Crystal structures of **51** (blue) and **52** (red) showing the connection between the carbon atoms employed to measure the backbone curvature; **b** Crystal structures of **54** (pink) and **56** (green); **c** Crystal structures of **55** (orange) and **56** (green); **d** Crystal structures of **51** (blue) and **54** (pink).

The degree of curvature of the backbone was then measured as the angle of inclination of two adjacent aromatic rings between the carbon atoms 1-C4, 1-C1 and 2-C4 (Figure 2.4 a, Table 2.2).

Table 2.2 Backbone angle of inclination for 2-*O*-alkylated dimers 51 and 52 and 3-*O*-alkylated dimers 54, 55 and 56, measured between 1-C1, 1-C4 and 2-C4 atoms.

Dimer	Angle of inclination
51	162.32°
52	163.85°
54	157.00°
55	161.45°
56	158.22°

As shown in Figure 2.4 a, b and c, the backbone of dimers of the same series retained the same curvature. However, superimposition of dimers **51** and **54** revealed a reduced backbone curvature of the 2-*O*-alkylated scaffold, which differs by about 5° (Figure 2.4 d). This data was also reflected in a higher RMSD (Root Mean Square Deviation) value obtained superimposing **51** and **54** compared to superimposition of **51** and **52** (0.153 Å *vs* 0.070 Å) and can be attributed to the difference in intramolecular H-bonding between the two scaffolds.

2.2.2 Intermolecular non-covalent interactions

The analysis on the intramolecular interactions shown by 2-*O* and 3-*O*-alkylated dimers gave preliminary insight into how non-covalent forces can influence the *syn*/*anti* preference of functional groups in these aromatic foldamers. Further studies on the solid-state packing of these dimers were performed to investigate how other forces such as steric and intermolecular interactions can influence conformational preference.

The three-dimensional packing of the homodimers **51** (Figure 2.5 a) and **54** (Figure 2.5 b) displayed intermolecular interactions between the isopropyl side-chains of two different molecules. A hydrophobic channel formed by the methyl unit of the C-terminal ester was also observed in both cases.

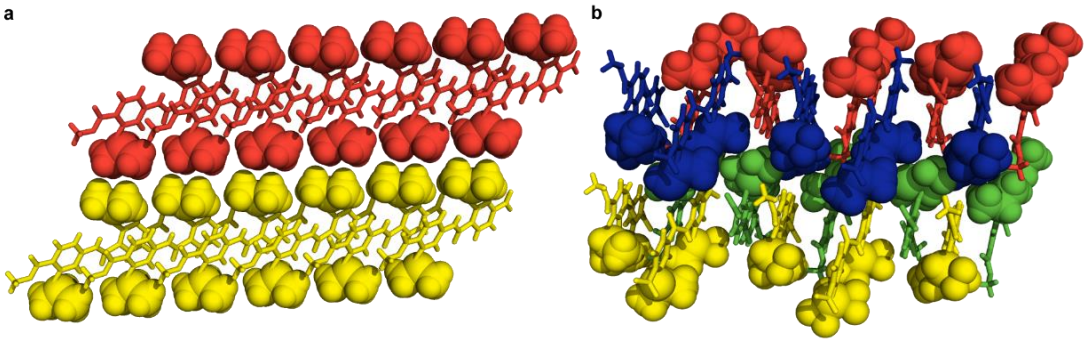

Figure 2.5 Packing diagrams for homofunctionalised dimers showing side-chain/side-chain interactions; isopropyl groups are shown in CPK format a Solid-state packing for dimer **51**; **b** Solid-state packing for dimer **54**. [Reprinted from *Tetrahedron*, Vol *68*, P. Prabhakaran, V. Azzarito, T. Jacobs, M. J. Hardie, C. A. Kilner, T. A. Edwards, S. L. Warriner, A. J. Wilson, "Conformational properties of *O*-alkylated benzamides", Pages No. 4485-4491, Copyright (2011), with permission from Elsevier (License number 3327630552830)]

In the heterofunctionalised 2-*O*-alkylated dimer **52**, intermolecular π-π stacking (3.7 Å) and benzylic CH-π (2.727 Å) interactions determined the arrangement of the side-chains in the three-dimensional space (Figure 2.6 a). The 3-*O*-alkylated dimer **55** (Figure 2.6 b) instead displayed intermolecular CH-π interactions between the isobutyl and the naphthyl groups of two different molecules (3.14-3.2 Å). Such an interaction could be the driving force for the *anti* orientation of the side-chains, explaining the conformation shown by this molecule.

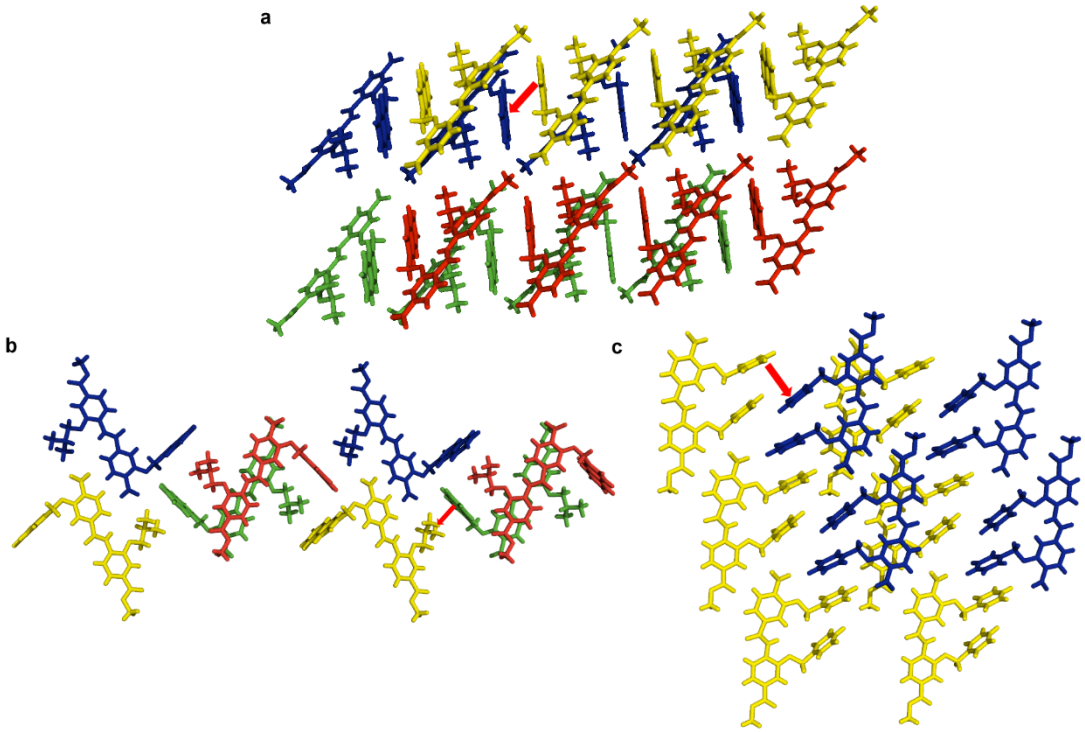

Figure 2.6 Partial three-dimentional packing diagrams a Solid-state packing for dimer **52** showing π-π stacking interactions; **b** Solid-state packing for dimer **55** showing CH-π interactions; **c** Solid-state packing for dimer **56** showing side-chain/side-chain interactions through π-π stacking. [Reprinted from *Tetrahedron*, Vol *68*, P. Prabhakaran, V. Azzarito, T. Jacobs, M. J. Hardie, C. A. Kilner, T. A. Edwards, S. L. Warriner, A. J. Wilson, "Conformational properties of *O*-alkylated benzamides", Pages No. 4485-4491, Copyright (2011), with permission from Elsevier (License number 3327630552830)]

Finally, the packing diagram for dimer **56** (Figure 2.6 c) displayed intermolecular π-π stacking (3.58 Å) between benzyl side-chains from different molecules, suggesting that intermolecular side-chain/side-chain interactions influence the orientation of the functional groups in this derivative.

In summary, the solid-state study seemed to suggest that the crystal packing plays a significant role in the side-chain positioning. However, the overall results showed that no specific driving force determined the solid-state conformational preference of these dimers and that the *syn*/*anti* ratio of functional groups was controlled by a subtle balance between intra- and intermolecular non-covalent interactions.

2.3 In silico studies

In order to investigate if a theoretical model could be employed to predict the conformational preference of these dimers, a conformational search by employing a full *Monte Carlo* search in Macromodel® was performed using the MMFFs (Merck Molecular Force Fields) method.[134] Energy minimisation was performed on dimers **51** and **54** in simulated water and chloroform respectively, in order to cover a sufficient range of polarities for comparison with the solid-state structures. The lowest energy conformations were superimposed with the respective crystal structures (Figure 2.7 a-b). The predicted models matched in both cases, showing an *anti* orientation for **51** and a *syn* orientation for **54**.

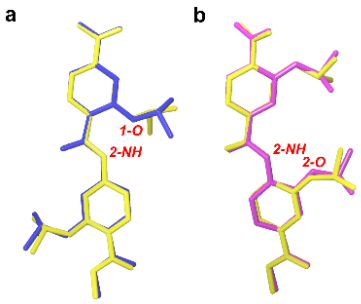

Figure 2.7 Lowest Energy conformation of dimers 51 (a) and 54 (b) (yellow) and superimposition with the crystal structures (in blue or pink respectively). Key distances: 51 2-NH···1-O = 1.957 Å (modelling) *vs* 1.857 Å (crystal structure); 54 2-NH···2-O = 2.385 Å (modelling) *vs* 2.194 Å (crystal structure).

The NH···O distance measured in both molecules, was in accordance with the empirical data and in agreement with the presence of S(6) and S(5) intramolecular H-bonding for the 2-*O* and the 3-*O*-alkylated dimers respectively. RMSD values of 0.019 Å for **51** and 0.045 Å for **54**, calculated pairing 1-C1, 1-C4, 2-C1 and 2-C4 atoms, showed the same preferred conformations between the predicted model and the crystal structure. Finally, an energy difference of + 2.963 kJ mol^{-1} from the *anti* conformation of the 2-*O*-alkylated dimer to the first *syn* conformation observed and an energy difference of + 2.409 kJ mol^{-1} from the *syn* conformation of the 3-*O*-alkylated dimer to its first *anti* conformation, further demonstrated that, within the constraints of the method (limitations of the force fields and assumptions regarding restrictions and media employed in the simulation), these models match with the respective crystal structures.

2.4 Solution-state conformational analyses

The analyses performed in the solid-state provided important information on the conformational properties of 2-*O* and 3-*O*-alkylated *p*-benzamide dimers. However, in order to design α-helix mimetics that can effectively interact with target proteins, a further understanding of the role that different non-covalent interactions can have on the conformational properties of these mimetics in solution could prove crucial.[135]

Solution-state structural analyses were therefore conducted on dimers of both series, focusing on the role played by H-bonding in defining preferred conformations.[29, 48]

2.4.1 1D NMR and *H*/*D* exchange studies

The down field shifts of amide protons in the ^{1}H-NMR spectra of dimers **51**-**56** indicated the presence of intramolecular H-bonding between the NH proton and the alkoxy oxygen atom (Table 2.3).

Table 2.3 Chemical shift data measured in $CDCl_3$.

Dimer	δ NH
51	10.17
52	9.97
53	10.01
54	8.78
55	8.80
56	8.74

The higher shifts of the amide proton in dimers **51**-**53** (> 9.8 ppm) compared to dimers **54**-**56** (< 9 ppm) was indicative of a strong S(6) intramolecular H-bonding, in accordance with studies performed on different classes of oligomers.[129, 136, 137]

With the aim of comparing the stability of a five-membered *vs* a six-membered intramolecular H-bonding constraint, the relative strength of the H-bonds in the two scaffolds was then investigated.

Linton and co-workers showed that the relative rates of a hydrogen/deuterium exchange in a ^{1}H-NMR titration can be correlated with the presence of intramolecular

H-bonds.[138] Even though the rate of this exchange can be affected by other parameters (*e.g.* the effect of electronic substituents on the acidity of the NH group and accessibility of the amide proton due to steric hindrance), it can also be correlated to the strength of the H-bonding in the molecule. The experiment was therefore performed on dimers **51** and **54** in 10% $CD_3OD/CDCl_3$ to ensure pseudo first order kinetics apply (Figure 2.8). To minimize variability, a constant baseline correction was applied and a distinct non-exchanging signal was used as an internal integration reference.

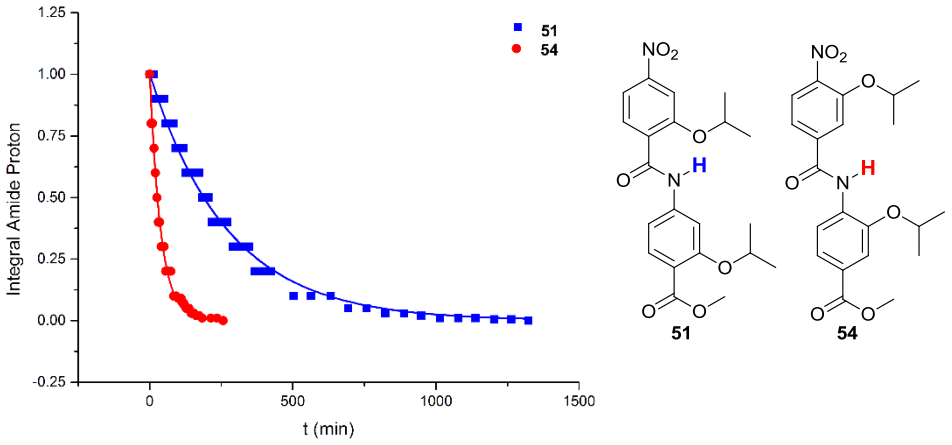

Figure 2.8 *H*/*D* Exchange kinetics for dimers 51 (blue) and 54 (red). [Reprinted from *Tetrahedron*, Vol *68*, P. Prabhakaran, V. Azzarito, T. Jacobs, M. J. Hardie, C. A. Kilner, T. A. Edwards, S. L. Warriner, A. J. Wilson, "Conformational properties of *O*-alkylated benzamides", Pages No. 4485-4491, Copyright (2011), with permission from Elsevier (License number 3327630552830)]

Rate constants (and corresponding half-lives) were determined from the slope of a non-linear least squares fit to the graph following Equation 2.1.

$$A_t = A_0 e^{-kt}$$

A_t = Integral of amide proton at time t; A_0 = Integral of amide proton at time zero (fixed at 1); k = reaction rate coefficient

Equation 2.1

The half-life of the *H*/*D* exchange was determined using Equation 2.2.

$$t_{1/2} = \frac{\ln 2}{k}$$

Equation 2.2

The obtained kinetic parameters for both dimers are given in Table 2.4.

Table 2.4 Kinetic constants and $t_{1/2}$ based on *H*/*D* exchange in 10% $CD_3OD/CDCl_3$ for dimers 51 and 54.

Dimer	$k_{H/D}$ (min^{-1})	$t_{1/2}$ (min)
51	0.00368 ± 0.00006	188 ± 3
54	0.0263 ± 0.0006	26.4 ± 0.6

The half-life of the *H*/*D* exchange studies revealed that the amide NH proton of the 2-*O*-alkylated dimer (S(6)) exchanges an order of magnitude slower than the amide proton of its regioisomeric 3-*O* alkylated analogue (S(5)), suggesting greater stabilisation for the six-membered system relative to the five-membered analogue.

2.4.2 2D NMR studies

^1H-^1H NOESY analyses were also carried out on the two model dimers **51** and **54**. At room temperature, the amide resonance in the 2-*O* linked dimer **51** displayed nOe correlations with the adjacent aromatic protons 2-H3 and 2-H5, suggesting a mixture of *anti* and *syn* conformations of the isopropyl side-chains in solution (Figure 2.9 a). Absence of cross-peaks with the proton 1-H6 suggested that rotation was constrained about the Ar-CO axis, confirming that the amide proton was locked into an S(6) intramolecular H-bonded ring, in agreement with the result shown in the solid-state.

In order to investigate the effect of temperature on the conformational flexibility of these derivatives, NOESY spectra were acquired at 212 K. As shown in Figure 2.9 b, at low temperature the ratio of intensities of the nOe correlations NH to 2H5/NH to 2H3 changes from 2.6:1 to 10:1, suggesting that the *anti* conformation became dominant.

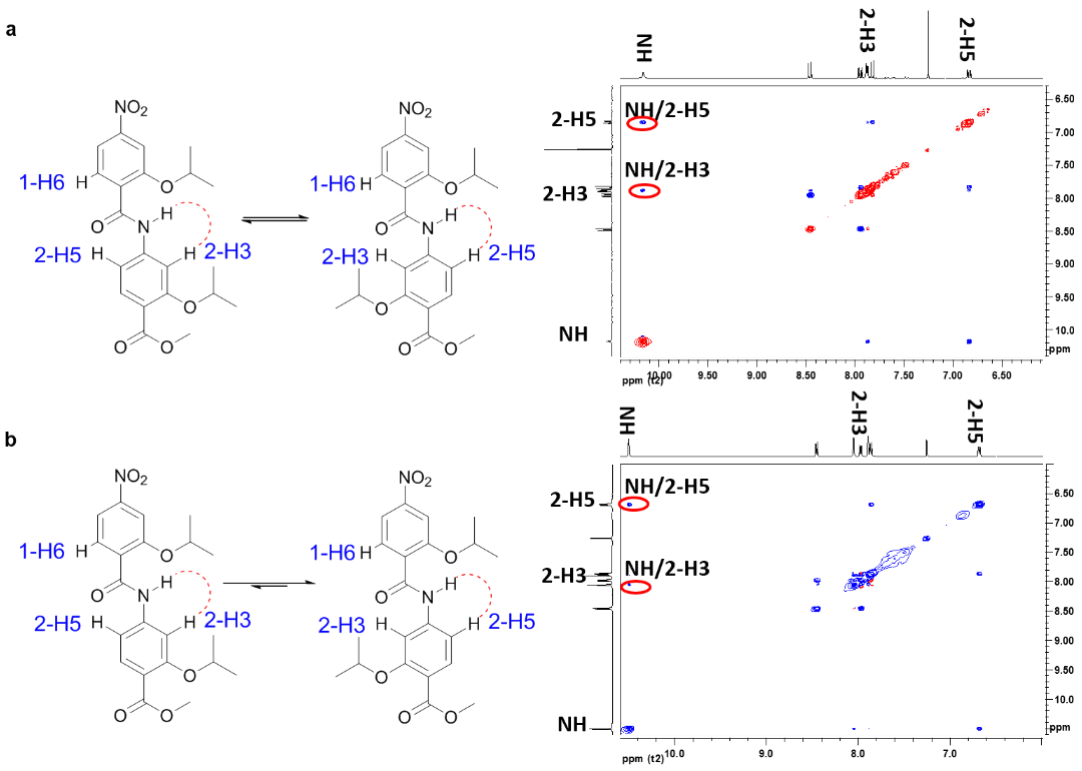

Figure 2.9 Partial 2D ^{1}H-^{1}H NOESY spectra of the 2-*O*-alkylated dimer 51 ($CDCl_3$, 10 mM) a 298 K; **b** 212 K. [Reprinted from *Tetrahedron*, Vol *68*, P. Prabhakaran, V. Azzarito, T. Jacobs, M. J. Hardie, C. A. Kilner, T. A. Edwards, S. L. Warriner, A. J. Wilson, "Conformational properties of *O*-alkylated benzamides", Pages No. 4485-4491, Copyright (2011), with permission from Elsevier (License number 3327630552830)]

The same studies performed on the 3-*O* linked dimer **54** at room temperature (Figure 2.10 a) showed cross-peaks between the amide NH proton and the adjacent aromatic residual protons 1-H2 and 1-H6 due to free rotation around the Ar-CO axis, whilst the absence of nOe correlations with proton 2-H5 suggested constrained rotation around the NH-Ar bond, probably due to an S(5) H-bonded interaction.

At 212 K, however, complete absence of NOE cross-peaks was observed between the amide proton and the aromatic resonance 1-H2, revealing that the *anti* conformation was favoured at this temperature (Figure 2.10 b).

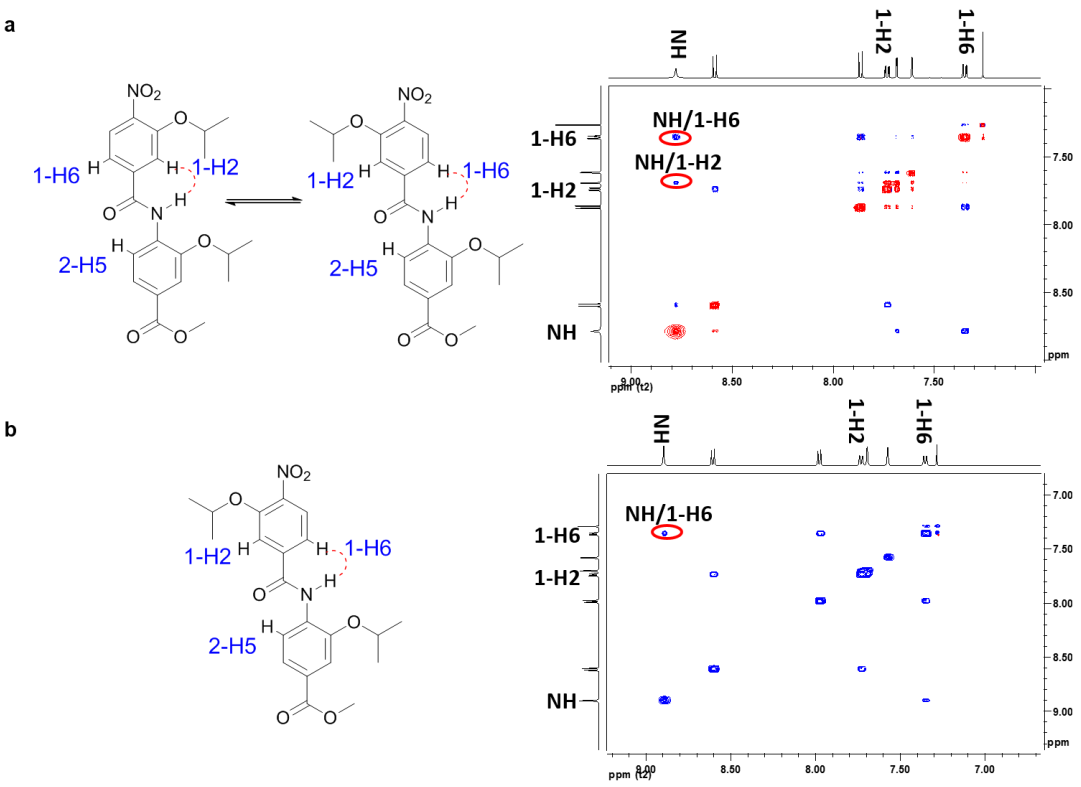

Figure 2.10 Partial 2D ^{1}H-^{1}H NOESY spectra of the 3-*O*-alkylated dimer 54 ($CDCl_3$, 10 mM) a 298 K; **b** 212 K. [Reprinted from *Tetrahedron*, Vol *68*, P. Prabhakaran, V. Azzarito, T. Jacobs, M. J. Hardie, C. A. Kilner, T. A. Edwards, S. L. Warriner, A. J. Wilson, "Conformational properties of *O*-alkylated benzamides", Pages No. 4485-4491, Copyright (2011), with permission from Elsevier (License number 3327630552830)]

2.5 Summary and conclusions

The design and synthesis of a new 2-*O*-alkylated benzamide foldamer was described. Conformational studies were performed in solid and solution-states and results were compared with the regioisomeric 3-*O*-alkylated template.

NMR studies and X-ray crystal structures confirmed the presence of intramolecular H-bonding (S(6) and S(5)) within the structures and suggested that this non-covalent constraint can promote an extended conformation in both scaffolds and restrict rotation around one of the aryl amide axes.

Solid-state conformational analyses showed that a combination of intramolecular non-covalent interactions and intermolecular side-chain/side-chain interactions can play a key role in influencing the conformational preference of these

p-benzamide derivatives. The *syn* or *anti* orientation of the side-chains was however mainly driven by the crystal packing and the nature of the groups involved.

H/*D* exchange data further suggested an increased stability of the six-membered H-bond over the five-membered analogues and 2D NOESY studies allowed to gather some insight into the distribution between *syn* and *anti* conformations for the two regioisomers, revealing that the *anti* orientation seems preferred in solution.

Overall, the results pointed to a complex interplay of interactions in defining the conformational properties of *O*-alkylated benzamide oligomers and should be considered in designing new oligoamide α-helix mimetics tailored to a range of biological targets.

Chapter 3

2-*O*-Alkylated *para*-benzamide α-helix mimetics: the role of scaffold curvature in modulating protein recognition

This chapter will discuss the design of a 2-*O*-alkylated *p*-benzamide α-helix mimetics targeted to the p53/*h*DM2 PPI. Conformational studies were performed on this scaffold and a Fluorescence Anisotropy (FA) competition assay allowed the identification of micromolar inhibitors of this interaction. Comparison with the previously reported regioisomeric 3-*O*-alkylated template[98, 99] permitted a preliminary evaluation of the role that backbone curvature has in determining molecular recognition properties.

The work reported in this chapter formed the basis of the following publication:

V. Azzarito, P. Prabhakaran, A. I. Bartlett, N. S. Murphy, M. J. Hardie, C. A. Kilner, T. A. Edwards, S. L. Warriner, A. J. Wilson, *Org. Biomol. Chem.* **2012**, *10*, 6469-6472.[118]

3.1 Design and *in silico* studies

The use of aromatic oligoamides as *proteomimetics* has been extensively pursued in the past decade and several members of this family have been shown to act as good inhibitors of a range of PPIs (see also Chapter 1).[29, 92, 93, 98, 99, 101, 102, 105]

Since the conformational analyses performed on 2-*O* and 3-*O* alkylated *p*-benzamide dimers (discussed in Chapter 2) showed that non-covalent interactions can influence conformational preference,[116, 117] it was envisaged that the preferred shape and properties induced by such interactions could have an impact on the molecular recognition properties of longer oligomers towards a protein partner.

In this regard, the Wilson group previously reported a 3-*O*-alkylated trimeric scaffold (Figure 3.1 a) as an effective α-helix mimetic and micromolar inhibitor of the p53/*h*DM2 interaction.[98, 99] This PPI has been widely employed as a target for small molecule development and it was therefore chosen as the model system for the study.[10, 41] An elongated regioisomeric 2-*O*-alkylated oligobenzamide scaffold was thus designed (Figure 3.1 b) to determine the effect that minor variations in backbone architecture and hydrogen bonding pattern (S(5), Figure 3.1 a *vs* S(6), Figure 3.1 b) can have on the inhibitory activity of these foldamers.[117]

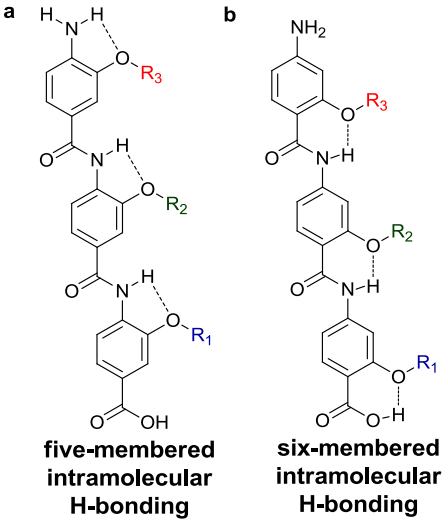

Figure 3.1 Regioisomeric oligobenzamides a 3-*O*-Alkylated scaffold; **b** 2-*O*-Alkylated scaffold.

With the aim of predicting the preferred conformations of the two regioisomeric benzamides, molecular modelling was performed on both scaffolds using *O*-isopropyl moieties (**57** and **58** Figure 3.2 a and c) as a model template (the conformational search on the 3-*O*-alkylated trimer was performed by N. S. Murphy). The structures were minimised by employing a full *Monte Carlo* search in the software Macromodel® using the MMFFs method.[134] Water was chosen as the implicit solvent and free rotation around the amide bonds was allowed in order to increase the accuracy of the conformational search. The α-helix mimicry of both scaffolds was evaluated by comparison with the p53 transactivation domain from the p53/*h*DM2 crystal structure (PDB ID: 1YCR) in which the three 'hot-spot' residues (Phe19, Trp23

and Leu26) are located at the *i*, *i* + 4, *i* + 7 positions of the helix respectively (Figure 3.2 b).[4]

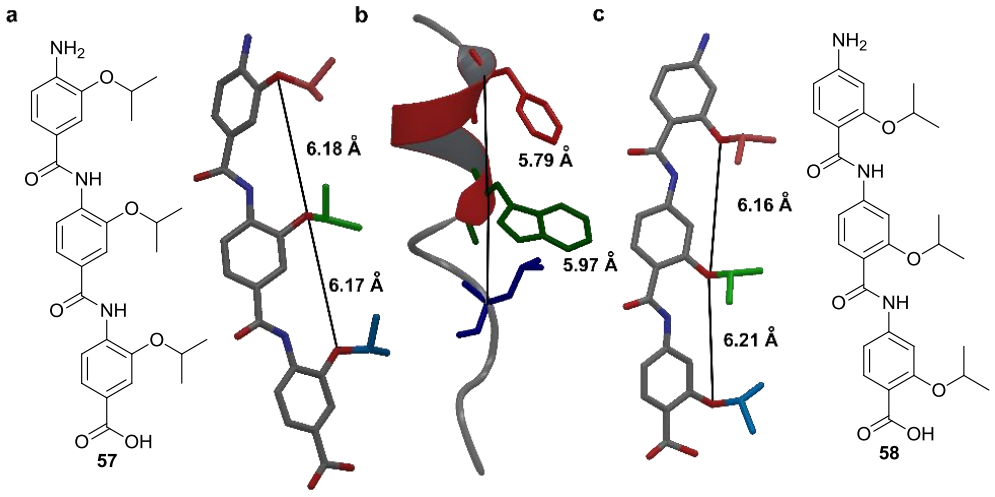

Figure 3.2 Evaluation of α-helix mimicry a 3-*O*-Alkylated trimer **57** and distances between the side chains; **b** Distance between the key aminoacids of the p53 helix (PDB ID: 1YCR); **c** 2-*O*-Alkylated trimer **58** and distances between the side chains. [V. Azzarito, P. Prabhakaran, A. I. Bartlett, N. S. Murphy, M. J. Hardie, C. A. Kilner, T. A. Edwards, S. L. Warriner, A. J. Wilson, *Org. Biomol. Chem.* **2012**, *10*, 6469-6472] - Reproduced by permission of The Royal Society of Chemistry

The results revealed the lowest energy conformation as the extended structure, in which all the amide bonds assumed a *trans* conformation. For poses where the side chains lie on the same face of the molecule, these matched the topography of the key p53 residues, with distances between the oxygens in good agreement with the distances between the α-carbons of the native helix 'hot-spots' (Figure 3.2 a-c).

The ensemble of structures within 1.5 kJ/mol, was aligned with the p53 helix (Figure 3.3 a-b). A mean value of the RMSD resulting from the superposition of the oxygen of the alkoxy group and the α-carbon of the key amino acids of the helix was calculated by aligning both scaffolds in parallel (Figure 3.3 a) and anti-parallel (Figure 3.3 b) orientations with respect to the direction of the polypeptide chain, confirming the good agreement between the native helix and the two designed mimetics.

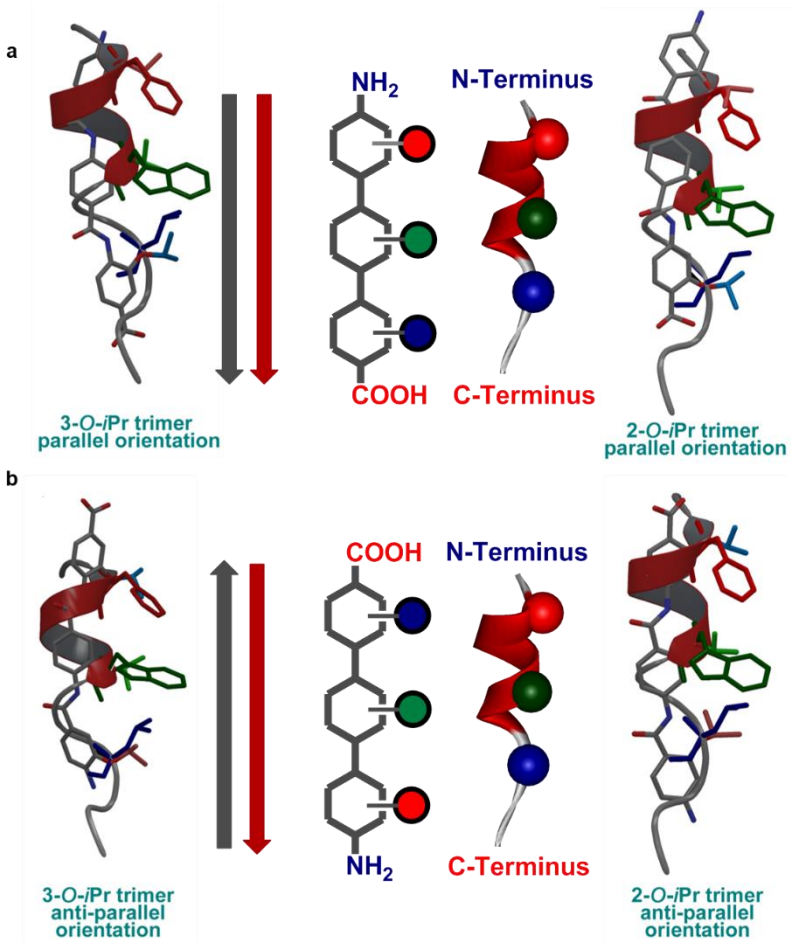

Figure 3.3 Superposition of oligobenzamide helix mimetics with the p53 polypeptide (PDB ID: 1YCR) a Parallel orientation overlay of **57** (RMSD = 0.4951 Å) and **58** (RMSD = 0.2170 Å) with the p53 α-helix; **b** Anti-parallel orientation overlay of **57** (RMSD = 0.4953 Å) and **58** (RMSD = 0.2171 Å) with the p53 α-helix.

Despite this observation, superposition of the two molecules highlighted a reduced curvature of the 2-*O*-alkylated scaffold in comparison to the 3-*O*-alkylated template (Figure 3.4 a). Defining 'curvature' for a three-dimensional object is a complex task, since it is challenging to accurately represent it and relate it to the spatial presentation of the side-chains. An attempt to quantify this concept was nevertheless made by determining the angle of inclination of two sequential aromatic rings (Figure 3.4 b), which resulted in an average difference of 3.5° between the regioisomers, measured from the sum of the two angles obtained for each molecule. Alternatively, the difference in pseudodiedhral angle between aromatic rings was considered, which led to angles of inclination of 168.8°-161.7° for the top and bottom units of the 2-*O*-alkylated trimer and 142.1°-144.9° for the 3-*O*-alkylated template (Figure 3.4 c).

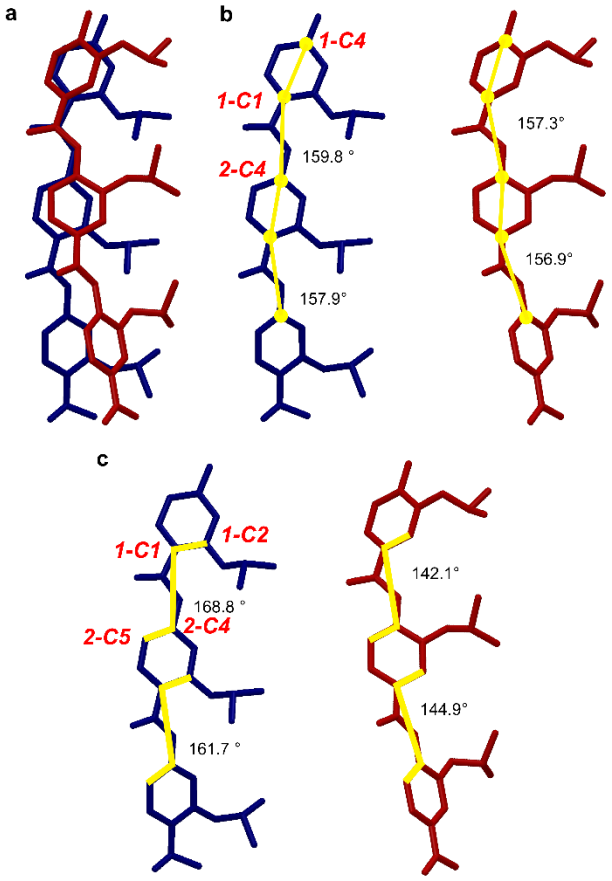

Figure 3.4 Backbone curvature studies a Superposition of trimers **58** (blue) and **57** (red) showing reduced curvature of the 2-*O*-alkylated scaffold; **b** Angles of inclination on trimers **58** (blue) and **57** (red) showing the carbon atoms used in the measurement; **c** Pseudodihedral angles on trimers **58** (blue) and **57** (red) showing the carbon atoms used in the measurement. [V. Azzarito, P. Prabhakaran, A. I. Bartlett, N. S. Murphy, M. J. Hardie, C. A. Kilner, T. A. Edwards, S. L. Warriner, A. J. Wilson, *Org. Biomol. Chem.* **2012**, *10*, 6469-6472] - Reproduced by permission of The Royal Society of Chemistry

Even though these measurements need to be considered carefully as they do not constitute a complete representation of the conformational space, the reduced curvature shown by the 2-*O*-alkylated scaffold in comparison to the 3-*O*-alkylated template could be attributed to the different H-bonded geometries (S(6) and S(5)) between these two molecules.

3.2 Trimer syntheses

A small library of 2-*O*-Alkylated *p*-benzamide trimers was synthesised in order to study the role that reduced curvature would play in conformational properties and binding affinity with the target protein. The synthetic route is shown in Scheme

3.1 and followed minor variations to the previously reported iterative route *via* sequential coupling reactions.[98, 117]

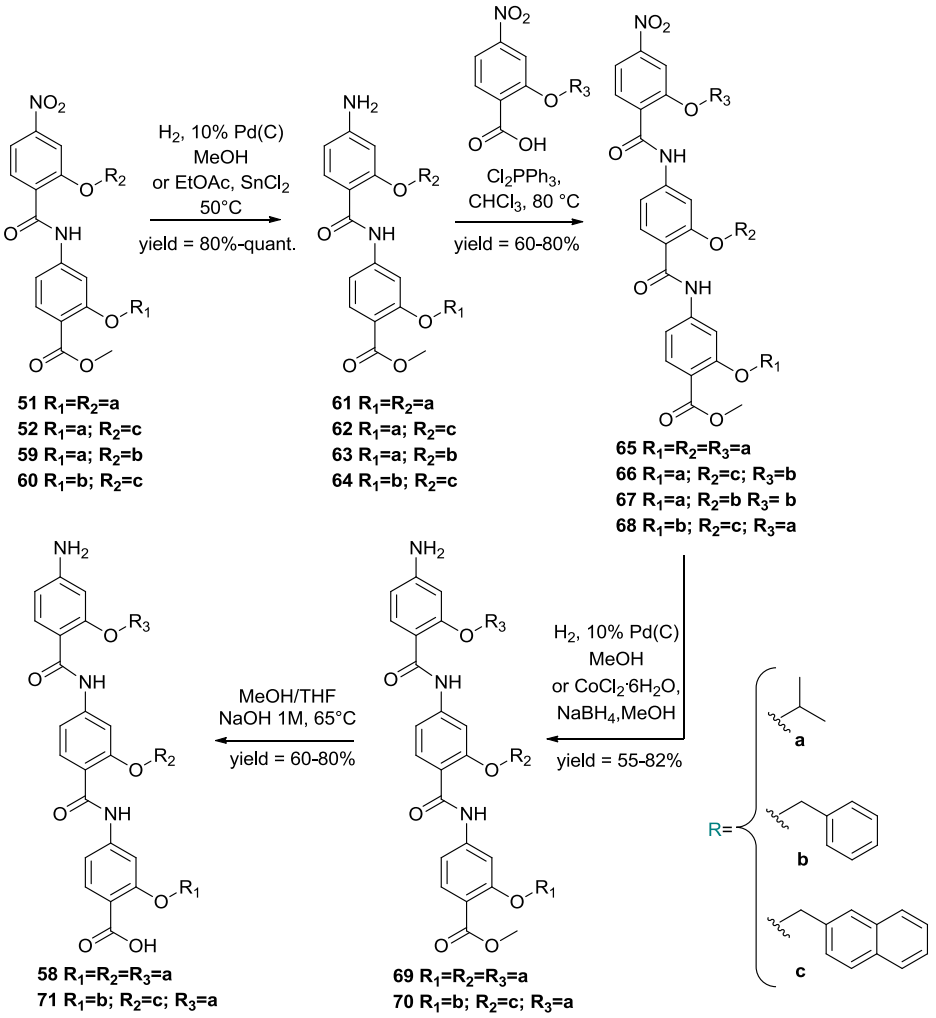

Scheme 3.1 Synthetic route to 2-*O*-alkylated *p*-benzamide trimers *via* a chain elongation approach.

p-Nitro benzoate dimers (**51**-**52**, **59**-**60**) were obtained as described in Chapter 2. The nitro moiety was unmasked to the aniline *via* a palladium-catalysed hydrogenation[126] or by a tin-chloride reduction,[127] leading to pure products (**61**-**64**) in good to excellent yields. A coupling reaction between a 2-alkoxy-4-nitro benzoic acid and the reduced dimers mediated by dichloro triphenylphosphorane[128] allowed *p*-nitro benzoate trimers (**65**-**68**) to be obtained in good yields and purity. Subsequent reduction of the nitro group of the oligoamide **65** by palladium-catalysed hydrogenation[126] led to the amino benzoate trimer **69**. The reduction of trimer **68** was instead performed using cobalt chloride hexahydrate and sodium borohydride.[139]

Unfortunately, the poor solubility of trimers **66** and **67** prevented the isolation of their aniline analogues. A final base-catalysed hydrolysis led to the desired amino-acid oligoamides **58** and **71**, which were obtained in good yields after an aqueous work-up.

Following a similar route, Dr P. Prabhakaran synthesised and purified the 3-*O*-alkylated trimers **57**, **72**, **73** and **74** (Figure 3.5) which were employed in these studies for comparison with their regioisomeric analogues.

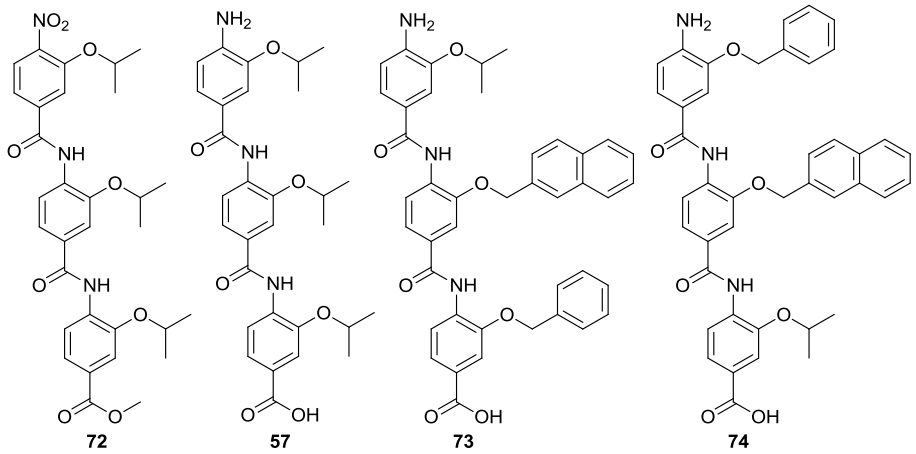

Figure 3.5 3-*O*-alkylated *p*-benzamide trimers employed in this study.

3.3 Solid-state conformational analysis

Solid-phase studies were conducted in order to investigate the conformational properties of these molecules. Unfortunately no crystals of a 2-*O*-alkylated trimer were obtained, however single crystals of a synthetic intermediate (**61**, Figure 3.6 a) were grown by the slow evaporation of a methanol solution (X-ray analysis performed by C. A. Kilner). The structure presented the isopropyl chains on opposite sides of the backbone in an *anti* orientation and the measured NH···O distances (1.9 Å) confirmed the presence of an S(6) intramolecular H-bond.[129]

Dr P. Prabhakaran also obtained a crystal of the nitro-ester 3-*O*-alkylated trimer **72** (Figure 3.6 b), which was grown by slow diffusion of methanol into a solution of compound in tetrahydrofuran. The X-ray structure confirmed the oligomer adopts an extended (all *trans*) structure in the solid state, placing the two bottom side-chains in a *syn* orientation and the isopropyl group at the *N*-terminus on the opposite face. The measured NH···O distances between the amide protons and the

alkoxy oxygen on the neighbouring side-chains were ~ 2.2 Å, in accordance with the range observed in foldamers constrained with S(5) intramolecular H-bonding.[125]

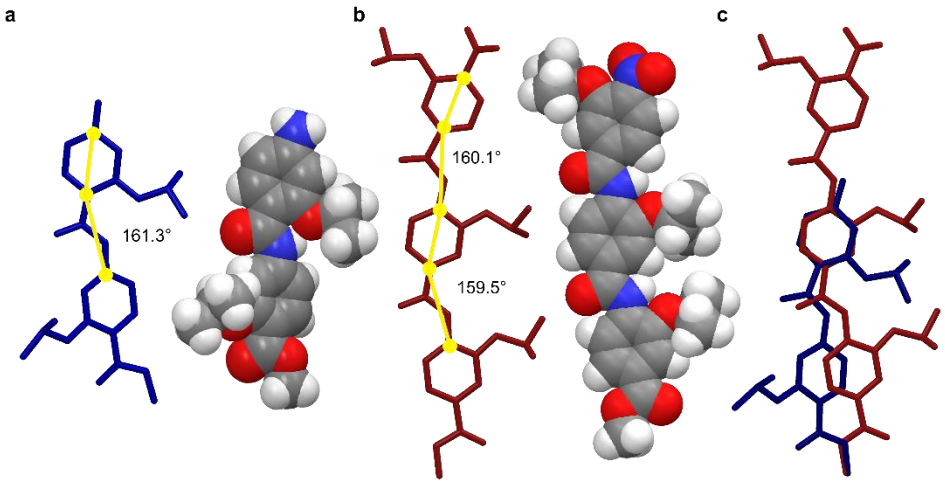

Figure 3.6 X-Ray studies on the backbone curvature a Solid state structure of dimer **61** shown in stick (blue) and CPK representation, displaying the backbone angle of inclination; **b** Solid state structure of trimer **72** shown in stick (red) and CPK representation, displaying the backbone angles of inclination; **c** Superposition of **61** (blue) and **72** (red) (RMSD = 0.2436 Å) showing the reduced curvature of the 2-*O*-alkylated scaffold. [V. Azzarito, P. Prabhakaran, A. I. Bartlett, N. S. Murphy, M. J. Hardie, C. A. Kilner, T. A. Edwards, S. L. Warriner, A. J. Wilson, *Org. Biomol. Chem.* **2012**, *10*, 6469-6472] - Reproduced by permission of The Royal Society of Chemistry

In order to evaluate the conformational difference of the two molecules, the degree of curvature of the backbone of dimer **61** and trimer **72** was measured as the angle of inclination of two sequential aromatic rings (Figure 3.6 a-b). Superposition of the two molecules was performed by using Maestro® (Figure 3.6 c). In support of the modelling studies, the 2-*O*-alkylated dimer showed a visibly reduced curvature in comparison to the 3-*O*-alkylated trimer, which can be attributed to the difference in H-bonding patterns. Where the five-membered H-bonding in trimer **72** induced the backbone to bend, the presence of a six-membered H-bonded ring in dimer **61** constrained the backbone allowing minimal distortion from the idealised backbone geometry. Furthermore, these studies highlighted the negligible influence that the moiety at the *N*-terminus (amino or nitro) plays on the final conformation, as comparison with the crystal structure of the analogous nitro-ester dimer **51**, shown in Chapter 2, revealed that the *anti* orientation of the side-chains was preferred in both cases.

3.4 Solution-state conformational analyses

Solution-state structural analyses were conducted on the model trimers **58** and **57** (Figure 3.7). The down field shifts of amide protons in the ^{1}H-NMR spectra indicated the presence of strong six-membered S(6) for **58** and five-membered S(5) for **57** intramolecular H-bonded rings between the amide proton and the alkoxy oxygen atom (Figure 3.7, Table 3.1).[129, 136, 137]

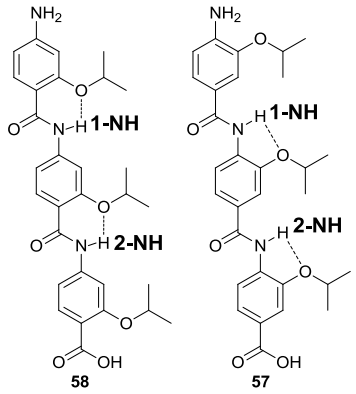

Figure 3.7 Model isopropyl trimers for solution-state studies showing the labelling for the amide protons.

Table 3.1 Chemical shift data measured in $CDCl_3$.

Trimer	δ 1-NH	δ 2-NH
58	10.28	10.47
57	8.74	8.90

This result was further confirmed by Variable Temperature (VT) NMR studies. ^{1}H NMR spectra of both trimers were acquired at temperatures ranging from 243 to 333 K (Figure 3.8 a-b).

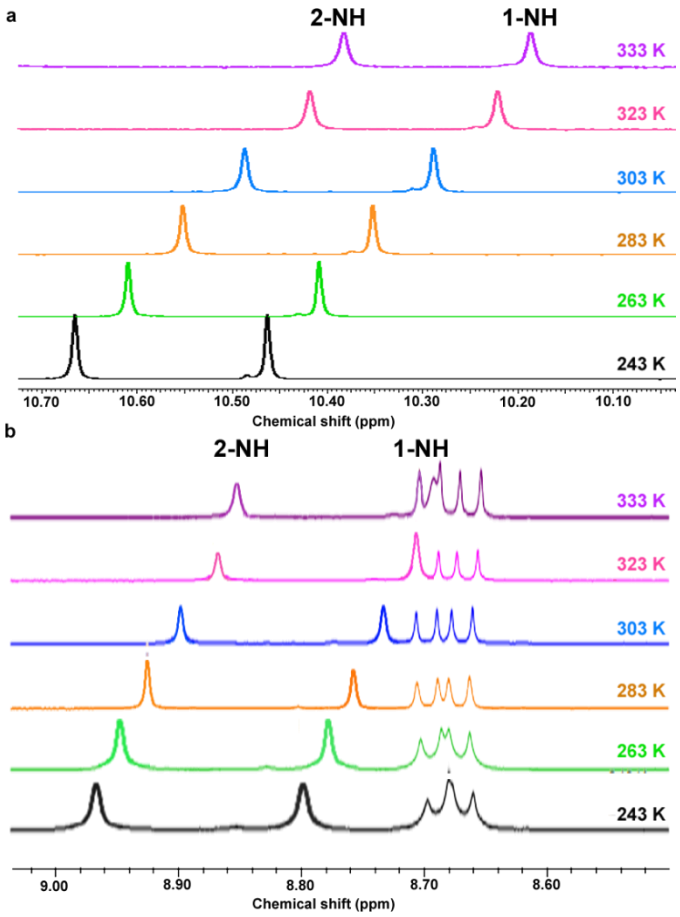

Figure 3.8 VT NMR Studies (10 mM $CDCl_3$, 500 MHz) a 2-*O*-alkylated trimer **58**; **b** 3-*O*-alkylated trimer **57**. [V. Azzarito, P. Prabhakaran, A. I. Bartlett, N. S. Murphy, M. J. Hardie, C. A. Kilner, T. A. Edwards, S. L. Warriner, A. J. Wilson, *Org. Biomol. Chem.* **2012**, *10*, 6469-6472] - Reproduced by permission of The Royal Society of Chemistry

Temperature coefficients (T_{coeff}) were calculated following Equation 3.1. The results revealed T_{coeff} of - 3 ppb K^{-1} for both the amide protons in trimer **58** and T_{coeff} of - 1 ppb K^{-1} for both the amide protons in trimer **57**.[140]

$$T_{coeff} = \frac{\delta_2 - \delta_1}{T_2 - T_1} \times 10^3 \quad \delta = \text{chemical shift in ppm, } T = \text{temperature in K}$$

Equation 3.1

Since internally hydrogen bonded amides are expected to show much smaller shifts with temperature (≤ 3 ppb K^{-1}) than protons which are accessible for H-bonding to external polar solvents (> 4 ppb K^{-1}),[20, 22-24] the small T_{coeff} observed suggested the

presence of an S(6) and an S(5) intramolecular H-bonding for trimers **58** and **57** respectively.

Dilution NMR studies were also conducted at concentrations ranging from 10 to 0.5 mM and the results are summarised in Figure 3.9 a-b.

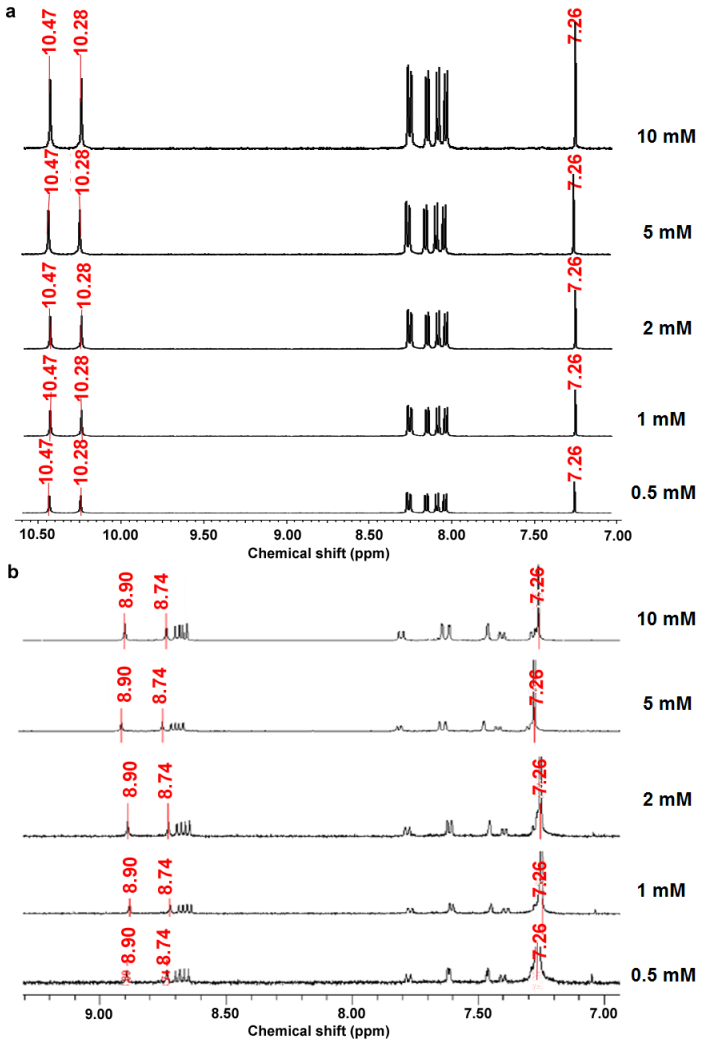

Figure 3.9 Dilution NMR Studies (10 mM $CDCl_3$, 500 MHz) a 2-*O*-alkylated trimer **58**; **b** 3-*O*-alkylated trimer **57**. [V. Azzarito, P. Prabhakaran, A. I. Bartlett, N. S. Murphy, M. J. Hardie, C. A. Kilner, T. A. Edwards, S. L. Warriner, A. J. Wilson, *Org. Biomol. Chem.* **2012**, *10*, 6469-6472] - Reproduced by permission of The Royal Society of Chemistry

The experiments revealed concentration independence for the amide proton resonances in both cases, thus providing further evidence that intermolecular hydrogen bonding is negligible in nature.

3.4.1 *H/D* Exchange studies

The relative strength of the H-bonds in the two scaffolds was also investigated by performing *H/D* exchange titration experiments in 10% $CD_3OD/CDCl_3$ to ensure pseudo first order kinetics (Figure 3.10).[138]

The half-life of the *H/D* exchange on the isopropyl trimers **58** and **57** (Table 3.2), calculated following Equation 2.1 and Equation 2.2 (Chapter 2), revealed that the amide hydrogens of the 2-*O*-alkylated scaffold exchange on a timescale that is an order of magnitude slower than the 3-*O*-alkylated analogue.

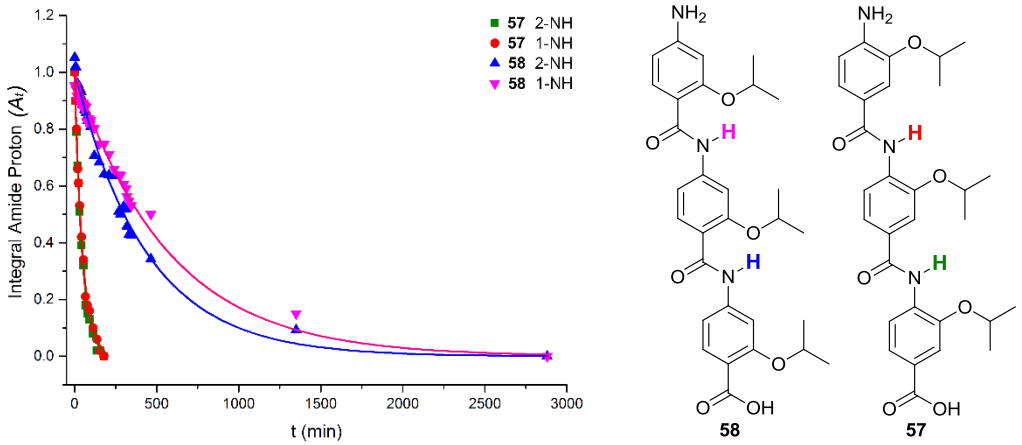

Figure 3.10 *H/D* Exchange kinetics for trimers 58 (1-NH pink, 2-NH blue) and 57 (1-NH red, 2-NH green). [V. Azzarito, P. Prabhakaran, A. I. Bartlett, N. S. Murphy, M. J. Hardie, C. A. Kilner, T. A. Edwards, S. L. Warriner, A. J. Wilson, *Org. Biomol. Chem.* **2012**, *10*, 6469-6472] - Reproduced by permission of The Royal Society of Chemistry

Table 3.2 Kinetic constants and $t_{1/2}$ based on *H/D* exchange in 10% $CD_3OD/CDCl_3$ for trimers 58 and 57.

Trimer	Amide proton	$k_{H/D}$ (min^{-1})	$t_{1/2}$ (min)
58	1-NH	0.00176 ± 0.00005	394 ± 12
58	2-NH	0.00230 ± 0.00005	301 ± 6
57	1-NH	0.0212 ± 0.0004	32.7 ± 0.6
57	2-NH	0.0225 ± 0.0005	30.8 ± 0.7

These results suggest greater stabilisation of the S(6) over the S(5) intramolecular H-bond, in agreement with studies performed on the 2-*O* and 3-*O*-alkylated dimers (see Chapter 2). The data however need to be considered carefully as the exchange kinetics may also be influenced by the steric accessibility of the amide protons and the observed difference could further arise from electronic

effects related to the acidity of the two protons. In this regard, it is worth noting that the NH at the *N*-terminus exchanges slightly slower than the NH at the carboxy terminus in both cases. This behaviour is probably due to the different electronic environment of these protons, as the acid moiety in the *para* position of 2-NH is more electron withdrawing than the amide function in the *para* position of 1-NH (reported Hammett constants: σ_p (CO_2H) = 0.45; σ_p ($CONH_2$) = 0.36).[141]

3.4.2 2D NMR studies

The results obtained by the NMR and *H/D* exchange studies seemed to suggest that even though both scaffolds adopt extended conformations, the rotation around the Ar-CO and NH-Ar axes are restricted by the nature of the hydrogen bonding involved, where S(6) intramolecular H-bonding in the 2-*O*-alkylated scaffold restricts the former and S(5) in the 3-*O*-alkylated scaffold restricts the latter. 2D ^{1}H-^{1}H NOESY experiments performed on the 2-*O*-alkylated trimer **58** and the 3-*O*-alkylated trimer **57** confirmed this behavior.

The NOESY spectra of **58** revealed the absence of correlations between the NH resonances and the ArCH resonances in the *ortho* position of the adjacent monomer, in agreement with restricted rotation around the Ar-CO axes (Figure 3.11).

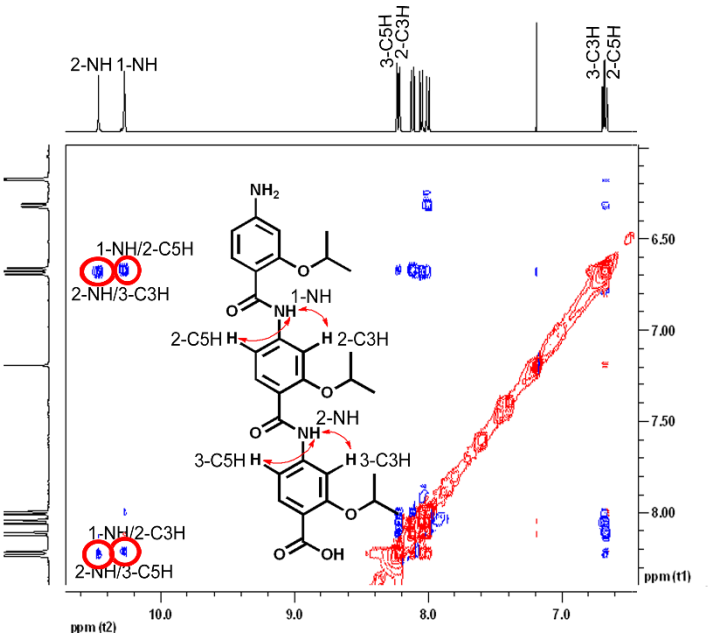

Figure 3.11 Partial ^{1}H-^{1}H NOESY spectra of 58 showing NOE cross-peak correlations. (10 mM $CDCl_3$, 500 MHz)

On the other hand, correlations between the aniline NH resonance and both its *ortho* ArCH resonances suggested free rotation around the NH-axes. The result is in contrast with earlier observations on the regioisomeric analogue **57**[1, 99] (Figure 3.12), where the S(5) H-bond restricted rotation about the NH-Ar axes and the Ar-CO bond was shown to be free to rotate.

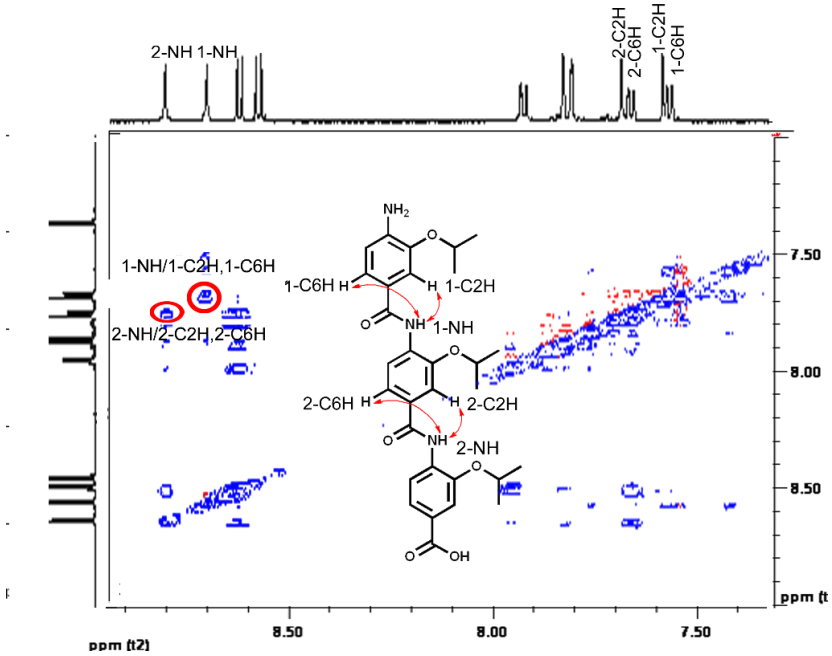

Figure 3.12 Partial ^{1}H-^{1}H NOESY spectra of 57 showing NOE cross-peak correlations. (10 mM $CDCl_3$, 500 MHz)

In spite of these constraints, correlations with the α-carbon of the adjacent isopropyl moieties (see section 6.1.4, Chapter 6) highlighted in both cases the presence of conformations with all the side chains aligned on the same face of the molecule, thus confirming that, in solution-phase, conformers mimicking the α-helix are accessible.

3.5 Fluorescence Anisotropy competition assay against the p53/*h*DM2 PPI

In order to evaluate the ability of this new scaffold to act as an effective α-helix mimetic, 2-*O*-alkylated trimers **58** and **71** and 3-*O*-alkylated trimers **57**, **73** and **74** were tested in a Fluorescence Anisotropy (FA) competition assay against the

p53/*h*DM2 PPI (assay performed by Dr A. I. Bartlett; see Appendix I for details on the FA assay).

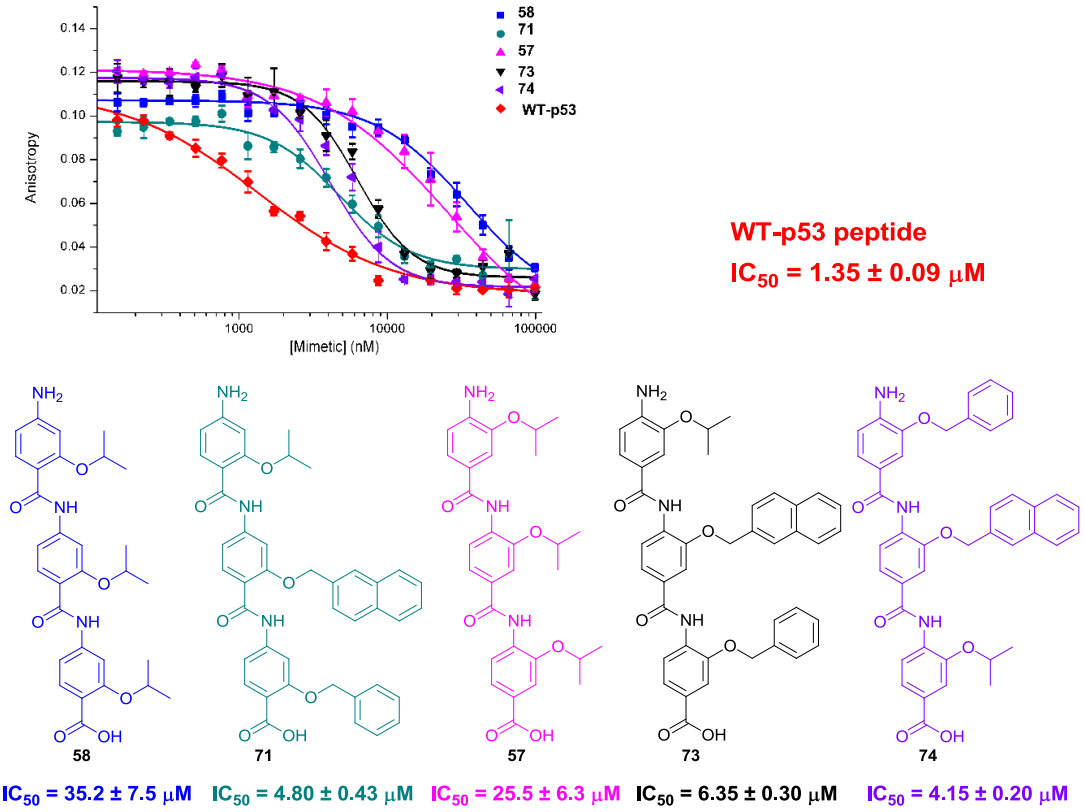

Figure 3.13 Fluorescence anisotropy p53/*h*DM2 competition assay data for WT-p53 peptide, 2-*O*-alkylated trimers 58 and 71 and 3-*O*-alkylated trimers 57, 73 and 74. (40 mM phosphate buffer pH 7.50, 200 mM sodium chloride, 0.02 mg mL^{-1} BSA) [V. Azzarito, P. Prabhakaran, A. I. Bartlett, N. S. Murphy, M. J. Hardie, C. A. Kilner, T. A. Edwards, S. L. Warriner, A. J. Wilson, *Org. Biomol. Chem.* **2012**, *10*, 6469-6472] - Reproduced by permission of The Royal Society of Chemistry

As shown in Figure 3.13, the assay allowed the identification of micromolar inhibitors of this PPI. Notably, isopropyl trimers **58** and **57** possessing moieties which do not mimic the native side-chains exhibited low potency, whereas trimers **71**, **73** and **74**, with side-chains matched to the p53 sequence, all displayed affinity in the same micromolar range as the native peptide.

Unexpectedly, comparison of the two regioisomeric oligoamides **71** and **73** revealed that both mimetics display similar inhibitory activity against this PPI. This result highlights an important point since the similar activity of the two scaffolds suggested that backbone curvature does not exert a major role on molecular recognition towards the *h*DM2 binding cleft.

This result could be rationalised by considering the conformational properties of these oligoamides. Even though the different intramolecular H-bonds in these two scaffolds result in different curvature of the backbones, in the molecular recognition process the mimetics will most likely try to adopt the best conformation possible in order to maximise their interaction with the protein binding cleft. As shown in Figure 3.14, since both the NH-Ar/Ar-CO axes and the alkoxy side-chains are free to rotate, this could result in a similar vectoral presentation of the binding groups of the two regioisomers, thus generating multiple pharmacophores which can be similarly effective for helix mimicry.

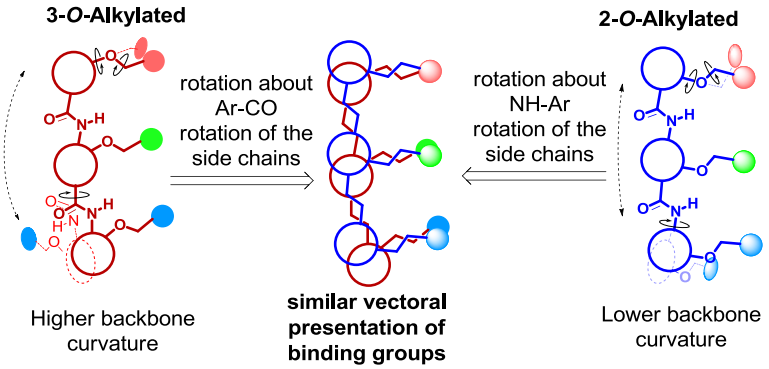

Figure 3.14 Schematic depicting rotatable bonds (one amide and one alkoxy is highlighted for each scaffold) in regioisomeric helix mimetics.

3.6 Summary and conclusions

In summary, the design, synthesis and structural studies of a new 2-*O*-alkylated α-helix mimetic scaffold was described. Comparison with a 3-*O*-alkylated regioisomeric template illustrated that helix mimetic curvature can be readily tuned by subtle placement of side-chain mimicking groups.

Preliminary evaluation of this new scaffold revealed minimal differences in potency for antagonism of the p53/*h*DM2 interaction, highlighting the complex relationship between helix mimetic conformation and molecular recognition. The combination of backbone and side-chain torsional angles enabled effective biological mimicry for both series, whilst suggesting strict geometrical matching of side chain presentation by *proteomimetic* scaffolds is not essential for effective inhibition of PPIs.

Chapter 4

Solid-phase synthesis and biological evaluation of hybrid α-helix mimetics

This chapter will discuss the design and synthesis of a hybrid α-helix mimetic, where the combination of previously reported synthetic building blocks with the most natural building block available (amino acids), allowed generation of a mimetic with access to a wider conformational space. Through structure-activity relationship (SAR) studies, micromolar inhibitors of two major PPIs involved in the development of cancer, p53/*h*DM2 and Mcl-1/NOXA B, were identified. Selectivity was also achieved between these PPIs, demonstrating that the structure of these mimetics can be tuned to achieve protein selective mimicry. The chiral nature of the scaffold further enabled stereocontrolled interactions and allowed the identification of the first examples of protein discrimination that is dependent on the absolute configuration of the α-helix mimetic and enantioselective recognition of the chiral helix mimetic by the protein. These results provide an important foundation for the development of a more detailed understanding of the conformational properties that govern molecular recognition processes involved in PPI inhibition and a starting point for elaboration of rule based approaches for the synthesis of functional proteomimetics.

4.1 Design and preliminary *in silico* studies

Structural rigidity introduced *via* either covalent or non-covalent constraints, has generally been accepted as a pre-requisite for α-helix mimetics to successfully replicate the topography of the native helix 'hot-spots' and function as effective mimetics.[1, 18, 29] However, the results obtained for the inhibitory activity of the 2-*O*-alkylated *vs.* the 3-*O*-alkylated scaffolds discussed in Chapter 3,[118] highlighted

the significant role played by the conformational properties of these molecules and the complexity of the molecular recognition process with the protein partner.

To further explore the effect of the backbone curvature and side-chain torsional angles in molecular recognition, modification of the oligobenzamide scaffold was envisaged through the introduction of different monomers with distinct H-bonding capabilities and stereoelectronic restraints. This idea led to the design of a new mimetic, where the structural rigidity of the oligobenzamide backbone was broken through substitution of the middle aryl-unit with an α-amino acid to generate a 'hybrid' α-helix mimetic (Figure 4.1).

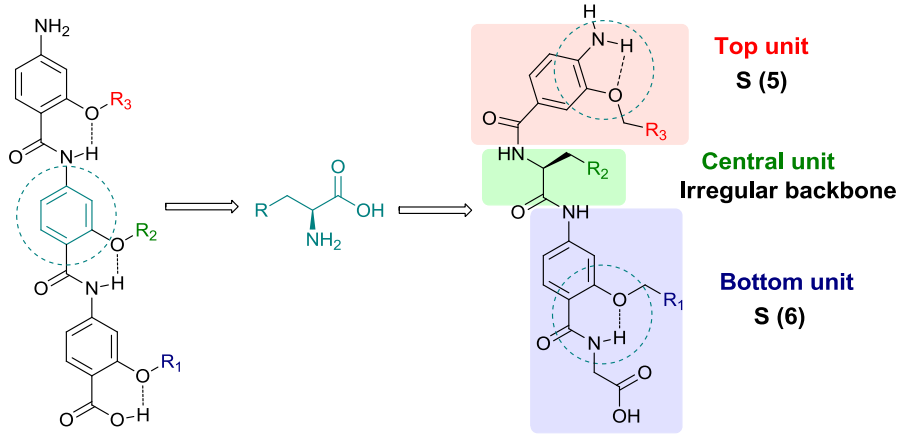

Figure 4.1 Design of a hybrid α-helix mimetic.

This new scaffold has the potential to adopt well-defined conformations through H-bonds at the top and bottom of the sequence, but the irregular backbone may permit adoption of multiple conformers of similar energy and access to different portions of conformational space. In order to investigate the effect of this structural change, the p53/*h*DM2 PPI was targeted for comparison of the new design with the 2-*O* and 3-*O*-alkylated scaffolds.

A conformational search was performed on the model molecule **75** (Figure 4.2 a) presenting R_1 = *i*Pr, R_3 = Bn and L-Phe as the central amino acid. The structure was minimised performing a full *Monte Carlo* search using the software Macromodel® with the MMFFs method.[134] Water was chosen as implicit solvent and free rotation around the amide bonds was allowed in order to increase the accuracy of the conformational search. In the lowest energy conformation the scaffold adopted an

extended structure with the top two side-chains lying on one face of the molecule and the bottom unit being slightly twisted towards the other side (Figure 4.2 a).

All the conformations within 1.5 kJ/mol from the lowest energy conformation were aligned with the p53 α-helix superimposing the oxygen of the alkoxy group or the α carbon of Phe and the α carbons of the key amino acids of the p53 helix (Phe19, Trp21, Leu26; Figure 4.2 b).

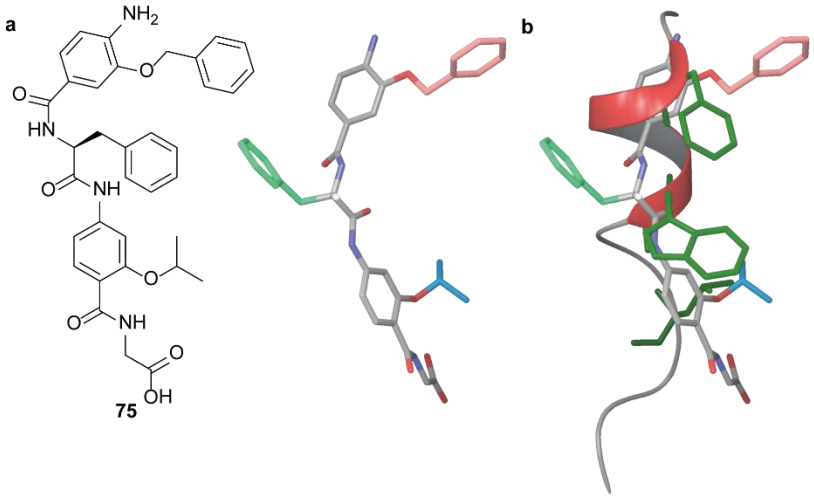

Figure 4.2 Molecular modelling studies for a hybrid α-helix mimetic a Structure and model of the hybrid **75**; **b** overlay of **75** with p53 (PDB ID: 1YCR, RMSD = 1.5284 Å).

As revealed by the high RMSD mean value (1.5284 Å) obtained from the superposition, the irregular backbone of the hybrid scaffold diverged from idealised helical mimicry. Nevertheless, the good overlay of the top and bottom side-chains with Phe19 and Leu26 and the increased number of degrees of freedom of this backbone compared to the 2-*O* and 3-*O*-alkylated oligobenzamides, suggested that mimicry of the helical functionality at the protein interface could be achieved. A more diverse ensemble of conformers with different side-chains projections was also accessible, suggesting that the molecule can have a better chance to accommodate subtle variations in binding sites.

A qualitative analysis of the conformational space accessible to the mimetics was performed by comparing the 3-*O* and 2-*O*-alkylated tri-methyl benzamides **76** and **77** with the methyl-functionalised hybrid **78** (Figure 4.3 a). Methyl moieties were chosen to exclude all the effects induced by additional side-chain rotations, so the inherent flexibility of the backbone could be easily identified.[142]

The structures were minimised in Macromodel®[134] and the three sets of conformers within 1.5 kJ/mol were superimposed without further manipulation.

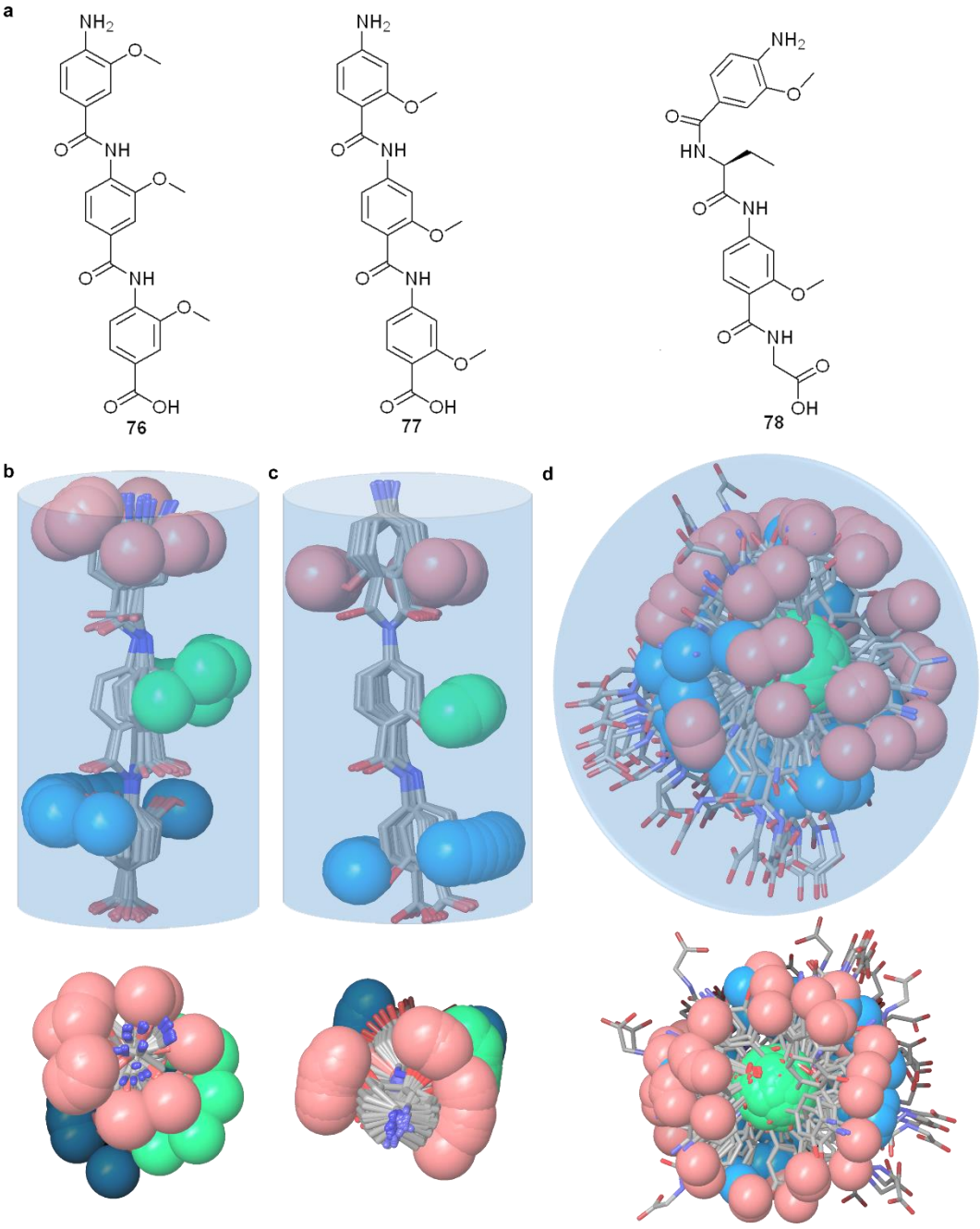

Figure 4.3 Investigation of the accessible conformational space (shown as a shaded 3D object) highlighting the orientation of the side-chains (shown in CPK format) a Structures of the 3-*O*-alkylated trimer **76**, the 2-*O*-alkylated trimer **77** and the hybrid **78**; **b** Side (top) and top (bottom) view of the 3-*O*-alkylated trimer **76**; **c** Side (top) and top (bottom) view of the 2-*O*-alkylated trimer **77**; **d** Side (top) and top (bottom) view of hybrid **78**.

As shown in Figure 4.3 b and c, oligobenzamide trimers **76** and **77** presented different combinations of *anti* and *syn* orientation of the side-chains (for the definition of *anti* and *syn*, see Chapter 2) but the accessible conformational space was in both cases restricted by the intrinsic rigidity of the scaffold and the ordered H-bonded network. On the other hand, hybrid **78**, where a difference of a few degrees in a bond torsion angle can result in diverse side-chain orientations, could access a significantly wider conformational space (Figure 4.3 d).

To confirm that some of these conformers could still mimic the helix binding mode, a set of minimised structures of hybrid **75** within 1.5 kJ/mol from the lowest energy conformation was docked with the crystal structure of *h*DM2 (PDB ID: 1YCR)[4] using the software Glide®.

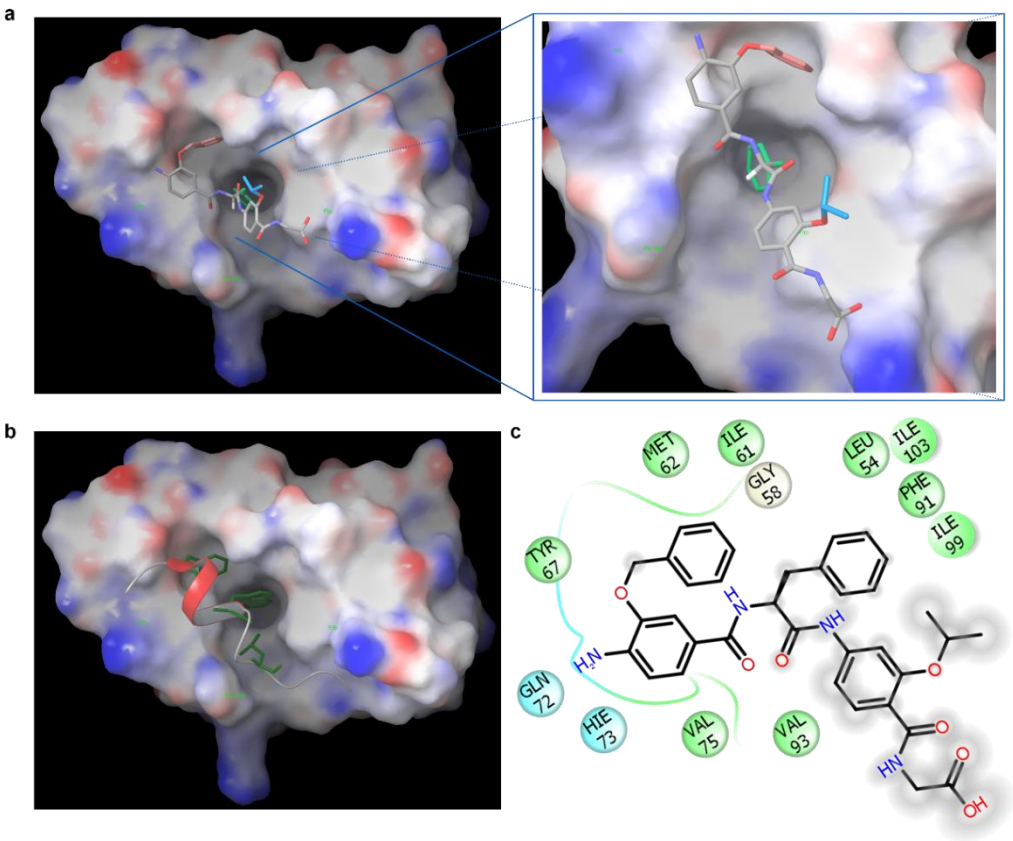

Figure 4.4 Docking studies (PDB ID: 1YCR) a Docked hybrid **75** with protein surface 3D representation and expansion; **b** p53/*h*DM2 interaction; **c** Docked hybrid **75** in schematic 2D representation highlighting the interacting amino acids (interactions taking place outside the hydrophobic cleft are represented with a grey shade).

Of all the poses generated, 77% assumed conformations which were binding in the *h*DM2 cleft. A representative example is shown in Figure 4.4 a and c. The native p53/*h*DM2 PPI is also shown in Figure 4.4 b for comparison.

The hybrid mimetic bound in the *h*DM2 cleft with the top two units of the sequence through hydrophobic contacts between the benzyl side-chain and Ile61 and between the middle Phe residue and Phe91. The bottom unit instead interacted outside the hydrophobic cleft, through a hydrophilic interaction between the carboxylic acid of the terminal Gly and the Lys51 residue at the protein interface.

Within the limitations of this qualitative analysis, these simulations indicated that this hybrid scaffold has the potential to adopt conformations that can access a broad conformational space and be recognised as a functional mimetic of the native α-helix.

4.2 Hybrid α-helix mimetic syntheses

In designing this new α-helix mimetic scaffold, a solid phase peptide synthesis (SPPS) strategy was envisioned.[100, 106] The synthesis uses the well-established Fmoc (9-fluorenylmethyloxycarbonyl) strategy and has the advantage of facilitating library generation and reducing the time of preparation.[143]

4.2.1 Building block syntheses

The isobutyl-functionalised 2-*O*-alkylated monomer **79** was synthesised using the route described in Chapter 2.

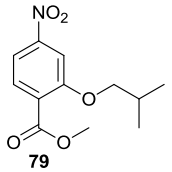

79

The synthesis of protected monomers of the 2-*O*-alkylated and the 3-*O*-alkylated series (synthesised by N. S. Murphy)[100] was then achieved by performing a hydrolysis of the ester moiety of the amino-ester monomers (see Chapter 2 for the synthesis of these intermediates) followed by Fmoc-protection of the amino group (Scheme 4.1).

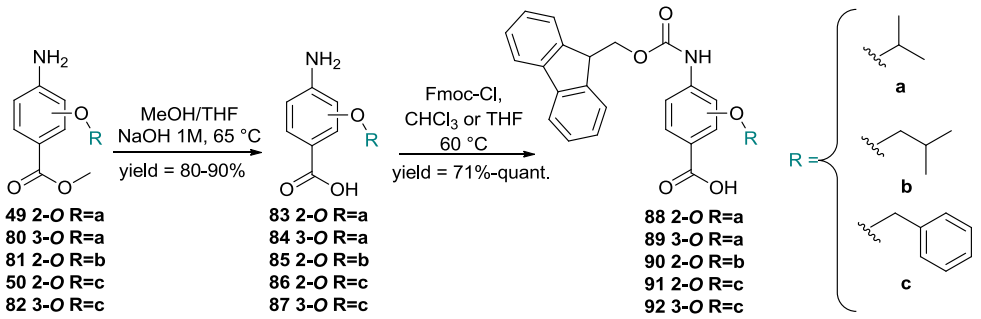

49 2-*O* R=a
80 3-*O* R=a
81 2-*O* R=b
50 2-*O* R=c
82 3-*O* R=c

83 2-*O* R=a
84 3-*O* R=a
85 2-*O* R=b
86 2-*O* R=c
87 3-*O* R=c

88 2-*O* R=a
89 3-*O* R=a
90 2-*O* R=b
91 2-*O* R=c
92 3-*O* R=c

Scheme 4.1 Synthetic route to Fmoc-protected building blocks of the 2-*O* and 3-*O*-alkylated *p*-aminobenzoic acid series.

The strategy proved efficient and gave access to pure products in good to excellent yields.

Fmoc-protected *N*-alkylated building blocks have also been developed within the group to build α-helix mimetics (synthesis performed by Dr K. Long, Scheme 4.2)[105, 106] and were made available to be introduced in the hybrid scaffold in order to achieve structural diversity.

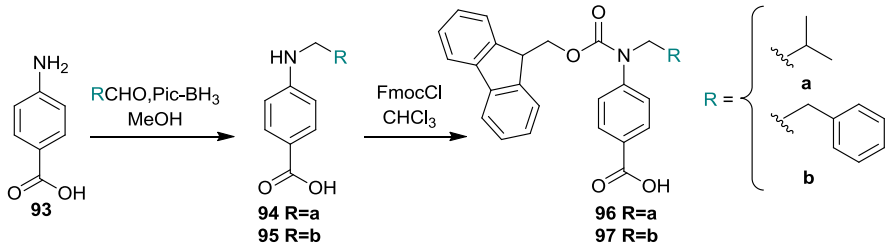

93

94 R=a
95 R=b

96 R=a
97 R=b

Scheme 4.2 Synthetic route to Fmoc-protected building blocks of *N*-alkylated *p*-aminobenzoic acid series.

4.2.2 Solid phase synthesis of hybrid α-helix mimetics

Hybrid α-helix mimetics were built through the SPPS (Scheme 4.3), using an automated microwave-assisted CEM Liberty® peptide synthesiser. The strategy, adapted from previously reported solid phase synthesis of 3-*O*-alkylated[100] and *N*-alkylated[106] oligobenzamides, used Fmoc-Gly or Fmoc-Leu preloaded Wang resins as solid supports.

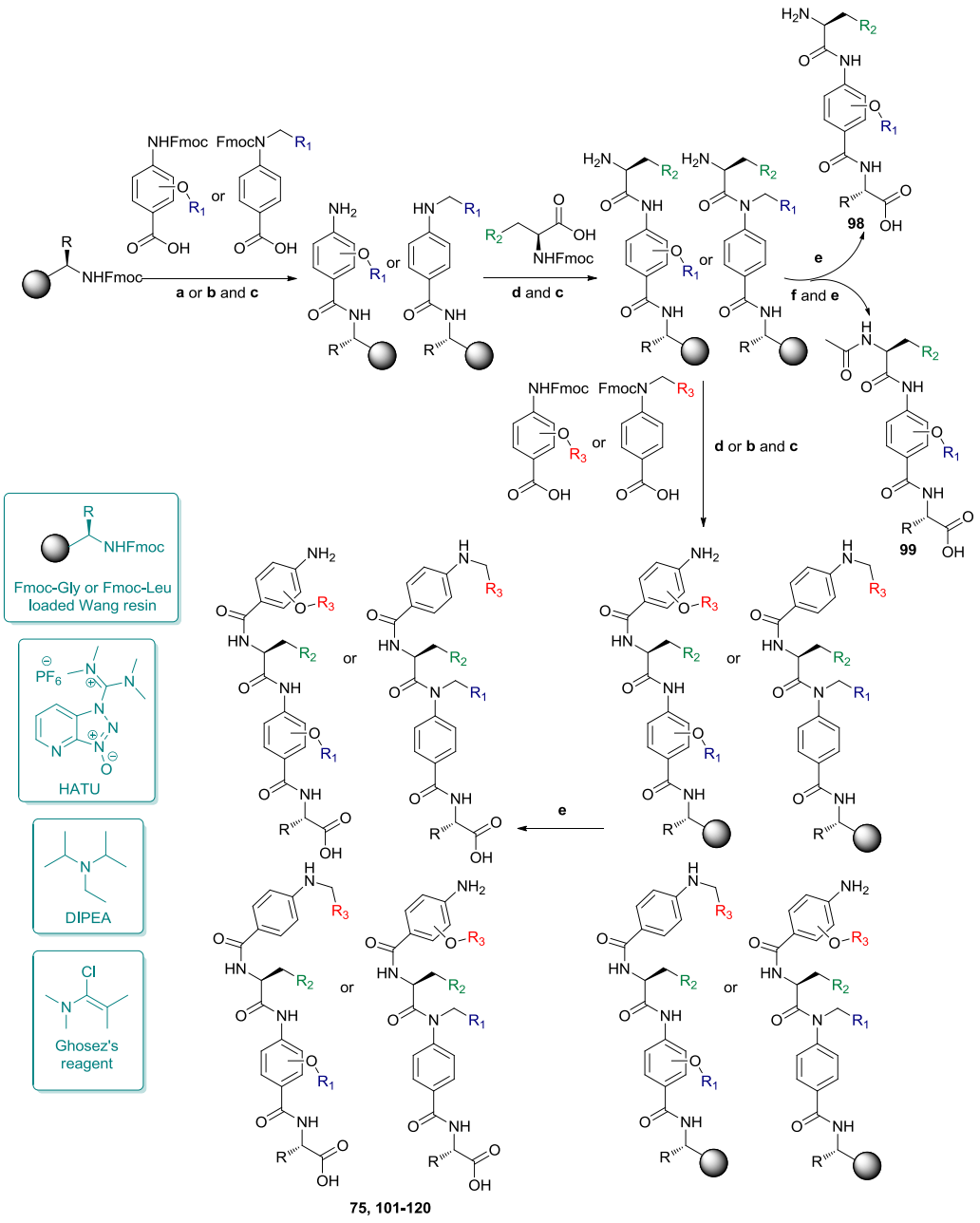

Scheme 4.3 Solid phase synthesis of hybrid α-helix mimetics **a** Loading: resin (1 equiv.) swelled in anhydrous DMF and deprotected with 20% (v/v) piperidine/DMF (two cycles of 3 min at 75 °C), 2-*O* or 3-*O*-alkylated monomer (1.5 equiv.) in anhydrous DMF pre-activated with HATU (1.9 equiv.) and DIPEA (3.8 equiv.), single coupling method (30 min at 50 °C); **b** Coupling of *N*-alkylated building blocks: monomer (3 equiv. per coupling) in anhydrous DMF pre-activated for a minimum of 2 hours with Ghosez's reagent (2.7 equiv. per coupling), double coupling method (2×20 min at 60 °C); **c** Deprotection: 20% (v/v) piperidine/DMF (two cycles of 3 min at 75 °C); **d** Coupling: amino acid (2.5 equiv. per coupling) or 2-*O* and 3-*O*-alkylated monomer (1.5 equiv. per coupling) in anhydrous DMF pre-activated with HATU (3 equiv. per coupling) and DIPEA (5 equiv. per coupling), double or triple coupling method (2 or 3×30 min at 60 °C); **e** Manual cleavage: 50% (v/v) TFA/CH_2Cl_2 (two cycles of 40 min at r.t.); **f** Manual *N*-acetylation: acetic anhydride (10 equiv.) in anhydrous DMF (overnight, r.t.).

After resin deprotection with piperidine, protected monomers were coupled using HATU[144] or Ghosez's reagent[145]. The successful use of HATU as a coupling reagent is particularly noteworthy, as standard peptide synthesis coupling reagents have been previously shown to be ineffective to couple aminobenzoic acid building blocks due to their reduced nucleophilic properties.[98, 100, 106] Elongation of the sequence was achieved through a series of sequential deprotection/coupling steps to load the central amino acid and the final monomer. The desired products were obtained in only 5 hours and, after manual cleavage with TFA, with purity higher than 80% (determined *via* LC-MS and ^{1}H-NMR) in moderate to good crude yields. In order to achieve an enhanced degree of purity to perform biological assays, the hybrid mimetics were then purified using mass-directed preparative HPLC (0.1% formic acid water/methanol or acetonitrile; 5-95% gradient).

Following this synthetic route, an initial 24-membered library was synthesised and purified (Table 4.1). The library included four control molecules: three dimeric versions of the hybrid scaffold (**98** and **99**, synthesis shown in Scheme 4.3; **100**, synthesis shown in Scheme 4.4) and a hybrid with an unfunctionalised *p*-aminobenzoic acid top unit (**101**).

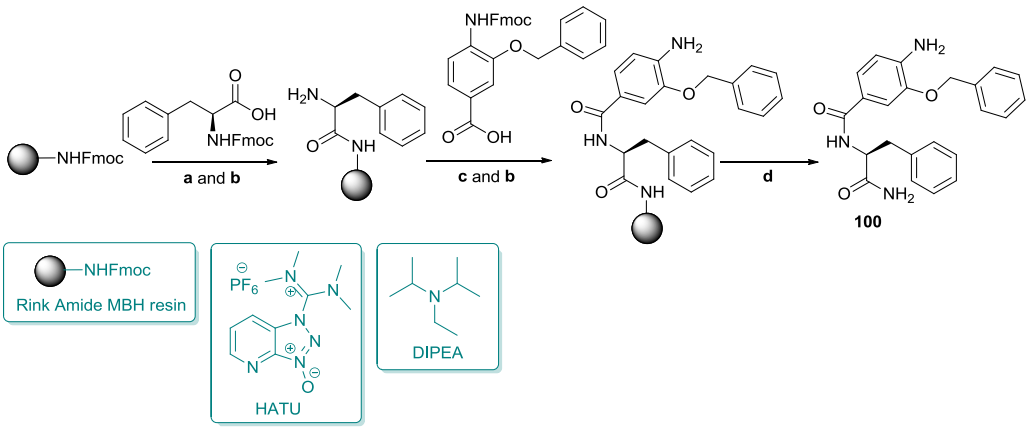

Scheme 4.4 Solid phase synthesis of a control hybrid α-helix mimetic a Loading: resin (1 equiv.) swelled in anhydrous DMF and deprotected with 20% (v/v) piperidine/DMF (two cycles of 3 min at 75 °C), amino acid (2.5 equiv. per coupling) in anhydrous DMF pre-activated with HATU (3 equiv. per coupling) and DIPEA (5 equiv. per coupling), double coupling method (2×30 min at 60 °C); **b** Deprotection: 20% (v/v) piperidine/DMF (two cycles of 3 min at 75 °C); **c** Coupling: *O*-alkylated monomer (1.5 equiv. per coupling) in anhydrous DMF pre-activated with HATU (3 equiv. per coupling) and DIPEA (5 equiv. per coupling), double coupling method (2×30 min at 60 °C); **d** Manual cleavage: 50% (v/v) TFA/CH_2Cl_2 (two cycles of 40 min at r.t.).

Table 4.1 Library of hybrid α-helix mimetics illustrating side-chain sequence and percentage of purity after mass-directed HPLC purification (determined *via* ^{1}H-NMR).

Hybrid number	Resin	R_1	AA	R_3	Purity
98	Gly	2-*O*-*i*Pr	L-Phe	-	95%
99	Gly	2-*O*-*i*Pr	*N*-acetyl-L- Phe	-	95%
100	Rink Amide	-	L-Phe	3-*O*-Bn	95%
101	Gly	2-*O*-*i*Pr	L-Phe	H	95%
75	Gly	2-*O*-*i*Pr	L-Phe	3-*O*-Bn	95%
102	Gly	2-*O*-*i*Pr	L-Phe	2-*O*-Bn	95%
103	Gly	2-*O*-*i*Pr	L-Phe	*N*-Bn	95%
104	Gly	3-*O*-*i*Pr	L-Phe	3-*O*-Bn	95%
105	Gly	3-*O*-*i*Pr	L-Phe	2-*O*-Bn	95%
106	Gly	3-*O*-*i*Pr	L-Phe	*N*-Bn	95%
107	Gly	*N*-*i*Bu	L-Phe	3-*O*-Bn	95%
108	Gly	*N*-*i*Bu	L-Phe	2-*O*-Bn	95%
109	Gly	*N*-*i*Bu	L-Phe	*N*-Bn	95%
110	Gly	2-*O*-*i*Pr	L-Phe	2-*O*-*i*Bu	95%
111	Gly	2-*O*-*i*Pr	L-Phe	2-*O*-*i*Bu	90%
112	L-Leu	2-*O*-*i*Pr	L-Leu	2-*O*-*i*Bu	90%
113	Gly	2-*O*-*i*Pr	L-Trp	3-*O*-Bn	90%
114	Gly	2-*O*-*i*Pr	L-Trp	2-*O*-Bn	90%
115	Gly	2-*O*-*i*Pr	L-Trp	2-*O*-*i*Bu	90%
116	Gly	2-*O*-*i*Pr	4-F- L-Phe	3-*O*-Bn	95%
117	Gly	2-*O*-*i*Pr	4-Br- L-Phe	3-*O*-Bn	95%
118	Gly	2-*O*-*i*Pr	4-Cl- L-Phe	3-*O*-Bn	95%
119	Gly	2-*O*-*i*Pr	L-Tyr	3-*O*-Bn	95%
120	Gly	2-*O*-*i*Pr	L-His	3-*O*-Bn	95%

In spite of the reduced reactivity of alkylated *p*-aminobenzoic acid building blocks[100, 106, 117, 118] the strategy efficiently coupled monomers of all three series containing both aliphatic and aromatic side-chains.

To extend the library, a further sub-family of functionalised hybrid α-helix mimetics was also synthesised. The sequence of the native p53 helix contains a proline residue at the $i + 8$ position (Pro27, on the same face as the key 'hot-spots'), a glutamic acid at the $i + 9$ position (Glu28), facing the solvent-exposed edge and a further glutamic acid at the top of the helix, located at the $i - 2$ position (Glu17, Figure 4.5).

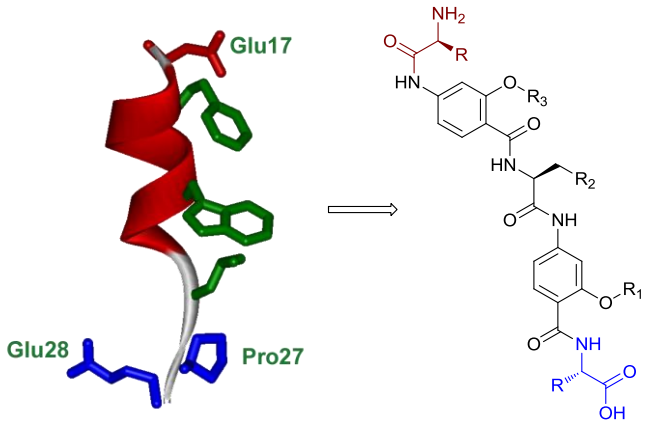

Figure 4.5 Design of amino acid functionalised hybrid α-helix mimetics showing the correspondence with the bottom (blue) and the top (red) amino acids of the p53 α-helix.

Extended hybrid mimetics were hence prepared with different amino acids at the start and end of the sequence following an expanded SPPS strategy as shown in Scheme 4.5 and Table 4.2.

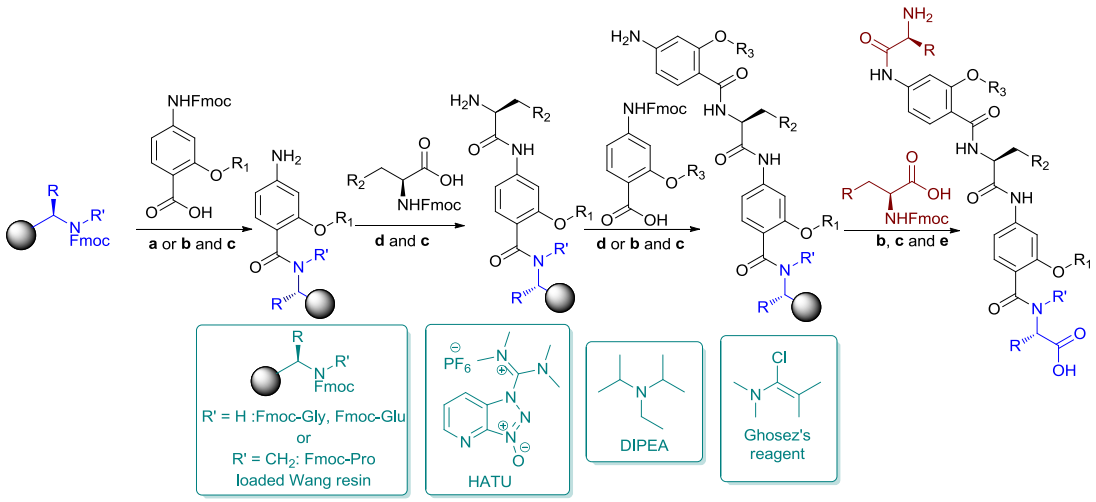

Scheme 4.5 Solid phase synthesis of amino acid-functionalised hybrid α-helix mimetics **a** Loading: resin (1 equiv.) swelled in anhydrous DMF and deprotected with 20% (v/v) piperidine/DMF (two cycles of 3 min at 75 °C), 2-*O*-alkylated monomer (1.5 equiv.) in anhydrous DMF pre-activated with HATU (1.9 equiv.) and DIPEA (3.8 equiv.), single coupling method (30 min at 50 °C); **b** Deprotection: 20% (v/v) piperidine/DMF (two cycles of 3 min at 75 °C); **c** Coupling: amino acid (2.5 equiv. per coupling) or 2-*O*-alkylated monomer (1.5 equiv. per coupling) in anhydrous DMF pre-activated with HATU (3 equiv. per coupling) and DIPEA (5 equiv. per coupling), double or triple coupling method (2 or 3×30 min at 60 °C); **d** Terminal coupling: amino acid (2.5 equiv. per coupling) in anhydrous DMF pre-activated for a minimum of 2 hours with Ghosez's reagent (3.2 equiv. per coupling), double coupling method (2×20 min at 60 °C); **e** Manual cleavage: 50% (v/v) TFA/CH_2Cl_2 (two cycles of 40 min at r.t.).

Table 4.2 Library of amino acid-functionalised hybrid α-helix mimetics illustrating side-chain sequence and percentage of purity after mass-directed HPLC purification (determined *via* ^{1}H-NMR).

Hybrid number	Resin	R_1	AA	R_3	Top AA	Purity
121	L-Glu	2-*O*-*i*Pr	L-Phe	2-*O*-*i*Bu	-	90%
122	L-Glu	2-*O*-*i*Pr	L-Phe	2-*O*-*i*Bu	L-Glu	90%
123	L-Glu	2-*O*-*i*Pr	L-Phe	2-*O*-*i*Bu	L-Arg	90%
124	L-Pro	2-*O*-*i*Pr	L-Phe	2-*O*-*i*Bu	-	90%
125	L-Pro	2-*O*-*i*Pr	L-Phe	2-*O*-*i*Bu	L-Glu	90%
126	L-Pro	2-*O*-*i*Pr	L-Phe	2-*O*-*i*Bu	L-Arg	90%
127	Gly	2-*O*-*i*Pr	L-Phe	2-*O*-*i*Bu	L-Glu	90%
128	Gly	2-*O*-*i*Pr	L-Phe	2-*O*-*i*Bu	L-Arg	90%

4.3 Solution-state conformational analyses: NMR studies

Solution-state structural analyses were conducted on the model hybrid mimetic **75** to elucidate the conformational properties of this new scaffold.

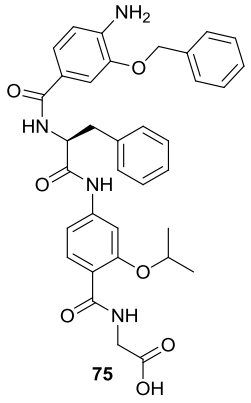

The 2D ^{1}H-^{1}H NOESY experiment (Figure 4.6) showed nOe correlations between the amide protons 2-NH and 3-Phe-NH of the top two units and the ArCH resonances in the *ortho* position of the adjacent monomer units, implying free rotation around the Ar-CO and NH-Ar axes (partial numbering of backbone is shown in Figure 4.6, complete numbering is given in section 6.2.2, Chapter 6). Furthermore, nOe correlations between the 1-Gly-NH and the 2-Hα proton, together with the absence of cross-peaks with the ArCH resonances in the *ortho* and *meta* positions of the adjacent monomer unit (2-H6 and 2-H5) indicated restricted rotation around this Ar-CO axis and intramolecular S(6) H-bonding with the oxygen of the adjacent isopropyl moiety. In addition, the absence of longer-range nOe correlations between the bottom

1-Gly-NH resonance and protons of the central Phe or top units, which may have been expected for a more closed conformation, is consistent with the molecule adopting a linear conformation in solution.

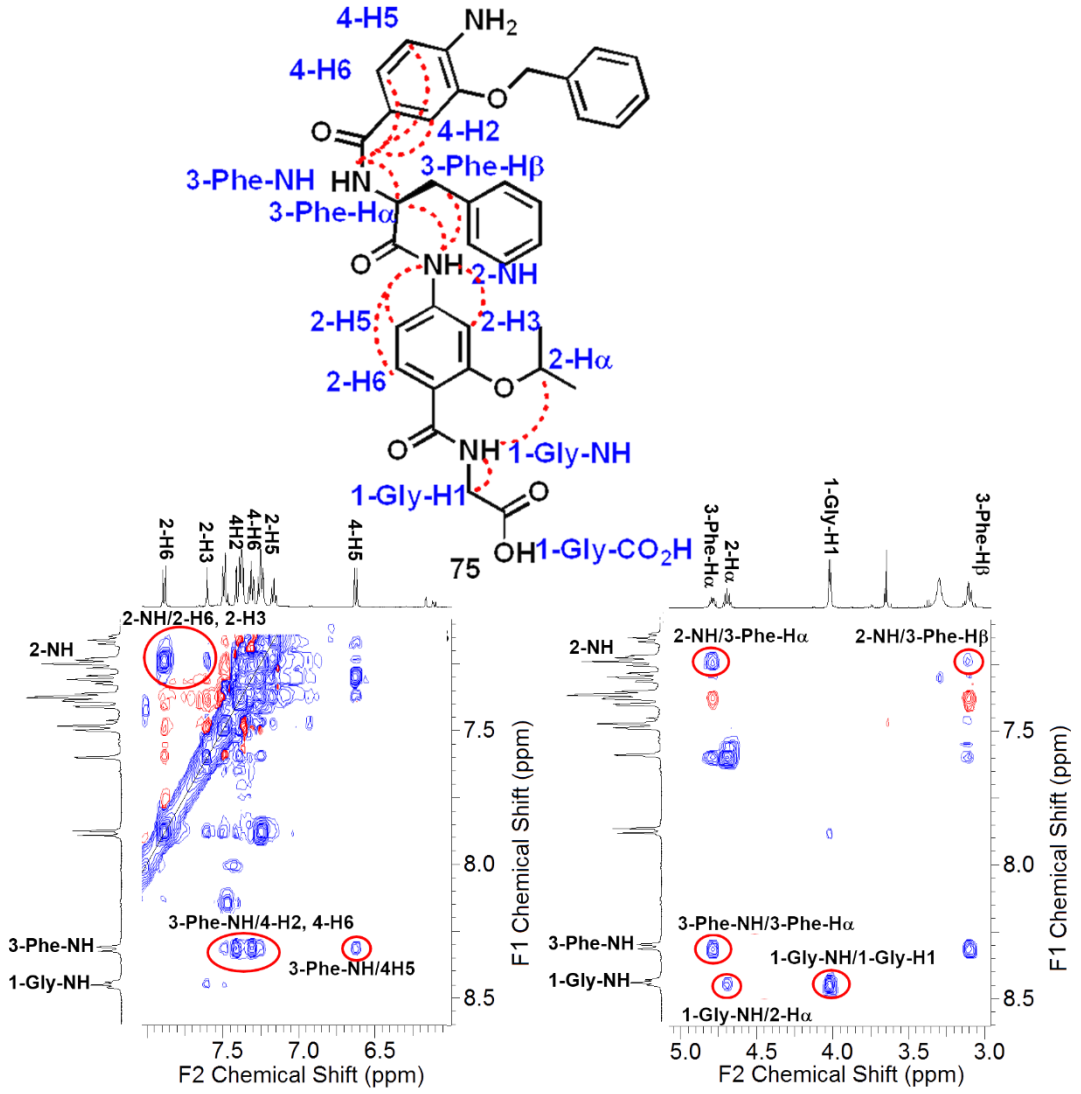

Figure 4.6 Partial ^{1}H-^{1}H NOESY spectra of the hybrid mimetic 75 showing nOe cross-peak correlations in the aromatic (left) and aliphatic (right) regions. (10 mM DMSO-d_6, 500 MHz)

Dilution NMR studies were performed acquiring ^{1}H NMR spectra at concentrations ranging from 10 to 1 mM (Figure 4.7; analysis performed by Dr J. Fisher).

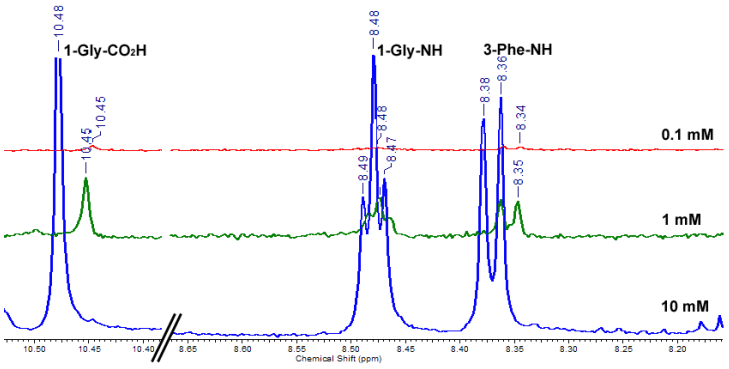

Figure 4.7 Partial ^{1}H-NMR spectra of hybrid 75 (DMSO-d_6, 500 MHz) at concentrations of 10 mM (blue), 1 mM (green) and 0.1 mM (red) showing the acid proton (1-Gly-CO_2H), the Gly-NH proton (1-Gly-NH) and the top amide proton of the sequence (3-Phe-NH).

As expected, a resonance shift was observed for the acid and the top amide protons, but no change was detected for the Gly-NH. This concentration independence confirmed this proton is engaged in an intramolecular H-bond.

Intramolecular H-bonding was further confirmed by VT NMR studies (spectra acquired by Dr J. Fisher) and the results are summarised in Figure 4.8.

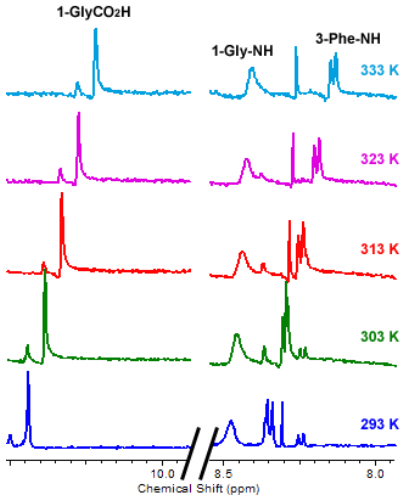

Figure 4.8 Partial ^{1}H-NMR spectra of hybrid 75 (10 mM DMSO-d_6, 500 MHz) at 293 K (blue), 303 K (green) 313 K (red), 323 K (magenta) and 333 K (light blue) showing the acid proton (1-Gly-CO_2H), the Gly-NH proton (1-Gly-NH) and the top amide proton of the sequence (3-Phe-NH).

Analysis of temperature coefficients (T_{coeff}, calculated following Equation 3.1, Chapter 3)[140] revealed T_{coeff} of – 5.5 ppb K^{-1} and - 5 ppb K^{-1} for the acid (1-GlyCO_2H) and the top amide (3-Phe-NH) protons respectively and T_{coeff} of – 1.75 ppb K^{-1} for the 1-Gly-NH proton. These data further supported the hypothesis that the Gly-NH proton

engages in a S(6) intramolecular H-bond, as internally hydrogen bonded amides are expected to show much smaller shifts with temperature than protons which are accessible for H-bonding to external polar solvents.[129, 136, 137, 146]

In order to investigate the conformational properties of derivatives with an alternative side-chain spacing, 2D ^{1}H-^{1}H NOESY experiments were conducted on hybrids **104** and **107**, containing a bottom 3-*O* or *N*-alkylated unit respectively.

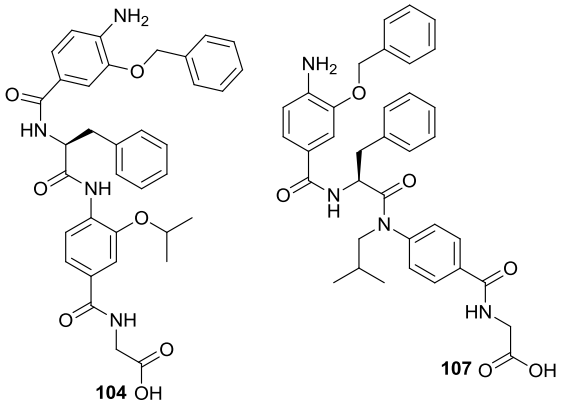

The nOe pattern for hybrid **104**, was consistent with the monomers adopting conformations observed in previous studies. For example, the range of nOe correlations observed for the 1-Gly-NH and the 3-Phe-NH both suggest free rotation around the Ar-CO axes in the absence of intramolecular H-bonding, The absence of a cross-peak between the amide proton 2-NH and the *ortho* 2-H5 proton is also consistent with restricted rotation around this NH-Ar axis and intramolecular S(5) H-bonding with the oxygen of the adjacent alkoxy moiety (Figure 4.9). The absence of longer-range nOe correlations between the bottom 1-Gly-NH resonance and protons of the top units may also suggest the hybrid adopts a linear conformation in solution.

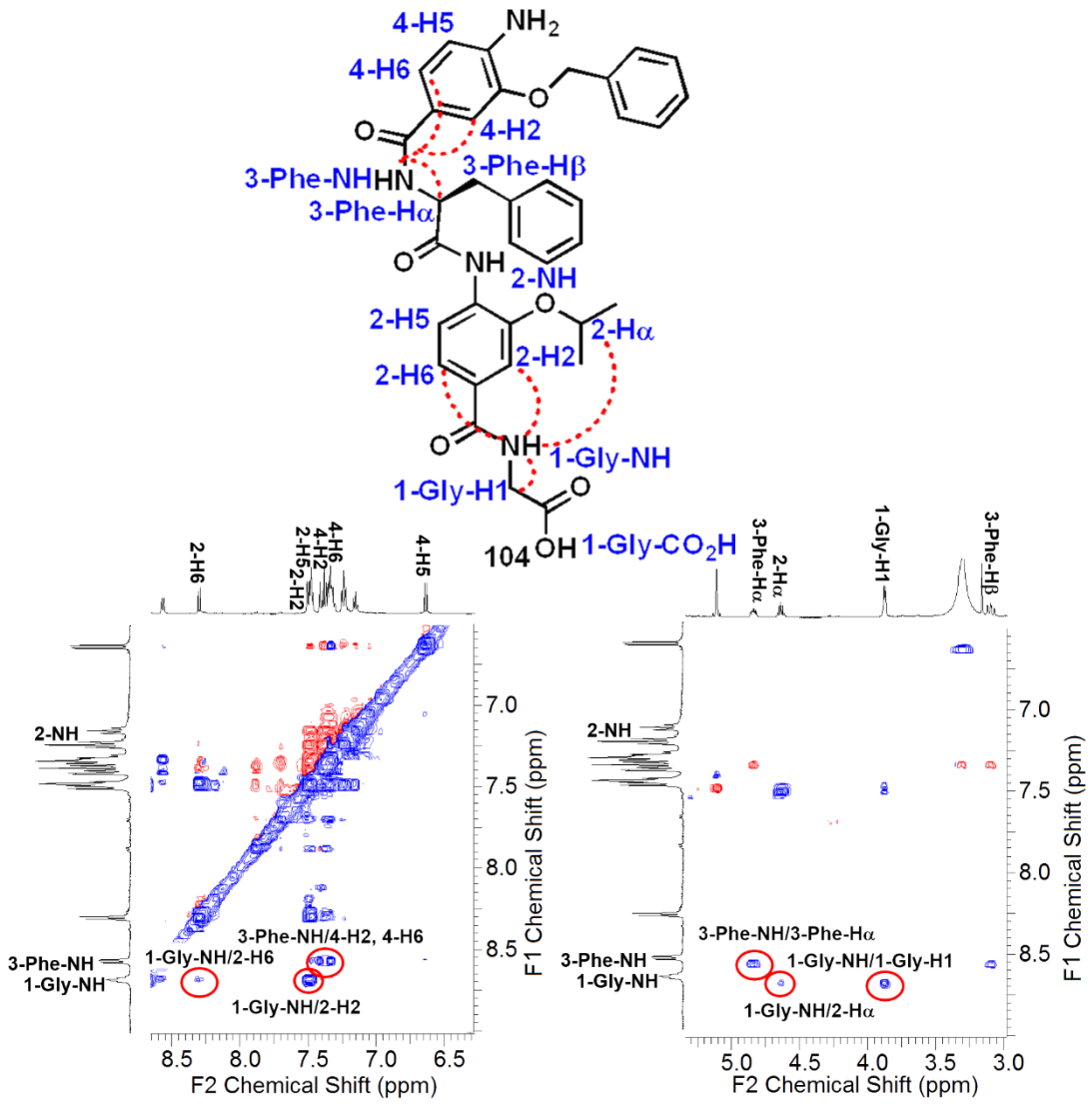

Figure 4.9 Partial ^{1}H-^{1}H NOESY spectrum of the hybrid mimetic 104 showing nOe cross-peak correlations in the aromatic (left) and aliphatic (right) regions. (10 mM DMSO-d$_6$, 500 MHz)

On the other hand, the *N*-alkylated unit of hybrid **107** did not possess protons that could engage in intramolecular H-bonding. As expected, nOe correlations between the 1-Gly-NH or 3-Phe-NH protons and the ArCH resonances in the *ortho* position of the adjacent monomer units implied free rotation around the Ar-CO and NH-Ar axes within the entire structure (Figure 4.10). However, nOe correlations were not observed between the Gly-NH and protons of the central Phe residue or of the top 3-*O*-alkylated unit and the absence of these longer-range correlations may suggest that the linear conformer was preferred in solution also for this hybrid.

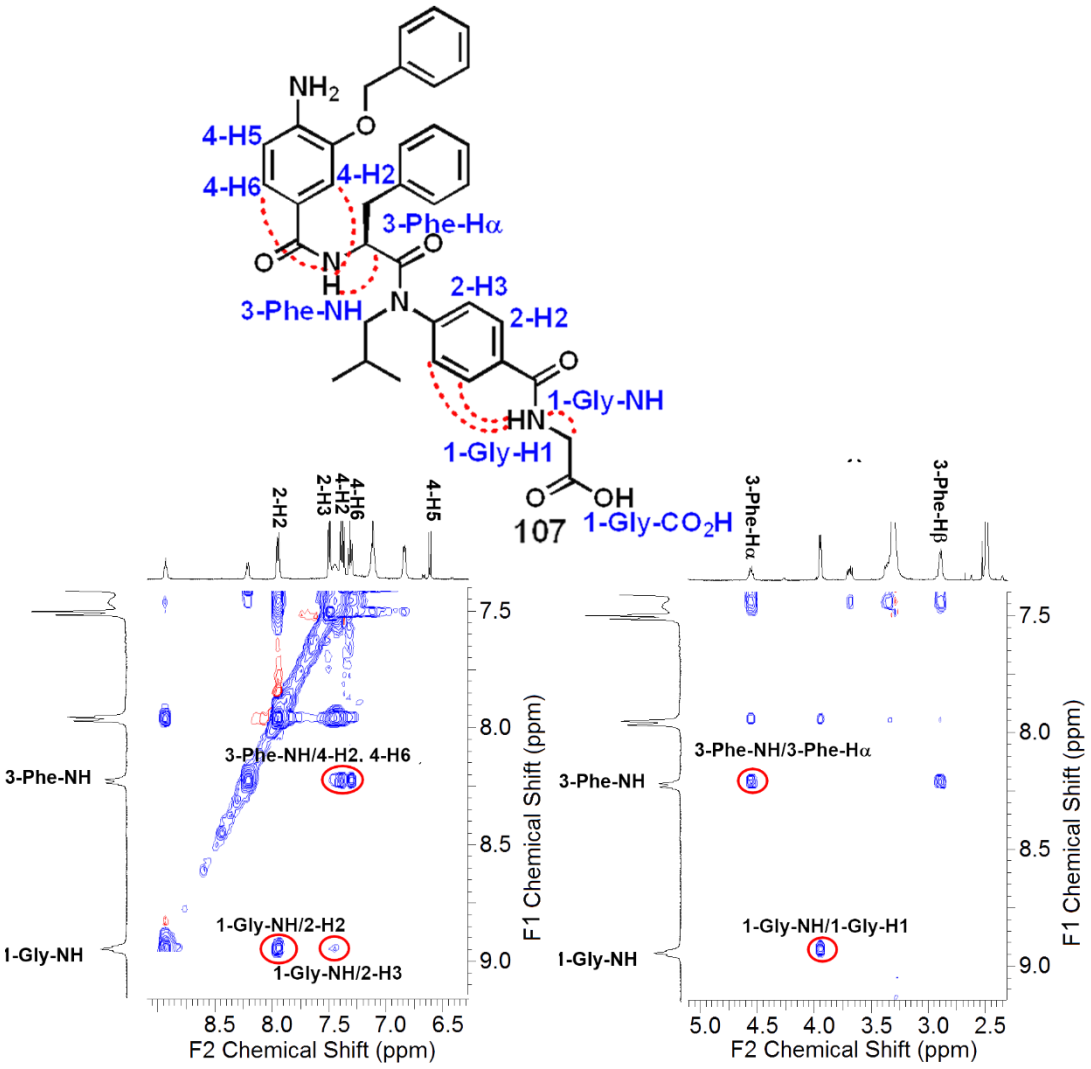

Figure 4.10 Partial ^{1}H-^{1}H NOESY spectrum of the hybrid mimetic 107 showing nOe cross-peak correlations in the aromatic (left) and aliphatic (right) regions. (10 mM DMSO-d_6, 500 MHz)

4.4 Proteolytic studies

The introduction of an α-amino acid in the middle of the hybrid sequence could render these mimetics more susceptible to enzymatic degradation and less suitable for cell-based assays. Proteolytic studies were performed on the model hybrid **75** and the wild-type (WT) p53 helix. Unfortunately, the poor solubility of 3-*O* and 2-*O*-alkylated benzamide mimetics did not allow analogous studies on the related scaffolds to be performed for direct comparison.

α-Chymotrypsin and Proteinase K were chosen for this analysis, as these enzymes selectively cleave amide bonds adjacent to aromatic functionalities (Scheme 4.6). Control studies were also performed by treating these substrates with no enzyme or Trypsin, as this protease cleaves amide bonds adjacent to arginine or lysine residues (Scheme 4.6) and therefore should not degrade any of the substrates considered.

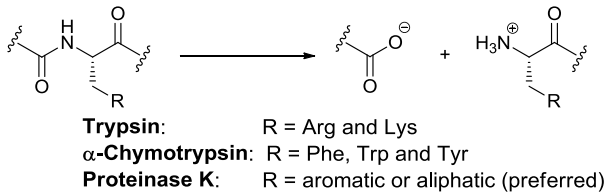

Scheme 4.6 Amide degradation mediated by Trypsin, α-Chymotrypsin and Proteinase K.

Hybrid **75** and WT-p53 were treated with the chosen enzyme in a 1:10000 enzyme/substrate ratio (see section 6.2.3, Chapter 6 for further details) and the degradation was followed with analytical HPLC. Figure 4.11 shows a representative example of the analytical HPLC traces resulting by the treatment of WT-p53 (Figure 4.11 a) and hybrid **75** (Figure 4.11 b) with α-Chymotrypsin. (HPLC traces for other enzymes are shown in section 6.2.3, Chapter 6).

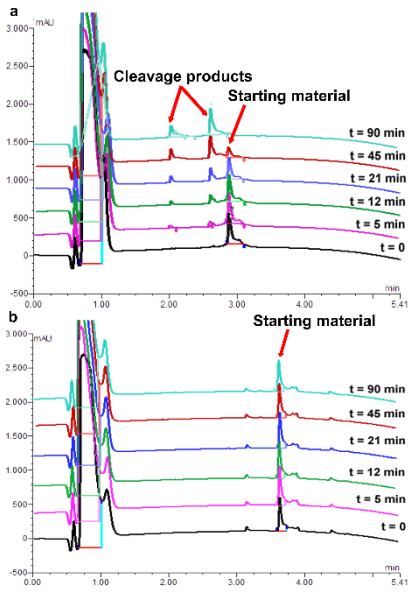

Figure 4.11 Proteolytic studies on the model hybrid 75 (1:10000 enzyme/substrate ratio) **a** Analytical HPLC trace for WT-p53 treated with α-Chymotrypsin; **b** Analytical HPLC trace for **75** treated with α-Chymotrypsin.

The data obtained were then analysed to extract kinetic values (Figure 4.12 a). To minimize variability, the area of the peak corresponding to DMSO was used as internal reference for correction. Rate constants were determined from a linear fit following Equation 4.1 and the half-life of the proteolysis was determined using Equation 2.2 (Chapter 2).

$$\ln\left(\frac{A_t}{A_0}\right) = -kt$$

A_t = Substrate areas at time t; A_0 = Substrate area at time zero; k = reaction rate coefficient

Equation 4.1

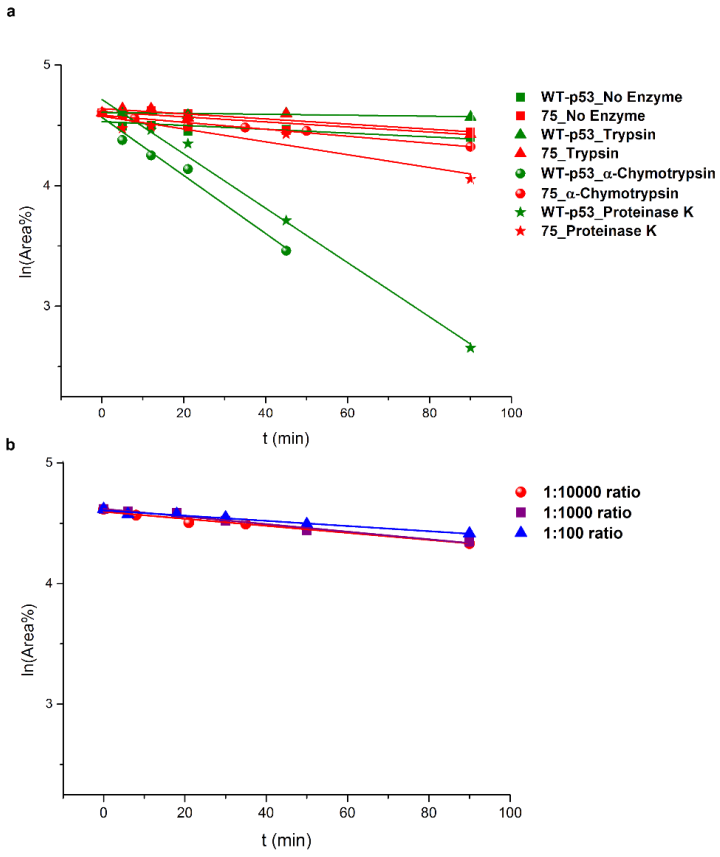

Figure 4.12 Kinetics of degradation from proteolytic studies **a** Kinetics of degradation of hybrid **75** (red) and WT-p53 (green) treated with no enzyme (square), Trypsin (triangle), α-Chymotrypsin (sphere) and Proteinase K (star) in 1 1:10000 enzyme/substrate ratio; **b** Kinetics of degradation from proteolytic studies of hybrid **75** at 1:10000 (red), 1:1000 (purple) and 1:100 (blue) α-Chymotrypsin /substrate ratio.

As shown in Figure 4.12 and Table 4.3, hybrid **75** displayed at least eight fold greater resistance to α-Chymotrypsin and four fold greater resistance to Proteinase K than the native peptide. It is however worth noting that even though the integral of the

starting material peak decreased over time, no degradation products could be seen in the HPLC trace (Figure 4.11 b).

Table 4.3 Table illustrating the calculated half-lives of degradation for WT-p53 and hybrid 75.

Substrate	$t_{1/2}$ No Enzyme	$t_{1/2}$ Trypsin	$t_{1/2}$ α-Chymotrypsin	$t_{1/2}$ Proteinase K
WT-p53	> 300 min	> 300 min	28.8 ± 2.2 min	30.8 ± 1.4 min
75	> 300 min	> 300 min	239 ± 22 min	130 ± 21 min

The greater resistance of hybrid **75** was also confirmed by increasing the ratio of α-Chymotrypsin to hybrid to 1:1000 and 1:100 (Figure 4.12 b), suggesting that this new scaffold has sufficient proteolytic stability to be employed in complex biological studies.

4.5 Proof-of-concept: targeting the p53/*h*DM2 PPI

4.5.1 Preliminary Fluorescence Anisotropy Competition Assays

To test the potential of this new scaffold to adopt an α-helix mimicking conformation, the activity of hybrid **75** and control hybrids **98**-**101** was tested in a FA competition assay targeting the p53/*h*DM2 PPI (molecular cloning and expression of *h*DM2(17-126) L33E no tag: Dr K. Long, Dr. A. Bartlett and Dr J. Miles; see Appendix I for details on the FA assay).[98]

The full competition curves, shown in Figure 4.13, provided encouraging results as hybrid **75** inhibited this PPI in the same micromolar range as the 2-*O* and 3-*O*-alkylated oligobenzamides. It is worth noting that Nutlin-3a (**4**, Chapter 1) displayed an IC_{50} of 534.7 ± 23.9 nM in this assay (the full competition curve is shown in Appendix I). The identification of an inhibitor with activity only an order of magnitude poorer by rational design shows the strength of this scaffold system.

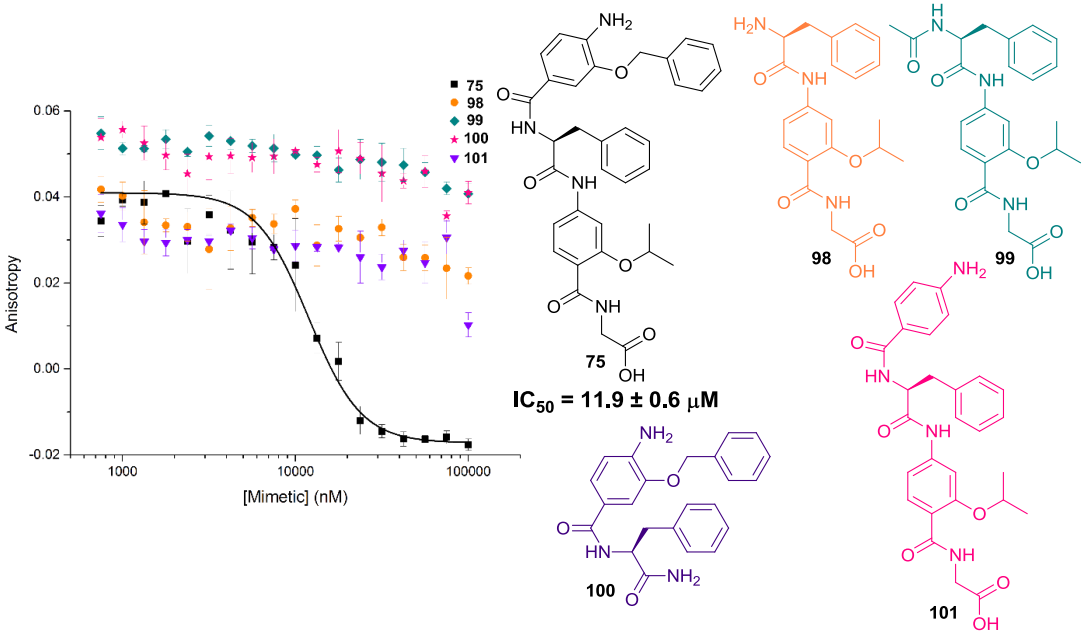

Figure 4.13 Preliminary FA competition assay Dose-response curves and structures of hybrids **75** (black), **98** (orange), **99** (dark cyan), **100** (purple) and **101** (magenta). (40 mM phosphate buffer pH 7.50, 200 mM sodium chloride, 0.02 mg mL^{-1} BSA)

These data also demonstrated that the entirety of the sequence was required to mimic the key 'hot-spot' residues and therefore achieve inhibition. In this regard, the inactivity of hybrid **100** indicated that the bottom unit plays a significant role in binding. Furthermore, absence of activity for hybrids **98** and **99** proved that the top monomer was also essential for activity and the lack of inhibition of hybrid **101** revealed that this unit needs to be functionalised with an interacting side-chain in order to achieve molecular recognition and retain binding affinity.

4.5.2 ^{1}H-^{15}N HSQC study of a model hybrid mimetic in complex with *h*DM2

In order to investigate the binding mode of these mimetics, Dr J. Miles from the Astbury Centre for Structural Molecular Biology performed ^{1}H-^{15}N HSQC perturbation shifts studies.[147] HSQC spectra were acquired for either the ^{15}N-labelled apo form of the protein (125 μM protein 100 mM sodium phosphate buffer at pH 7.3, 2.5% glycerol, 1 mM DTT, 6% DMSO, 25 °C) or the protein in complex with a 200 μM solution of hybrid **75** after overnight incubation.

As shown in Figure 4.14, distinct complexation-induced shifts were observed upon addition of **75**. Once mapped onto the crystal structure of p53/*h*DM2 (PDB ID:

1YCR and 4HFZ; Figure 4.14 c-d),[4, 148] the study showed that shift changes were induced throughout the protein and were comparable to those induced by the p53 peptide in an experiment previously published by the group.[105]

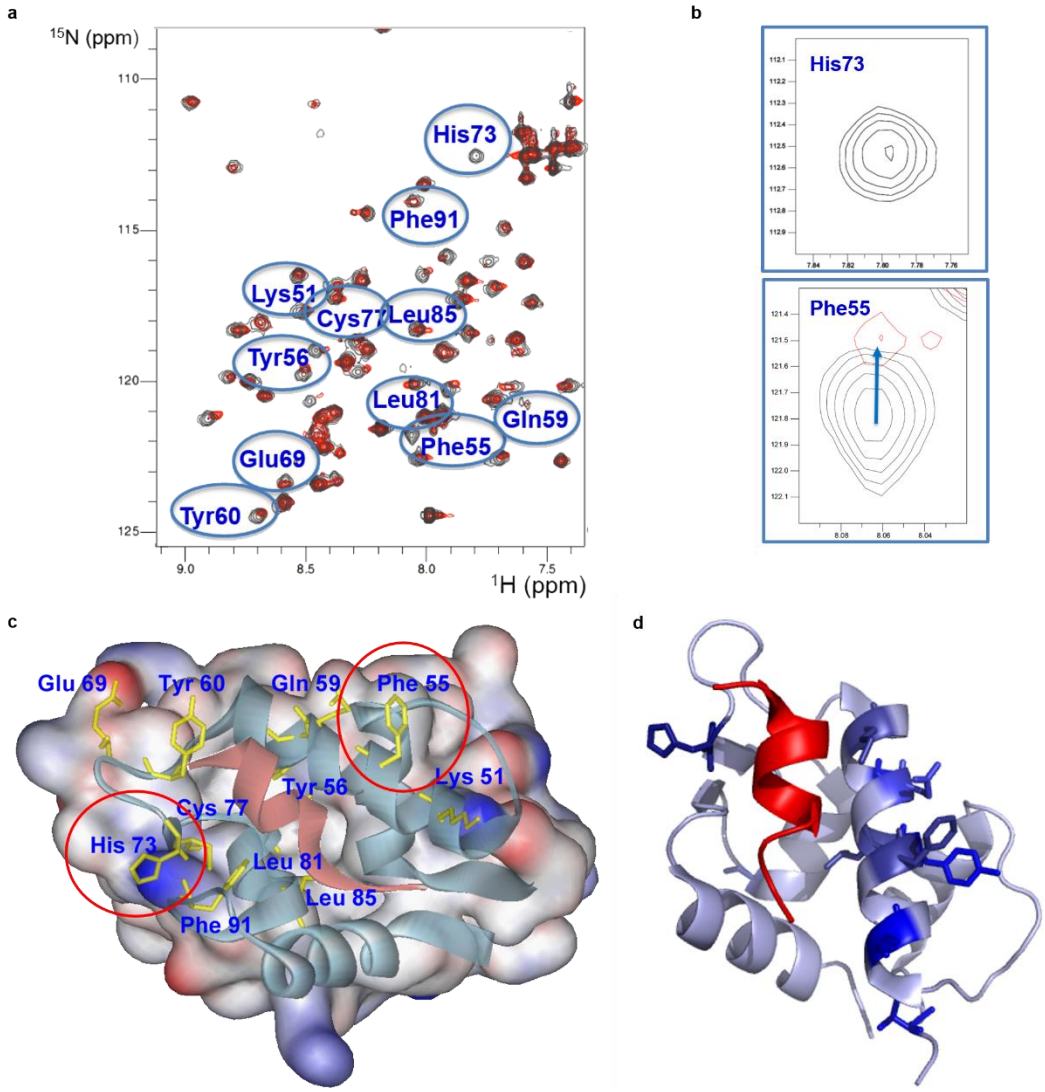

Figure 4.14 ^{1}H-^{15}N HSQC study (600 MHz, 100 mM sodium phosphate buffer pH 7.3, 2.5% glycerol, 1 mM DTT, 6% DMSO, 25 °C) a HSQC spectrum of the ^{15}N-labelled 125 μM solution of *h*DM2 (black) overlapped with the HSQC spectrum of *h*DM2 (125 μM) in complex with a 200 μM solution of **75** (red), highlighting the moving residues; **b** Expansions showing the chemical shift of two relevant residues: His73 (top) and Phe55 (bottom); **c** ^{1}H-^{15}N HSQC chemical shift perturbation mapping onto the crystal structure of p53/*h*DM2 (PDB ID: 1YCR) highlighting the position of the key Phe55 and His73 residues; **d** ^{1}H-^{15}N HSQC chemical shift perturbation mapping onto the crystal structure of p53/*h*DM2 (PDB ID: 4HFZ) highlighting the shift changes of the residues on a dark blue (significant movement) to grey (minor movement) gradient.

Shifts of residues around the helix binding cleft such as Phe55 and His73, which are located at opposite edges of the hydrophobic cleft (Figure 4.14 b-d), further

confirmed that the mimetic binds in the peptide binding site. In particular, the cross-peak of His73 broadened to the extent of being no longer visible, indicating that a specific yet transient interaction was taking place. Notably, shift changes at both ends of the *h*DM2 cleft also supported the hypothesis that the hybrid adopts an extended conformation.

4.6 Fluorescence Anisotropy competition assays against the p53/*h*DM2 PPI: SAR studies

Encouraged by the preliminary results obtained on hybrid **75**, the full library of hybrid mimetics was tested against the p53/*h*DM2 interaction to obtain structure-activity relationship (SAR) data.

4.6.1 The effect of the middle unit

The lack of activity of the control hybrids **98**-**101** showed that the bottom and top units of the sequence were essential for binding. In order to gather better insight on the role of the central unit, a series of hybrids was functionalised with different middle α-amino acids.

Hybrids **113**-**115** were synthesised, which presented a tryptophan *in lieu* of the phenylalanine to mimic the natural 'hot-spot' residue. Full competition curves for p53/*h*DM2 inhibition are shown in Figure 4.15.

The best inhibitor of this series (**113**) did not exhibit any improved activity when compared to hybrid **75** (IC_{50} = 11.9 ± 0.6 μM). This result was unexpected as it was envisaged that the presence of a middle amino acid with perfect mimicry of the natural residue would have led to enhanced affinity for this PPI. Even more interesting was the reduced activity of hybrids **114** and **115** with 2-*O*-alkylated top monomers, as it highlighted the important role that the spacing of the side-chains plays for effective recognition (see also section 4.6.2).

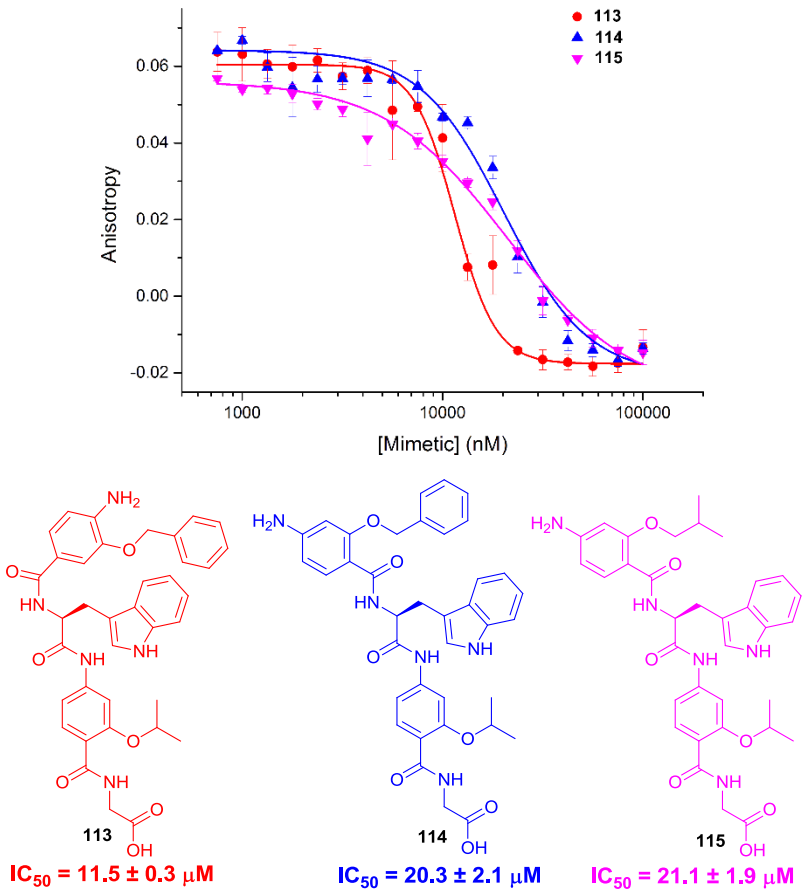

Figure 4.15 L-Trp hybrids: Dose-response curves against the p53/*h*DM2 PPI. (40 mM phosphate buffer pH 7.50, 200 mM sodium chloride, 0.02 mg mL^{-1} BSA)

To better understand the role of the middle unit, hybrid **75** was compared to molecules functionalised with *p*-fluoro (**116**), *p*-bromo (**117**) and *p*-chloro-phenylalanine (**118**) at the middle position. Tyrosine (**119**) and histidine (**120**) functionalised hybrids were also synthesised to gather information on the role of more polar substituents. Figure 4.16 summarises the result of a FA competition assay against the p53/*h*DM2 PPI. Dose-response curves for hybrids **75** and **113** were also included for comparison.

The dramatic difference in activity of these hybrids reinforced the hypothesis that the function of the middle amino acid is key for effective inhibition. Hybrid **117**, the best hybrid α-helix mimetic identified in the entire library, showed low-micromolar inhibition. Hybrids **118** and **116** followed in potency, highlighting the effect of the halo-substitution with potency following the order *p*-Br > *p*-Cl > *p*-F.

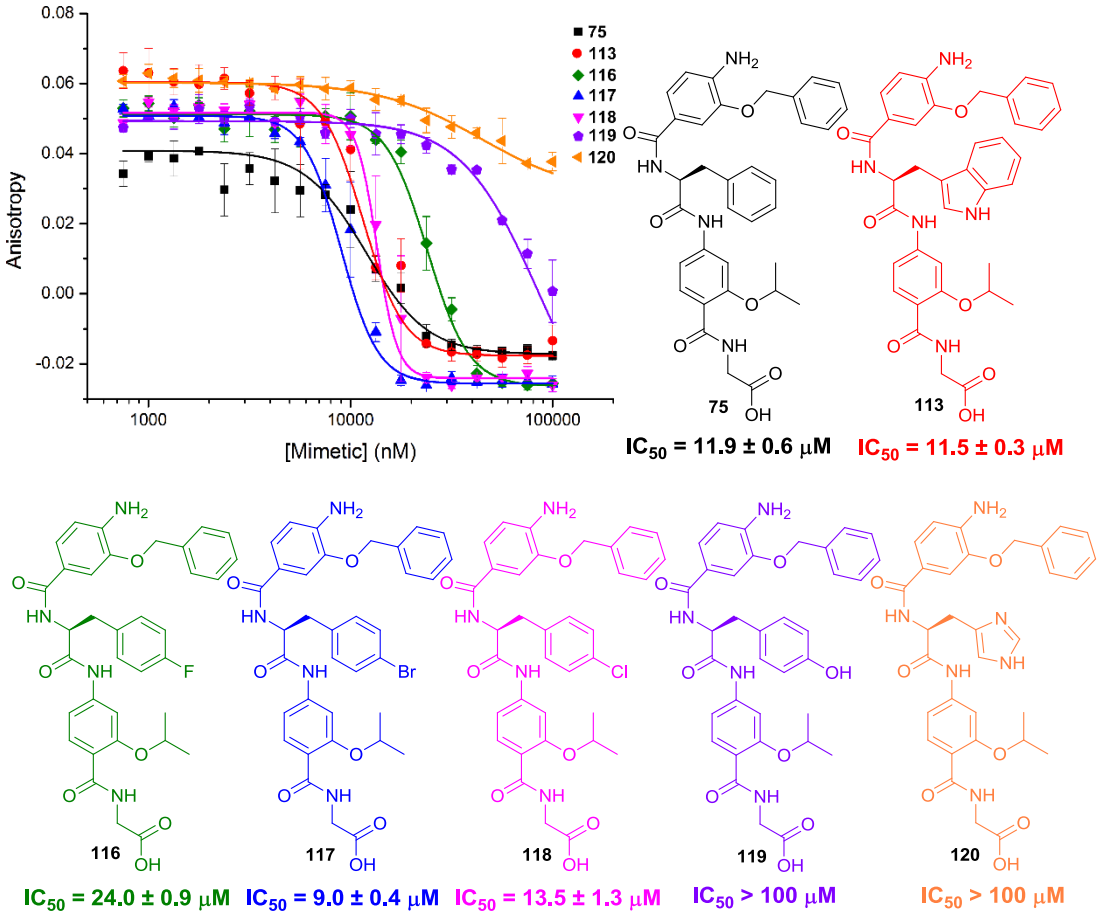

Figure 4.16 Halo-series and polar substituents: Dose-response curves against the p53/*h*DM2 PPI. (40 mM phosphate buffer pH 7.50, 200 mM sodium chloride, 0.02 mg mL^{-1} BSA)

A QSAR (quantitative SAR) analysis was therefore performed on hybrids **75** and **116-119** in an attempt to determine the driving force for this activity trend. Four different parameters were considered to investigate the effect of the *p*-substituent on the benzyl ring of Phe: i. hydrophobicity of the substituents, expressed as π values;[149] ii. electronic effects related to the electron withdrawing properties of the substituents, expressed as σ_p Hammett constants;[149] iii. H-bonding interactions, expressed as α^H (donor) or β^H (acceptor) values;[150] iv. steric effects of the substituents, expressed as molar refraction (MR) values.[149] The logarithm of the IC_{50} values was plotted against all four parameters and the result is shown in Figure 4.17 a-e.

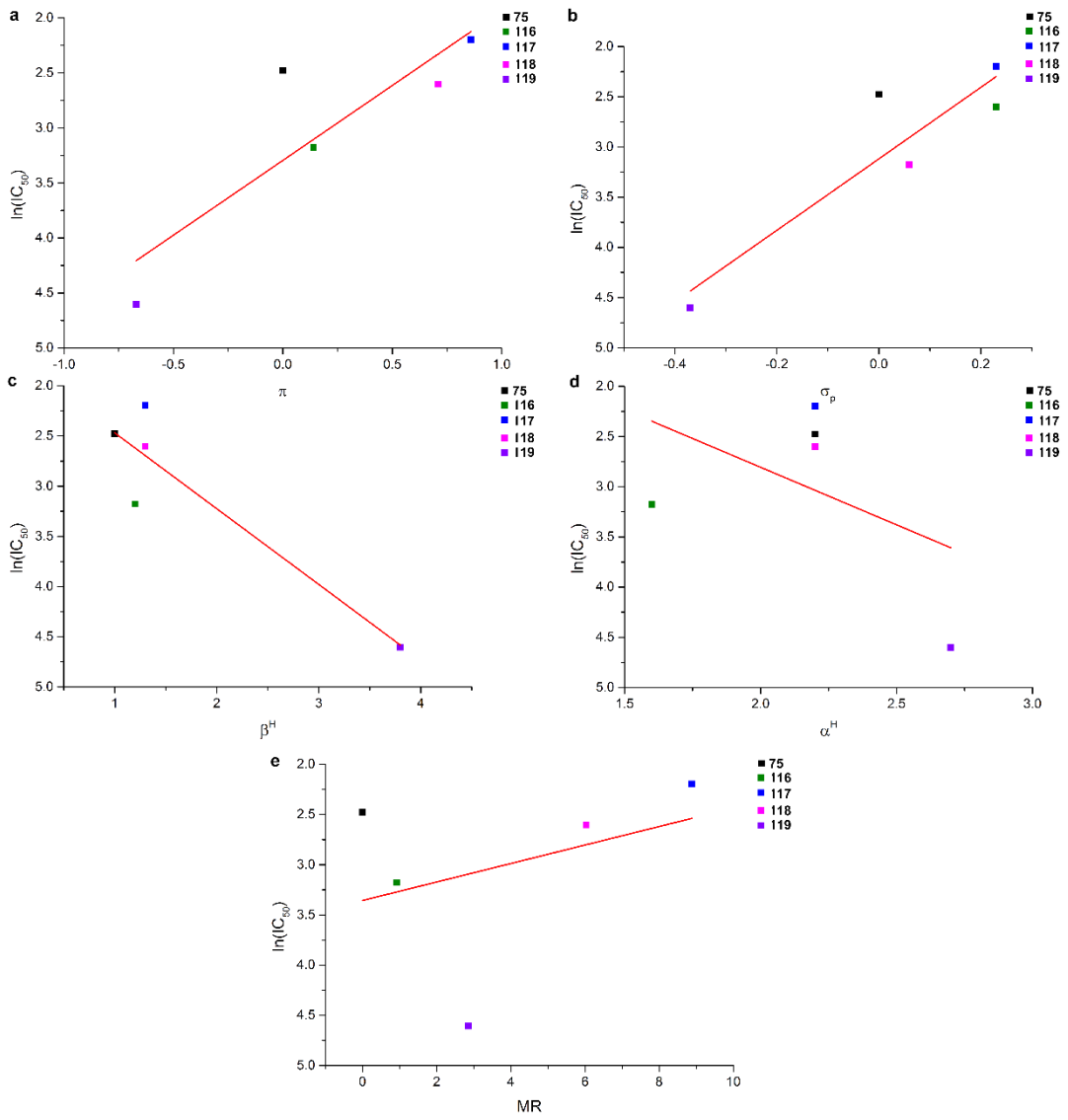

Figure 4.17 QSAR analysis a Hydrophobic effect; **b** Electronic effect; **c** H-bonding acceptor effect; **d** H-bonding donor effect; **e** Steric effect.

A linear correlation was found with π and σ_p values, suggesting that more hydrophobic and more electron withdrawing groups favour binding affinity (Figure 4.17 a-b). On the other hand, the H-bonding ability of these substituents did not show a direct correlation with the activity (Figure 4.17 c-d). The steric effect seemed to have a linear correlation when considering the halo-substituted derivatives, but the trend was not consistent throughout the series and the result is therefore not conclusive (Figure 4.17 e).

Unfortunately, it was not possible to determine which parameter between hydrophobicity and electronic effects gives the strongest contribution to the activity as the parameter values for these substituents cross-correlate (Figure 4.18).

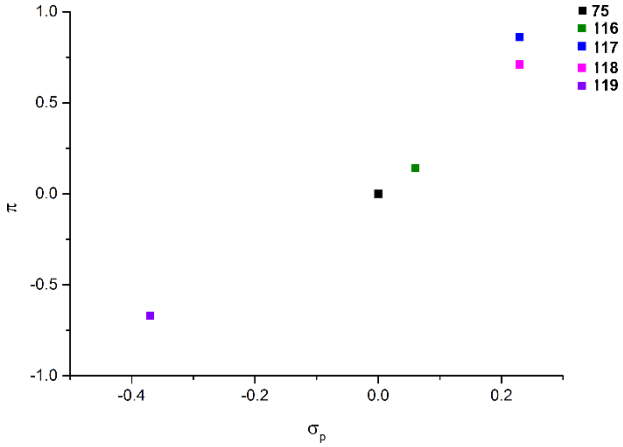

Figure 4.18 Correlation between π and σ_p values.

Given the hydrophobic nature of the protein binding cleft, it is however possible to hypothesise that the hydrophobicity of the interacting side-chain may play the dominant role in maximising the affinity. Substituents with uncorrelated π and σ_p values (*e.g. p*-nitrile: π = -0.57, σ_p = 0.66; *p*-methyl: π = 0.56, σ_p = -0.17)[149] will be introduced in future in order to validate this hypothesis.

4.6.2 The role of side-chain spacing

The result obtained on hybrids **113-115** suggested that the spacing between interacting side-chains plays a key role for effective recognition.

To further investigate this aspect of SAR, hybrids **75** and **102-109** were designed to include a combination of 2-*O*, 3-*O* and *N*-alkylated monomers. Since the alkylation topography is different for each of these building blocks, this library should possess different side-chain spacing and allow further information on which conformational features these mimetics require for molecular recognition.

The mimetics were divided into three families (2-*O*, 3-*O* and an *N*-alkylated series) named after the first monomeric unit at the bottom of the sequence, and tested against the p53/*h*DM2 PPI. Full competition curves for the whole library are shown

in Appendix II and revealed a similar trend of activity within each family. Figure 4.19 shows the results for hybrids **75**, **104** and **107**, which are representative of each series.

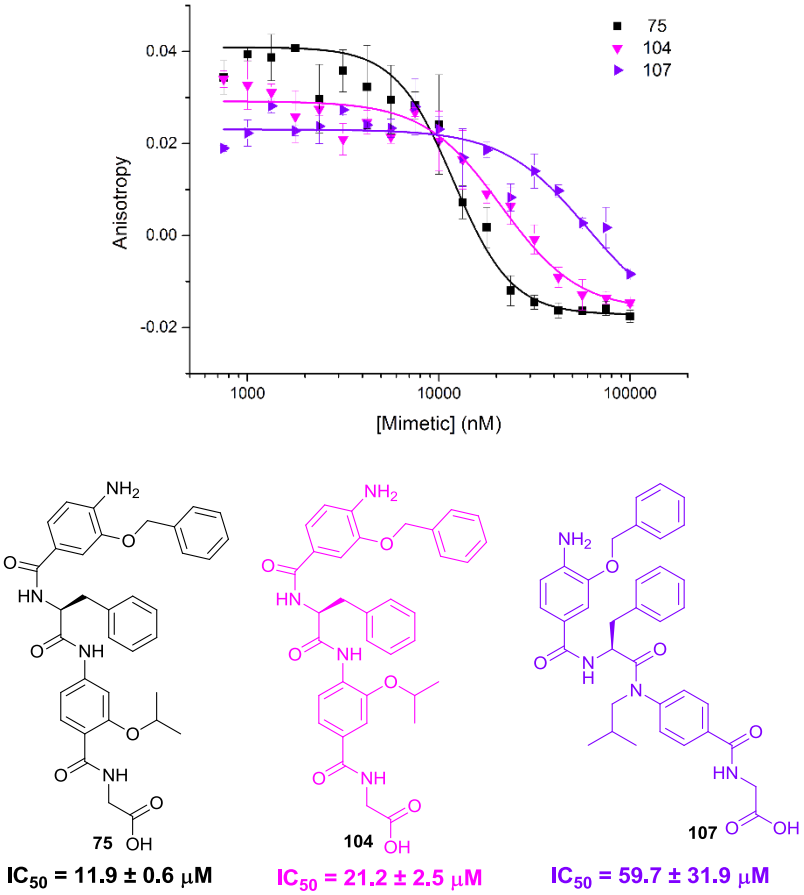

Figure 4.19 Side-chain spacing studies targeting the p53/*h*DM2 PPI: Dose-response curves against the p53/*h*DM2 PPI. (40 mM phosphate buffer pH 7.50, 200 mM sodium chloride, 0.02 mg mL^{-1} BSA)

The assay confirmed that the side-chain spacing has a significant effect on the binding affinity, with mimetics containing a 2-*O*-alkylated building block at the bottom position being better inhibitors than the corresponding 3-*O*-alkylated hybrids and five fold better inhibitors than hybrids of the *N*-alkylated series (see also Appendix II).

The previous activity of the 2-*O* and 3-*O*-alkylated oligobenzamides[98, 118] (see Chapter 3), seemed to suggest that the precise spacing of the side-chains was not a key element to control inhibition, as in the presence of a well-defined backbone the residues could adopt the best possible conformation in order to maximise the interaction with the protein partner. These hybrid mimetics, however, show that when

introducing irregularity in the main core of the backbone, which gives a wider variation of structure, the side-chain spacing starts to play a crucial role. Sequence-dependent SAR therefore suggests that the interaction between the protein and these mimetics is not simply driven by a strong hydrophobic component, but instead through a well-defined process of recognition of the mimetic structure.

The enhanced activity of the 2-*O*-alkylated series revealed that the entirety of the sequence and the presence of the top side-chain are key for inhibition (Section 4.5.1), and that a 2-*O*-alkylated bottom monomer is optimal for maximum activity, thus reinforcing the hypothesis that these hybrid mimetics can recognise the protein cleft through a specific 3-dimensional structural motif.

4.6.3 Aliphatic and amino acid-functionalised hybrid mimetics

A small family of mimetics presenting aliphatic functionalities (**110**-**112**) was synthesised and tested in a FA competition assay against the p53/*h*DM2 PPI.

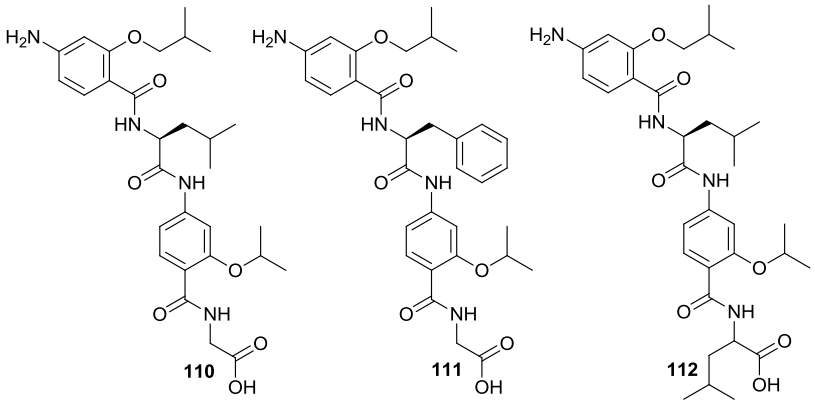

Full competition curves, shown in Appendix II, revealed a remarkable loss of activity in mimetic **111**, which presents R_1 = *i*Pr, R_3 = *i*Bu and L-Phe as the central amino acid. The activity was however recovered in the presence of a leucine middle unit (hybrids **110** and **112**). The reasons for the difference in activity between these molecules are unclear. The presence of small hydrophobic functionalities may favour self-aggregation of these molecules and/or multimeric or non-specific binding to the protein. Further experiments, such as docking studies and ^{1}H-^{15}N HSQC analyses with a ^{15}N-labelled protein, will be performed in future to clarify this result.

Amino acid (AA)-functionalised hybrids **121**-**128** were also tested in full competition against the p53/*h*DM2 interaction (full competition curves are shown in Appendix II).

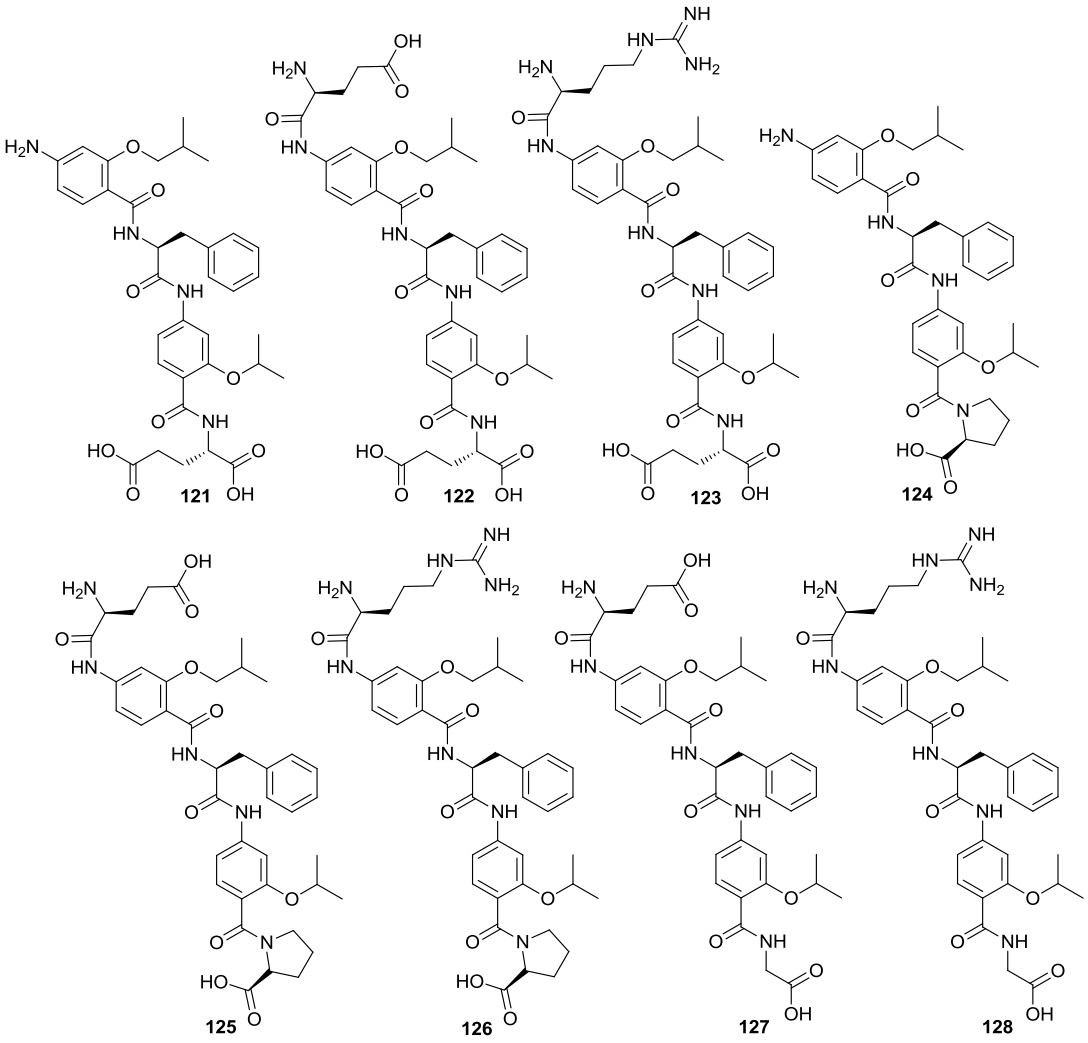

These mimetics were designed to mimic the additional *i* + 8 (Pro27), *i* + 9 (Glu28) and *i* - 2 (Glu17) residues of the p53 helix, but surprisingly a general loss of activity was observed for the entire family. A combination of electronic effects and/or steric clash of the terminal functionalities with the protein cleft may be the reasons for these results. Future investigation (*e.g.* docking studies and crystal trials) will be done in order to clarify these data.

4.6.4 Hybrid α-helix mimetics/*h*DM2 SAR: Summary

A 32-membered library of hybrid α-helix mimetics was designed, synthesised and tested in a FA competition assay to disrupt the p53/*h*DM2 PPI.

Dose-response curves afforded important information regarding the key structural features of these molecules and allowed the development of preliminary SAR rules for this family of mimetics.

In summary, the entirety of the sequence and a functionalised top *p*-aminobenzamide unit needed to be present to achieve inhibition. The activity was also shown to be related to a careful balance between the irregular backbone of this scaffold and a defined side-chain spacing to allow structural recognition. Hybrids of the 2-*O*-alkylated series exhibited the best conformational influence, revealing the importance of this bottom unit.

The central amino acid was shown to be key for effective inhibition. A QSAR analysis revealed that the binding affinity is maximised in the presence of less polar and more electron withdrawing side-chains. Bromo-functionalisation of the phenylalanine residue allowed the identification of the best inhibitor of this family of mimetics.

Together, these structural data backed the validity of the strategy adopted in designing this α-helix mimetic scaffold, and showed that careful tuning of scaffold and side-chains can lead to matched ligands for inhibition.

4.7 Targeting the Bcl-2 family PPIs with hybrid α-helix mimetics

As discussed in Chapter 1, proteins of the Bcl-2 family have a central role in the regulation of *apoptosis* and are therefore attractive targets for therapeutic purposes.[3] Since BH3-only pro-apoptotic proteins of this family also mediate PPIs through three or four key residues of an α-helix, it was envisaged that hybrid α-helix mimetics could also be successfully employed to target and inhibit this family of PPIs.

A Fluorescence Anisotropy competition assay was therefore developed in a joint effort with Dr K. Long and D.J. Yeo in order to target the Mcl-1/NOXA B PPI, which allowed testing of the library of hybrid mimetics (molecular cloning and expression of Mcl-1 (172-327): Dr A. Bartlett and Dr J. Miles; synthesis of FITC-NOXA B (68-87): Dr P. Prabhakaran; for details on the assay development see Appendix I).

4.7.1 FA competition assays against the Mcl-1/NOXA B PPI

Hybrids of the 2-*O*, 3-*O* and *N*-alkylated series (**75**, **102-109**) were initially tested for comparison with the side-chain spacing data obtained through the p53/*h*DM2 SAR. Unexpectedly, all these mimetics showed little or poor inhibitory activity against the Mcl-1/NOXA B PPI (full competition curves shown in Appendix II). A pivotal example was the difference in activity for hybrid **75** which showed, selectivity between these two PPIs (Figure 4.20).

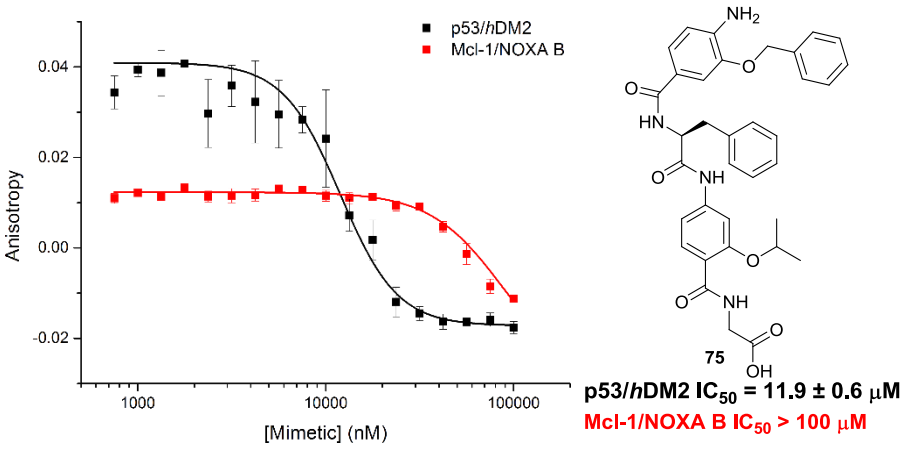

Figure 4.20 Dose-response curves of hybrid 75 against p53/*h*DM2 (black) and Mcl-1/NOXA B (red). (40 mM phosphate buffer pH 7.50, 200 mM sodium chloride, 0.02 mg mL^{-1} BSA)

Docking studies were performed to investigate the reasons for the inactivity of this hybrid towards Mcl-1/NOXA B inhibition. The set of structures within 1.5 kJ/mol from the lowest energy conformation, previously minimised in Macromodel®,[134] was docked with the crystal structure of Mcl-1 (PDB ID: 2JM6)[27] using the software Glide®. Of all the poses generated, only 3% assumed conformations which were binding in the Mcl-1 cleft. Most of the structures were

instead adopting conformations where the backbone of the two bottom residues entered the cleft thus inducing the side-chains to engage in interactions with amino acids outside the NOXA B binding pocket. A representative example is shown in Figure 4.21 a and c. The native Mcl-1/NOXA B PPI is also shown in Figure 4.21 b for comparison.

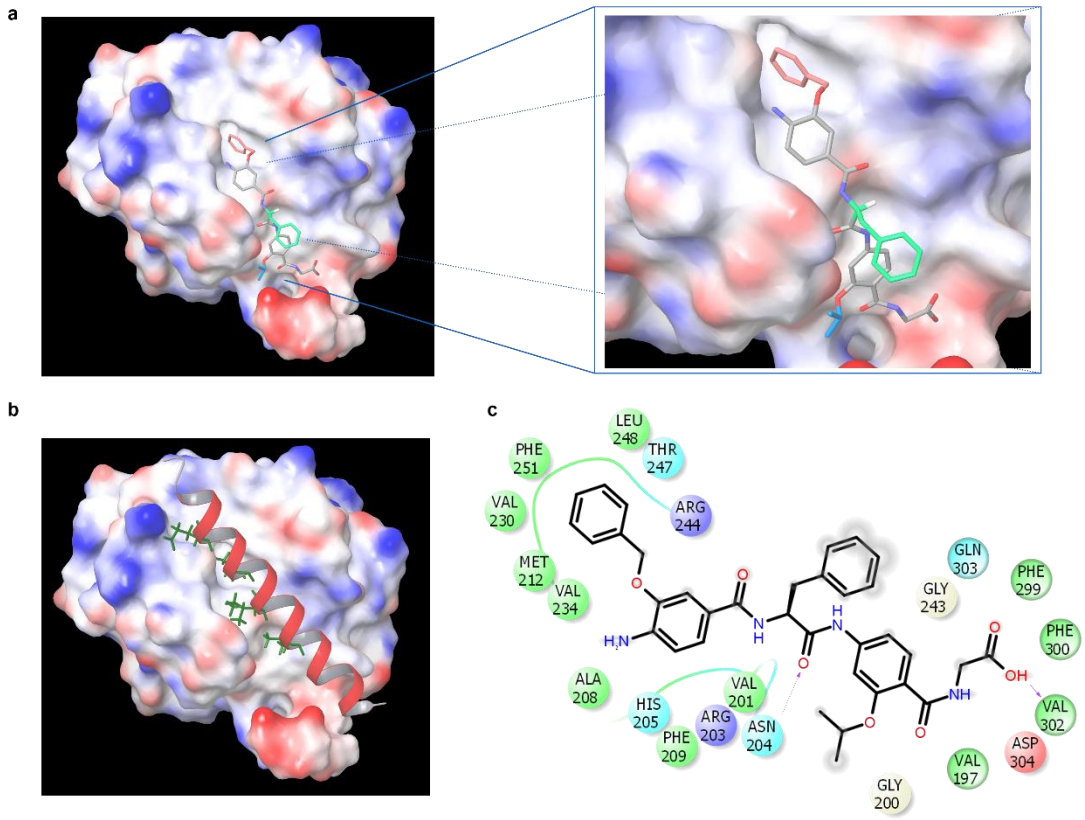

Figure 4.21 Docking studies (PDB ID: 2JM6) a Docked hybrid **75** with protein surface 3D representation and expansion; **b** Mcl-1/NOXA B interaction; **c** Docked hybrid **75** in schematic 2D representation highlighting the interacting amino acids (interactions taking place outside the hydrophobic cleft are represented with a grey shade).

Within the constraints of the method (limitations of the force fields, assumptions regarding conformational restrictions and media for simulation), this analysis indicates that the side-chains of this hybrid are not matched to the NOXA B sequence and that this molecule does not act as a good mimetic of this helix.

Intrigued by this surprising result, hybrids with the middle Trp unit were subsequently tested. The assay led to the identification of one hit, hybrid **113**, which disrupted this Bcl-2 family PPI with an IC_{50} of 24.1 ± 1.4 μM (Figure 4.22).

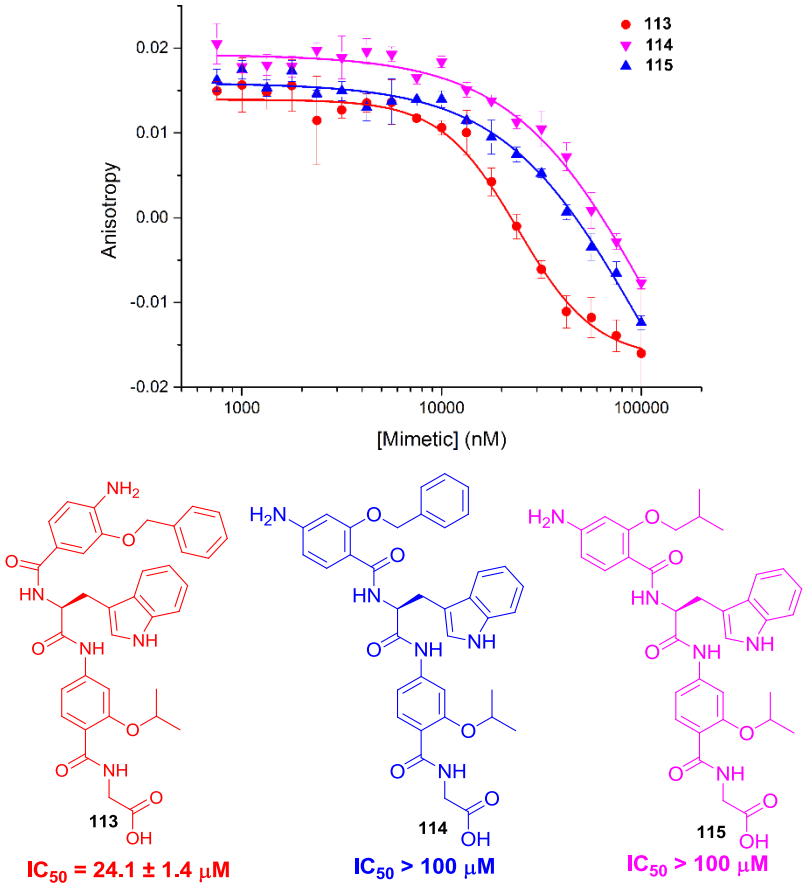

Figure 4.22 L-Trp hybrids: Dose-response curves against the Mcl-1/NOXA B PPI. (40 mM phosphate buffer pH 7.50, 200 mM sodium chloride, 0.02 mg mL^{-1} BSA)

The general trend of this series matched the previous result in the p53/*h*DM2 assay, showing reduced activity of hybrids presenting a top 2-*O*-alkylated functionality (section 4.6.1). The effect resulting from the combination of the side-chain spacing and the presence of a Trp middle amino acid seemed however to increase in targeting Mcl-1, resulting in nearly an order of magnitude difference in activity between hybrids **113** and **114**.

Hybrids with different middle unit functionalisation were also tested in a FA competition assay. As shown in Figure 4.23, halo-substituted hybrids **116**-**118** were identified as inhibitors of this PPI. Likewise the results obtained in targeting the p53/*h*DM2 PPI, the *p*-bromo functionalised hybrid **117** was shown to be the best inhibitor of the series.

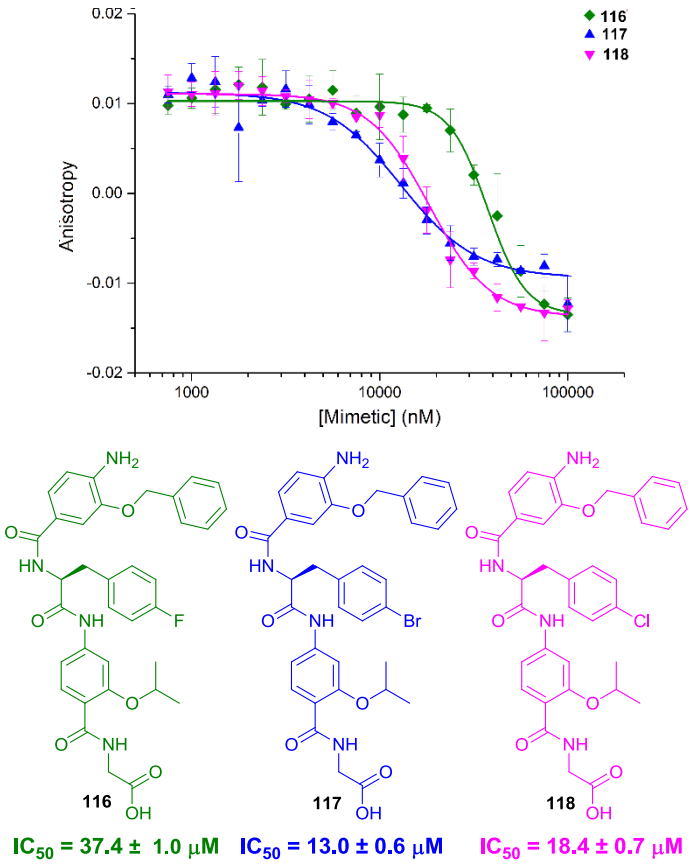

Figure 4.23 Halo-series: Dose-response curves against the Mcl-1/NOXA B PPI. (40 mM phosphate buffer pH 7.50, 200 mM sodium chloride, 0.02 mg mL^{-1} BSA)

These data were particularly noteworthy, as comparison with hybrid **75** revealed that the simple *para* substitution of the benzyl ring of the Phe residue with a halogen moiety enabled tuning of the potency of this molecule, achieving effective recognition with both protein partners, hence modulating selectivity.

The other members of the library were subsequently tested against the Mcl-1/NOXA B interaction. Dose-response curves, shown in Appendix II, showed however that none of these molecules were acting as inhibitors of this PPI. In this regard, the lack of activity of hybrids of the aliphatic series (**110**-**112**), originally designed to mimic the common aliphatic 'hot-spots' of the Bcl-2 family's α-helices, was particularly surprising and it further suggested that these molecules do not interact simply through hydrophobic contacts, but instead they are involved in a more complex recognition process.

The comparison of results obtained from the FA competition assays against Mcl-1/NOXA B with those obtained against p53/*h*DM2, revealed that these hybrid α-helix mimetics present a high level of selectivity towards recognition with the *h*DM2 cleft. However, the identification of four hybrids inhibitors of the Mcl-1/NOXA B PPI (**113**, **116-118**) was noteworthy, as studies performed on the WT- p53 peptide (described in Appendix II) revealed that in spite of its ability to be recognised by Mcl-1 in a direct binding assay, p53 is not able to compete with NOXA B in this interaction.

The tuneable selectivity displayed by these hybrid α-helix mimetics, therefore proved that this scaffold could be a powerful starting point to develop a better understanding of the properties that drive effective binding and to build rules to allow a tailored design of effective and selective PPIs therapeutics.

4.8 Stereocontrolled interaction of α-helix mimetics

The chiral nature of the hybrid scaffold, naturally led to questions regarding the role played by the strereochemistry of these mimetics in the protein recognition. Chirality has been widely recognised as a pivotal element in drug design[151] and some of the most potent small-molecule PPI inhibitors are chiral in nature.[10, 35, 37] However, this aspect has not been thoroughly investigated in designing type III α-helix mimetics, as the matched topography with the binding residues of a native helix constitutes the main structural pre-requisite.[1]

Since these hybrid mimetics enabled investigation of this important aspect, three additional hybrid derivatives incorporating D-amino acids were synthesised following the SPPS route illustrated in Scheme 4.3, section 4.2.2 (Table 4.4).

Table 4.4 Library of D-hybrid α-helix mimetics illustrating side-chain sequence and percentage of purity after mass-directed HPLC purification (determined *via* ^{1}H-NMR).

Hybrid number	Resin	R_1	D-AA	R_3	Purity
129	Gly	2-*O*-*i*Pr	D-Phe	3-*O*-Bn	95%
130	Gly	2-*O*-*i*Pr	D-Trp	3-*O*-Bn	90%
131	Gly	2-*O*-*i*Pr	D-Trp	2-*O*-Bn	90%

Hybrid **129** was initially tested in competition assays against the p53/*h*DM2 and the Mcl-1/NOXA B PPIs and compared to its L-Phe analogue **75**. The remarkable result, shown in Figure 4.24 a-b, revealed that the chiral element of the backbone plays a significant contribution in the interaction allowing enantioselective recognition of the two α-helix mimetics by these different proteins.

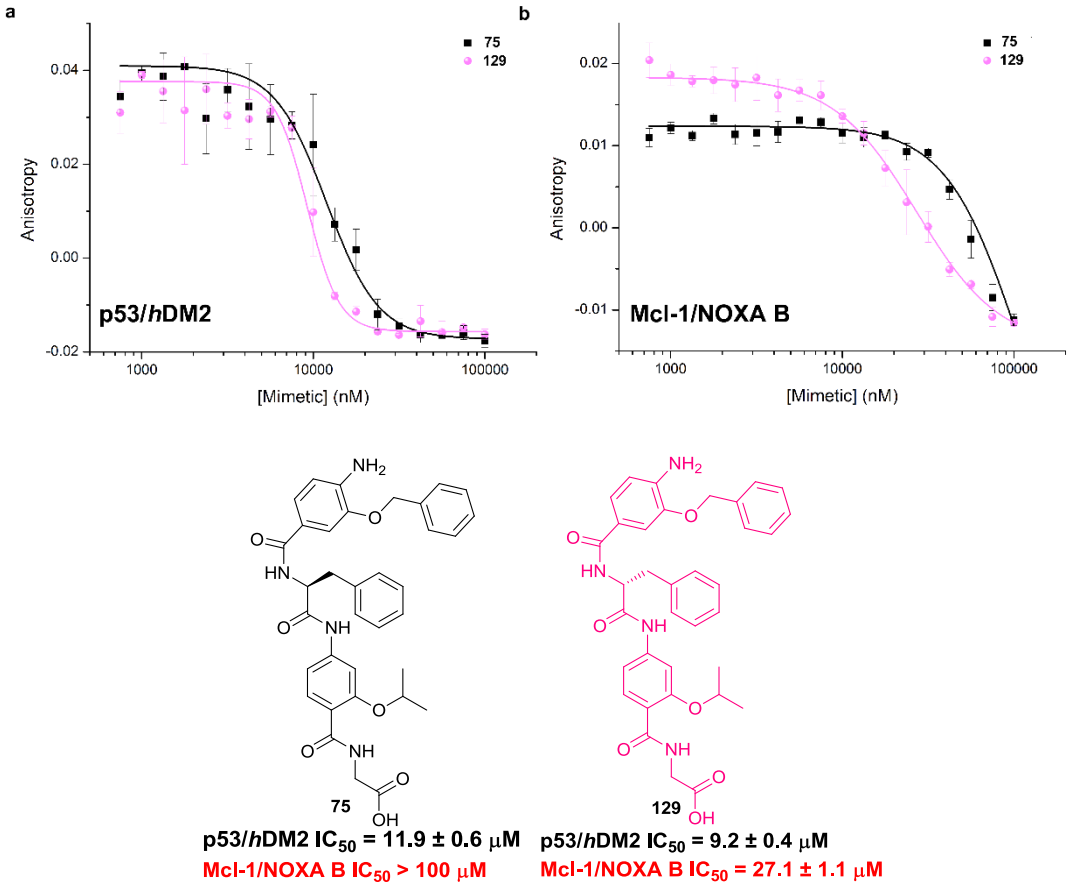

Figure 4.24 Dose-response curves of L-Phe (75) and D-Phe (129) hybrid mimetics a FA competition assays against p53/*h*DM2; **b** FA competition assays against Mcl-1/NOXA B. (40 mM phosphate buffer pH 7.50, 200 mM sodium chloride, 0.02 mg mL^{-1} BSA)

This result provided more evidence that the recognition process is not simply driven by the hydrophobic contribution of the side-chains, but instead requires careful control of the presentation of the binding motif. Whereas hybrid **75**, incorporating an L-Phe, displayed selectivity towards the *h*DM2 cleft, its D-Phe analogue hybrid **129** showed low-micromolar inhibition towards both PPIs. The stereochemistry of the middle unit could hence be used to control the selectivity of binding between the two protein systems. The data obtained from the competition assay against

Mcl-1/NOXA B (Figure 4.24 b) further revealed that enantiodependent differentiation of the two mimetics by the same protein could also be achieved.

Docking studies were performed on hybrid **129**. The structure was minimised in Macromodel®,[134] and the set of conformers within 1.5 kJ/mol from the lowest energy conformation, was initially docked with the crystal structure of *h*DM2 (PDB ID: 1YCR)[4] using the software Glide® (docking study shown in Appendix II). In line with the docking experiment of the L-Phe analogue (**75**, section 4.1), 69% of all the poses generated assumed conformations that were binding in the *h*DM2 cleft, thus confirming the binding data obtained from the FA assay.

Docking experiments were subsequently performed with the crystal structure of Mcl-1 (PDB ID: 2JM6).[27]

Of all the poses generated, 62% assumed conformations that were binding in the Mcl-1 cleft and a representative example is shown in Figure 4.25 a and d. The docked L-Phe analogue (**75**) and the native Mcl-1/NOXA B PPI are also shown in Figure 4.25 b and c for comparison.

The D-hybrid mimetic bound in the Mcl-1 cleft with all three residues through hydrophobic contacts (between the benzyl side-chain and Phe251, between the middle Phe residue and Phe209/Ala208 and between the isopropyl side-chain and Val246). These interactions suggest good matching between the position of the side-chains of this mimetic to the NOXA B sequence. Within the limitations of the method, comparison of this result with studies performed on hybrid **75** (Figure 4.25 b) for which only 3% of the generated poses were assuming binding conformations (section 4.7.1), could explain the enantioselective recognition of this scaffold.

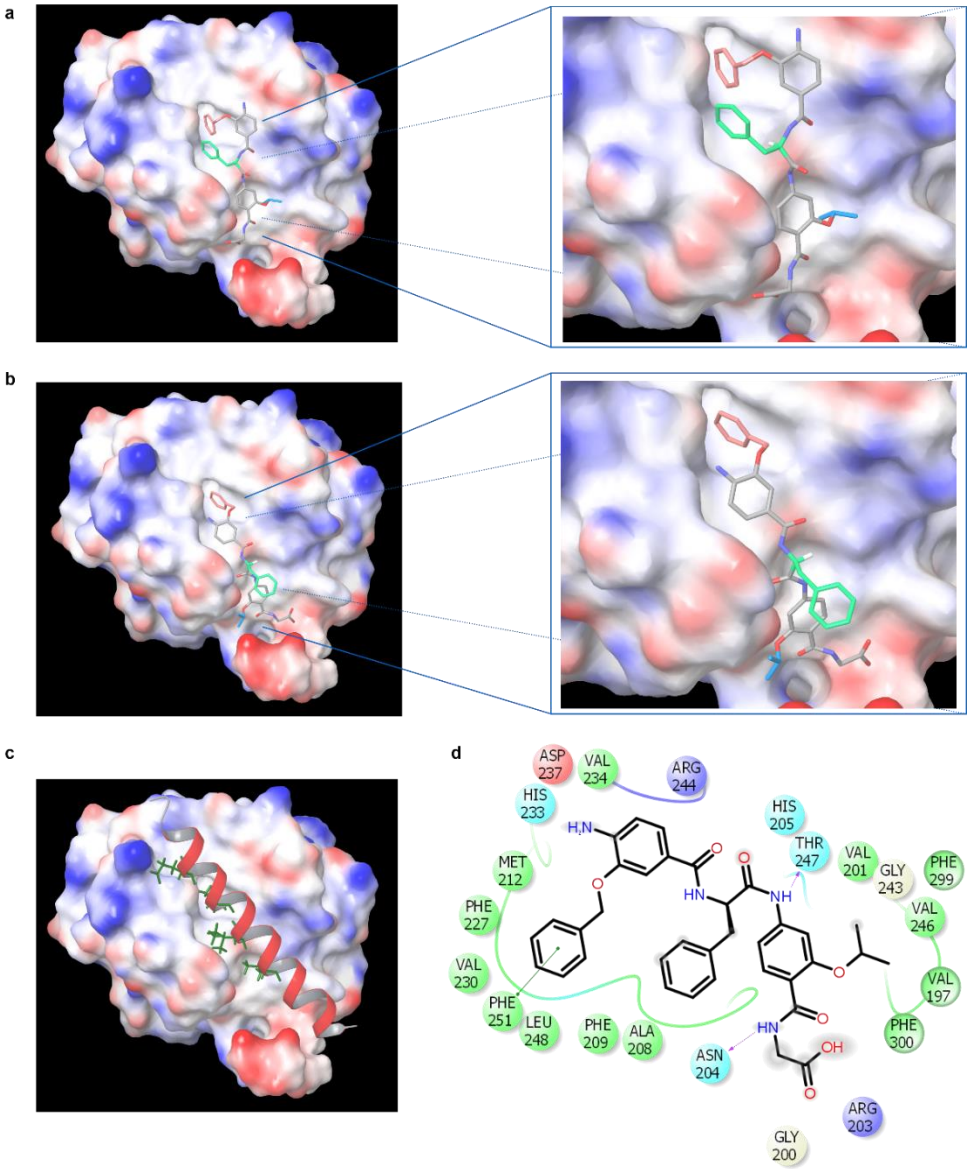

Figure 4.25 Docking studies for the D-Phe (129) hybrid mimetic (PDB ID: 2JM6) a Docked hybrid **129** with protein surface 3D representation and expansion; **b** Docked hybrid **75** with protein surface 3D representation and expansion; **c** Mcl-1/NOXA B interaction; **d** Docked hybrid **129** in schematic 2D representation highlighting the interacting amino acids (interactions taking place outside the hydrophobic cleft are represented with a grey shade).

The important role of the chiral element of the backbone was further supported by the results gathered from competition assays on hybrids **130** and **131** (Figure 4.26 a-b). Competition against the p53/*h*DM2 interaction (Figure 4.26 a) displayed an interesting potency pattern. A two-fold difference in activity was found between hybrids **113** and its D-Trp analogue **130**, with the L-hybrid being the best inhibitor. The opposite inhibitory activity was instead obtained between hybrids **114** and **131**,

for which the D-analogue was better recognised in the assay, thus overcoming the reduced activity of hybrid **114** presenting a 2-*O*-Bn top monomer. Interestingly, the binding data obtained against the Mcl-1/NOXA B PPI (Figure 4.26 b), showed that hybrid **113** was the only mimetic with substantial inhibition of this interaction, thus providing further evidence that the protein can differentially recognise these chiral mimetics.

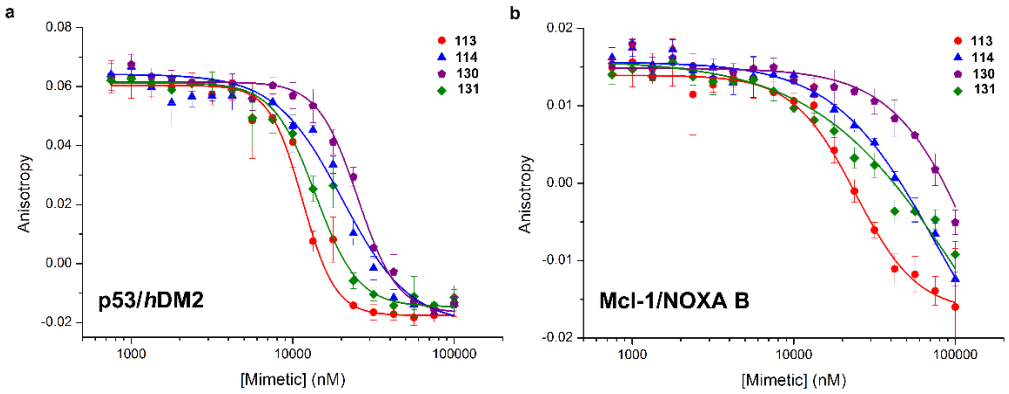

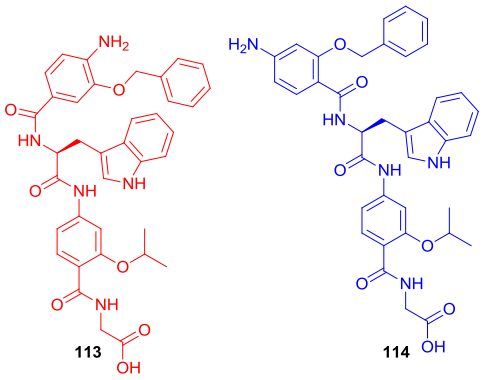

p53/*h*DM2 IC_{50} = 11.5 ± 0.3 μM
Mcl-1/NOXA B IC_{50} = 24.1 ± 1.4 μM

p53/*h*DM2 IC_{50} = 20.3 ± 2.1 μM
Mcl-1/NOXA B IC_{50} > 100 μM

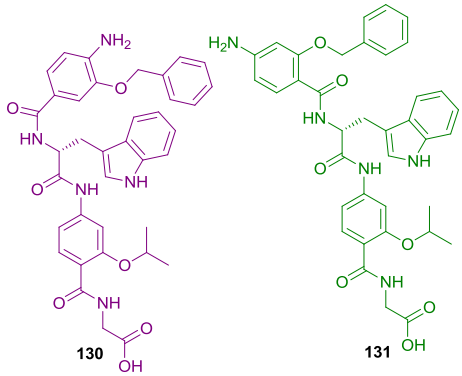

p53/*h*DM2 IC_{50} = 25.2 ± 0.7 μM
Mcl-1/NOXA B IC_{50} > 100 μM

p53/*h*DM2 IC_{50} = 13.8 ± 0.6 μM
Mcl-1/NOXA B IC_{50} > 100 μM

Figure 4.26 Dose-response curves of L-Trp (113 and 114) and D-Trp (130 and 131) hybrid mimetics a FA competition assay against p53/*h*DM2; **b** FA competition assay against Mcl-1/NOXA B. (40 mM phosphate buffer pH 7.50, 200 mM sodium chloride, 0.02 mg mL^{-1} BSA)

Comparison of the inhibitory activity towards both PPIs, revealed that hybrid mimetics **114**, **130** and **131**, together with the L-Phe analogue **75**, exhibited complete selectivity for the *h*DM2 cleft, thus constituting the first example of a library of enantioselectively recognised type III α-helix mimetics.

4.9 Summary and conclusions

A novel hybrid α-helix mimetic scaffold was designed and shown to be a selective and enantioselectively recognised inhibitor of PPIs involved in the development of cancer.

Molecular modelling and docking studies indicated that this hybrid scaffold has the potential to access a wide conformational space and be recognised as a functional mimetic of the native α-helix. Conformational analyses further revealed that H-bonded functionalities can introduce restraints in this irregular backbone and proteolytic studies demonstrated that this scaffold is resistant to enzymatic degradation and consequently suitable for cellular assays.

FA competition assays of a 35-membered library assembled through a robust SPPS strategy, were performed against the p53/*h*DM2 PPI. Low micromolar inhibitors of this interaction were identified and ^{1}H-^{15}N HSQC studies proved that these molecules indeed bind in the *h*DM2 cleft. A tailored SAR analysis showed the role of the conformational properties of these mimetics in the molecular recognition process with the protein partner. The activity was related to a series of structural features: i. the importance of the complete sequence and of a functionalised top *p*-aminobenzamide unit; ii. a careful balance between the irregular backbone of this scaffold and a defined side chain spacing which required a S(6) H-bonded 2-*O*-alkylated bottom unit; iii. the key role played by the middle amino acid unit, favouring more hydrophobic and electron withdrawing side-chains.

FA assays against the Mcl-1/NOXA B Bcl-2 family PPI, led to the identification of four further inhibitors of this interaction and, most importantly, revealed a high level of selectivity of these hybrid mimetics towards *h*DM2.

Finally, introduction of a D-amino acid middle unit highlighted the importance of the stereochemical configuration in the 3D space in order to achieve effective recognition, thus allowing the identification of the first reported examples of enantioselective recognition of type III α-helix mimetics by different proteins and enantiodependent differentiation of proteomimetics by a protein partner.

All together, these data emphasised that the interaction of these mimetics with the protein partner is driven by a well-defined process of recognition of the mimetic structure, which goes beyond the hydrophobic contribution of the side-chains. The preliminary results obtained on this family of α-helix mimetics therefore constitute a validated starting point for the development of a detailed understanding of the conformational properties necessary for PPI inhibition and to elaborate rule based approaches in order to achieve effective mimicry and enable selective targeting of PPIs.

Chapter 5

Thesis summary and future directions

Protein-protein interactions (PPIs) play a pivotal role in mediating a number of biological processes involved in the development of infected or diseased states.[2-4] Since α-helices constitute the most abundant motif at protein interfaces, significant research effort has been focused on targeting α-helix mediated PPIs.[15]

Although traditional drug-discovery approaches provided potent inhibitors of some PPIs,[10,11,12,13] they lack generality for the generation of drug candidates as they can only afford tailored answers. The development of rule based approaches to design effective inhibitors would therefore be highly desirable.

A powerful strategy for the inhibition of PPIs is the development of α-helix mimetics (Chapter 1). In designing these molecules, the helical core is recapitulated using a rod-shaped object presenting side chains in a topography comparable to that of the native helix. Encouraging results have been obtained through the design of foldamers, which are sequence-specific oligomers adopting well-defined three dimensional conformations to reproduce the secondary structural features of biological macromolecules.[29] Type I mimetics (foldamers reproducing the local topography of the helix by matching the peptide backbone) and type III mimetics (non-peptidic structures that match the topography of the original helix motif by mimicking the spatial orientation of its key residues) able to function as inhibitors of PPIs have been reported in the last few years.[1, 30] In spite of the potential shown by these foldamers, the discovery of mimetics that can target PPIs in a *predictable* manner remains nevertheless a major challenge.

Previous work carried out in the Wilson group on 3-*O*-alkylated benzamide proteomimetics,[98, 99] constituted the starting point for the work presented in this thesis, which was aimed at developing a better understanding of the conformational properties of aromatic oligoamides, in order to identify key features required to

reproduce the functional role of α-helices and to achieve specificity and selectivity towards different PPIs.

A regioisomeric 2-*O*-alkylated oligobenzamide scaffold was initially designed to determine how minor variations in the backbone architecture and hydrogen bonding pattern affect the conformational properties of this scaffold. [117,118] Conformational analyses in solid and solution-states were performed on 2-*O*-alkylated *p*-benzamide dimers and compared with the regioisomeric 3-*O*-alkylated template (Chapter 2). The study was performed to understand the role played by non-covalent interactions in defining conformational preferences and long range inter/intramolecular order for this class of aromatic foldamers. NMR studies and X-ray crystal structures showed the presence of intramolecular H-bonding (S(6) and S(5) respectively) within the structures and revealed that these non-covalent constraints can restrict rotation around one of the aryl amide axes. The overall results showed that no specific driving force determined the conformational preference of these *O*-alkylated benzamide dimers and that the *syn*/*anti* ratio of functional groups was controlled by a complex interplay of interactions both in solution and solid -state.

2-*O* and 3-*O*-Alkylated trimers were subsequently considered in order to investigate the impact of non-covalent interactions on the preferred shape and properties of these longer oligomers (Chapter 3). Structural analyses revealed that a more stable S(6) intramolecular H-bonding in the 2-*O*-alkylated scaffold results in a reduced curvature of the backbone. FA competition assays against the p53/*h*DM2 PPI were performed in order to study how the influence of the conformational differences between the two regioisomers modulated protein recognition. Micromolar inhibitors were identified for both families; however, the two regioisomers displayed minimal difference in the inhibitory activity.

Despite the different intramolecular H-bonds and curvature of the backbones in these two scaffolds, the result suggested that in the presence of a well-defined structure, the residues would adopt the best possible conformation in order to maximise the interaction with the protein partner. Since side-chains are free to rotate, this could therefore result in a similar vectoral presentation of the binding groups of

the two regioisomers, thus generating multiple pharmacophores which can be similarly effective for helix mimicry.

The design of a new hybrid α-helix mimetic was subsequently conceived, where the structural rigidity of the oligobenzamide backbone was broken through substitution of the middle aryl-unit with an amino acid, introducing irregularity and different H-bonded conformations (Chapter 4). As shown by *in silico* studies, this strategy allowed the generation of a mimetic with access to a wider conformational space but still able to function as a mimetic of the native α-helix. FA assays of a 35-membered library assembled through a robust SPPS strategy, were performed against the p53/*h*DM2 and the Mcl-1/NOXA B PPIs. Dose-response curves allowed the identification of low micromolar inhibitors of both interactions and afforded important information for the development of preliminary SAR rules for this family of mimetics.

Importantly, these hybrid mimetics were shown to be strongly selective towards *h*DM2, demonstrating that the molecular properties of these derivatives can be tuned to achieve protein selective mimicry. The chiral nature of the scaffold further highlighted the importance of stereocontrol in 3D space and allowed the identification of the first examples of enantioselective recognition of type III α-helix mimetics by different proteins and enantiodependent differentiation of proteomimetics by a protein partner.

The results obtained on the family of hybrid mimetics furnished some quantitative structure-activity relationship data. This scaffold therefore represents a potential starting point to elaborate rule based approaches for the design of proteomimetics aimed at effective PPI inhibition. In order to achieve this goal, a better understanding of the conformational properties that modulate protein recognition is however needed.

Research efforts are ongoing within the group in order to gather further information. A collaboration with Dr J. Fisher is currently occurring in order to employ the NMR data collected on hybrid **75** as restraints for simulated annealing to generate a more accurate ensemble of conformers for structural studies. Attempts to obtain co-crystal structures of hybrid derivatives bound to *h*DM2 or Mcl-1 are also

ongoing. The success of this experiment would be remarkable, as it would allow elucidation of the binding mode of these mimetics and provide important information on conformational properties. The ability of these mimetics to act in cells will also be investigated in a *Luciferase* assay and/or in p53 or p21 pull-down assays. These tests have already been developed by Dr A. Barnard and assays on the library of hybrid mimetics will be performed shortly.

Future directions should focus on additional studies regarding the conformational space accessible by these molecules. Possible modifications include the investigation of the binding activity of hybrids presenting a reverse-dipole sequence (Figure 5.1 a). Data on these derivative could in fact give insights on the role played by the dipole of these molecules and add information on the effect of the side-chain spacing.

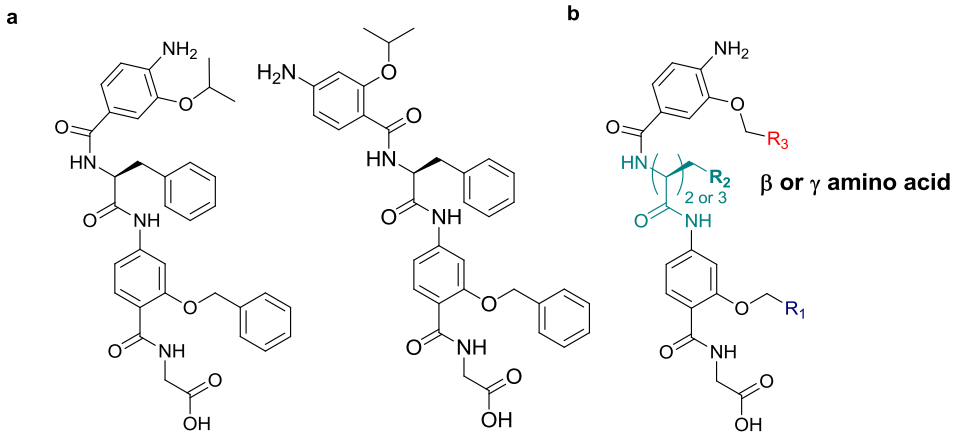

Figure 5.1 Possible modifications to the hybrid structure a Hybrids with a reverse-dipole sequence; **b** Hybrids with β or γ amino acids.

A further modification that could be introduced is the use of β or γ-amino acid as middle units (Figure 5.1 b), as the addition of one or two methylene units could affect the conformational properties of these molecules and have an impact on the binding affinity.

In order to expand on the SAR data, further side-chains need to be employed within the structure. Suggestions for these modifications are shown in Figure 5.2.

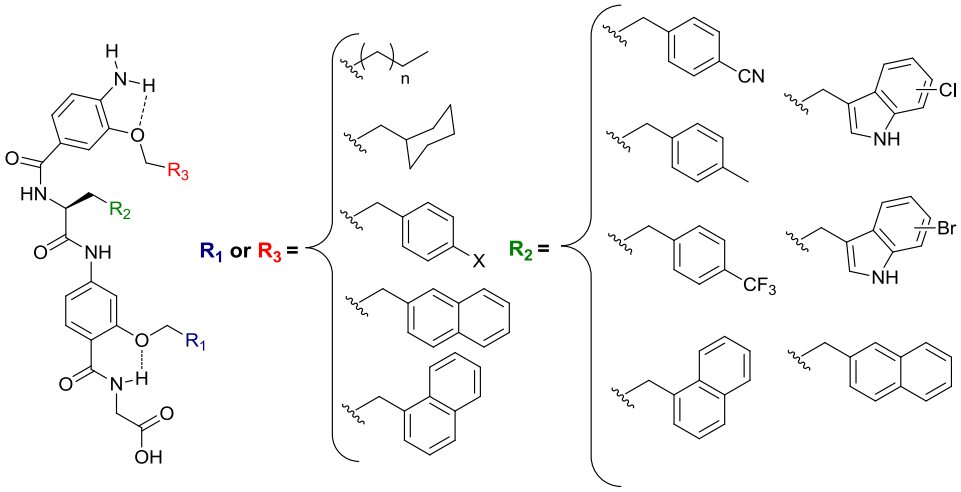

Figure 5.2 Suggested modification of the side-chains for additional SAR studies.

The use of functionalised amino acids will also necessitate the development of a robust synthetic strategy to obtain unnatural derivatives and access diversity. In particular, the effect of the halo-functionality on the activity of the hybrids and the role of the Trp moiety on selectivity (discussed in Chapter 4), suggest that the introduction of a halo-Trp could have an important effect in increasing the potency of these mimetics.

In order to support the results obtained and determine dissociation constants (not obtainable with the FA assay, see Appendix I), the development of an orthogonal biophysical assay should also be pursued. Attempts in this direction have been made and are discussed in Appendix III, but the results have not been reproducible so far and necessitate further efforts.

Finally, these mimetics should be tested against other PPIs of therapeutic importance in order to obtain additional information on their selectivity. This work will require additional molecular biology efforts to express the desired proteins and the development of new assays. As an example, research is currently ongoing within the group to develop a FA assay against the Bcl-x_L/BAK PPI and the library will be tested against this interaction as soon as the test is available.

The 2-*O*-alkylated and the hybrid α-helix mimetics investigated during this PhD, provided knowledge on the impact exerted by the conformational properties and structural features of these derivatives on PPI inhibition. Additional work is being

carried out within the group on 3-*O*-alkylated, *N*-alkylated and di-functionalised libraries of mimetics, which are being tested against different PPIs, thus affording auxiliary data on the structure-activity relationship of aromatic oligobenzamides.

The combination of these results could therefore help in addressing the key questions regarding the design of effective foldamers and allow accumulation of the quantitative understanding necessary to build a rule based approach and achieve potent and selective PPI inhibition.

Chapter 6

Experimental Section

General methods

Unless otherwise stated, all the chemicals and reagents were obtained commercially from Sigma-Aldrich, Fisher Scientific, Alfa Aesar or Merck and used without further purification. Amino acid derivatives, coupling reagents and resins were purchased from Merck Millipore. All solvents used were HPLC grade. Analytical Thin Layer Chromatography was performed on precoated silica gel plates (Kieselgel 60F254, Merck). Column chromatographic purifications were performed either with flash silica gel or with aluminium oxide Brockmann I (50, 200 μm) from Acros Organics. NMR spectra were recorded in $CDCl_3$ or CD_3OD , unless otherwise stated, either on DPX300, AV 400 MHz or AV 500 MHz Bruker NMR spectrometers. All chemical shifts are reported in δ ppm downfield of TMS and peak multiplicities as singlet (s), doublet (d), quartet (q), quintet (quin), septet (sep), doublet of doublets (dd), broad singlet (bs), and multiplet (m). Signal assignment, where possible/necessary, was made with the help of 2D-NMR techniques (COSY, HMQC, HMBC, and NOESY). High resolution mass spectra (HRMS) were obtained using either a Waters GCT Premier mass spectrometer, using electron impact (EI), a Bruker micrOTOF using electrospray ionisation (ESI), or a Bruker MaXis Impact, using electrospray ionisation (ESI). Liquid chromatography mass spectra (LC-MS) were run on an Agilent 1200 LC system equipped with a Phenomenex Luna C18(2) 50 × 2 mm column, 5 μm particle size, on an acetonitrile/water gradient (5-95% acetonitrile, 0.1% formic acid, over 3 minutes) and a Bruker Daltonics HTCUltra™ system equipped with an Ion trap MS detector. Analytical HPLC experiments were run on an Agilent 1290 Infinity LC series system equipped with an Ascentis® Express Peptide ES-C18 100 × 2.1 mm column, 2.7 μm particle size, on an acetonitrile/water gradient (5-95% acetonitrile, 0.1% TFA, over 5 minutes). Mass-directed HPLC purifications were run on an Agilent

1260 Infinity Preparative HPLC system equipped with a Waters XBridge™ Prep C18 19 × 100 mm column, 5 μm particle size, on an acetonitrile or methanol/water gradient (5-95% acetonitrile or methanol over 8 minutes) and an Agilent 6120 Quadrupole system equipped with a quadrupole MS detector, using electrospray ionisation (ESI). Infra-red (IR) analyses were performed using a Perkin Elmer FT-IR spectrometer or a Bruker Platinum-ATR system equipped with an Alpha FT-IR spectrometer and the samples were analysed as solids. Optical rotations were recorded on a Schmidt Haensch Polatronic H 532 polarimeter using the sodium D line (589 nm). $[\alpha]_D$ are reported in units of 10^{-1} deg dm^2 g^{-1}. Melting points were determined using a Griffin and George melting point apparatus and are uncorrected. CHN analyses were performed by the School of Chemistry Microanalysis facility using a Carlo Erba elemental analyser MOD 1106 instrument. Single crystal X-ray data were collected on a Bruker SMART APEX CCD Area diffractometer with graphite monochromatized (Mo Kα = 0.71073Å) radiation at room temperature.

6.1 Synthesis of 2-*O*-alkylated benzamides (Chapters 2 and 3)

Synthetic procedures

A generic procedure was followed using minor modifications to the previously reported work[98] for the *O*-alkylation, ester hydrolysis, nitro group reduction and coupling reactions to make novel oligomers. These procedures are described briefly below:

(a) Procedure for *O*-Alkylation

Alkyl halide (1.2 equiv.) was added to a solution of the phenol (1 equiv.) in dry DMF under an argon or nitrogen atmosphere, followed by potassium carbonate (3 equiv.) and the reaction mixture was stirred at 50 ^oC for 12-48 h. After complete consumption of starting material based on TLC, the reaction mixture was diluted with ethyl acetate and acidified with 1N hydrochloric acid solution. The product was extracted into ethyl acetate (3 × 30 mL) and the combined organic layers were washed with water and

dried over anhydrous sodium sulfate. The crude product obtained after the removal of solvent was purified either by crystallization or column chromatography.

(b) Procedure for ester hydrolysis

Ester (1 equiv.) in a mixture of tetrahydrofuran-methanol (10 mL) was subjected to hydrolysis using 1 M sodium hydroxide solution. After completion of the reaction (24-36 h), the pale yellow precipitate obtained on acidification was extracted into dichloromethane and the organic layer was washed with water until the pH was neutral. The organic layer was dried over anhydrous sodium sulfate. The product isolated after the removal of the solvent was used for the next step.

(c) Procedure for nitro reduction

Tin (II) chloride dihydrate (5 equiv.) was added to a solution of nitro compound (1 equiv.) in ethyl acetate, and the reaction mixture was stirred at 50 ^{o}C for 12-48 h. The reaction was diluted with ethyl acetate, basified with 1N sodium hydroxide solution and the product was extracted into ethyl acetate (3 × 30 mL). The organic layer was dried over anhydrous sodium sulfate and the product isolated after the removal of the solvent was used for the next step without further purification.

(d) Procedure for the coupling

Dichloro triphenylphosphorane (4.5 equiv.) was added to a stirred solution of amine (1.2 equiv.) and acid (1 equiv.) in anhydrous chloroform (5 mL per 50 mg of acid) under an argon atmosphere and the solution was heated to reflux (80 °C) until TLC analysis showed complete conversion. The crude product obtained after the removal of chloroform was treated with ethyl acetate (20-30 mL), filtered and washed with ethyl acetate (3x10 ml) to obtain a pale yellow coloured solid.

Numbering system for 2-*O*-alkylated benzamides

To simplify the numbering and NMR assignment of the 2-*O*-alkylated benzamides, a sequential nomenclature has been devised, where each of the monomer building blocks is considered separately (Figure 6.1). The monomers are numbered from 1 to 3 starting from the *N*-terminus and named as [*R*-(*n*-HABA)], where *R* is the alkoxy side-chain, *n*- indicates the position of the alkoxy moiety on the aromatic ring (*e.g.* for a 2-*O*-alkylated monomer $n = 2$) and HABA is the acronym for Hydroxy Amino

Benzoic Acid. Within each monomer, the numbering is the same: the carbons from the aminobenzoic acid are numbered using the standard system (the aromatic carbon bearing the carboxylic acid is C1, the one bearing the amine is C4). Then, the lateral chain is numbered: the carbon attached to the oxygen is the Cα, and the numbering of the aliphatic part of the side chain continues with Cβ, etc. In the case of aromatic side chains, the aromatic carbons are numbered CAr1, CAr2, etc.

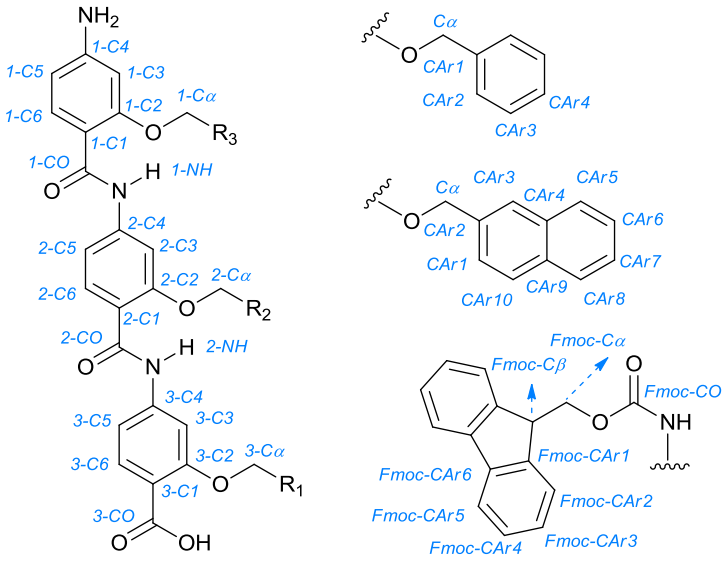

Figure 6.1 Numbering of atoms in 2-*O*-alkylated benzamides.

The numbering of the protons is based on the carbon numbering. To differentiate each individual carbon/proton, the monomer number is added as a prefix to the carbon/proton number.

6.1.1 Monomer building blocks and dimers

Methyl-2-hydroxy-4-nitrobenzoate (42)

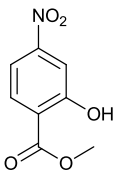

A stirred solution of 2-hydroxy-4-nitro benzoic acid (10.0 g, 54.6 mmol, 1 equiv.) and concentrated sulphuric acid (1.0 mL, 18.8 mmol) in anhydrous methanol (200 mL) under an argon atmosphere was heated at reflux (65 ºC). After 96 h stirring, TLC analysis (SiO_2, 7:3 cyclohexane:ethyl acetate) showed complete conversion and the reaction mixture was concentrated to leave a pale yellow solid which was poured into ethyl acetate and washed twice with water (2 × 100 mL). The organic layer was dried (sodium

sulphate), filtered and concentrated under reduced pressure to leave the pure product as a pale yellow powder (10.6 g, 98%); R_f 0.51 (SiO_2, 30% ethyl acetate in cyclohexane); ^{1}H NMR (CD_3OD, 300 MHz) δ: 7.97 (d, *J* = 5.4 Hz, 1 H, H6), 7.65 (s, 1 H, H3), 7.62 (d, *J* = 5.4 Hz, 1 H, H5), 3.91 (s, 3 H, OCH_3) ppm; ^{13}C NMR ($CDCl_3$, 75 MHz) δ: 170.7 (CO), 163.2 (C2), 153.8 (C4), 133.09 (C6), 119.36 (C1), 114.9 (C5), 113.8 (C3), 53.9 (OC) ppm; IR (neat) ν (cm^{-1}): 3627 , 2965, 1733, 1661, 1665, 1558, 1440, 1387, 1237; ESI-MS Found: 196 $(M-H)^-$; Elemental analysis calculated: C, 48.74; H, 3.58; N, 7.10); Found: C, 49.05; H, 3.65; N, 7.00.

O_2N-[*O*-*i*Pr-(2-HABA)]-CO_2Me (43)

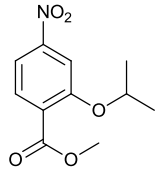

Using general procedure for *O*-alkylation (a). Potassium carbonate (6.3 g, 45.7 mmol, 3 equiv.); methyl-2-hydroxy-4-nitrobenzoate **42** (3.0 g, 15.2 mmol, 1 equiv.); 2-bromopropane (2.0 mL, 21.3 mmol, 1.4 equiv.); anhydrous *N*,*N*-dimethylformamide (30 mL). Purification by column chromatography (Aluminium oxide, 10% dichloromethane in cyclohexane) to leave a bright yellow oil (3.6 g, quant.); R_f 0.65 (Aluminium oxide, 50% dichloromethane in cyclohexane:); ^{1}H NMR ($CDCl_3$, 300 MHz) δ: 7.84 (d, *J* = 5.1 Hz, 1H, H6), 7.80 (s, 1 H, H3), 7.79 (d, *J* = 5.1 Hz, 1 H, H5), 4.75-4.70 (m, *J* = 4.2 Hz, 1 H, Hα), 3.92 (s, 3 H, OCH_3), 1.43 (d, *J* = 4.2 Hz, 6 H, Hβ) ppm; ^{13}C NMR ($CDCl_3$, 75 MHz) δ: 166.0 (CO), 158.0 (C2), 150.9 (C4), 132.3 (C6), 127.9 (C1), 115.1 (C5), 109.5 (C3), 69.7 (Cα), 52.8 (OC), 22.3 (Cβ) ppm; IR (neat) ν (cm^{-1}): 3117, 2980, 1748,1614, 1590, 1538 1486; ESI-MS Found: 262 $(M+Na)^+$; HRMS calculated for $C_{11}H_{13}N_1NaO_5$ $(M+Na)^+$: 262.0686; Found: 262.0677.

O_2N-[*O*-Bn-(2-HABA)]-CO_2Me (44)

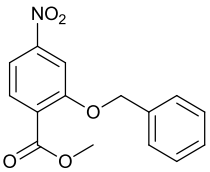

Using general procedure for *O*-alkylation (a). Potassium carbonate (6.3 g, 45.7 mmol, 3 equiv.); methyl-2-hydroxy-4-nitrobenzoate **42** (3.0 g, 15.2 mmol, 1 equiv.); benzyl bromide (2.5 mL, 21.3 mmol, 1.4 equiv.); anhydrous *N*,*N*-dimethylformamide (30 mL). Purification by recrystallisation from cyclohexane to leave white needle crystals (2.85 g, 65%); m.p. 89-90 ºC; R_f 0.82 (Aluminium oxide, 10% dichloromethane in cyclohexane); ^{1}H NMR ($CDCl_3$, 300 MHz) δ: 7.92 (d, *J* = 8.1 Hz, 1 H, H6), 7.87-7.82 (m, 2 H, H3, H5), 7.50 (d, *J* = 6.9 Hz, 1 H, HAr4), 7.43-7.34 (m, 4 H, HAr2, HAr3),

5.27 (s, 2 H, Hα), 3.94 (s, 3 H, OCH_3) ppm; ^{13}C NMR ($CDCl_3$, 75 MHz) δ: 165.7 (CO), 158.6 (C2), 151.0 (C4), 135.8 (CAr1), 132.6 (C6), 129.1 (CAr3), 128.7 (CAr4), 127.4 (CAr2), 127.0 (C1),115.7 (C5), 103.9 (C3), 71.5 (Cα), 53.0 (OC) ppm; IR (neat) ν(cm^{-1}): 3107, 3038, 3006, 2954, 2923, 2871, 2833, 1731, 1592, 1533, 1251; ESI-MS Found: 310 $(M+Na)^+$; Elemental analysis calculated: C, 62.72; H, 4.56; N, 4.88; Found: C, 62.80; H, 4.55; N, 4.85.

O_2N-[*O*-CH_2-2-Naph-(2-HABA)]-CO_2Me (45)

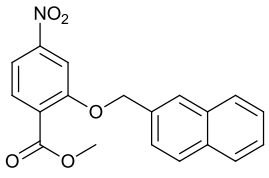

Using general procedure for *O*-alkylation (a). Potassium carbonate (6.3 g, 45.7 mmol, 3 equiv.); methyl-2-hydroxy-4-nitrobenzoate **42** (3.0 g, 15.2 mmol, 1 equiv.); 2-bromomethyl naphthalene (4.7 g, 21.3 mmol, 1.4 equiv.); anhydrous *N*,*N*-dimethylformamide (30 mL). Purification by recrystallisation from cyclohexane to leave a colourless powdery solid (5.1 g, quant.); m.p. 143-144 ºC; R_f 0.66 (Aluminium oxide, 50% dichloromethane in cyclohexane); ^1H NMR ($CDCl_3$, 300 MHz) δ: 7.96-7.84 (m, 7 H, H6, H3, HAr3, HAr5, HAr8, HAr10, HAr1), 7.59 (d, J = 5.1 Hz, 1 H, H5), 7.52-7.50 (m, 2 H, HAr5, HAr6), 5.43 (s, 2 H, Hα), 3.96 (s, 3 H, OCH_3) ppm; ^{13}C NMR ($CDCl_3$, 75 MHz) δ: 165.7 (CO), 158.6 (C2), 151.0 (C4), 133.7 (CAr2), 133.6 (C6), 133.2 (CArH), 129.5 (CArH), 129.0 (CAr4), 128.8 (CAr9), 128.4 (CArH), 128.2 (CArH), 127.1 (CArH), 126.8 (CArH), 126.7 (CArH), 126.6 (C1), 115.7 (C5), 108.9 (C3), 71.7 (Cα), 53.0 (OC) ppm; IR (neat) ν(cm^{-1}): 3124, 3058, 3007, 2953, 2871, 2833, 1731, 1590, 1536, 1347; ESI-MS Found: 360 $(M+Na)^+$; Elemental analysis calculated: C, 67.65; H, 4.48; N, 4.15; Found C, 67.75; H, 4.50; N, 4.05.

O_2N-[*O*-*i*Pr-(2-HABA)]-CO_2H (46)

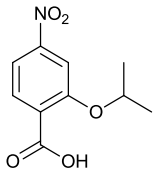

Using general procedure for ester hydrolysis (b). O_2N-[*O*-*i*Pr-(2-HABA)]-CO_2Me **43** (700.0 mg, 2.9 mmol, 1 equiv.); sodium hydroxide 1 M (5 mL); anhydrous methanol (50 mL). On cooling, the reaction mixture was acidified to pH ≈ 1 (5 mL, hydrochloric acid 1 N) to induce precipitation as a white creamy solid. The product was then collected by filtration and dried thoroughly under vacuum to leave a colourless solid (561.6 mg, 86%); m.p. 146-

147 ºC; R_f 0.06 (SiO_2, 100% dichloromethane); ^{1}H NMR ($CDCl_3$, 300 MHz) δ: 8.34 (d, *J* = 8.4 Hz, 1 H, H6), 7.95 (d, *J* = 8.7 Hz, 1 H, H5), 7.91 (s, 1 H, H3), 5.21-4.80 (m, *J* = 6.3 Hz, 1 H, Hα), 1.57 (d, *J* = 6.3 Hz, 6 H, Hβ) ppm; ^{13}C NMR ($CDCl_3$, 75 MHz) δ: 164.0 (CO), 157.1 (C2), 151.9 (C4), 135.4 (C6), 124.3 (C1), 115.9 (C5), 109.6 (C3), 75.8 (Cα), 22.2 (Cβ) ppm; IR (neat) ν(cm^{-1}): 2976, 1698, 1586, 1528, 1348, 1244; ESI-MS Found: 248 $(M+Na)^+$; Elemental analysis calculated: C, 53.33; H, 4.92; N 6.22; Found: C, 53.55; H, 4.95; N, 6.15.

O_2N-[*O*-Bn-(2-HABA)]-CO_2H (47)

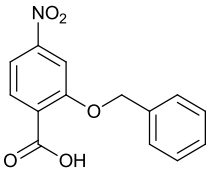

Using general procedure for ester hydrolysis (b). O_2N-[*O*-Bn-(2-HABA)]-CO_2Me **44** (1.0 g, 3.5 mmol, 1 equiv.); sodium hydroxide 1 M (5 mL); anhydrous methanol (25 mL); anhydrous tetrahydrofuran (25 mL). On cooling, the reaction mixture was acidified to pH ≈ 1 (5 mL, hydrochloric acid 1 N) to induce precipitation as a white creamy solid. The product was then collected by filtration and dried thoroughly under vacuum to leave a colourless solid (551.8 mg, 58%); m.p. 170-171 ºC; R_f 0.13 (SiO_2, 10% acetone and 2% ethanol in chloroform); ^{1}H NMR ($CDCl_3$, 300 MHz) δ: 8.35 (d, *J* = 8.2Hz, 1 H, H6), 8.0 (d, *J* = 8.2 Hz, 1 H, H5), 7.96 (s, 1 H, H3), 7.49-7.43 (m, 5 H, HAr2, HAr3, HAr4), 5.32 (s, 2 H, Hα) ppm; ^{13}C NMR ($CDCl_3$, 75 MHz) δ: 158.0 (CO), 151.9 (C2), 135.3 (C4), 133.7 (C6), 130.0 (CAr1), 129.7 (CAr4), 128.5 (CAr3), 123.9 (CAr2), 117.1 (C5), 108.9 (C3), 90.9 (C1), 73.4 (Cα) ppm; IR (neat) ν(cm^{-1}): 3062, 1682, 1586, 1525, 1382, 1256; ESI-MS Found: 274 $(M+H)^+$, 585 $(2M+K)^+$; Elemental analysis calculated: C, 61.54; H, 4.06; N, 5.13; Found: C, 61.60; H, 3.95; N, 5.30.

O_2N-[*O*-CH_2-2-Naph-(2-HABA)]-CO_2H (48)

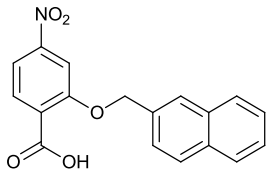

Using general procedure for ester hydrolysis (b). O_2N-[*O*-CH_2-2-Naph-(2-HABA)]-CO_2Me **45** (2.0 g, 5.9 mmol, 1 equiv.); sodium hydroxide 1 M (10 mL); anhydrous methanol (50 mL); anhydrous tetrahydrofuran (50 mL). On cooling, the reaction mixture was acidified to pH ≈ 1 (10 mL, hydrochloric acid 1 N) to induce precipitation as a bright yellow creamy solid. The product was then collected by filtration and dried thoroughly under vacuum to leave a bright yellow powder (1.5

g, 81%). R_f 0.94 (10% acetone and 2% ethanol in chloroform); ^{1}H NMR (acetone-d_6, 300 MHz) δ: 8.11 (d, *J* = 8 Hz, 1 H, H6), 8.05 (s, 1 H, H3), 8.02 (s, 1 H, HAr3), 7.97-7.91 (m, 4 H, H5, HAr6, HAr7, HAr1), 7.96 (dd, *J* = 8.7, 1.2 Hz, 1 H, HAr10), 7.55-7.52 (m, 2 H, HAr5, HAr8), 5.63 (s, 2 H, Hα) ppm; ^{13}C NMR (acetone-d_6, 75 MHz) δ: 166.7 (CO), 157.2 (C2), 150.1 (C4), 134.2 (CAr2), 133.1 (C6), 132.9 (CArH), 131.4 (CAr), 129.0 (CArH), 128.5 (CArH), 128.1 (CArH), 128.0 (CArH), 126.8 (CArH), 126.6 (CAr), 125.6 (CArH), 115.8 (C5), 109.0 (C3), 90.9 (C1), 70.8 (Cα); IR (neat) ν (cm^{-1}): 2934 , 1670, 1612, 1533, 1348, 1266 ; ESI-MS Found: 346 $(M+Na)^+$.

H_2N-[*O*-*i*Pr-(2-HABA)]-CO_2Me (49)

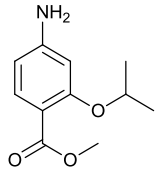

To a stirred solution of O_2N-[*O*-*i*Pr-(2-HABA)]-CO_2Me **43** (1.6 g, 6.7 mmol, 1 equiv.) in anhydrous methanol (50 mL) under a nitrogen atmosphere was added 10% Pd(C) (140.7 mg). The nitrogen atmosphere was evacuated under vacuum and hydrogen gas (2L) introduced *via* a balloon. The reaction mixture was stirred for 12h until TLC analysis (SiO_2, 7:3 cyclohexane:ethyl acetate) showed complete conversion. The reaction mixture was passed through a celite pad, washed twice with methanol and concentrated. The resulting grey oil was then dried under reduced pressure to leave a grey creamy solid (1.2 g, 86%); R_f 0.16 (SiO_2, 30% ethyl acetate in cyclohexane); ^{1}H NMR ($CDCl_3$, 300 MHz) δ: 7.71 (d, *J* = 8.7 Hz, 1 H, H6), 6.23 (d, *J* = 8.4 Hz, 1 H, H5), 6.21 (s, 1 H, H3), 4.52-4.47 (m, *J* = 6.0 Hz, 1 H, Hα), 3.98 (br, 2 H, NH_2), 3.81 (s, 3 H, OCH_3),1.36 (d, *J* = 6.0 Hz, 6 H, Hβ) ppm; ^{13}C NMR ($CDCl_3$, 75 MHz) δ: 166.4 (CO), 160.3 (C2), 151.6 (C4), 134.1 (C6), 107.0 (C1), 101.7 (C5), 111.0 (C3), 71.9 (Cα), 51.3 (OC), 22.1 (Cβ) ppm; IR (neat) ν (cm^{-1}): 3466, 3376, 3257, 2988, 2946, 2838, 1678, 1431, 1326, 1255; ESI-MS Found: 210 $(M+H)^+$, 232 $(M+Na)^+$; HRMS *m*/*z* calculated for $C_{11}H_{15}N_1NaO_3$ $(M+Na)^+$: 232.0944; Found: 232.0942.

H_2N-[*O*-Bn-(2-HABA)]-CO_2H (50)

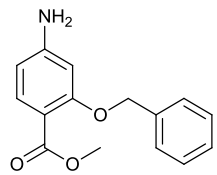

Using general procedure for nitro reduction (c) (heated at 50 °C). O_2N-[*O*-Bn-(2-HABA)]-CO_2Me **44** (1 g, 3.5 mmol, 1 equiv.); ethyl acetate (100 mL); tin (II) chloride dihydrate (4.7 g, 20.9

mmol, 6 eq). After 60h TLC analysis (SiO_2, dichloromethane) showed complete conversion and on cooling was added sodium hydroxyde 10% (400 mL) until pH ≈ 9. The mixture was poured into ethyl acetate and washed twice with water (2 × 250 mL) and once with brine (200 mL). The organic layer was dried (sodium sulphate), filtered and concentrated to leave a colourless solid (839 mg, 94%); m.p. 104-105 ºC; R_f 0.21 (SiO_2, Eluent: dichloromethane); ^{1}H NMR ($CDCl_3$, 300 MHz) δ: 7.78 (d, *J* = 7.5 Hz, 1 H, H6), 7.51 (d, *J* = 7.8 Hz, 2 H, HAr2), 7.41-7.36 (m, 2 H, HAr3), 7.31 (d, *J* = 7.2 Hz, 1 H, HAr4), 6.24 (d, *J* = 7.5 Hz, 1 H, H5), 6.23 (s, 1 H, H3), 5.12 (s, 2 H, Hα), 4.00 (br, 2 H, NH_2), 3.84 (s, 3 H, OCH_3) ppm; ^{13}C NMR ($CDCl_3$, 75 MHz) δ: 166.5 (CO), 160.7 (C2), 151.2 (C4), 136.8 (CAr1), 134.2 (C6), 128.4 (CAr3), 127.7 (CAr4), 126.8 (CAr2), 110.0 (C1), 107.4 (C5), 99.9 (C3), 70.4 (Cα), 51.5 (OC) ppm; IR (neat) ν (cm^{-1}): 3466, 3343, 3222, 1624, 1513, 1442, 1329; ESI-MS Found: 258 $(M+H)^+$, 537 $(2M+Na)^+$; Elemental analysis calculated: C, 70.02; H, 5.88; N, 5.44; Found C, 69.80; H, 6.05; N, 5.35.

O_2N-[*O-i*Pr-(2-HABA)]-[*O-i*Pr-(2-HABA)]-CO_2Me (51)

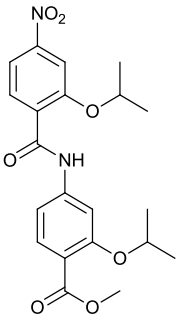

Using general procedure for coupling reaction (d) (heated at 80 °C). H_2N-[*O-i*Pr-(2-HABA)]-CO_2Me **49** (209.4 mg, 0.05 mmol, 1.2 equiv.); O_2N-[*O-i*Pr-(2-HABA)]-CO_2H **46** (113.0 mg, 0.05 mmol, 1 equiv.); anhydrous chloroform (20 mL); dichloro triphenylphosphorane (750.0 mg, 2.3 mmol, 4.5 equiv.). The product was purified by column chromatography (SiO_2, gradient ethyl acetate in cyclohexane) to leave the pure dimer as a yellow powder (113.7 mg, 55%); m.p. 119-120 ºC; R_f 0.16 (SiO_2, 30% ethyl acetate in cyclohexane); ^{1}H NMR ($CDCl_3$, 300 MHz) δ: 10.16 (br, 1 H, 1-NH), 8.45 (d, *J* = 8.7 Hz, 1 H, 1-H6), 7.95 (d, *J* = 8.7 Hz, 1 H, 2-H6), 7.89 (s, 1 H, 2-H3), 7.88 (s, 1 H, 1-H3), 7.82 (d, *J* = 8.7 Hz, 1 H, 1-H5), 6.85 (d, *J* = 8.7 Hz, 1 H, 2-H5), 5.00-4.88 (m, *J* = 6.0 Hz, 1 H, 1-Hα), 4.70-4.66 (m, *J* = 6.3 Hz, 1 H, 2-Hα), 3.88 (s, 3 H, 2-OCH_3), 1.61 (d, *J* = 6.0 Hz, 6 H, 1-Hβ), 1.50 (d, *J* = 6.0 Hz, 6 H, 2-Hβ) ppm; ^{13}C NMR ($CDCl_3$, 75 MHz) δ: 166.6 (2-CO), 161.9 (1-CO), 159.6 (1-C2), 156.1 (2-C2),152.0 (2-C4), 142.9 (1-C4), 134.3 (1-C6), 133.2 (2-C6), 127.9 (1-C1), 118.3 (2-C1), 116.5 (1-C5), 111.3 (2-C5), 109.5 (2-C3), 107.4 (1-C3), 74.4 (1-Cα), 72.5 (2-Cα), 52.1 (2-OC), 22.4 (1-Cβ, 2-Cβ) ppm; IR (neat) ν

(cm^{-1}): 3341, 2978, 2931, 2874, 2855, 1692, 1679, 1586, 1520, 1437, 1424, 1345; ESI-MS Found: 418 $(M+H)^+$, 855 $(2M+Na)^+$; HRMS calculated for $C_{21}H_{25}N_2O_7$ $(M+H)^+$: 417.1656; Found: 417.1657.

O_2N-[*O*-CH_2-2-Naph-(2-HABA)]-[*O*-*i*Pr-(2-HABA)]-CO_2Me (52)

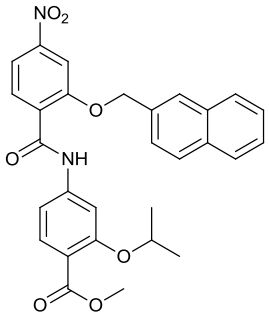

Using general procedure for coupling reaction (d) (heated at 80 °C). H_2N-[*O*-*i*Pr-(2-HABA)]-CO_2Me **49** (100 mg, 0.48 mmol, 1.2 equiv.); O_2N-[*O*-CH_2-2-Naph-(2-HABA)]-CO_2H **48** (109.0 mg, 0.34 mmol, 1 equiv.); anhydrous chloroform (10 mL); dichloro triphenylphosphorane (520 mg, 1.50 mmol, 4.5 equiv.). The product was purified by filtration on a silica pad (SiO_2, Eluent: 10% ethyl acetate in dichloromethane) to leave a yellow powder (175 mg, quant.); R_f 0.55 (SiO_2, 10% ethyl acetate in dichloromethane:); ^{1}H NMR ($CDCl_3$, 300 MHz) δ: 9.97 (br, 1 H, 1-NH), 8.53 (d, *J* = 8.4 Hz, 1 H, 1-H6), 8.10 (s, 1 H, 1-H3), 8.05 (s, 1 H, 1-HAr3), 8.04 (d, *J* = 8.4 Hz, 1 H, 1-H5), 8.01-7.87 (m, 3 H, 3 × 1-HAr), 7.66-7.58 (m, 3 H, 3 × 1-HAr), 7.47 (d, *J* = 8.4 Hz, 1 H, 2-H6), 7.21 (s, 1 H, 2-H3), 6.21 (d, *J* = 8.4 Hz, 1 H, 2-H5), 5.50 (s, 2 H, 1-Hα), 4.20-4.15 (m, *J* = 5.7 Hz, 1 H, 2-Hα), 3.81 (s, 3 H, 2-OCH_3), 1.16 (d, *J* = 5.7 Hz, 6 H, 2-Hβ) ppm; ^{13}C NMR ($CDCl_3$, 75 MHz) δ: 166.6 (2-CO), 161.5 (1-CO), 159.1 (2-C2), 157.1 (1-C2), 151.1 (1-C4), 142.6 (2-C4), 134.5 (1-C6), 134.1 (1-CAr2), 133.6 (1-CAr4), 132.9 (2-C6), 131.4 (1-CAr5), 129.9 (1- CArH), 128.9 (1- CArH), 128.5 (1- CArH), 128.4 (1-CArH), 127.8 (1- CArH), 127.6 (1- CArH), 126.9 (1-CAr3), 126.0 (2-C1), 117.4 (1-C1), 117.1 (1-C5), 111.5 (2-C5), 108.4 (1-C3), 106.8 (2-C3), 73.4 (1-Cα), 72.0 (2-Cα), 52.0 (2-OC), 22.2 (2-Cβ) ppm; IR (neat) ν(cm^{-1}): 3343, 2972-2932, 1688, 1602, 1548, 1521; ESI-MS Found: 1051 $(2M+Na)^+$; HRMS calculated for $C_{29}H_{27}N_2O_7$ $(M+H)^+$ and $C_{29}H_{27}N_2NaO_7$ $(M+Na)^+$: 515.1813 and 537.1632; Found: 515.1789 and 537.1612; Elemental analysis calculated: C, 67.70; H, 5.09; N, 5.44; Found: C, 67.85; H, 5.10; N, 5.30.

O_2N-[*O*-Bn-(2-HABA)]-[*O*-Bn-(2-HABA)]-CO_2Me (53)

Using general procedure for coupling reaction (d) (heated at 80 °C). H_2N-[*O*-Bn-(2-HABA)]-CO_2Me **50** (52 mg, 0.20 mmol, 1.2 equiv.); O_2N-[*O*-Bn-(2-HABA)]-CO_2H **47** (46 mg, 0.17 mmol, 1 equiv.); anhydrous chloroform (5 mL); dichloro

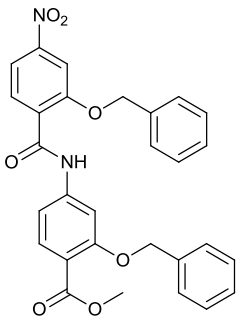

triphenylphosphorane (257 mg, 0.76 mmol, 4.5 equiv.). The product was purified by filtration on a silica pad (SiO_2, 10% ethyl acetate in dichloromethane) to leave a colourless solid (87 mg, 99%); R_f 0.86 (SiO_2, 30% ethyl acetate in dichloromethane); ^{1}H NMR ($CDCl_3$, 500 MHz) δ: 10.01 (br, 1 H, 1-NH), 8.51 (d, *J* = 8.3 Hz, 1 H, 1-H6), 8.04 (s, 1 H, 1-H3), 8.03 (d, *J* = 8.3 Hz, 1 H, 1-H5), 7.70 (d, *J* = 8.3 Hz, 1 H, 2-H6), 7.52 (s, 1 H, 2-H3), 7.59-7.51 (m, 8 H, 1-HAr2, 1-HAr3, 2-HAr2, 2-HAr3), 7.40 (t, *J* = 7.1 Hz, 1 H, 1-HAr4), 7.32 (t, *J* = 7.1 Hz, 1 H, 2-HAr4), 6.35 (d, *J* = 8.3 Hz, 1 H, 2-H5), 5.34 (s, 2 H, 1-Hα), 5.06 (s, 2 H, 2-Hα), 3.87 (s, 3 H, 2-OCH_3) ppm; ^{13}C NMR ($CDCl_3$, 125 MHz) δ: 166.0 (2-CO), 161.1 (1-CO), 159.4 (2-C2), 156.6 (1-C2), 150.7 (1-C4), 142.6 (2-C4), 136.5 (1-C6), 134.0 (2-C6), 132.8 (1-C1), 129.9 (1-CAr1), 129.1 (2-CAr2, 2-CAr3), 128.5 (1-CAr4), 127.8 (2-CAr4), 127.0 (2-CAr1), 126.7 (1-CAr2, 1-CAr3), 116.7 (1-C5), 115.9 (2-C1), 111.2 (2-C5), 107.9 (1-C3), 104.9 (2-C3), 72.9 (1-Cα), 70.5 (2-Cα), 51.9 (2-OC) ppm; IR (neat) ν (cm^{-1}): 3340, 2927, 1695 , 1674, 1601, 1588, 1520, 1507; ESI-MS Found: 1047 $(2M+Na)^+$; HRMS calculated for $C_{29}H_{24}N_2NaO_7$ $(M+Na)^+$: 535.1476; Found: 535.1477.

O_2N-[*O*-Bn-(2-HABA)]-[*O*-*i*Pr-(2-HABA)]-CO_2Me (59)

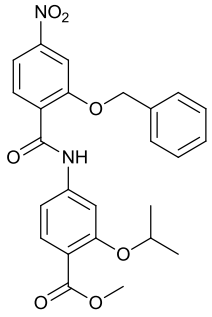

Using general procedure for coupling reaction (d) (heated at 80 °C). H_2N-[*O*-*i*Pr-(2-HABA)]-CO_2Me **49** (100.0 mg, 0.48 mmol); O_2N-[*O*-Bn-(2-HABA)]-CO_2H **47** (109.0 mg, 0.40 mmol); anhydrous chloroform (5 mL); dichloro triphenylphosphorane (520 mg, 1.50 mmol). The product was purified by filtration on a silica pad (SiO_2, 20% ethyl acetate in dichloromethane:) to leave a yellow powder (170.0 mg, 92%); R_f 0.39 (SiO_2, 20% ethyl acetate in dichloromethane:); ^{1}H NMR ($CDCl_3$, 300 MHz) δ: 9.95 (br, 1 H, 1-NH), 8.52 (d, *J* = 8.7 Hz, 1 H, 1-H6), 8.04 (s, 1 H, 1-H3), 8.02 (d, *J* = 8.7 Hz, 1 H, 1-H5), 7.63 (d, *J* = 8.7 Hz, 1 H, 2-H6), 7.51-7.59 (m, 5 H, 1-HAr2, 1-HAr3, 1-HAr4), 7.53 (s, 1 H, 2-H3), 6.28 (d, *J* = 8.7 Hz, 2 H, 2-H5), 5.38-5.31 (s, 2 H, 1-Hα), 4.50 (m, *J* = 6.0 Hz, 1 H, 2-Hα), 3.85 (s, 3 H, 2-OCH_3), 1.35 (d, *J* = 6.0 Hz, 6 H, 2-Hβ) ppm; ^{13}C NMR ($CDCl_3$, 75 MHz) δ: 166.6 (2-CO), 161.4 (1-CO), 159.3 (2-C2), 157.0 (1-C2), 151.2

(1-C4), 142.7 (2-C6), 134.4 (1-C6), 134.2 (1-CAr1), 132.9 (2-C4), 130.2 (1-CAr4), 129.8 (1-CAr2), 129.4 (1-CAr3), 127.2 (1-C1), 117.4 (2-C1), 117.0 (1-C5), 111.4 (2-C5), 108.3 (1-C3), 107.3 (2-C3), 73.3 (1-Cα), 72.3 (2-Cα), 52.1 (2-OC), 22.4 (2-Cβ); IR (neat) ν (cm^{-1}): 3343, 2979, 2949, 1688, 1601, 1547, 1507; ESI-MS Found: 465 $(M+H)^+$ and 951 $(2M+Na)^+$; HRMS calculated for $C_{25}H_{24}N_2NaO_7$ $(M+Na)^+$: 487.1476; Found: 487.1484.

O_2N-[*O*-CH_2-2-Naph-(2-HABA)]-[*O*-Bn-(2-HABA)]-CO_2Me (60)

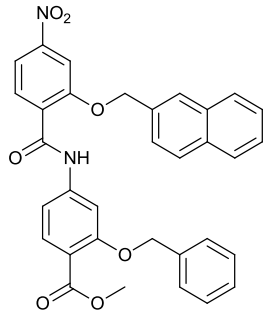

Using general procedure for coupling reaction (d) (heated at 80 °C). H_2N-[*O*-Bn-(2-HABA)]-CO_2Me **50** (342.2 mg, 1.3 mmol, 1 equiv.); O_2N-[*O*-CH_2-2-Naph-(2-HABA)]-CO_2H **48** (600 mg, 1.9 mmol, 1.4 equiv.); anhydrous chloroform (25 mL); dichloro triphenylphosphorane (2.2 g, 6 mmol, 4.5 equiv.). The product was purified by column chromatography (SiO_2, gradient diethyl ether in ethyl acetate) to leave the pure dimer as a yellow solid (488.0 mg, 65%); m.p. 159-160 ºC; R_f 0.38 (SiO_2, 30% ethyl acetate in cyclohexane); ^{1}H NMR ($CDCl_3$, 300 MHz) δ: 9.99 (br, 1 H, 1-NH), 8.51 (d, *J* = 8.7 Hz, 1 H, 1-H6), 8.08 (d, *J* = 8.7 Hz, 1 H, 1-H5), 7.97-8.04 (m, 4 H, 1-H3, 2-HAr2, 2-HAr4), 7.88 (dd, *J* = 6.6, 2.1 Hz, 2 H, 2-HAr3), 7.64 (d, *J* = 6.9 Hz, 1 H, 2-H6), 7.50-7.58 (m, 4 H, 4 × 1-HAr), 7.43 (s, 1 H, 2-H3), 7.35 (m, 4 H, 2-H5, 3 × 1-HAr), 5.49 (s, 2 H, 1-Hα), 4.82 (s, 2 H, 2-Hα), 3.83 (s, 3 H, 2-OCH_3) ppm; ^{13}C NMR ($CDCl_3$, 75 MHz) δ: 166.4 (2-CO), 161.5 (1-CO), 159.7 (2-C2), 157.1 (1-C2), 151.1 (2-C4), 142.9 (1-C4), 136.8 (2-CAr1), 134.4 (1-C6), 134.0 (1-CAr2), 133.6 (1-.CAr4), 133.1 (2-C6), 131.4 (CArH), 129.9 (CArH), 128.8 (CArH), 128.7 (CArH), 128.5 (CArH), 128.3 (CArH), 128.1 (CArH), 127.8 (CArH), 127.6 (CArH), 127.4 (CAr), 125.9 (CArH), 117.1 (1-C5), 116.4 (2-C1), 111.6 (2-C5), 108.4 (1-C3), 105.2 (2-C3), 90.9 (1-C1), 73.5 (1-Cα), 70.7 (2-Cα), 52.2 (2-OC) ppm; IR (neat) ν_{max} cm^{-1}: 3338, 2930, 1679, 1590, 1529, 1482, 1442, 1343; ESI-MS Found: 1148 $(2M+Na)^+$; HRMS *m/z* calculated for $C_{33}H_{27}N_2O_7$ $(M+H)^+$: 563.1813; Found: 563.1806 .

H_2N-[*O*-*i*Pr-(2-HABA)]-[*O*-*i*Pr-(2-HABA)]-CO_2Me (61)

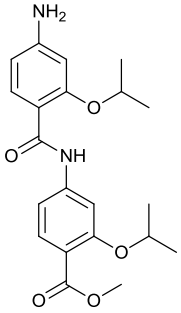

To a stirred solution of O_2N-[*O*-*i*Pr-(2-HABA)]-[*O*-*i*Pr-(2-HABA)]-CO_2Me **51** (300.0 mg, 0.72 mmol, 1 equiv.) in anhydrous methanol (15 mL) under an argon atmosphere was added 10% Pd(C) (30.0 mg). The argon atmosphere was evacuated under vacuum and hydrogen gas (2 L) introduced *via* a balloon. The reaction mixture was stirred for 6 h and than was passed through a celite pad, washed twice with methanol and concentrated. The resulting grey oil was then dried under reduced pressure to leave a grey creamy solid (212.0 mg, 76%); m.p. 175-176 ºC; R_f 0.50 (SiO_2, 10% ethyl acetate in dichloromethane); ^{1}H NMR ($CDCl_3$, 300 MHz) δ: 10.27 (br, 1 H, 1-NH), 8.12 (d, *J* = 8.7 Hz, 1 H, 1-H6), 7.94 (s, 1 H, 2-H3), 7.84 (d, *J* = 8.7 Hz, 1 H, 2-H6), 6.84 (d, *J* = 8.7 Hz, 1 H, 2-H5), 6.42 (d, *J* = 8.7 Hz, 1 H, 1-H5), 6.27 (s, 1 H, 1-H3), 4.85-4.75 (sept, *J* = 6.0 Hz, 1 H, 1-Hα), 4.75-4.67 (sept, *J* = 6.0 Hz, 1 H, 2-Hα), 4.08 (br, 2 H, 1-NH_2), 3.90 (s, 3 H, 2-OCH_3), 1.56-1.54 (d, *J* = 6.0 Hz, 6 H, 1-Hβ), 1.46-1.44 (d, *J* = 6.0 Hz, 6 H, 2-Hβ) ppm; ^{13}C NMR ($CDCl_3$, 126 MHz) δ: 166.8 (2-CO), 164.4 (1-CO), 159.8 (2-C2), 157.7 (1-C2), 152.0 (1-C4), 144.3 (2-C4), 134.6 (1-C6), 133.1 (2-C6), 116.0 (2-C1), 112.8 (1-C1), 111.0 (2-C5), 108.7 (1-C5), 107.0 (2-C3), 99.8 (1-C3), 72.7 (1-Cα), 72.3 (2-Cα), 52.0 (2-OC), 22.7 (1-Cβ), 22.5 (2-Cβ) ppm; IR (neat) ν_{max} cm^{-1}: 3444, 3332, 3240, 2977-2928, 1715; ESI-MS Found: 387 $(M+H)^+$, 795 $(2M+Na)^+$; HRMS *m/z* calculated for $C_{21}H_{27}N_2O_5$ $(M+H)^+$: 387.1914; Found: 387.01925; calculated for $C_{21}H_{27}N_2NaO_5$ $(M+Na)^+$: 409.1734; Found: 409.1740.

H_2N-[*O*-CH_2-2-Naph-(2-HABA)] -[*O*-*i*Pr-(2-HABA)]-CO_2Me (62)

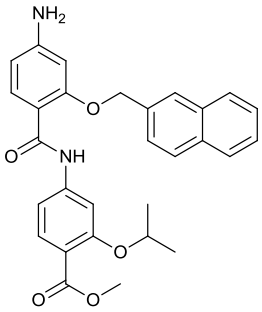

Using general procedure for nitro reduction (c) (heated at 50 °C). O_2N-[*O*-CH_2-2-Naph-(2-HABA)]-[*O*-*i*Pr-(2-HABA)]-CO_2Me **52 (**700.0 mg, 1.36 mmol) in ethyl acetate (25 mL); tin (II) chloride dihydrate (1.84 g, 8.17 mmol). The product was purified by column chromatography (SiO_2, 10% ethyl acetate in dichloromethane) to leave a colourless solid (502.2 mg, 76%); R_f 0.20 (SiO_2, 10% ethyl acetate in dichloromethane); ^{1}H NMR ($CDCl_3$, 500 MHz) δ: 9.93 (br, 1 H, 1-NH), 8.13 (d, *J* = 8.5 Hz, 1 H, 1-H6), 7.97 (s, 1 H, 1-HAr1),

7.94 (d, *J* = 8.5 Hz, 1 H, 1-HAr8), 7.91 (d, *J* = 7.5 Hz, 1 H, 1-HAr5), 7.86 (d, *J* = 7.0 Hz, 1 H, 1-HAr10), 7.54-7.62 (m, 3 H, 1-HAr3, 1-HAr6, 1-HAr7), 7.43 (d, *J* = 8.5 Hz, 1 H, 2-H6), 7.28 (s, 1 H, 2-H3), 6.43 (d, *J* = 8.5 Hz, 1 H, 1-H5), 6.42 (s, 1 H, 1-H3), 6.37 (d, *J* = 8.5 Hz, 1 H, 2-H5), 5.30 (s, 2 H, 1-Hα), 4.21-4.16 (m, 1 H, *J* = 6.0 Hz, 2-Hα), 4.15 (br, 2 H, 1-NH_2), 3.75 (s, 3 H, 2-OCH_3), 1.14 (d, *J* = 6.0 Hz, 6 H, 2-Hβ) ppm; ^{13}C NMR ($CDCl_3$, 126 MHz) δ: 166.3 (2-CO), 163.7 (1-CO), 158.9 (2-C2), 158.5 (1-C2), 151.8 (1-C4), 143.7 (2-C4), 134.4 (1-C6), 133.4 (1-CAr2), 133.2 (1-CAr4), 132.5 (2-C6), 132.3 (1-CAr8), 129.1 (1-CAr9), 128.1 (1-CAr5), 128.0 (1-CAr), 127.9 (1-CAr), 127.0 (1-CAr), 126.9 (1-CAr), 125.8 (1-CAr10), 115.8 (2-C1), 111.3 (1-C1), 110.8 (1-C3), 108.3 (2-C3), 106.0 (2-C5), 98.0 (1-C5), 71.7 (1-Cα), 71.4 (2-Cα), 51.6 (2-OC), 21.82 (2-Cβ) ppm; IR (neat) ν_{max} cm^{-1}: 3494, 3353, 2985, 2953, 1700, 1659, 1598, 1504; ESI-MS Found: 485 $(M+H)^+$; Elemental analysis calculated: C, 71.47; H, 5.57; N, 5.95; Found: C, 71.50; H, 5.90; N, 5.70.

H_2N-[*O*-Bn-(2-HABA)] -[*O*-*i*Pr-(2-HABA)]-CO_2Me (63)

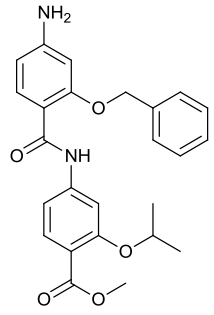

Using general procedure for nitro reduction (c) (heated at 50 °C). O_2N-[*O*-Bn-(2-HABA)]-[*O*-*i*Pr-(2-HABA)]-CO_2Me **59** (120.0 mg, 0.26 mmol) in ethyl acetate (15 mL); tin (II) chloride dihydrate (352.0 mg, 1.6 mmol) Yellow solid (117.0 mg, quant.); R_f 0.22 (SiO_2, 10% ethyl acetate in dichloromethane); ^{1}H NMR ($CDCl_3$, 500 MHz) δ: 9.87 (br, 1 H, 1-NH), 8.04 (d, *J* = 8.5 Hz , 1 H, 2-H6), 7.41-7.52 (m, 7 H, 2-H3, 1-H6, 5 × 1-HAr), 6.35 (d, *J* = 8.5 Hz, 1 H, 2-H5), 6.28 (s, 1 H, 1-H3), 6.11 (d, *J* = 8.0 Hz, 1 H, 1-H5), 5.06 (s, 1 H, 1-Hα), 4.45-4.33 (m, *J* = 6.0 Hz, 1 H, 2-Hα), 4.06 (br, 2 H, 1-NH_2), 3.76 (s, 3 H, 2-OCH_3), 1.26 (d, *J* = 6.0 Hz, 6 H, 2-Hβ), ppm; ^{13}C NMR ($CDCl_3$, 126 MHz) δ: 165.4 (2-CO), 162.6 (1-CO), 158.1 (2-C2), 157.4 (1-C2), 150.7 (2-C4), 142.8 (1-C4), 134.0 (2-C6), 133.3 (1-CAr1), 131.3 (1-C6), 128.2 (1-CAr4), 128.1 (2 × 1-CAr), 127.8 (2 × 1-CAr), 114.4 (2-C1), 110.36 (1-C1), 109.7 (1-C3), 107.3 (2-C3), 105.4 (2-C5), 96.9 (1-C5), 70.7 (1-Cα), 70.6 (2-Cα), 50.5 (2-OC), 21.0 (2-Cβ) ppm; IR (neat) ν_{max} cm^{-1}: 3471, 3347, 2924, 1704, 1595, 1527; ESI-MS Found: 435 $(M+H)^+$; HRMS *m/z* calculated for $C_{25}H_{27}N_2O_5$ $(M+H)^+$: 435.1914; Found 435.1909; calculated for $C_{25}H_{26}N_2NaO_5$ $(M+Na)^+$: 457.1734; Found: 457.1734.

H_2N-[*O*-CH_2-2-Naph-(2-HABA)] -[*O*-Bn-(2-HABA)]-CO_2Me (64)

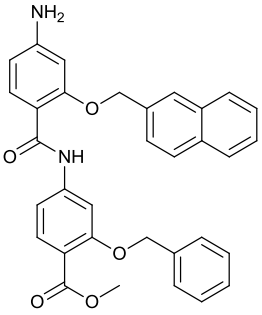

Using general procedure for nitro reduction (c) (heated at 50 °C). O_2N-[*O*-CH_2-2-Naph-(2-HABA)]-[*O*-Bn-(2-HABA)]-CO_2Me **60** (150 mg, 0.27 mmol, 1 equiv.) in ethyl acetate (5 mL), tin (II) chloride dehydrate (305 mg, 1.35 mmol, 5 eq). Colourless solid (92 mg, 64%); R_f 0.39 (SiO_2, 10% ethyl acetate in dichloromethane); ^{1}H NMR ($CDCl_3$, 300 MHz) δ: 10.00 (br, 1 H, 1-NH), 8.14 (d, *J* = 8.4 Hz, 1 H, 1-H6), 7.98 (s, 1 H, 1-HAr3), 7.95 (d, *J* = 8.7 Hz, 1 H, 1-HAr1), 7.87-7.85 (m, 4 H, 2 × HAr), 7.62 (d, *J* = 8.4 Hz, 1 H, 1-HAr10), 7.55 (s, 1 H, 2-H3), 7.50-7.54 (m, 2 H, 2 × HAr), 7.47 (d, *J* = 8.4 Hz, 1 H, 2-H6), 7.40-7.29 (m, 5 H, 5 × HAr), 6.43 (d, *J* = 8.4 Hz, 1 H, 1-H5), 6.40 (s, 1 H, 1-H3), 6.30 (d, *J* = 8.4 Hz, 1 H, 2-H5), 5.30 (s, 2 H, 1-Hα), 4.84 (s, 2 H, 2-Hα), 4.13 (br, 2 H, 1-NH_2), 3.82 (s, 3 H, 2-OCH_3) ppm; ^{13}C NMR ($CDCl_3$, 75 MHz) δ: 166.7 (2-CO), 164.1 (1-CO), 159.8 (2-C2), 158.9 (1-C2), 152.3 (1-C4), 144.4 (2-C4), 137.1 (2-CAr1), 134.8 (2-C6), 133.9 (1-CAr2), 133.7 (CAr), 133.0 (2 × CArH), 132.8 (CArH), 129.6 (1-CAr3), 128.7 (CAr), 128.4 (CAr), 128.3 (CAr), 128.2 (CAr), 127.9 (CAr), 127.4 (CArH), 126.1 (CArH), 114.8 (2-C1), 111.9 (1-C1),111.3 (2-C5), 108.8 (1-C5), 104.7 (2-C3), 98.5 (1-C3), 72.3 (1-Cα), 70.6 (2-Cα), 52.1 (2-OC) ppm; IR (neat) ν_{max} cm^{-1}: 3464, 3355, 3224, 2950, 1712; ESI-MS Found: 533 $(M+H)^+$; HRMS *m/z* calculated for $C_{33}H_{29}N_2O_5$ $(M+H)^+$: 533.2071; Found: 533.2076; calculated for $C_{33}H_{28}N_2NaO_5$ $(M+Na)^+$: 555.1890; Found: 555.1873.

6.1.2 2-*O*-Alkylated benzamide trimers

O_2N-[*O*-*i*Pr-(2-HABA)] -[*O*-*i*Pr-(2-HABA)]-[*O*-*i*Pr-(2-HABA)]-CO_2Me (65)

Using general procedure for coupling reaction (d) (heated at 80 °C). H_2N-[*O*-*i*Pr-(2-HABA)]-[*O*-*i*Pr-(2-HABA)]-CO_2Me **61** (150 mg, 0.39 mmol, 1.2 equiv.); O_2N-[*O*-*i*Pr-(2-HABA)]-CO_2H **46** (73.0 mg, 0.32 mmol, 1 equiv.); anhydrous chloroform (10 mL); dichloro triphenylphosphorane (494 mg, 1.45 mmol, 4.5 equiv.). The product was purified by column chromatography (SiO_2, 10% ethyl acetate in dichloromethane) to leave the pure trimer as a yellow solid (114 mg, 49%); m.p. 119-120 ºC; R_f 0.16 (SiO_2, 30% ethyl acetate in dichloromethane); ^{1}H NMR ($CDCl_3$, 300

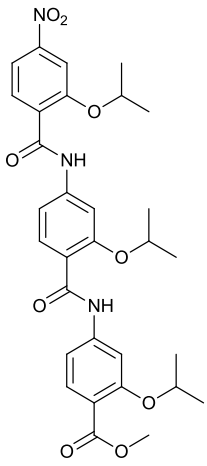

MHz) δ: 10.40 (br, 1 H, 2-NH), 10.31 (br, 1 H, 1-NH), 8.48 (d, *J* = 8.7 Hz, 1 H, 1-H6), 8.28 (d, *J* = 8.7 Hz, 1 H, 2-H6), 8.24 (s, 1 H, 2-H3), 7.97 (d, *J* = 8.7 Hz, 1 H, 1-H5), 7.94 (s, 2 H, 3-H3, 1-H3), 7.83 (d, *J* = 8.4 Hz, 1 H, 3-H6), 6.88 (d, *J* = 8.4 Hz, 1 H, 3-H5), 6.80 (d, , *J* = 8.4 Hz, 1 H, 2-H5), 5.10-5.03 (sep, *J* = 6.0 Hz, 1 H, 1-Hα), 5.02-4.95 (sep, *J* = 6.0 Hz, 1 H, 2-Hα), 4.79-4.67 (sep, *J* = 6.0 Hz, 1 H, 3-Hα), 3.88 (s, 3 H, 3-OCH_3), 1.68-1.66 (d, *J* = 6.0 Hz, 6 H, 1-Hβ), 1.64-1.62 (d, *J* = 6.0 Hz, 6 H, 2-Hβ), 1.48-1.46 (d, *J* = 6.0 Hz, 6 H, 3-Hβ) ppm; ^{13}C NMR ($CDCl_3$, 75 MHz) δ: 165.2 (3-CO), 163.5 (2-CO), 162.1 (1-CO), 159.7 (3-C2), 157.1 (2-C2), 156.1 (1-C2), 151.2 (1-C4), 143.8 (3-C4), 143.0 (2-C4), 134.3 (1-C6), 133.5 (2-C6), 133.2 (3-C6), 127.7 (2-C1), 118.4 (1-C1), 116.6 (3-C1), 116.5 (1-C5), 112.5 (2-C5), 111.2 (3-C5), 109.5 (1-C3), 107.2 (3-C3), 106.1 (2-C3), 74.5 (1-Cα), 73.4 (2-Cα), 72.4 (3-Cα), 52.0 (3-OC), 22.7 (1-Cβ), 22.6 (2-Cβ), 22.5 (3-Cβ) ppm; IR (neat) ν_{max} cm^{-1}: 3342, 2974, 1677, 1598, 1527; HRMS *m/z* calculated for $C_{31}H_{36}N_3O_9$ $(M+H)^+$: 594.2446; Found: 594.2440; calculated for $C_{31}H_{35}N_3NaO_9$ $(M+Na)^+$: 616.2266; Found: 616.2282; Elemental analysis calculated: C, 62.72; H, 5.94; N, 7.08; Found C, 62.95; H, 6.05; N, 6.95.

O_2N-[*O*-Bn-(2-HABA)]-[*O*-CH_2-2-Naph-(2-HABA)]-[*O*-*i*Pr-(2-HABA)]-CO_2Me (66)

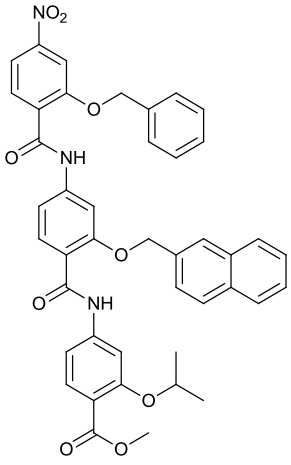

Using general procedure for coupling reaction (d) (heated at 80 °C). H_2N-[*O*-CH_2-2-Naph-(2-HABA)]-[*O*-*i*Pr-(2-HABA)]-CO_2Me **62** (300.0 mg, 0.62 mmol); O_2N-[*O*-Bn-(2-HABA)]-CO_2H **47** (145.0 mg, 0.53 mmol); anhydrous chloroform (15 mL); dichloro triphenylphosphorane (809.0 mg, 2.4 mmol). The product was purified by filtration on a silica pad (SiO_2, 10% ethyl acetate in dichloromethane) to leave the pure trimer as a yellow powder (279.0 mg, 71%); R_f 0.69 (SiO_2, 10% ethyl acetate in dichloromethane); ^{1}H NMR ($CDCl_3$, 500 MHz) δ: 10.09 (br, 1 H, 1-NH), 9.95 (br, 1 H, 2-NH), 8.47 (d, *J* = 8.5 Hz, 1 H, 3-H6), 7.95-8.05 (m, 7 H, HAr), 7.84 (dd, *J* = 18, 8.5 Hz, 1 H, HAr), 7.42-7.57 (m, 9 H, HAr), 7.37 (d, *J* = 8.5 Hz, 1 H, 3-H5), 7.17 (s, 1 H, 3-H3), 6.34 (d,

J = 8.5 Hz, 1 H, HAr), 6.12 (d, *J* = 8.5 Hz, 1 H, HAr), 5.29 (s, 2 H, 2-Hα), 5.23 (s, 2 H, 1-Hα), 4.11-4.05 (m, *J* = 6.0 Hz, 1 H, 3-Hα), 3.68 (s, 3 H , 3-OCH_3), 1.08 (d, *J* = 6.0 Hz, 6 H, 3-Hβ) ppm; ^{13}C NMR ($CDCl_3$, 126 MHz) δ: 166.1 (3-CO), 163.7 (2-CO), 161.4 (1-CO), 159.1 (CAr), 159.0 (CAr), 157.3(CAr), 156.7 (CAr), 150.5 (CAr), 143.1 (CAr), 142.7 (CAr), 133.9 (CArH), 133.5 (CArH), 133.1 (CAr), 132.9 (CArH), 132.3 (CArH), 132.0 (CAr), 129.3 (CAr), 129.1 (3 × CArH), 129.0 (3 × CArH), 128.2 (CArH), 128.0 (CArH), 127.9 (CArH), 127.0 (CArC), 126.9 (CArH), 125.9 (CArH), 116.8 (CAr), 116.4 (CArH), 115.9 (CArH), 112.4 (CAr), 110.9 (CArH), 108.0 (3-C5), 106.0 (CArH), 103.7 (CAr), 72.8 (2-Cα), 72.0 (1-Cα), 71.3 (3-Cα), 51.4 (3-OC), 21.7 (3-Cβ) ppm; IR (neat) ν_{max} cm^{-1}: 3352-3327, 2969, 1676, 1599, 1538, 1524, 1437, 1412, 1351; ESI-MS Found: 738 $(M-H)^-$; HRMS *m/z* calculated for $C_{43}H_{37}N_3NaO_9$ $(M+Na)^+$: 762.2422; Found: 762.2437.

O_2N-[*O*-Bn-(2-HABA)]-[*O*-Bn-(2-HABA)]-[*O-i*Pr-(2-HABA)]-CO_2Me (67)

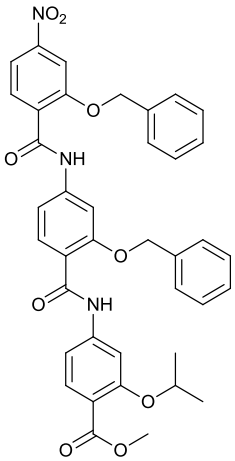

Using general procedure for coupling reaction (d) (heated at 80 °C). H_2N-[*O*-Bn-(2-HABA)]-[*O-i*Pr-(2-HABA)]-CO_2Me **63** (100.0 mg, 0.23 mmol); O_2N-[*O*-Bn-(2-HABA)]-CO_2H **47** (46.0 mg, 0.19 mmol); anhydrous chloroform (5 mL); dichloro triphenylphosphorane (291.0 mg, 0.86 mmol). The product was purified by filtration on a silica pad (SiO_2, 10% ethyl acetate in dichloromethane) to leave the pure trimer as a yellow powder (108.0 mg, 83%); R_f 0.55 (SiO_2, 10% ethyl acetate in dichloromethane); ^{1}H NMR ($CDCl_3$, 500 MHz) δ: 10.19 (br, 1 H, 1-NH), 10.04 (br, 1 H, 2-NH), 8.56 (d, *J* = 8.7 Hz, 1 H, 1-H6), 8.07-8.13 (m, 3 H, 3 × HAr), 8.01 (s, 1 H, 2-H3), 7.59 (s, 1 H, 3-H3), 7.53-7.65 (m, 11 H, 11 × HAr), 6.23 (d, *J* = 8.7 Hz, 1 H, 3-H5), 6.20 (d, *J* = 8.7 Hz, 1 H, 2-H5), 5.40 (s, 2 H, 1-Hα), 5.18 (s, 2 H, 2-Hα), 4.55-4.50 (m, *J* = 6.0 Hz, 1 H, 3-Hα), 3.87 (s, 3 H, 3-OCH_3), 1.37 (d, *J* = 6.0 Hz, 6 H, 3-Hβ) ppm; ^{13}C NMR ($CDCl_3$, 75 MHz) 166.3 (3-CO), 162.8 (2-CO), 161.2 (1-CO), 159.0 (CAr), 157.5 (CAr), 156.7 (CAr), 150.8 (CAr), 143.2 (CAr), 142.6 (CAr), 134.8 (CArH), 133.9 (CArH), 133.7 (CAr), 133.0 (CArH), 132.4 (CArH), 130.0 (CArH), 129.5 (CArH), 129.4 (2 × CArH), 129.3 (CAr), 129.2 (3 × CArH), 129.0 (2 × CArH), 126.5 (CAr), 117.9 (CAr), 116.7 (CArH), 116.0 (CArH),

112.4 (3-C5), 110.8 (2-C5), 108.0 (CArH), 106.5 (3-C3), 103.8 (2-C3), 73.0 (1-Cα), 72.1 (2-Cα), 71.8 (3-Cα), 51.6 (3-OC), 22.0 (3-Cβ) ppm; IR (neat) ν_{max} cm^{-1}: 3352, 3330, 2975, 1682, 1594, 1537, 1523, 1437, 1412, 1348; ESI-MS Found: 690 $(M-H)^-$; HRMS *m/z* calculated for $C_{39}H_{36}N_3O_9$ $(M+H)^+$: 690.2446; Found: 690.2461.

O_2N-[*O*-*i*Pr-(2-HABA)]-[*O*-CH_2-2-Naph-(2-HABA)]-[*O*-Bn-(2-HABA)]-CO_2Me (68)

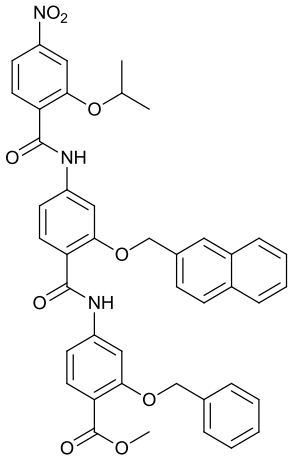

Using general procedure for coupling, H_2N-[*O*-CH_2-2-Naph-(2-HABA)]-[*O*-Bn-(2-HABA)]-CO_2Me **64** (250 mg, 0.47 mmol, 1.2 equiv.); O_2N-[*O*-*i*Pr-(2-HABA)]-CO_2H **46** (88.0 mg, 0.39 mmol, 1 equiv.); anhydrous chloroform (15 mL); dichloro triphenylphosphorane (594 mg, 1.76 mmol, 4.5 equiv.). The product was purified by column chromatography (SiO_2, 10% ethyl acetate in dichloromethane) to leave the pure trimer as a colourless solid (167 mg, 48%); R_f 0.51 (SiO_2, 10% ethyl acetate in dichloromethane); ^{1}H NMR (500 MHz, DMF-d_7) δ: 10.75 (br, 1 H, 1-NH), 10.53 (br, 1 H, 2-NH), 8.41 (s, 1 H, HAr), 8.20- 8.17 (m, 14 H, 14 × HAr), 7.85 (s, 1 H, HAr), 7.84-7.82 (d, *J* = 10 Hz, 1 H, HAr), 7.71-7.70 (m, 2 H, 2 × HAr), 7.58 (t, *J* = 10 Hz, 2 H, 2 × HAr), 5.74 (s, 2 H, 3-Hα), 5.18 (s, 2 H, 2-Hα), 5.14- 5.07 (sep, *J* = 5 Hz , 1 H, 1-Hα), 3.99 (s, 3 H, 3-OCH_3), 1.61-1.60 (d, *J* = 5 Hz , 6 H, 1-Hβ) ppm; ^{13}C NMR (500 MHz, DMF-d_7) δ: 166.9 (CO), 165.8 (CO), 164.1 (CO), 159.4 (CO), 156.9 (CAr), 156.0 (CAr), 150.4 (CAr), 144.5 (CAr), 143.7 (CAr), 137.3 (CAr), 134.1 (2-C6), 133.6 (3-C6), 133.6 (CAr), 132.5 (1-C6), 132.2 (CArH), 131.4 (CArH), 131.3 (CArH), 128.8 (2 × CArH), 128.5 (CAr), 128.3 (CAr), 128.0 (3 × CArH), 127.9 (CArH), 127.7 (CArH), 127.4 (CAr), 126.7 (2-C5), 126.4 (3-C5), 115.7 (1-C5), 115.2 (CAr), 112.3 (CAr), 111.3 (4-C3), 109.8 (2-C3), 109.3 (CAr), 104.7 (CAr), 104.3 (CAr), 72.5 (1-Cα), 71.3 (3-Cα), 70.2 (2-Cα), 51.4 (3-OC), 21.5 (1-Cβ) ppm; IR (neat) ν_{max} cm^{-1}: 3334, 2961, 1682, 1583, 1525; HRMS *m/z* calculated for $C_{43}H_{37}N_3NaO_9$ $(M+Na)^+$: 762.2422; Found: 762.2426.

H_2N-[*O*-*i*Pr-(2-HABA)]-[*O*-*i*Pr-(2-HABA)]-[*O*-*i*Pr-(2-HABA)]-CO_2Me (69)

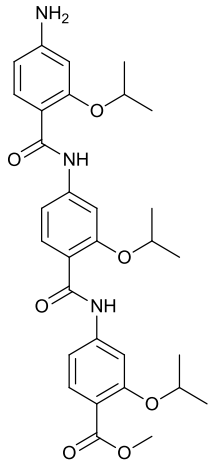

To a stirred solution of O_2N-[*O*-*i*Pr-(2-HABA)]-[*O*-*i*Pr-(2-HABA)]-[*O*-*i*Pr-(2-HABA)]-CO_2Me **65** (100.0 mg, 0.17 mmol, 1 equiv.) in anhydrous methanol (5 mL) under an argon atmosphere was added 10% Pd(C) (15.0 mg). The argon atmosphere was evacuated under vacuum and hydrogen gas (2 L) introduced *via* a balloon. The reaction mixture was stirred for 6 h and then was passed through a celite pad, washed twice with methanol and concentrated. The product was purified by column chromatography (SiO_2, gradient ethyl acetate in dichloromethane) to leave the pure trimer as a yellow solid (76 mg, 79%); R_f 0.29 (SiO_2, 10% ethyl acetate in dichloromethane); ^{1}H NMR ($CDCl_3$, 500 MHz) δ: 10.40 (br, 1 H, 2-NH), 10.31 (br, 1 H, 1-NH), 8.28 (s, 1 H, 2-H3), 8.18 (d, *J* = 8.5 Hz, 1 H, 2-H6), 8.06-8.05 (d, *J* = 8.5 Hz, 1 H, 1-H6), 7.89 (s, 1 H, 3-H3), 7.81-7.79 (d, *J* = 8.5 Hz, 1 H, 3-H6), 6.85-6.84 (d, *J* = 8.5 Hz, 1 H, 3-H5), 6.70-6.68 (d, *J* = 8.5 Hz, 1 H, 2-H5), 6.38-6.36 (d, 1 H, *J* = 8.5 Hz, 1-H5), 6.22 (s, 1 H, 1-H3), 4.99-4.92 (sep, *J* = 6.0 Hz, 1 H, 2-Hα), 4.79-4.72 (sep, *J* = 6.0 Hz, 1 H, 3-Hα), 4.70-4.64 (sep, *J* = 6.0 Hz, 1 H, 1-Hα), 4.06 (br, 2 H, 1-NH_2), 3.85 (s, 3 H, 3-OCH_3), 1.55-1.54 (d, *J* = 6.0 Hz, 6 H, 2-Hβ), 1.52-1.51 (d, *J* = 6.0 Hz, 6 H, 3-Hβ), 1.41-1.40 (d, *J* = 6.0 Hz, 6 H, 1-Hβ) ppm; ^{13}C NMR ($CDCl_3$, 126 MHz) δ: 166.4 (3-CO), 164.2 (1-CO), 163.5 (2-CO), 159.3 (3-C2), 157.4 (1-C2), 156.8 (2-C2), 151.7 (1-C4), 144.0 (2-C4), 143.7 (3-C4), 134.2 (1-C6), 132.8 (2-C6, 3-C6), 116.6 (2-C1), 115.8 (3-C1), 112.1 (1-C1), 111.8 (2-C5), 110.8 (3-C5), 108.3 (1-C5), 106.6 (3-C3), 105.2 (2-C3), 99.3 (1-C3), 72.7 (2-Cα), 72.4 (3-Cα), 71.9 (1-Cα), 51.7 (3-OC), 22.4 (1-Cβ), 22.3 (2-Cβ), 22.1 (3-Cβ) ppm; IR (neat) ν_{max} cm^{-1}: 3468, 3334, 2974, 1714, 1674, 1654, 1600, 1578, 1543, 1509, 1247; ESI-MS found: 564 $(M+H)^+$; HRMS *m/z* calculated for $C_{31}H_{38}N_3O_7$ $(M+H)^+$:564.2704; Found: 564.2601; calculated for $C_{31}H_{37}N_3NaO_7$ $(M+Na)^+$: 586.2524; Found: 586.2404 .

H_2N-[*O*-*i*Pr-(2-HABA)]-[*O*-CH_2-2-Naph-(2-HABA)]-[*O*-Bn-(2-HABA)]-CO_2Me (70)

O_2N-[*O*-*i*Pr-(2-HABA)]-[*O*-CH_2-2-Naph-(2-HABA)]-[*O*-Bn-(2-HABA)]-CO_2Me **68** (50.0 mg, 0.068 mmol, 1 equiv.) and cobalt chloride hexahydrate (193 mg, 0.810

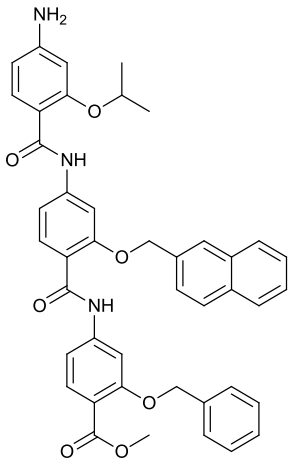

mmol, 12 equiv.) were dissolved in dichloromethane (20 mL) and methanol (40 mL). Sodium borohydride (38.0 mg, 1.00 mmol, 15 equiv.) was then added in portion with stirring and evolution of hydrogen gas was observed with the resulting formation of a black precipitate. When the reaction was complete as observed by TLC analysis, the reaction mixture was passed through a celite pad and the residual organic was washed with hydrochloric acid 1 N (2 × 100 mL) and brine (100 mL). The solution was dried (sodium sulphate) and the solvent was removed under reduced pressure. The product was purified by column chromatography (SiO_2, gradient ethyl acetate in dichloromethane) to leave the pure trimer as a yellow solid (12.5 mg, 26%); R_f 0.31 (SiO_2, 10% ethyl acetate in dichloromethane); ^{1}H NMR ($CDCl_3$, 500 MHz) δ: 10.35 (br, 1 H, 2-NH), 10.10 (br, 1 H, 1-NH), 8.45 (s, 1 H, 3-H3), 8.20-8.18 (d, *J* = 8.5 Hz , 1 H, 3-H6), 8.03-8.02 (d, *J* = 9.0 Hz , 1 H, 1-H6), 7.97 (s, 1 H, HAr), 7.90-7.88 (d, *J* = 8.5 Hz , 1 H, HAr), 7.81-7.78 (m, 1 H, HAr), 7.60-7.59 (d, *J* = 8.5 Hz , 1 H, HAr), 7.40-7.45 (m, 5 H, 5 × HAr), 7.25-7.29 (m, 4 H, 4 × HAr), 6.73-6.71 (d, *J* = 8.5 Hz, 1 H, 3-H5), 6.33 (t, *J* = 9.0 Hz, 2 H, 1-H5, HAr), 6.19 (s, 1 H, 1-H3), 5.41 (s, 2 H, 3-Hα), 4.73 (s, 2 H, 2-Hα), 4.73-4.67 (sep, *J* = 6.5 Hz, 1 H, 1-Hα), 3.75 (s, 3 H, 3-OCH_3), 1.48-1.47 (d, *J* = 6.5 Hz, 6 H, 1-Hβ) ppm; ^{13}C NMR ($CDCl_3$, 126 MHz) δ: 166.2 (3-CO), 164.3 (1-CO), 163.3 (2-CO), 159.4 (CAr), 157.9 (CAr), 157.5 (CAr), 144.3 (CAr), 143.7 (CAr), 136.6 (CAr), 134.2 (CAr), 133.4 (CAr), 133.3 (CAr), 132.9 (CAr), 132.7 (CAr), 132.5 (CAr), 129.1 (CArH), 128.3 (CArH), 128.2 (CArH), 128.1 (CArH), 127.9 (CArH), 127.6 (CArH), 127.0 (4 × CArH), 126.9 (CArH), 126.0 (CArH), 115.7 (CAr), 114.7 (CAr), 112.0 (3-C5), 111.9 (CAr), 111.1 (CArH), 108.3 (CArH), 104.3 (CArH), 103.9 (3-C3), 99.3 (1-C3), 72.4 (2-Cα), 72.1 (3-Cα), 70.1 (1-Cα), 51.7 (3-OC), 22.4 (1-Cβ) ppm; IR (neat) ν_{max} cm^{-1}: 3337, 2976, 1704, 1664, 1582, 1525, 1423; ESI-MS found: 710 $(M+H)^+$; HRMS *m/z* calculated for $C_{43}H_{40}N_3O_7$ $(M+H)^+$: 710.2861; Found: 710.2860.

H_2N-[*O*-*i*Pr-(2-HABA)]-[*O*-*i*Pr-(2-HABA)]-[*O*-*i*Pr-(2-HABA)]-CO_2H (58)

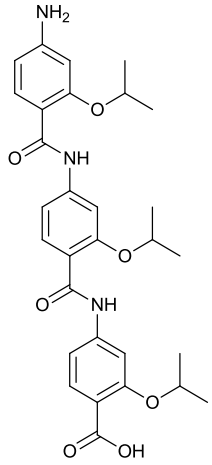

Using minor modifications to ester hydrolysis (heated at 65 ºC), H_2N-[*O*-*i*Pr-(2-HABA)]-[*O*-*i*Pr-(2-HABA)]-[*O*-*i*Pr-(2-HABA)]-CO_2Me **69** (50 mg, 0.089 mmol, 1 equiv.); sodium hydroxide 1 M (3 mL); anhydrous methanol (25 mL). On cooling, the reaction mixture was acidified to pH ~ 1 (3 mL, hydrochloric acid 1 N) and extracted with dichloromethane (3 × 150 mL). The organic was dried (sodium sulphate) and the solvent removed under reduced pressure to leave a pale yellow solid (50 mg, 99%); R_f 0.08 (SiO_2, 10% ethyl acetate in dichloromethane); ^{1}H NMR ($CDCl_3$, 500 MHz) δ: 10.53 (br, 1 H, 2-NH), 10.34 (br, 1 H, 1-NH), 8.39-8.28 (d, *J* = 8.5 Hz, 1 H, 3-H5), 8.30 (s, 1 H, 2-H3), 8.19-8.18 (d, *J* = 8.5 Hz, 1 H, 2-H6), 8.13-8.11 (d, *J* = 8.5 Hz, 1 H, 3-H6), 8.04-8.06 (d, *J* = 8.5 Hz, 1 H, 1-H6), 6.76-6.73 (d, *J* = 8.5 Hz, 1 H, 3-H3), 6.75 (s, 1 H, 2-H5), 6.39-6.38 (d, *J* = 8.5 Hz, 1 H, 1-H5), 6.25 (s, 1 H, 1-H3), 5.02-4.95 (sep, *J* = 6.0 Hz, 1 H, 2-Hα), 5.01-4.94 (sep, *J* = 6.0 Hz, 1 H, 3-Hα), 4.80-4.73 (sep, *J* = 6.0 Hz, 1 H, 1-Hα), 4.13 (br, 2 H, 1-NH_2), 1.58-1.57 (d, *J* = 6.0 Hz, 6 H, 3-Hβ), 1.54-1.52 (d, *J* = 6.0 Hz, 6 H, 1-Hβ), 1.52-1.51 (d, *J* = 6.0 Hz, 6 H, 2-Hβ) ppm; ^{13}C NMR ($CDCl_3$, 126 MHz) δ: 164.4 (3-CO), 163.2 (1-CO), 162.8 (2-CO), 156.6 (3-C2), 156.4 (1-C2), 155.9 (2-C2), 150.1 (1-C4), 143.9 (3-C4), 143.3 (2-C4), 133.2 (1-C6), 133.1 (3-C6), 131.7 (2-C6), 115.0 (2-C1), 112.1 (3-C1), 111.4 (3-C3), 110.9 (1-C1), 110.8 (2-C5), 107.3 (1-C5), 104.1 (2-C3), 104.0 (3-C5), 98.3 (1-C3), 73.1 (2-Cα), 71.8 (3-Cα), 71.3 (1-Cα), 21.4 (2-Cβ), 21.3 (3-Cβ), 21.0 (1-Cβ) ppm; IR (neat) ν_{max} cm^{-1}: 3446, 3321, 2977-2929, 1721, 1665, 1607, 1579, 1518; ESI-MS found: 550 $(M+H)^+$; HRMS *m/z* calculated for $C_{30}H_{36}N_3O_7$ $(M+H)^+$: 550.2548; Found: 550.2533.

H_2N-[*O*-*i*Pr-(2-HABA)]-[*O*-CH_2-2-Naph-(2-HABA)]-[*O*-Bn-(2-HABA)]-CO_2H (71)

Using minor modifications to ester hydrolysis (heated at 65 ºC), O_2N-[*O*-*i*Pr-(2-HABA)]-[*O*-CH_2-2-Naph-(2-HABA)]-[*O*-Bn-(2-HABA)]-CO_2Me **70** (23 mg, 0.032 mmol, 1 equiv.); sodium hydroxide 1 M (2 mL); anhydrous methanol (10 mL) anhydrous tetrahydrofuran (10 mL).. On cooling, the reaction mixture was acidified

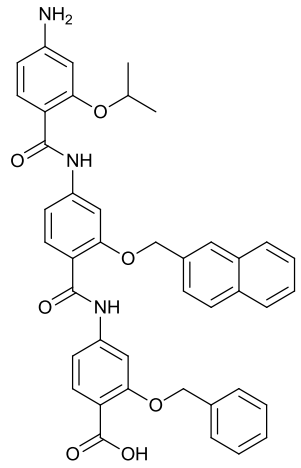

to pH ~ 1 (5 mL, hydrochloric acid 1 N) and extracted with dichloromethane (3 × 150 mL). The organic was dried (sodium sulphate) and the solvent removed under reduced pressure and the crude was purified by column chromatography (SiO_2, gradient ethyl acetate in dichloromethane) to leave the pure trimer as a colourless solid (8.4 mg, 38%); R_f 0.14 (SiO_2, 10% ethyl acetate in dichloromethane); ^{1}H NMR ($CDCl_3$, 500 MHz) δ: 10.36 (br, 1 H, 1-NH), 10.22 (br, 1 H, 2-NH), 8.47 (s, 1 H, 3-H3), 8.20-8.18 (d, *J* = 8.7 Hz , 1 H, 3-H6), 8.04-8.03 (d, *J* = 8.3 Hz , 1 H, HAr), 7.79-7.81 (m, 2 H, 2 × HAr), 7.71 (s, 1 H, HAr), 7.64-7.63 (d, *J* = 8.7 Hz , 1 H, HAr), 7.60-7.59 (d, *J* = 8.3 Hz , 1 H, HAr), 7.48-7.44 (m, 2 H, 2 × HAr), 7.33-7.26 (m, 5 H, 5 × HAr), 6.72-6.70 (d, *J* = 8.7 Hz, 1 H, HAr), 6.34-32 (d, *J* = 8.7 Hz, 1 H, HAr), 6.18 (s, 1 H, 1-H3), 6.18-6.16 (d, *J* = 8.7 Hz, 1 H, 1-H5), 5.41 (s, 2 H, 3-Hα), 4.86 (s, 2 H, 2-Hα), 4.75-4.68 (sep, *J* = 6.5 Hz, 1 H, 1-Hα), 4.06 (br, 2 H, 1-NH_2),1.49-1.48 (d, *J* = 6.5 Hz, 6 H, 1-Hβ) ppm; ^{13}C NMR (DMSO-d_6, 125 MHz) δ: 166.4 (3-CO), 163.9 (1-CO), 163.8 (2-CO), 158.3 (CAr), 157.2 (CAr), 156.8 (CAr), 154.2 (CAr), 143.5 (CAr), 136.7 (CArH), 133.8 (CArH), 132.9 (CAr), 132.8 (CAr), 132.7 (CArH), 132.1 (CArH), 131.4 (CArH), 128.2 (3 × CArH), 127.7 (CArH), 127.6 (2 × CArH), 127.1 (3 × CArH), 126.8 (CAr), 126.4 (CArH), 126.3 (CAr), 125.8 (CArH), 117.9 (CAr), 115.6 (CArH), 111.4 (CArH), 110.8 (CArH), 109.0 (CArH), 106.9 (1-C5), 104.1 (1-C3), 103.5, 98.0, 71.6 (1-Cα), 70.5 (3-Cα), 69.5 (2-Cα), 21.9 (1-Cβ) ppm; IR (neat) ν_{max} cm^{-1}: 3333, 2926, 1715, 1668, 1582, 1520; ESI-MS found: 696 $(M+H)^+$; HRMS *m/z* calculated for $C_{42}H_{37}N_3NaO_7$ $(M+Na)^+$: 718.2524; Found: 718.2545.

6.1.3 Single crystal X-ray crystallographic studies

Crystal data of O_2N-[*O*-*i*Pr-(2-HABA)]-[*O*-*i*Pr-(2-HABA)]-CO_2Me (51)

Yellow needle shaped crystals of **51** were grown by slow evaporation of a chloroform solution. Despite long exposures and high power, the crystal diffracted weakly and consequently the complete structure of the molecule was not determined. Compound **51** crystallizes in the triclinic space group $P\bar{1}$ with one molecule in the asymmetric

unit. All non-hydrogen atoms were refined anisotropically. All hydrogen atoms could be located in a difference Fourier map but, in the final stages of the refinement, they were placed in calculated positions and refined using a riding model. A yellow needle of size 0.28 x 0.09 x 0.04 mm was used for the data collection; multi-scan acquisition; θ range = 2.02 ≤ θ ≤ 28.44°; Formula = $C_{21}H_{24}N_2O_7$; Formula weight = 416.42; a = 6.5749(7) Å; b = 12.8076(15) Å; c = 13.3529(17) Å; α = 101.778(6)°; β = 100.815(6)°; γ = 90.011(6)°; V =1080.3(2) $Å^3$; Z = 2; D (calculated) =1.28 Mg/m^3; μ = 0.097 mm-1; Reflections collected 36646; Independent reflections = 5330 [R(int) = 0.0641]; Observed reflections = 3481 [I >2σ(I)]; absorption correction max. and min. transmission = 0.9961 and 0.9734; R value = 0.0446, wR_2 = 0.0981. CCDC 846382 contains the supplementary crystallographic data. These data can be obtained free of charge from the Cambridge Crystallographic Data Centre via www.ccdc.cam.ac.uk/data_request/cif.

Crystal data of O_2N-[*O*-CH_2-2-Naph-(2-HABA)]-[*O*-*i*Pr-(2-HABA)]-CO_2Me (52)

Single crystals of **52** were grown by slow evaporation of a methanol solution. A colorless prism of approximate size 0.30 x 0.16 x 0.15 mm was used for data collection. Multiscan acquisition. θ range = 1.92 ≤ θ ≤ 30.69°, Formula = $C_{30}H_{30}N_2O_8$; Formula weight = 546.56; Crystals belong to triclinic, Space group $P\bar{1}$; a = 10.5500(10) Å, b = 11.3420(11) Å c = 12.6649(12) Å, α = 101.747(5)°, β = 99.324(5)°, γ = 104.299(5)°, Volume =1401.3(2) $Å^3$, Z = 2, Density (calculated): 1.295 Mg/m^3, μ = 0.095 mm-1, Reflections collected 89846; Independent reflections 8518 [R(int) = 0.0594]; Observed reflections 6564 [I >2σ(I)]; R value = 0.0502, wR_2 = 0.1349. CCDC 846383 contains the supplementary crystallographic data. These data can be obtained free of charge from the Cambridge Crystallographic Data Centre via www.ccdc.cam.ac.uk/data_request/cif.

Crystal data of H_2N-[*O*-*i*Pr-(2-HABA)]-[*O*-*i*Pr-(2-HABA)]-CO_2Me (61):

Single crystals of **61** were grown by the slow evaporation of a methanol solution. A colourless prismatic crystal of dimensions 0.12 x 0.11 x 0.06 mm was used for the data collection; T = 150.2 K, θ range = 1.87 ≤ θ ≤ 28.55°, Crystals belong to Monoclinic; Space group $P2_1/c$; Formula = $C_{21}H_{26}N_2O_5$; Formula weight = 386.44; *a*

= 9.0441(7) Å, *b* = 13.9383(10) Å, *c* = 17.5956(12) Å, α = 90°, β = 99.421(4)°, γ = 90°; V = 2188.2(3) Å^3; *Z* = 4, D (calculated): 1.173 g/cm^3, μ = 0.084 mm^{-1}, Reflections collected 53179; Independent reflections 5489; Observed reflections 3170 [$I > 2\sigma(I)$]; *R* value = 0.0743, wR_2 = 0.2001. CCDC 870275 contains the supplementary crystallographic data. These data can be obtained free of charge from the Cambridge Crystallographic Data Centre via www.ccdc.cam.ac.uk/data_request/cif.

6.1.4 2D NOESY Spectra

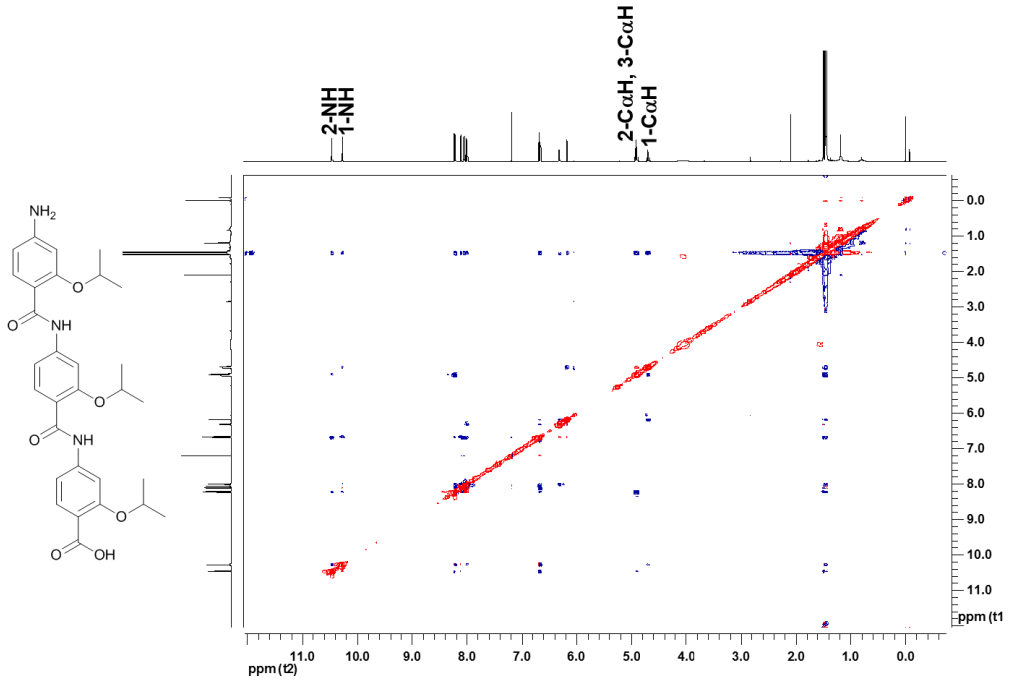

Figure 6.2 ^{1}H-^{1}H NOESY spectrum of 58 (10 mM $CDCl_3$, 500 MHz).

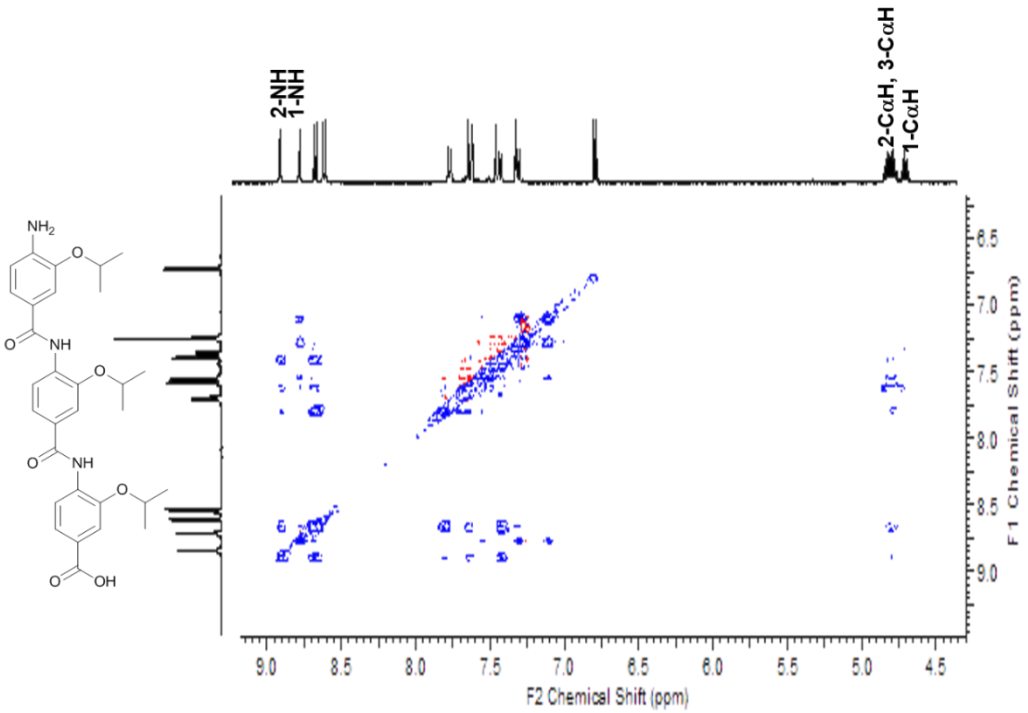

Figure 6.3 ^{1}H-^{1}H NOESY spectrum of 57 (10 mM $CDCl_3$, 500 MHz).

6.2 Synthesis of hybrid α-helix mimetics (Chapter 4)

6.2.1 Monomer building blocks

Synthetic procedures

(e) Procedure for Fmoc-protection

To a refluxing solution of amino benzoic acid (1 equiv) in anhydrous chloroform or tetrahydrofuran (10 mL) was added dropwise a solution of Fmoc-chloride (1.2 equiv.) in chloroform (15 mL) over a period of 30 minutes. The reaction mixture was allowed to stir for 48 h and the solvent was removed under reduced pressure. The resulting oil was crystallized from a mixture of dichloromethane-hexane.

O_2N-[*Oi*Bu-(2-HABA)]-CO_2Me (79)

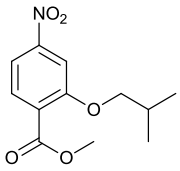

Using general procedure for *O*-alkylation (a). Potassium carbonate (7.6 g, 54.8 mmol, 3 equiv.); methyl-2-hydroxy-4-nitrobenzoate **42** (3.6 g, 18.3 mmol, 1 equiv.); 1-bromo-2-methylpropane (2.8 mL, 25.6 mmol, 1.4 equiv.); anhydrous *N*,*N*-dimethylformamide (100 mL). Purification by column chromatography (SiO_2, 100% Ethyl acetate) to leave a bright yellow oil (4.15 g, 90%); R_f 0.86 (SiO_2, 30% ethylacetate in dichloromethane); ^{1}H NMR (CD_3OD, 500 MHz) δ: 7.77 (d, *J* = 8.5 Hz, 1 H, H6), 7.75 (s, 1 H, H3), 7.72 (d, *J* = 8.5 Hz 1 H, H5), 3.90 (s, 3 H, OCH_3), 3.87 (d, *J* = 6 Hz, 2 H, Hα), 2.14-2.09 (apparent quin, *J* = 6 Hz, 1 H, Hβ), 1.07 (d, *J* = 6 Hz, 6H, Hγ) ppm; ^{13}C NMR (CD_3OD ,126 MHz) δ: 167.1 (CO), 159.9 (C2), 152.1 (C4), 132.8 (C6), 127.5 (C1), 115.7 (C3), 108.8 (C5), 76.9 (Cα), 53.0 (OC), 29.5 (Cβ), 19.6 (Cγ) ppm; IR (neat) ν(cm^{-1}): 3120, 2961, 1737, 1709, 1616, 1589, 1530 1489; HRMS *m*/*z* calculated for $C_{12}H_{15}NNaO_5$ $(M+Na)^+$: 276.0842; Found: 276.0853; Elemental analysis calculated: C, 56.91; H, 5.97; N, 5.53; Found: C, 57.15; H, 6.05; N, 5.45.

H_2N-[*Oi*Bu-(2-HABA)]-CO_2Me (81)

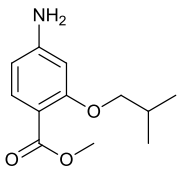

To a stirred solution of O_2N-[*Oi*Bu-(2-HABA)]-CO_2Me **79** (3.86 g, 15.2 mmol, 1 equiv.) in anhydrous methanol (120 mL) under a nitrogen atmosphere was added 10% Pd(C) (386 mg). The nitrogen atmosphere was evacuated under vacuum and hydrogen gas (2L) introduced *via* a balloon. The reaction mixture was stirred for 24h until TLC analysis showed complete conversion. The reaction mixture was passed through a celite pad, washed twice with methanol and concentrated. The resulting grey oil was then dried under reduced pressure to leave a grey gel (3.4 g, quant.); R_f 0.56 (SiO_2, 30% ethylacetate in dichloromethane); ^{1}H NMR ($CDCl_3$, 500 MHz) δ: 7.75 (d, *J* = 8.5 Hz, 1 H, H6), 6.21 (s, 1 H, H3), 6.18 (d, *J* = 8.5 Hz 1 H, H5), 4.10 (br, 2 H, NH_2), 3.84 (s, 3 H, OCH_3), 3.72 (d, *J* = 6.5 Hz, 2 H, Hα), 2.19-2.11 (apparent quin, *J* = 6.5 Hz, 1 H, Hβ), 1.04 (d, *J* = 6.5 Hz, 6H, Hγ) ppm; ^{13}C NMR ($CDCl_3$, 126 MHz) δ: 166.6 (CO), 161.3 (C2), 152.1 (C4), 134.2 (C6), 109.2 (C1), 106.3 (C3), 98.7 (C5), 75.0 (Cα), 51.3 (OC), 28.3 (Cβ), 19.3 (Cγ) ppm; IR (neat) ν(cm^{-1}): 3635, 3445, 2977, 1732,

1433, 1395, 1221; HRMS *m/z* calculated for $C_{12}H_{17}NNaO_3$ $(M+Na)^+$: 246.1101; Found: 246.1107.

H_2N-[*Oi*Pr-(2-HABA)]-CO_2H (83)

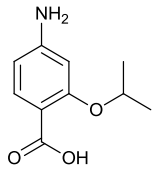

Using general procedure for ester hydrolysis (b) (heated at 65 ºC), H_2N-[*Oi*Pr-(2-HABA)]-CO_2Me **49** (500 mg, 2.4 mmol, 1 equiv.); sodium hydroxide 1 M (5 mL); anhydrous methanol (40 mL). On cooling, the reaction mixture was acidified to pH ≈ 1 (ca 5 mL, hydrochloric acid 1 N) and extracted with dichloromethane (3 × 50 mL). The organic was dried (sodium sulphate) and the solvent removed under reduced pressure to leave the pure product as a yellow solid (449 mg, 96%); R_f 0.51 (SiO_2, 40% ethylacetate in dichloromethane); ^{1}H NMR ($CDCl_3$, 500 MHz) δ: 10.83 (s, 1 H, CO_2H), 7.86 (d, *J* = 8.5 Hz, 1 H, H6), 6.27 (s, 1 H, H3), 6.17 (d, *J* = 8.5 Hz 1 H, H5), 4.72-4.67 (apparent quin, *J* = 6 Hz, 1 H, Hα), 4.20 (br, 2 H, NH_2), 1.38 (d, *J* = 6 Hz, 6H, Hβ) ppm; ^{13}C NMR ($CDCl_3$, 126 MHz) δ: 165.0 (CO), 157.2 (C2), 151.9 (C4), 134.3 (C6), 107.5 (C5), 106.9 (C1), 97.7 (C3), 72.4 (Cα), 21.0 (Cβ) ppm; IR (neat) ν (cm^{-1}): 3437, 3356, 3246, 2978, 1685, 1600, 1507, 1456, 1383, 1270; ESI-MS found: 194 $(M-H)^-$; HRMS *m/z* calculated for $C_{10}H_{13}NNaO_3$ $(M+Na)^+$: 218.0788; Found: 218.0796.

H_2N-[*Oi*Bu-(2-HABA)]-CO_2H (85)

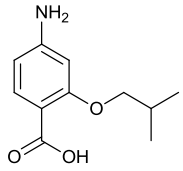

Using general procedure for ester hydrolysis (b) (heated at 65 ºC), H_2N-[*Oi*Bu-(2-HABA)]-CO_2Me **81** (3.4 g, 15.2 mmol, 1 equiv.); sodium hydroxide 1 M (75 mL); anhydrous methanol (150 mL); anhydrous tetrahydrofuran (150 mL). On cooling, the reaction mixture was acidified to pH ≈ 1 (ca 100 mL, hydrochloric acid 1 N) and extracted with dichloromethane (3 × 250 mL). The organic was dried (sodium sulphate) and the solvent removed under reduced pressure to leave the pure product as a yellow solid (3.11 g, 98%); R_f 0.53 (SiO_2, 30% ethylacetate in dichloromethane); ^{1}H NMR ($CDCl_3$, 500 MHz) δ: 10.74 (s, 1 H, CO_2H), 7.97 (d, *J* = 8.5 Hz, 1 H, H6), 6.37 (s, 1 H, H3), 6.25 (d, *J* = 8.5 Hz 1 H, H5), 3.96 (d, *J* = 6.5 Hz, 2 H, Hα), 2.25-2.19 (apparent quin, *J* = 6.5 Hz, 1 H, Hβ), 1.10 (d, *J* = 6.5 Hz, 6H, Hγ) ppm; ^{13}C NMR ($CDCl_3$, 126 MHz) δ: 165.8 (CO), 159.5 (C2), 152.9 (C4), 135.5 (C6), 108.3 (C5), 107.2 (C1), 97.5 (C3),

76.1 (Cα), 28.1 (Cβ), 19.2 (Cγ) ppm; IR (neat) ν(cm^{-1}): 35937, 3436, 2979, 1732, 1430, 1222; HRMS *m*/*z* calculated for $C_{11}H_{16}NO_3$ $(M+H)^+$: 210.1125; Found: 210.1129; Elemental analysis calculated: C, 63.14; H, 7.23; N, 6.69; Found: C, 63.25; H, 7.35; N, 6.45.

H_2N-[*O*Bn-(2-HABA)]-CO_2H (86)

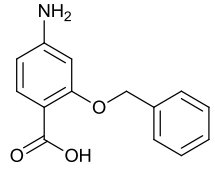

Using general procedure for ester hydrolysis (b) (heated at 65 ºC). H_2N-[*O*Bn-(2-HABA)]-CO_2Me **50** (300.0 mg, 1.2 mmol); sodium hydroxide 1 M (3 mL); anhydrous methanol (15 mL) and anhydrous tetrahydrofuran (15 mL). On cooling, the reaction mixture was acidified to pH ≈ 1 (ca 5 mL, hydrochloric acid 1 N) and extracted with dichloromethane (3 × 150 mL). The organic was dried (sodium sulphate) and the solvent removed under reduced pressure. The product was eventually purified by column chromatography (SiO_2, gradient dichloromethane:ethyl acetate) to leave a grey gel (228.7 mg, 80%); R_f 0.40 (SiO_2, 20% ethylacetate in dichloromethane); ^{1}H NMR ($CDCl_3$, 500 MHz) δ: 10.54 (s, 1 H, CO_2H), 7.96 (d, *J* = 8 Hz, 1 H, H6), 7.44-7.34 (m, 5 H, HAr2, HAr3, HAr4), 6.36 (d, *J* = 8 Hz 1 H, H5), 6.30 (s, 1 H, H1), 5.20 (s, 2 H, Hα), 4.25 (br, 2 H, NH_2) ppm; ^{13}C NMR ($CDCl_3$, 126 MHz) δ: 166.0 (CO), 159.3 (C2), 153.5 (C4), 135.4 (C6), 134.5 (CAr1), 129.1 (CAr), 129.0 (CAr4), 127.3 (CAr), 108.6 (C5), 106.9 (C1), 97.9 (C3), 71.9 (Cα) ppm; IR (neat) ν(cm^{-1}): 3470, 3359, 3237, 1704, 1602, 1453; ESI-MS found: 244 $(M+H)^+$, 509 $(2M+Na)^+$; HRMS *m*/*z* calculated for $C_{14}H_{14}NO_3$ $(M+H)^+$: 244.0968; Found: 244.0969.

FmocNH-[*Oi*Pr-(2-HABA)]-CO_2H (88)

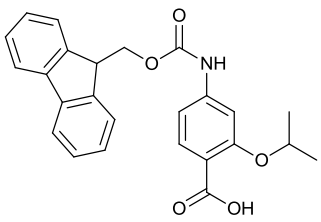

Using general procedure for Fmoc-protection (e). H_2N-[*Oi*Pr-(2-HABA)]-CO_2H **83** (350.0 mg, 1.8 mmol); anhydrous chloroform (12 mL); Fmoc-Chloride (555.0 mg, 2.14 mmol) in chloroform (15 mL). The reaction mixture was allowed to stir for 46 h until TLC analysis showed complete conversion. The solvent was removed under reduced pressure and the resulting oil was crystallized from a mixture of dichloromethane-hexane to leave the pure product as a colourless solid (448 mg, 60%); R_f 0.60 (SiO_2, 30% ethylacetate in dichloromethane); ^{1}H NMR ($CDCl_3$, 500 MHz) δ: 8.11 (d, *J* = 8.5 Hz, 1 H, H6),

7.82 (d, *J* = 7.5 Hz, 2 H, Fmoc-HAr5), 7.68 (br, 1 H, NH), 7.64 (d, *J* = 7.5 Hz, 2 H, Fmoc-HAr2), 7.46 (t, *J* = 7.5 Hz, 2 H, Fmoc-HAr4), 7.37 (d, *J* = 7.5 Hz, 2 H, Fmoc-HAr3), 6.98 (s, 1 H, H3), 6.76 (d, *J* = 8.5 Hz 1 H, H5), 4.94-4.89 (apparent quin, *J* = 6 Hz, 1 H, Hα), 4.61 (d, *J* = 6.5 Hz, 2 H, Fmoc-Hα), 4.31 (t, *J* = 6.5 Hz, 1 H, Fmoc-Hβ), 1.49 (d, *J* = 6 Hz, 6H, Hβ) ppm; ^{13}C NMR ($CDCl_3$, 126 MHz) δ: 165.2 (CO), 157.6 (C2), 159.2 (Fmoc-CO), 143.8 (C4), 143.4 (Fmoc-CAr1), 141.4 (Fmoc-CAr6), 134.5 (C6), 127.9 (Fmoc-CAr4), 127.2 (Fmoc-CAr3), 124.8 (Fmoc-CAr2), 120.2 (Fmoc-CAr5), 113.3 (C1), 111.5 (C5), 103.3 (C3), 74.2 (Cα), 67.2 (Fmoc-Cα), 47.0 (Fmoc-Cβ), 22.0 (Cβ) ppm; IR (neat) ν(cm^{-1}): 3282, 2978, 1714, 1593, 1531, 1414, 1217; ESI-MS found: 416 $(M-H)^-$; HRMS *m*/*z* calculated for $C_{25}H_{23}NNaO_5$ $(M+Na)^+$: 440.1468; Found: 440.1478; Elemental analysis calculated: C, 71.93; H, 5.55; N, 3.36; Found: C, 71.90; H, 5.60; N, 3.30.

FmocNH-[*Oi*Bu-(2-HABA)]-CO_2H (90)

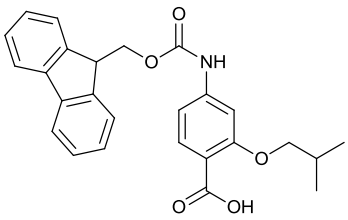

Using general procedure for Fmoc-protection (e). H_2N-[*Oi*Bu-(2-HABA)]-CO_2H **85** (3.1 g, 14.8 mmol); anhydrous tetrahydrofuran (180 mL); Fmoc-Chloride (11.5 g, 44.4 mmol) in tetrahydrofuran (60 mL). The reaction mixture was allowed to stir for 48 h until TLC analysis showed complete conversion. The solvent was removed under reduced pressure and the resulting oil was crystallized from a mixture of dichloromethane-hexane to leave the pure product as a pale yellow solid (5.43 g, 85%); R_f 0.66 (SiO_2, 30% ethylacetate in dichloromethane); ^{1}H NMR ($CDCl_3$, 500 MHz) δ: 8.11 (d, *J* = 8.5 Hz, 1 H, H6), 7.82 (d, *J* = 7.5 Hz, 2 H, Fmoc-HAr5), 7.67 (br, 1 H, NH), 7.64 (d, *J* = 7.5 Hz, 2 H, Fmoc-HAr2), 7.46 (t, *J* = 7.5 Hz, 2 H, Fmoc-HAr4), 7.37 (d, *J* = 7.5 Hz, 2 H, Fmoc-HAr3), 7.01 (s, 1 H, H3), 6.78 (d, *J* = 8.5 Hz 1 H, H5), 4.61 (d, *J* = 6.5 Hz, 2 H, Fmoc-Hα), 4.31 (t, *J* = 6.5 Hz, 1 H, Fmoc-Hβ), 4.05 (d, *J* = 6.5 Hz, 2 H, Hα), 2.83-2.23 (apparent quin, *J* = 6.5 Hz, 1 H, Hβ), 1.09 (d, *J* = 6.5 Hz, 6H, Hγ) ppm; ^{13}C NMR ($CDCl_3$, 126 MHz) δ: 165.0 (CO), 158.8 (C2), 152.9 (Fmoc-CO), 144.0 (C4), 143.4 (Fmoc-CAr1), 141.4 (Fmoc-CAr6), 134.5 (C6), 128.0 (Fmoc-CAr4), 127.2 (Fmoc-CAr3), 124.8 (Fmoc-CAr2), 120.2 (Fmoc-CAr5), 112.2 (C1), 111.3 (C5), 101.9 (C3), 76.5 (Cα), 67.2 (Fmoc-Cα), 47.0 (Fmoc-Cβ), 28.1 (Cβ), 19.2 (Cγ) ppm;

IR (neat) ν (cm^{-1}): 3627, 3435, 2979, 1732, 1430, 1222; HRMS *m*/*z* calculated for $C_{26}H_{25}NNaO_5$ $(M+Na)^+$: 454.1625; Found: 454.1628.

FmocNH-[*O*Bn-(2-HABA)]-CO_2H (91)

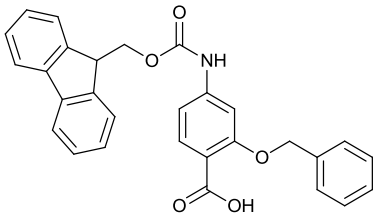

Using general procedure for Fmoc-protection (e). H_2N-[*O*Bn-(2-HABA)]-CO_2H **86** (150.0 mg, 0.62 mmol); anhydrous chloroform (4 mL); Fmoc-Chloride (192.0 mg, 0.74 mmol) in chloroform (3 mL). The reaction mixture was allowed to stir for 50 h until TLC analysis showed complete conversion. The solvent was removed under reduced pressure and the resulting oil was crystallized from a mixture of dichloromethane-hexane to leave the pure product as a colourless solid (205.7 mg, 71%); R_f 0.30 (SiO_2, (SiO_2, 30% ethylacetate in dichloromethane); ^{1}H NMR ($CDCl_3$, 500 MHz) δ: 8.16 (d, *J* = 8.3 Hz, 1 H, H6), 7.86 (d, *J* = 7.5 Hz, 2 H, Fmoc-HAr5), 7.83 (br, 1 H, NH), 7.69 (d, *J* = 7.5 Hz, 2 H, Fmoc-HAr2), 7.47-7.51 (m, 5 H, HAr2, HAr3, HAr4), 7.39 (t, *J* = 7.5 Hz, 4 H, Fmoc-HAr4, Fmoc-HAr3), 7.33 (s, 1 H, H3), 6.88 (d, *J* = 8.3 Hz 1 H, H5), 5.33 (s, 2 H, Hα), 4.65 (d, *J* = 6.5 Hz, 2 H, Fmoc-Hα), 4.34 (t, *J* = 6.5 Hz, 1 H, Fmoc-Hβ) ppm; ^{13}C NMR ($CDCl_3$, 126 MHz) δ: 165.2 (CO), 158.5 (C2), 153.0 (Fmoc-CO), 144.2 (C4), 143.4 (Fmoc-CAr1), 141.4 (Fmoc-CAr6), 134.6 (C6), 134.1 (CAr1), 129.2 (CAr4), 129.1 (CAr), 128.2 (Fmoc-CAr4), 127.9 (Fmoc-CAr3), 127.2 (CAr), 124.9 (Fmoc-CAr2), 120.2 (Fmoc-CAr5), 112.4 (C1), 111.7 (C5), 102.4 (C3), 72.3 (Cα), 67.2 (Fmoc-Cα), 47.0 (Fmoc-Cβ) ppm; IR (neat) ν (cm^{-1}): 3333, 1722, 1702, 1612, 1524, 1411; ESI-MS found: 488 $(M+Na)^+$; HRMS *m*/*z* calculated for $C_{29}H_{24}NO_5$ $(M+H)^+$: 466.1649; Found: 466.1644.

6.2.2 Solid phase synthesis of hybrid α-helix mimetics

Synthetic procedures

A generic procedure was followed by adapting the previously reported solid phase synthesis of 3-*O*-alkylated[100] and *N*-alkylated[106] oligobenzamides. The reactions were all carried out on a CEM Liberty® automated microwave assisted peptide synthesiser. The procedure is described briefly below:

Resin preparation

127 mg of Fmoc-Gly-Wang resin (0.79 mmol g^{-1}, 100-200 mesh; carrier: polystyrene, crosslinked with 1% DVB) were used for hybrid mimetics **75**, **98**, **99**, **101**-**111**, **113**-**120**, **127**, **128**, and **129**-**131**; 170 mg of Rink Amide MBH resin (0.59 mmol g^{-1}) were used for hybrid mimetic **100**; 156 mg of Fmoc-Leu-Wang resin (0.64 mmol g^{-1}) were used for hybrid mimetic **112**; 185 mg of Fmoc-Glu(OtBu)-Wang resin (0.54 mmol g^{-1}, 100-200 mesh) were used for hybrid mimetics **121**-**123**; 196 mg of Fmoc-Pro-Wang resin (0.51 mmol g^{-1}) were used for hybrid mimetics **124**-**126**. The resin was swelled in Corning® tubes in DMF for at least 30 minutes prior to coupling. Standard washing and deprotection cycles were carried out on the synthesiser. A filtered drain took place in between every wash as follows: wash the reaction vessel from the top ('DMF top', 5 mL), then from the bottom ('DMF bottom', 7 mL), then 'DMF top' (5 mL).

Fmoc deprotection

Before coupling of each monomer and after the last coupling reaction, two deprotection cycles were carried out on the CEM synthesiser using 6 mL of a 25% piperidine solution in DMF, under microwave heating at 75 °C. The initial deprotection lasted 30 seconds and was followed by a 'DMF top' wash and filtered drain. After a second addition of deprotection mixture, the deprotection was maintained under microwave heating for 3 minutes, and was again followed by DMF washes.

Coupling of 2-*O* and 3-*O*-alkylated monomers to the resin

Prior to the reaction, each fully protected monomer (1.5 equiv.) was dissolved in anhydrous DMF (2.5 mL) in a dry 50 mL Corning® tube (stored in an oven at 60 °C for at least 24 hours), and pre-activated with HATU (1.9 equiv.) and DIPEA (3.8 equiv.) at room temperature. A single coupling method of 30 min was carried out under microwave heating at 50 °C.

Coupling of *N*-alkylated monomers

Prior to the reaction, each fully protected monomer (3 equiv. per coupling) was dissolved in anhydrous chloroform (2.5 mL per coupling, *i.e.* 5 mL for a double

coupling) in a dry 50 mL Corning® tube (stored in an oven at 60 °C for at least 24 hours), and pre-activated with Ghosez's reagent (2.7 equiv. per coupling) at room temperature for 1-3 hours under a nitrogen atmosphere. For each monomer, a double coupling of 20 minutes was carried out under microwave heating at 60 °C.

Coupling of middle amino acids

Prior to the reaction, each fully protected aminoacid (2.5 equiv. per coupling) was dissolved in anhydrous DMF (2.5 mL per coupling) in a dry 50 mL Corning® tube (stored in an oven at 60 °C for at least 24 hours), and pre-activated with HATU (3 equiv. per coupling) and DIPEA (5 equiv. per coupling) at room temperature for 1-3 hours under a nitrogen atmosphere. For natural amino acid derivatives, a double coupling of 30 minutes was carried out under microwave heating at 60 °C. For non-natural amino acids, a triple coupling of 30 minutes was carried out under microwave heating at 60 °C.

Coupling of 2-*O* and 3-*O*-alkylated monomers

Prior to the reaction, each fully protected monomer (1.5 equiv. per coupling) was dissolved in anhydrous DMF (2.5 mL per coupling) in a dry 50 mL Corning® tube (stored in an oven at 60 °C for at least 24 hours), and pre-activated with HATU (3 equiv. per coupling) and DIPEA (5 equiv. per coupling) at room temperature. A double coupling method of 30 min was carried out under microwave heating at 60 °C.

Coupling of top amino acids

Prior to the reaction, each fully protected aminoacid (2.5 equiv. per coupling) was dissolved in anhydrous chloroform (2.5 mL per coupling) in a dry 50 mL Corning® tube (stored in an oven at 60 °C for at least 24 hours), and pre-activated with Ghosez's reagent (3.2 equiv. per coupling) at room temperature for 1-3 hours under a nitrogen atmosphere. For each amino acid, a double coupling of 20 minutes was carried out under microwave heating at 60 °C.

Cleavage

The cleavage step was carried out manually, in 3 mL 'Extract-Clean' polypropylene reservoirs fitted with 20 µm polyethylene frits, both available from Alltech. The resin was transferred to a reservoir then washed with dichloromethane (2 × 3 mL × 2 min)

and diethylether (2 × 3 mL × 2 min). 3 mL of a 1:1 mixture of TFA in dichloromethane was added and the mixture was allowed to stir at room temperature for 40 minutes. The content of the reservoir was collected and the procedure was repeated. The combined solution was then concentrated under reduced pressure and the resulting oil was washed with hexane and diethylether to afford a solid.

Purification

The hybrid mimetics were purified using mass-directed preparative HPLC (0.1% formic acid water/methanol or acetonitrile; 5-95% gradient) to afford the desired products with purity higher than 90-95%. A representative example is shown in Figure 6.4.

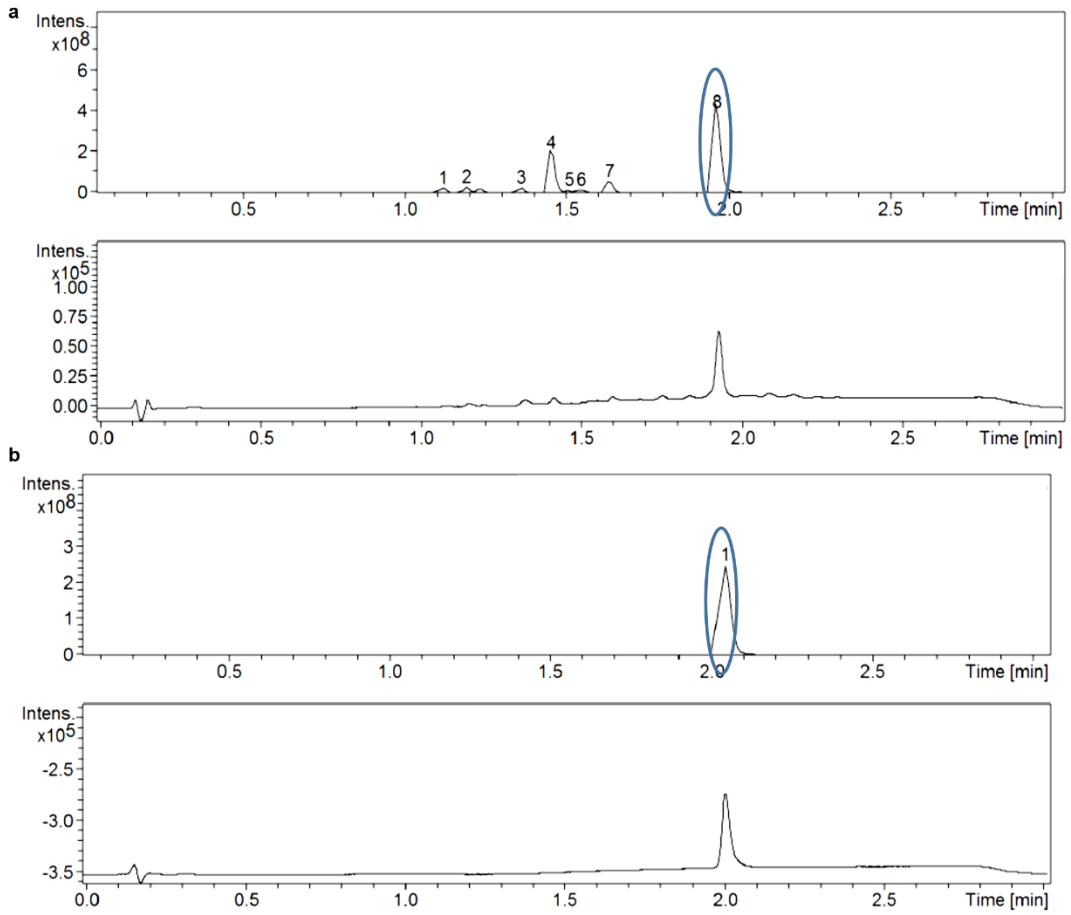

Figure 6.4 Purification of hybrid α-helix mimetics using mass-directed HPLC a MS (top) and UV (bottom) chromatograms of hybrid **75** before purification; **b** MS (top) and UV (bottom) chromatograms of hybrid **75** after purification.

Determination of the optical rotation

Due to the limited amount of material available, the optical rotation was determined only for hybrids **75** and **129**, carrying an L-Phe and a D-Phe as central units, in order to prove that amino acids do not undergo racemisation in the condition used.

Numbering system for hybrid α-helix mimetics

To simplify the numbering and NMR assignment of the hybrid α-helix mimetics, a sequential nomenclature has been devised, where each of the monomer building blocks is considered separately (Figure 6.5). The monomers are numbered from 1 to 4 (or 5) starting from the *C*-terminus. *O*-Alkylated monomers are named as [*R*-(*n*-HABA)], where *R* is the alkoxy side-chain, *n*- indicates the position of the alkoxy moiety on the aromatic ring (*e.g.* for a 2-*O*-alkylated monomer *n* = 2) and HABA is the acronym for Hydroxy Amino Benzoic Acid; *N*-alkylated monomers are named as [*R*-(ABA)], where *R* is the *N*-alkyl side-chain, and ABA is the acronym for Amino Benzoic Acid. . Within each alkylated monomer, the numbering is the same: the carbons from the aminobenzoic acid are numbered using the standard system (the aromatic carbon bearing the carboxylic acid is C1, the one bearing the amine is C4). Then, the lateral chain is numbered: the carbon attached to the oxygen is the Cα, and the numbering of the aliphatic part of the side chain continues with Cβ, etc. In the case of aromatic side chains, the aromatic carbons are numbered CAr1, CAr2, etc. Amino acids are numbered using the standard convention.

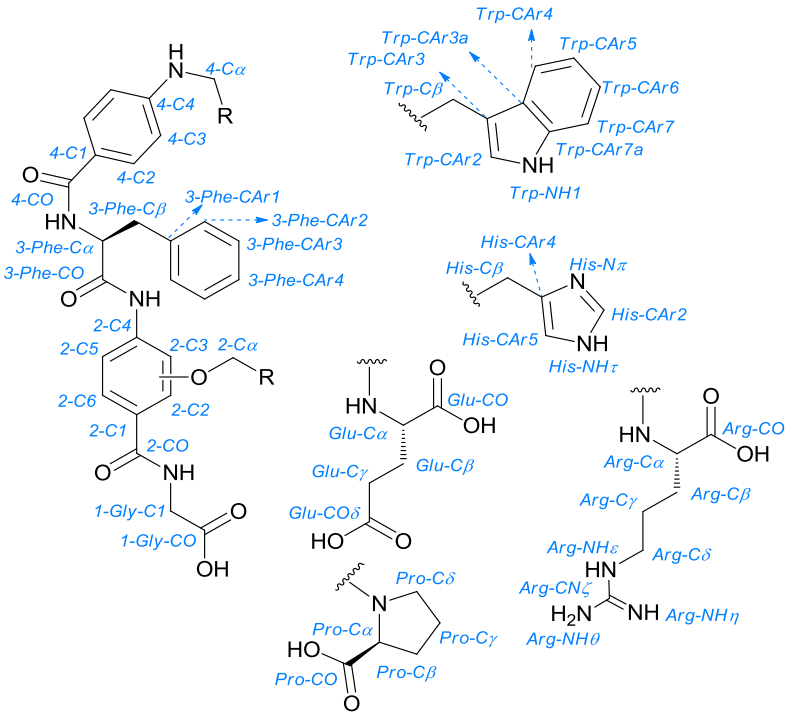

Figure 6.5 Numbering of atoms in hybrid α-helix mimetics.

The numbering of the protons is based on the carbon numbering. To differentiate each individual carbon/proton, the monomer number is added as a prefix to the carbon/proton number.

H_2N-[*O*-Bn-(3-HABA)]-Phe-[*O*-*i*Pr-(2-HABA)]-Gly-CO_2H (75)

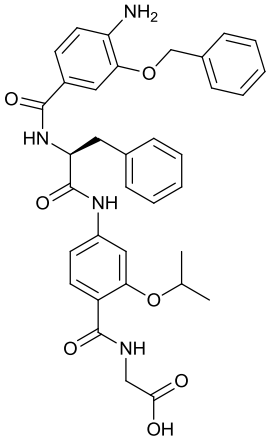

Pale orange solid, > 95% pure by NMR; isolated yield: 11.6 mg, 19%; R_f 0.50 (SiO_2, 20% methanol in acetonitrile); $[\alpha]_D^{27.5}$ = + 22.8° (c 0.008 g mL^{-1}, methanol); ^1H NMR (DMSO-d_6, 500 MHz) δ: 10.46 (s, 1H,1-Gly-CO_2H), 8.49 (t, *J* = 5 Hz, 1 H, 1-Gly-NH), 8.36 (d, *J* = 8 Hz, 1 H, 3-Phe-NH), 7.91 (d, *J* = 8.5 Hz, 1 H, 2-H6), 7.64 (s, 1 H, 2-H3), 7.53 (d, *J* = 8.5 Hz, 2 H, 3-Phe-HAr2), 7.45 (s, 1 H, 4-H2), 7.43-7.40 (m, 5 H, 4-HAr2, 4-H-Ar3, 4-HAr4), 7.35 (t, *J* = 8.5 Hz, 2 H, 3-Phe-HAr3), 7.30 (d, *J* = 8.5 Hz, 2 H, 4-H6, 2-H5), 7.28 (br, 1H, 2-NH), 7.20 (t, *J* = 8.5 Hz, 1H, 3-Phe-HAr4), 6.66 (d, *J* = 8.5 Hz, 1 H, 4-H5), 5.34 (br, 2H, 4-NH_2), 5.17 (s, 2 H, 4-Hα), 4.85-4.81 (dd, *J* = 8.5 , 5.5 Hz, 1 H, 3-Phe-Hα), 4.76-4.71 (apparent quin, *J* = 6 Hz, 1 H, 2-Hα), 4.05 (d, *J* = 5 Hz, 2 H, 1-Gly-H1), 3.16-3.12 (dd, *J* = 8.5

, 5.5 Hz, 2 H, 3-Phe-Hβ), 1.45-1.43 (dd, *J* = 8.5, 6 Hz, 6 H, 2-Hβ) ppm; ^{13}C NMR (DMSO-d_6, 126 MHz) δ: 171.5 (1-Gly-CO), 166.4 (4-CO), 163.9 (2-CO), 156.2 (3-Phe-CO), 144.0 (4-C3), 143.1 (2-C2), 141.5 (4-C4), 138.2 (2-C4), 137.2 (2-C6), 131.9 (4-CAr1), 129.2 (3-Phe-CAr3), 128.4 (4-CAr2, 4-CAr3), 128.1 (4-CAr4), 127.7 (4-C2), 127.4 (3-Phe-CAr2, 3-Phe-CAr4), 126.3 (3-Phe-CAr1), 121.8 (4-C6), 120.8 (4-C1), 116.6 (2-C1), 112.3 (4-C5), 111.4 (2-C5), 104.7 (2-C3), 71.9 (2-Cα), 69.4 (4-Cα), 55.9 (3-Phe-Cα), 41.7 (1-Gly-C1), 37.1 (3-Phe-Cβ), 21.6 (2-Cβ) ppm; IR (neat) ν(cm^{-1}): 3344, 2922, 1682, 1594, 1494, 1257, 1208; ESI-MS found: 625 $(M+H)^+$; HRMS *m/z* calculated for $C_{35}H_{37}N_4O_7$ $(M+H)^+$: 625.2657; Found: 625.2666.

H_2N-Phe-[*O*-*i*Pr-(2-HABA)]-Gly-CO_2H (98)

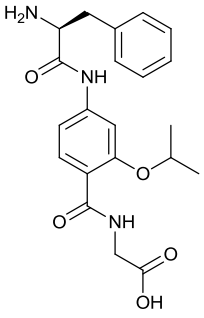

Colourless solid, > 95% pure by NMR; isolated yield: 10 mg, 25%; R_f 0.05 (SiO_2, 20% methanol in acetonitrile); $[\alpha]_D^{26.6}$ = + 37.3° (c 0.003 g mL^{-1}, methanol); ^{1}H NMR (DMSO-d_6, 500MHz) δ: 8.51 (t, *J* = 5 Hz, 1 H, 1-Gly-NH), 8.20 (s, 1 H, 2-NH), 7.90 (d, *J* = 8.5 Hz, 1 H, 2-H6), 7.59 (s, 1 H, 2-H3), 7.29 (d, *J* = 8.5 Hz, 2 H, 3-Phe-HAr), 7.27 (s, 1 H3-Phe-HAr4), 7.26 (d, *J* = 8.5 Hz, 2 H, 3-Phe-HAr), 7.23 (d, *J* = 8.5 Hz, 1 H, 2-H5), 4.66 - 4.76 (apparent quin, *J* = 6 Hz, 1 H, 2-Hα), 3.99 (d, *J* = 5 Hz, 2 H, 1-Gly-H1), 3.78 (t, *J* = 5.5 Hz, 2 H, 3-Phe-Hα), 3.10-3.06 (dd, *J* = 12.8, 5.5 Hz, 1 H, 3-Phe-Hβ), 2.88-2.85 (dd, *J* = 12.8, 5.5 Hz, 1 H, 3-Phe-Hβ'), 1.42 ppm (d, *J* = 6 Hz, 6 H, 2-Hβ); ^{13}C NMR (DMSO-d_6, 126MHz) δ: 171.4 (1-Gly-CO), 164.0 (2-CO), 156.4 (3-Phe-CO), 142.5 (2-C2, 2-C4), 136.8 (3-Phe-CAr1), 132.2 (2-C6), 129.5 (3-Phe-CAr), 128.6 (3-Phe-CAr), 126.9 (3-Phe-CAr4), 117.3 (2-C1), 111.6 (2-C3), 105.1 (2-C5), 72.1 (2-Cα), 56.1 (3-Phe-Cα), 40.4 (1-Gly-C1), 40.1 (3-Phe-Cβ), 21.7 (2-Cβ) ppm; IR (neat) ν(cm^{-1}): 3356, 2979, 2930, 1693, 1629, 1593, 1491, 1258, 1229; ESI-MS found: 400 $(M+H)^+$; HRMS *m/z* calculated for $C_{21}H_{26}N_3O_5$ $(M+H)^+$: 400.1867; Found: 400.1872.

Ac-HN-Phe-[*O*-*i*Pr-(2-HABA)]-Gly-CO_2H (99)

Colourless solid, > 95% pure by NMR; isolated yield: 45.5 mg, quant.; R_f 0.17 (SiO_2, 20% methanol in acetonitrile); $[\alpha]_D^{26.9}$ = + 18.1° (c 0.005 g mL^{-1}, methanol); ^{1}H NMR (DMSO-d_6, 500 MHz) δ: 10.35 (s, 1H, 1-Gly-CO_2H), 8.46 (t, *J* = 5 Hz, 1 H, 1-Gly-

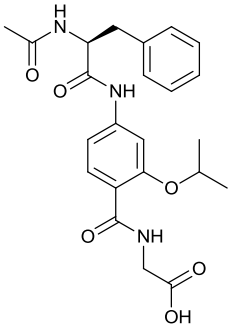

NH), 8.32 (d, *J* = 8.5 Hz, 1 H, 3-Phe-NH), 7.89 (d, *J* = 8.5 Hz, 1 H, 2-H6), 7.59 (s, 1 H, 2-H3), 7.30-7.27 (m, 6 H, 3-Phe-HAr and 2-NH), 7.22 (d, *J* = 8.5 Hz, 1 H, 2-H5), 4.68 - 4.73 (apparent quin, *J* = 6 Hz, 1 H, 2-Hα), 4.64-4.67 (m, *J* = 5.5 Hz, 2 H, 3-Phe-Hα), 4.05 (d, *J* = 5 Hz, 2 H, 1-Gly-H1), 3.07-3.03 (dd, *J* = 12.8, 5.5 Hz, 1 H, 3-Phe-Hβ), 2.90-2.85 (dd, *J* = 12.8, 5.5 Hz, 1 H, 3-Phe-Hβ'), 1.82 (s, 1 H, Ac-H1), 1.43-1.41 (dd, *J* = 6, 9.5 Hz, 6 H, 2-Hβ) ppm; ^{13}C NMR (DMSO-d_6, 126 MHz) δ: 171.2 (1-Gly-CO), 169.3 (Ac-CO), 163.9 (2-CO), 156.2 (3-Phe-CO), 142.9 (2-C2), 137.6 (2-C4), 131.9 (2-C6), 129.5 (3-Phe-CAr1), 129.1 (3-Phe-CAr), 128.1 (3-Phe-CAr), 126.4 (3-Phe-CAr4), 116.7 (2-C1), 111.4 (2-C3), 104.7 (2-C5), 71.2 (2-Cα), 55.0 (3-Phe-Cα), 41.6 (1-Gly-C1), 37.5 (3-Phe-Cβ), 22.3 (Ac-C1), 21.6 (2-Cβ) ppm; IR (neat) ν(cm^{-1}): 3285, 3063, 2981, 2931, 1640, 1596, 1495, 1258, 1186; ESI-MS found: 442 $(M+H)^+$; HRMS *m/z* calculated for $C_{23}H_{27}N_3NaO_6$ $(M+Na)^+$: 464.1792; Found: 464.1794.

H_2N-[*O*-Bn-(3-HABA)]-Phe-$CONH_2$ (100)

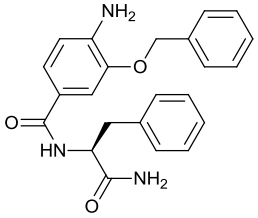

Colourless solid, > 95% pure by NMR; isolated yield: 9.6 mg, 25%; R_f 0.03 (SiO_2, 20% methanol in acetonitrile); $[\alpha]_D^{26.9}$ = -36.0° (c 0.002 g mL^{-1}, methanol); ^{1}H NMR (DMSO-d_6, 500 MHz) δ: 8.05 (d, *J* = 8.5 Hz, 1 H, 1-Phe-NH), 7.51 (d, *J* = 7.5 Hz, 2 H, 2-HAr2), 7.46 (s, 1 H, 2-H2), 7.41 (t, *J* = 8 Hz, 2 H, 1-Phe-HAr3), 7.35 (d, *J* = 7.5 Hz, 1 H, 2-HAr4), 7.32 (d, *J* = 8 Hz, 2 H, 1-Phe-HAr2), 7.27 (d, *J* = 8.5 Hz, 1 H, 2-H6), 7.24 (t, *J* = 7, 5 Hz, 2 H, 2-HAr3), 7.16 (t, *J* = 8 Hz, 1 H, 1-Phe-HAr4), 7.06 (s, 2H, 1-NH_2), 6.63 (d, *J* = 8.5 Hz, 1 H, 2-H5), 5.29 (s, 2H, 2-NH_2), 5.15 (s, 2H, 2-Hα), 4.63 - 4.58 (apparent quin, *J* = 4.5 Hz, 1 H, 1-Phe-Hα), 3.11-3.07 (dd, *J* = 13.5, 4.5 Hz, 1 H, 1-Phe-Hβ), 3.0-2.96 (dd, *J* = 13.5, 4.5 Hz, 1 H, 1-Phe-Hβ') ppm; ^{13}C NMR (DMSO-d_6, 126 MHz) δ: 173.7 (1-Phe-CO), 166.0 (2-CO), 144.1 (2-C3), 141.4 (2-C4), 138.7 (2-CAr1), 137.2 (1-Phe-CAr1), 129.1 (1-Phe-CAr2), 129.1 (4-C4), 128.4 (1-Phe-CAr3), 128.0 (2-CAr4), 127.4 (2-CAr2, 2-CAr3), 126.1 (1-Phe-CAr4), 121.5 (2-C6), 121.3 (2-C1), 112.3 (2-C2), 111.3 (2-C5), 69.4 (2-Cα), 54.5 (1-Phe-Cα), 35.1 (1-Phe-Cβ) ppm; IR (neat) ν(cm^{-1}): 3482, 3386, 3303, 2925, 2853, 1682,

1615, 1579, 1499, 1260, 1228; ESI-MS found: 801 $(2M+Na)^+$; HRMS *m/z* calculated for $C_{23}H_{24}N_3O_3$ $(M+H)^+$: 390.1812; Found: 390.1821.

H_2N-[ABA]-Phe-[*O*-*i*Pr-(2-HABA)]-Gly-CO_2H (101)

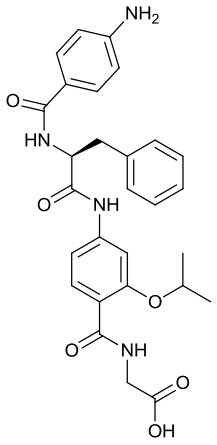

Pale brown solid, > 95% pure by NMR; isolated yield: 15.8 mg, 19%; R_f 0.18 (SiO_2, 20% methanol in acetonitrile); $[\alpha]_D^{27.0}$ = + 26.0° (c 0.005 g mL^{-1}, methanol); ^{1}H NMR (DMSO-d_6, 500 MHz) δ: 10.41 (s, 1H,1-Gly-CO_2H), 8.46 (t, *J* = 5 Hz, 1 H, 1-Gly-NH), 8.25 (d, *J* = 8.5 Hz, 1 H, 3-Phe-NH), 7.90 (d, *J* = 8.5 Hz, 1 H, 2-H6), 7.60 (s, 1 H, 2-H3), 7.59 (d, *J* = 8.5 Hz, 2 H, 4-H2), 7.40 (d, *J* = 7.5 Hz, 1 H, 3-Phe-HAr2), 7.32 (d, *J* = 7.5 Hz, 1 H, 3-Phe-HAr2'), 7.29 (s, 1H, 2-NH), 7.25 (d, *J* = 8.5 Hz, 1 H, 2-H5), 7.20-7.18 (dd, *J* = 7, 5 Hz, 1 H, 3-Phe-HAr4), 7.13 (d, *J* = 7.5 Hz, 1 H, 3-Phe-HAr3), 6.54 (d, *J* = 8.5 Hz, 2 H, 4-H3), 4.82 - 4.79 (m, *J* = 5.5 Hz, 1 H, 3-Phe-Hα), 4.75-4.70 (apparent quin, *J* = 6 Hz, 1 H, 2-Hα), 4.06 (d, *J* = 5 Hz, 2 H, 1-Gly-H1), 3.14-3.07 (dd, *J* = 12.8, 5.5 Hz, 2 H, 3-Phe-Hβ), 1.43-1.41 (dd, *J* = 6, 9.5 Hz, 6 H, 2-Hβ) ppm; ^{13}C NMR (DMSO-d_6, 126 MHz) δ: 171.2 (1-Gly-CO), 166.5 (4-CO), 163.9 (2-CO), 156.2 (3-Phe-CO), 151.6 (2-C2), 143.8 (2-C4), 138.2 (3-Phe-CAr4), 131.9 (2-C6), 129.2 (3-Phe-CAr2), 129.1 (4-C4), 129.0 (4-C2), 128.3 (3-Phe-CAr3), 128.0 (3-Phe-CAr3'), 126.3 (3-Phe-CAr4), 116.6 (2-C1), 112.6 (4-C3), 112.6 (2-C5), 111.3 (2-C3), 71.9 (2-Cα), 55.8 (3-Phe-Cα), 41.6 (1-Gly-C1), 37.0 (3-Phe-Cβ), 21.6 (2-Cβ) ppm; IR (neat) ν(cm^{-1}): 3359, 3023, 2980, 2931, 1721, 1630, 1596, 1494, 1259, 1184; ESI-MS found: 519 $(M+H)^+$; HRMS *m/z* calculated for $C_{28}H_{30}N_4NaO_6$ $(M+Na)^+$: 541.2057; Found: 541.2063.

H_2N-[*O*-Bn-(2-HABA)]-Phe-[*O*-*i*Pr-(2-HABA)]-Gly-CO_2H (102)

Yellow solid, > 95% pure by NMR; isolated yield: 10 mg, 16%; R_f 0.63 (SiO_2, 20% methanol in acetonitrile); $[\alpha]_D^{26.2}$ = + 38.3° (c 0.002 g mL^{-1}, methanol);^{1}H NMR (DMSO-d_6, 500 MHz) δ: 10.40 (s, 1H,1-Gly-CO_2H), 8.46 (t, *J* = 4.5 Hz, 1 H, 1-Gly-NH), 8.11 (d, *J* = 7.5 Hz, 1 H, 3-Phe-NH), 7.87 (d, *J* = 8.5 Hz, 1 H, 2-H6), 7.59 (d, *J* = 8.5 Hz, 1 H, 4-H6), 7.58 (s, 1 H, 2-H3), 7.50 (d, *J* = 7 Hz, 2 H, 4-HAr2), 7.42 (t, *J* = 7 Hz 3 H, 3-Phe-HAr4, 4-HAr3), 7.36 (t, *J* = 7 Hz, 1 H, 4-HAr4), 7.18 (s, 1H, 2-

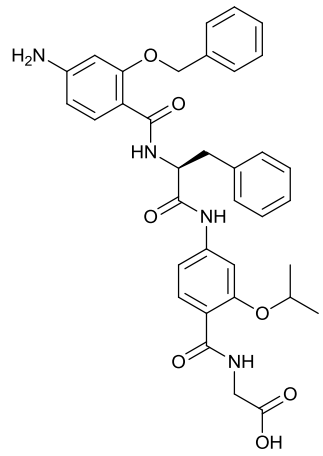

NH), 7.17 (t, *J* = 7 Hz, 2 H, 3-Phe-HAr3), 7.12 (d, *J* = 8.5 Hz, 1 H, 2-H5), 6.93 (d, *J* = 7 Hz, 2H, 3-Phe-HAr2), 6.31 (s, 1H, 4-H3), 6.17 (d, *J* = 8.5 Hz, 1 H, 4-H5), 5.77 (s, 2H, 4-NH_2), 5.20-5.12 (dd, *J* = 31.5, 11.5 Hz, 2 H, 4-Hα), 4.82-4.78 (dd, *J* = 9.5 , 4.5 Hz, 1 H, 3-Phe-Hα), 4.71-4.66 (apparent quin, *J* = 6 Hz, 1 H, 2-Hα), 3.99 (d, *J* = 4.5 Hz, 2 H, 1-Gly-H1), 3.03-2.99 (dd, *J* = 9.5 , 4.5 Hz, 1 H, 3-Phe-Hβ), 2.65-2.61 (dd, *J* = 9.5 , 4.5 Hz, 1 H, 3-Phe-Hβ'), 1.41-1.38 (dd, *J* = 8.5, 6 Hz, 6 H, 2-Hβ) ppm; ^{13}C NMR (DMSO-d_6, 126 MHz) δ: 171.0 (1-Gly-CO), 164.6 (2-CO), 163.9 (4-CO), 158.3(4-C2), 156.2 (3-Phe-CO), 153.6 (4-C4), 142.9 (2-C2), 137.1 (2-C4), 136.2 (4-CAr1), 132.7 (4-C6), 131.9 (2-C6), 128.9 (4-CAr4), 128.6 (4-CAr2, 4-CAr3), 128.1 (3-Phe-CAr2, 3-Phe-CAr3, 3-Phe-CAr4), 126.4 (3-Phe-CAr1), 116.6 (2-C1), 111.3 (2-C5), 108.0 (4-C5), 106.5 (4-C1), 104.7 (2-C3), 97.1 (4-C3), 71.9 (2-Cα), 69.9 (4-Cα), 55.2 (3-Phe-Cα), 41.7 (1-Gly-C1), 37.8 (3-Phe-Cβ), 21.6 (2-Cβ) ppm; IR (neat) ν (cm^{-1}): 3357, 2980, 2932, 1690, 1596, 1494, 1259, 1208; ESI-MS found: 625 $(M+H)^+$; HRMS *m/z* calculated for $C_{35}H_{37}N_4O_7$ $(M+H)^+$: 625.2657; Found: 625.2660.

H_2N-[*N*-Bn-(ABA)]-Phe-[*O*-*i*Pr-(2-HABA)]-Gly-CO_2H (103)

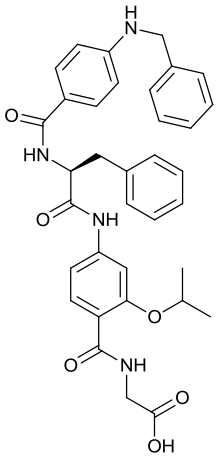

Pale yellow solid, > 95% pure by NMR; isolated yield: 9 mg, 15%; R_f 0.49 (SiO_2, 20% methanol in acetonitrile);); $[\alpha]_D^{26.1}$ = + 44.7° (c 0.004 g mL^{-1}, methanol); ^{1}H NMR (DMSO-d_6, 500 MHz) δ: 10.37 (s, 1H,1-Gly-CO_2H), 8.44 (t, *J* = 5 Hz, 1 H, 1-Gly-NH), 8.22 (d, *J* = 8 Hz, 1 H, 3-Phe-NH), 7.87 (d, *J* = 8.5 Hz, 1 H, 2-H6), 7.59 (s, 1 H, 2-H3), 7.58 (d, *J* = 8.5 Hz, 2 H, 4-H2), 7.36 (d, *J* = 8 Hz, 2 H, 4-HAr2), 7.24-7.29 (m, 5 H, 3-Phe-HAr2, 3-Phe-HAr3, 3-Phe-HAr4), 7.26 (d, *J* = 8.5 Hz, 1 H, 2-H5), 7.25 (s, 1H, 2-NH), 7.24-7.21 (dd, *J* = 8, 5 Hz, 2H, 4-HAr3), 7.15 (t, *J* = 8 Hz, 1 H, 4-HAr4), 6.80 (t, *J* = 6 Hz, 1 H, 4-NH), 6.55 (d, *J* = 8 Hz, 2 H, 4-H3), 4.78-4.74 (dd, *J* = 8.5 , 5.5 Hz, 1 H, 3-Phe-Hα), 4.71-4.67 (apparent quin, *J* = 6 Hz, 1 H, 2-Hα), 4.31 (d, *J* = 6 Hz, 2 H, 4-Hα), 4.01 (d, *J* = 5 Hz, 2 H, 1-Gly-H1), 3.11-3.60 (dd, *J* = 8.5 , 5.5 Hz, 2 H, 3-Phe-Hβ), 1.40-1.38 (dd, *J* = 8.5, 6 Hz, 6 H, 2-Hβ) ppm; ^{13}C NMR

(DMSO-d_6, 126 MHz) δ: 171.2 (1-Gly-CO), 166.5 (4-CO), 164.0 (2-CO), 156.2 (3-Phe-CO), 151.8 (4-C4), 143.1 (2-C2), 138.2 (2-C4), 134.6 (2-C6), 131.9 (4-CAr1), 129.5 (4-CAr2, 4-CAr3), 129.1(3-Phe-CAr2, 3-Phe-CAr4), 128.3 (4-C2), 128.1 (3-Phe-CAr3), 127.1 (4-CAr4), 126.3 (3-Phe-CAr1), 120.3 (4-C1), 116.5 (2-C1), 112.4 (4-C3), 111.3 (2-C5), 104.7 (2-C3), 71.9 (2-Cα), 55.8 (3-Phe-Cα), 45.9(4-Cα), 41.6 (1-Gly-C1), 37.0 (3-Phe-Cβ), 21.6 (2-Cβ) ppm; IR (neat) ν(cm^{-1}): 3336, 3029, 2925, 1680, 1605, 1494, 1256, 1222;ESI-MS found: 609 $(M+H)^+$; HRMS *m/z* calculated for $C_{35}H_{37}N_4O_6$ $(M+H)^+$: 609.2708; Found: 609.2716.

H_2N-[*O*-Bn-(3-HABA)]-Phe-[*O*-*i*Pr-(3-HABA)]-Gly-CO_2H (104)

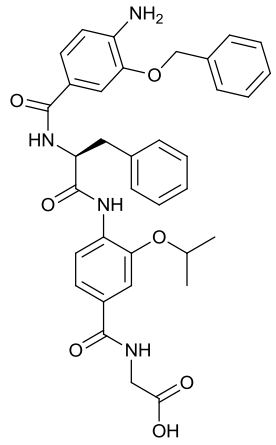

Yellow solid, > 95% pure by NMR; isolated yield: 10 mg, 16%; R_f 0.13 (SiO_2, 20% methanol in acetonitrile); $[\alpha]_D^{26.4}$ = -31.7° (c 0.003 g mL^{-1}, methanol);^{1}H NMR (DMSO-d_6, 500 MHz) δ: 9.28 (s, 1H,1-Gly-CO_2H), 8.69 (t, *J* = 5.5 Hz, 1 H, 1-Gly-NH), 8.56 (d, *J* = 8 Hz, 1 H, 3-Phe-NH), 7.29 (d, *J* = 8.5 Hz, 1 H, 2-H6), 7.51 (s, 1 H, 2-H2), 7.48 (d, *J* = 8.5 Hz, 1 H, 2-H5), 7.46 (d, *J* = 7 Hz, 2 H, 4-HAr2), 7.41 (s, 1 H, 4-H2), 7.38 (t, *J* = 7 Hz, 2 H,4-HAr3), 7.35 (d, *J* = 8 Hz, 1 H, 4-H6), 7.33 (d, *J* = 7.5 Hz, 2 H, 3-Phe-HAr2), 7.32 (s, 1H, 2-NH), 7.24 (t, *J* = 7.5 Hz, 3 H, 3-Phe-HAr3, 4-HAr4), 7.15 (t, *J* = 7.5 Hz, 1H, 3-Phe-HAr4), 6.63 (d, *J* = 8 Hz, 1 H, 4-H5), 5.37 (br, 2H, 4-NH_2), 5.11 (s, 2 H, 4-Hα), 4.86-4.82 (dd, *J* = 8, 4.5 Hz, 1 H, 3-Phe-Hα), 4.66-4.61 (apparent quin, *J* = 6 Hz, 1 H, 2-Hα), 3.87 (d, *J* = 5.5 Hz, 2 H, 1-Gly-H1), 3.12-3.07 (dd, *J* = 10.5 , 4.5 Hz, 2 H, 3-Phe-Hβ), 1.16-1.13 (dd, *J* = 8.5, 6 Hz, 6 H, 2-Hβ) ppm; ^{13}C NMR (DMSO-d_6, 126 MHz) δ: 171.3 (1-Gly-CO), 170.4 (2-CO), 166.7 (4-CO), 165.7 (3-Phe-CO), 145.7 (2-C4), 144.1 (4-C4), 141.9 (4-C3), 138.5 (2-C1), 137.1 (4-C4), 131.3 (2-C3), 129.1 (3-Phe-CAr2), 128.4 (4-CAr2, 4-CAr4), 128.1 (4-CAr3), 127.7 (4-CAr1), 127.3 (3-Phe-CAr3, 3-Phe-CAr4), 126.2 (3-Phe-CAr1), 121.8 (4-C6), 120.2 (2-C5), 118.4 (2-C6), 112.3 (4-C5, 2-C2), 111.4 (4-C2), 71.4 (2-Cα), 69.4 (4-Cα), 55.6 (3-Phe-Cα), 41.73 (1-Gly-C1), 35.5 (3-Phe-Cβ), 21.4 (2-Cβ) ppm; IR (neat) ν(cm^{-1}): 3286, 3034, 2980, 2930, 1680, 1614, 1494, 1273, 1210; ESI-MS found: 625 $(M+H)^+$; HRMS *m/z* calculated for $C_{35}H_{36}N_4NaO_7$ $(M+Na)^+$: 647.2476; Found: 647.2480.

H_2N-[*O*-Bn-(2-HABA)]-Phe-[*O*-*i*Pr-(3-HABA)]-Gly-CO_2H (105)

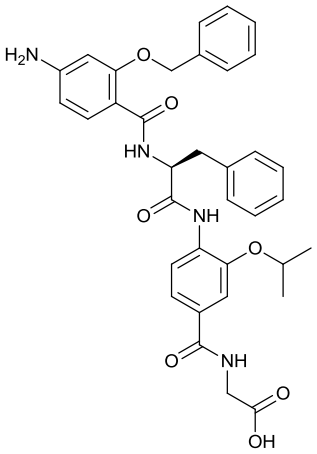

Colourless solid, > 95% pure by NMR; isolated yield: 10 mg, 16%; R_f 0.11 (SiO_2, 20% methanol in acetonitrile);); $[\alpha]_D^{26.5}$ = + 16.2° (c 0.002 g mL^{-1}, methanol); ^{1}H NMR (DMSO-d_6, 500 MHz) δ: 9.28 (s, 1H,1-Gly-CO_2H), 8.67 (t, *J* = 5.5 Hz, 1 H, 1-Gly-NH), 8.23 (d, *J* = 7.5 Hz, 1 H, 3-Phe-NH), 8.21 (d, *J* = 8.5 Hz, 1 H, 2-H6), 7.64 (d, *J* = 8.5 Hz, 1 H, 4-H6), 7.50 (s, 1 H, 2-H2), 7.46 (d, *J* = 8.5 Hz, 1 H, 2-H5), 7.44 (d, *J* = 7 Hz, 2 H, 4-HAr2), 7.41 (s, 1H, 2-NH), 7.40-7.36 (m, 3 H, 4-HAr3, 4-HAr4), 7.16 (t, *J* = 7 Hz, 2 H, 3-Phe-HAr3), 7.13 (t, *J* = 7 Hz, 1 H, 3-Phe-HAr4), 6.96 (d, *J* = 7 Hz, 2H, 3-Phe-HAr2), 6.28 (s, 1H, 4-H3), 6.18 (d, *J* = 8.5 Hz, 1 H, 4-H5), 5.81 (s, 2H, 4-NH_2), 5.19-5.12 (dd, *J* = 23, 12 Hz, 2 H, 4-Hα), 4.88-4.84 (sept, *J* = 4.5 Hz, 1 H, 3-Phe-Hα), 4.65-4.61 (apparent quin, *J* = 6 Hz, 1 H, 2-Hα), 3.87 (d, *J* = 5.5 Hz, 2 H, 1-Gly-H1), 3.15-3.12 (dd, *J* = 9.5 , 4.5 Hz, 1 H, 3-Phe-Hβ), 2.71-2.66 (dd, *J* = 9.5 , 4.5 Hz, 1 H, 3-Phe-Hβ'), 1.15-1.13 (dd, *J* = 8.5, 6 Hz, 6 H, 2-Hβ) ppm; ^{13}C NMR (DMSO-d_6, 126 MHz) δ: 170.1 (1-Gly-CO), 165.7 (2-CO), 165.1 (4-CO), 158.4 (4-C4), 153.8 (3-Phe-CO), 145.9 (2-C4), 137.4 (2-C1), 136.2 (4-C2), 132.8 (4-C6), 131.1 (2-C3), 128.8 (3-Phe-CAr2), 128.6 (4-CAr3, 4-CAr4), 128.2 (3-Phe-CAr1, 3-Phe-CAr3), 127.9 (4-CAr2), 127.3 (4-CAr1), 126.4 (3-Phe-CAr4), 120.03 (2-C5), 118.8 (2-C6), 112.3 (2-C2), 107.4 (4-C1), 106.5 (4-C5), 96.6 (4-C3), 71.3 (2-Cα), 69.8 (4-Cα), 55.2 (3-Phe-Cα), 41.5 (1-Gly-C1), 36.5 (3-Phe-Cβ), 21.4 (2-Cβ) ppm; IR (neat) ν (cm^{-1}): 3692, 3356, 2980, 2921, 1688, 1631, 1598, 1494, 1269, 1209; ESI-MS found: 625 $(M+H)^+$; HRMS *m/z* calculated for $C_{35}H_{36}N_4NaO_7$ $(M+Na)^+$: 647.2476; Found: 647.2481.

H_2N-[*N*-Bn-(ABA)]-Phe-[*O*-*i*Pr-(3-HABA)]-Gly-CO_2H (106)

Colourless solid, > 95% pure by NMR; isolated yield: 15 mg, 25%); R_f 0.12 (SiO_2, 20% methanol in acetonitrile); $[\alpha]_D^{26.5}$ = - 13.5° (c 0.003 g mL^{-1}, methanol); ^{1}H NMR (DMSO-d_6, 500 MHz) δ: 9.25 (s, 1H,1-Gly-CO_2H), 8.67 (t, *J* = 5.5 Hz, 1 H, 1-Gly-NH), 8.52 (d, *J* = 8 Hz, 1 H, 3-Phe-NH), 8.29 (d, *J* = 8.5 Hz, 1 H, 2-H6), 7.59 (s, *J* = 8.5 Hz, 2 H, 4-H2), 7.50 (s, 1 H, 2-H2), 7.46 (d, *J* = 8.5 Hz, 1 H, 2-H5), 7.34-7.30 (m, 6 H, 3-Phe-HAr2, 4-HAr2, 4-HAr3), 7.28 (s, 1H, 2-NH), 7.24 (t, *J* = 7.5 Hz, 2 H, 3-

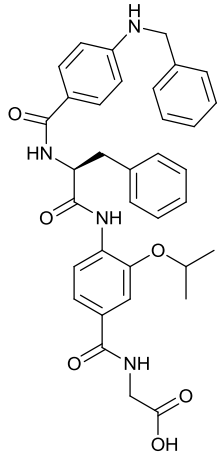

Phe-HAr3), 7.23 (t, *J* = 7.5 Hz, 1 H, 4-HAr4), 7.15 (t, *J* = 7.5 Hz, 1H, 3-Phe-HAr4), 6.86 (t, *J* = 6 Hz, 1H, 4-NH), 6.56 (d, *J* = 8.5 Hz, 2 H, 4-H3), 4.83-4.79 (sept, *J* = 7.5 Hz, 1 H, 3-Phe-Hα), 4.65-4.60 (apparent quin, *J* = 6 Hz, 1 H, 2-Hα), 4.31 (d, *J* = 6 Hz, 2 H, 4-Hα), 3.86 (d, *J* = 5.5 Hz, 2 H, 1-Gly-H1), 3.10-3.05 (dd, *J* = 11 , 3.5 Hz, 2 H, 3-Phe-Hβ), 1.13-1.07 (dd, *J* = 11.5, 6 Hz, 6 H, 2-Hβ) ppm; ^{13}C NMR (DMSO-d_6, 126 MHz) δ: 171.3 (1-Gly-CO), 170.4 (2-CO), 166.7 (4-CO), 165.7 (3-Phe-CO), 151.5 (4-C4), 145.7 (2-C4), 138.5 (2-C1), 131.3 (2-C3), 129.0 (4-CAr4), 128.9 (4-C2), 128.3 (4-CAr2, 4-CAr3), 128.1 (3-Phe-CAr1), 127.1 (3-Phe-CAr2, 3-Phe-CAr3), 126.7 (3-Phe-CAr4), 126.2 (4-CAr1), 120.1 (4-C1), 119.8 (2-C5), 118.3 (2-C6), 112.3 (2-C2), 111.1 (4-C3), 71.3 (2-Cα), 55.6 (3-Phe-Cα), 45.8 (4-Cα), 41.4 (1-Gly-C1), 35.5 (3-Phe-Cβ), 21.4 (2-Cβ) ppm; IR (neat) ν(cm^{-1}): 3328, 3030, 2977, 2928, 1685, 1632, 1601, 1494, 1267, 1208; ESI-MS found: 609 $(M+H)^+$; HRMS *m/z* calculated for $C_{35}H_{36}N_4NaO_6$ $(M+Na)^+$: 631.2527; Found: 631.2532.

H_2N-[*O*-Bn-(3-HABA)]-Phe-[*N*-*i*Bu-(ABA)]-Gly-CO_2H (107)

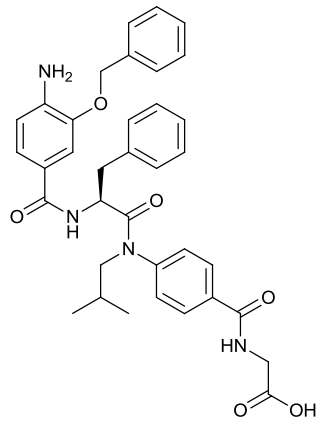

Yellow solid, > 95% pure by NMR; isolated yield: 5.7 mg, 9%; R_f 0.72 (SiO_2, 20% methanol in acetonitrile); $[\alpha]_D^{26.5}$ = + 160.1° (c 0.003 g mL^{-1}, methanol); ^{1}H NMR (DMSO-d_6, 500 MHz) δ: 9.21 (s, 1H,1-Gly-CO_2H), 8.97 (t, *J* = 5.5 Hz, 1 H, 1-Gly-NH), 8.25 (d, *J* = 7.5 Hz, 1 H, 3-Phe-NH), 7.97 (d, *J* = 8 Hz, 2 H, 2-H2), 7.51 (d, *J* = 7 Hz, 2 H, 4-HAr2), 7.48 (br, 2 H, 2-H3), 7.42 (d, *J* = 7 Hz, 2 H, 3-Phe-HAr3), 7.40 (t, *J* = 7 Hz, 1 H 3-Phe-HAr4), 7.35 (d, *J* = 8.5 Hz, 1 H, 4-H6), 7.33 (s, 1 H, 4-H2), 7.16-7.13 (m, , 3 H, 3-Phe-HAr2, 4-H-Ar4), 6.87 (t, *J* = 7 Hz, 2 H, 4-H-Ar3), 6.64 (d, *J* = 8.5 Hz, 1 H, 4-H5), 5.32 (br, 2H, 4-NH_2), 5.17 (s, 2 H, 4-Hα), 4.61-4.57 (dd, *J* = 7, 4.5 Hz, 1 H, 3-Phe-Hα), 3.98 (d, *J* = 5.5 Hz, 2 H, 1-Gly-H1), 3.75-3.71 (m, 1 H, 2-Hα), 3.42-3.38 (m, 1 H, 2-Hα'), 2.92 (d, *J* = 4.5 Hz, 2 H, 3-Phe-Hβ), 1.68-1.63 (apparent quin, *J* = 5.5 Hz, 1 H, 2-Hβ), 0.87-0.85 (dd, *J* = 7.5, 5.5 Hz, 6 H, 2-Hγ) ppm; ^{13}C NMR (DMSO-d_6, 126 MHz) δ: 171.6 (1-Gly-CO), 171.2 (4-CO), 166.2 (3-Phe-CO), 165.8 (2-CO), 144.1 (4-C1), 141.4 (4-C3),

138.0 (2-C1), 137.2 (4-C4), 128.8 (2-C2), 128.4 (3-Phe-CAr2, 3-Phe-CAr3, 3-Phe-CAr4), 128.1 (4-CAr4), 127.7 (2-C3), 127.4 (4-CAr1, 4-CAr2, 4-CAr3), 126.3 (3-Phe-CAr1), 121.8 (4-C6), 120.8 (2-C4), 112.3 (4-C5), 111.3 (4-C2), 72.8 (2-Cα), 69.4 (4-Cα), 55.6 (3-Phe-Cα), 41.2 (1-Gly-C1), 36.5 (3-Phe-Cβ), 26.3 (2-Cγ), 19.8 (2-Cβ) ppm; IR (neat) ν(cm^{-1}): 3367, 2962, 2933, 1701, 1629, 1594, 1495, 1259, 1199; ESI-MS found: 623 $(M+H)^+$; HRMS *m/z* calculated for $C_{36}H_{38}N_4NaO_6$ $(M+Na)^+$: 645.2683; Found: 645.2686.

H_2N-[*O*-Bn-(2-HABA)]-Phe-[*N*-*i*Bu-(ABA)]-Gly-CO_2H (108)

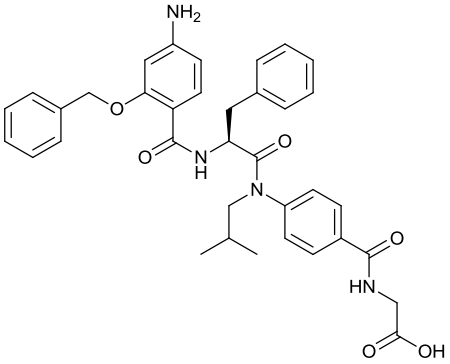

Colourless solid, > 95% pure by NMR; isolated yield: 1 mg, 2%; R_f 0.22 (SiO_2, 20% methanol in acetonitrile); $[\alpha]_D^{26.5}$ = + 57.9° (c 0.003 g mL^{-1}, methanol);^{1}H NMR (DMSO-d_6, 500 MHz) δ: 8.95 (t, *J* = 5.5 Hz, 1 H, 1-Gly-NH), 8.07 (d, *J* = 7 Hz, 1 H, 3-Phe-NH), 7.93 (d, *J* = 8.5 Hz, 2 H, 2-H2), 7.60 (d, *J* = 8.5 Hz, 1 H, 4-H6), 7.58 (d, *J* = 7 Hz, 2 H, 4-HAr2), 7.47 (t, *J* = 7 Hz, 3 H, 4-HAr3, 4-HAr4), 7.40 (d, *J* = 8.5 Hz, 1 H, 2-H3), 7.12-7.10 (m, 3 H, 3-Phe-HAr3, 3-Phe-HAr4), 6.49 (d, *J* = 7 Hz, 2H, 3-Phe-HAr2), 6.35 (s, 1H, 4-H3), 6.19 (d, *J* = 8.5 Hz, 1 H, 4-H5), 5.80 (s, 2H, 4-NH_2), 5.23-5.15 (dd, *J* = 22, 11 Hz, 2 H, 4-Hα), 4.59-4.55 (dd, *J* = 7, 4.5 Hz, 1 H, 3-Phe-Hα), 3.96 (d, *J* = 5.5 Hz, 2 H, 1-Gly-H1), 3.73-3.69 (dd, *J* = 8.5, 5 Hz, 1 H, 2-Hα), 3.32-3.30 (dd, *J* = 8.5, 5 Hz, 1 H, 2-Hα'), 2.80-2.76 (dd, *J* = 9.5, 4.5 Hz, 1 H, 3-Phe-Hβ), 2.38-2.35 (dd, *J* = 9.5, 4.5 Hz, 1 H, 3-Phe-Hβ'), 1.63-1.58 (apparent quin, *J* = 5 Hz, 1 H, 2-Hβ), 0.84-0.81 (dd, *J* = 7.5, 5 Hz, 6 H, 2-Hγ) ppm; ^{13}C NMR (DMSO-d_6, 126 MHz) δ: 171.2 (1-Gly-CO), 171.1 (4-CO), 165.7 (3-Phe-CO), 164.2 (2-CO), 158.2 (4-C4), 153.5 (4-C2), 144.3 (2-C4), 136.2 (2-C1), 132.9 (4-C6), 128.6 (4-CAr2, 4-CAr3), 128.6 (2-C2), 128.3 (2-C3), 128.2 (3-Phe-CAr2,3-Phe-CAr3, 3-Phe-CAr4), 128.2 (4-CAr4), 128.0 (4-CAr1), 126.4 (3-Phe-CAr1), 108.0 (4-C5), 106.5 (4-C1), 97.1 (4-C3), 69.9 (4-Cα), 55.6 (2-Cα), 52.0 (3-Phe-Cα), 41.2 (1-Gly-C1), 37.6 (3-Phe-Cβ), 26.3 (2-Cβ), 19.8 (2-Cγ) ppm; IR (neat) ν(cm^{-1}): 3359, 2923, 1701, 1631, 1596, 1495, 1259, 1199; ESI-MS found: 623 $(M+H)^+$; HRMS *m/z* calculated for $C_{36}H_{39}N_4O_6$ $(M+Na)^+$: 623.2864; Found: 623.2867.

H_2N-[*N*-Bn-(ABA)]-Phe-[*N*-*i*Bu-(ABA)]-Gly-CO_2H (109)

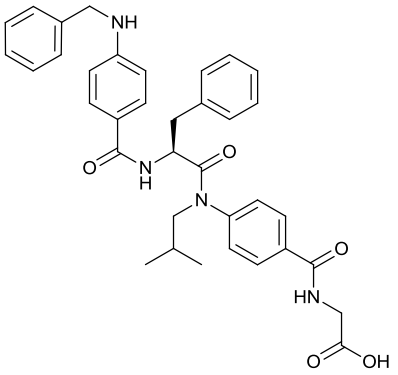

Colourless solid, > 95% pure by NMR; isolated yield: 4 mg, 7%; R_f 0.30 (SiO_2, 20% methanol in acetonitrile); $[\alpha]_D^{26.6}$ = + 113.1° (c 0.002 g mL^{-1}, methanol); ^{1}H NMR (DMSO-d_6, 500 MHz) δ: 8.97 (t, *J* = 5.5 Hz, 1 H, 1-Gly-NH), 8.17 (d, *J* = 7 Hz, 1 H, 3-Phe-NH), 7.97 (d, *J* = 8.5 Hz, 2 H, 2-H2), 7.60 (d, *J* = 8.5 Hz, 2 H, 4-H2), 7.48 (br, 2 H, 2-H3), 7.36-7.31 (m, 5 H, 3-Phe-HAr2, 3-Phe-HAr3, 4-NH), 7.24 (t, *J* = 7 Hz, 1 H 3-Phe-HAr4), 7.13 -7.11 (m, 3 H, 4-HAr3, 4-HAr4), 6.83 (d, *J* = 7.5 Hz, 2 H, 4-HAr2), 6.56 (d, *J* = 8.5 Hz, 1 H, 4-H3), 4.56-4.52 (dd, *J* = 7, 4.5 Hz, 1 H, 3-Phe-Hα), 4.33 (s, 2 H, 4-Hα), 3.97 (d, *J* = 5.5 Hz, 2 H, 1-Gly-H1), 3.74-3.69 (dd, *J* = 8.5, 5 Hz, 1 H, 2-Hα), 3.38-3.36 (dd, *J* = 8.5, 5 Hz, 1 H, 2-Hα'), 2.88 (d, *J* = 4.5 Hz, 2 H, 3-Phe-Hβ), 1.66-1.61 (apparent quin, *J* = 5 Hz, 1 H, 2-Hβ), 0.85-0.83 (dd, *J* = 7.5, 5 Hz, 6 H, 2-Hγ) ppm; ^{13}C NMR (DMSO-d_6, 126 MHz) δ: 171.6 (1-Gly-CO), 171.2 (4-CO), 166.2 (3-Phe-CO), 165.8 (2-CO), 151.2 (4-C4), 139.6 (2-C4), 138.1 (2-C1), 129.0 (4-CAr4), 128.8 (2-C2), 128.4 (4-C2), 128.3 (3-Phe-CAr2, 3-Phe-CAr3, 3-Phe-CAr4), 128.1 (3-Phe-CAr1), 127.1 (4-CAr2, 4-CAr3), 126.7 (2-C3), 126.3 (4-CAr1), 120.5 (4-C1), 111.0 (4-C3), 72.6 (2-Cα), 55.6 (3-Phe-Cα), 45.9 (4-Cα), 41.2 (1-Gly-C1), 37.3 (3-Phe-Cβ), 26.3 (2-Cγ), 19.8 (2-Cβ) ppm; IR (neat) ν(cm^{-1}): 3359, 3243, 2960, 2931, 1701, 1630, 1595, 1495, 1260, 1199; ESI-MS found: 607 $(M+H)^+$; HRMS *m/z* calculated for $C_{36}H_{38}N_4NaO_5$ $(M+Na)^+$: 629.2734; Found: 629.2741.

H_2N-[*O*-*i*Bu-(2-HABA)]-Leu-[*O*-*i*Pr-(2-HABA)]-Gly-CO_2H (110)

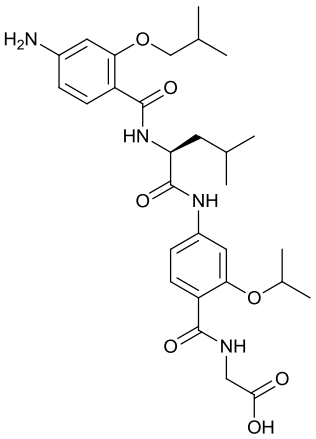

Pale yellow solid, > 95% pure by NMR; isolated yield: 7.5 mg, 14%; R_f 0.24 (SiO_2, 20% methanol in acetonitrile); ^{1}H NMR (DMSO-d_6, 500 MHz) δ: 10.48 (s, 1H,1-Gly-CO_2H), 8.47 (t, *J* = 5 Hz, 1 H, 1-Gly-NH), 8.12 (d, *J* = 8 Hz, 1 H, 3-Leu-NH), 7.90 (d, *J* = 8 Hz, 1 H, 2-H3), 7.67 (d, *J* = 8.5 Hz, 1 H, 4-H6), 7.64 (s, 1 H, 2-H3), 7.26 (d, *J* = 8 Hz, 1 H, 2-H5), 6.27 (s, 1 H, 4-H3), 6.21 (d, *J* = 8.5 Hz, 1 H, 4-H5), 5.79 (br, 2H, 4-NH_2), 4.80 - 4.75 (apparent quin, *J* = 7 Hz, 1 H, 3-Leu-Hα), 4.73-4.69 (apparent quin, *J* = 6 Hz, 1 H, 2-Hα), 4.03 (d, *J* = 5 Hz, 2 H, 1-Gly-H1), 3.86 (d, *J* = 6 Hz, 2 H, 4-Hα), 2.19-2.14 (m, *J* = 6 Hz, 1 H, 4-Hβ), 1.72-1.66 (m, *J* = 6 Hz, 1 H, 3-Leu-Hγ), 1.62-1.61 (dd, *J* = 12.8, 7 Hz, 2 H, 3-Leu-Hβ), 1.43-1.41 (dd, *J* = 6, 9.5 Hz, 6 H, 2-Hβ), 1.08 (d, *J* = 6 Hz, 6 H, 4-Hγ), 0.96-0.94 (dd, *J* = 6, 4 Hz, 6 H, 3-Leu-Hδ) ppm; ^{13}C NMR (DMSO-d_6, 126 MHz) δ: 171.0 (1-Gly-CO), 171.2 (3-Leu-CO), 164.5 (4-CO), 163.9 (2-CO), 158.7 (4-C2), 156.2 (4-C1), 153.6 (4-C4), 143.0 (2-C4), 132.8 (4-C6), 131.9 (2-C6), 116.6 (2-C1), 111.3 (2-C5), 107.8 (4-C5), 106.2 (2-C3), 104.7 (2-C2), 96.6 (4-C3), 74.6 (4-Cα), 71.9 (2-Cα), 51.9 (3-Leu-Cα), 41.8 (1-Gly-C1), 41.6 (3-Leu-Cβ), 27.8 (4-Cβ), 24.5 (3-Leu-Cγ), 22.9 (3-Leu-Cδ), 21.7 (2-Cβ), 19.1 (4-Cγ) ppm; IR (neat) ν(cm^{-1}): 3355, 3087, 2957, 2932, 1691, 1627, 1593, 1494, 1258, 1199; ESI-MS found: 557 $(M+H)^+$; HRMS *m/z* calculated for $C_{29}H_{40}N_4NaO_7$ $(M+Na)^+$: 579.2789; Found: 579.2798.

H_2N-[*O*-*i*Bu-(2-HABA)]-Phe-[*O*-*i*Pr-(2-HABA)]-Gly-CO_2H (111)

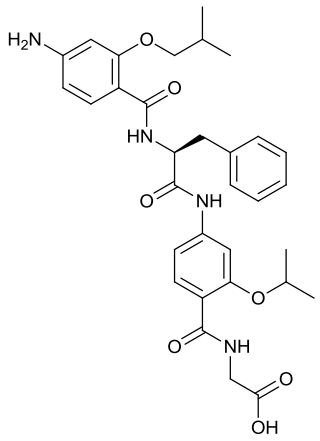

Pale yellow solid, > 90% pure by NMR; isolated yield: 10 mg, 17%; R_f 0.54 (SiO_2, 20% methanol in acetonitrile); ^{1}H NMR (DMSO-d_6, 500 MHz) δ: 10.43 (s, 1H,1-Gly-CO_2H), 8.65 (t, *J* = 5 Hz, 1 H, 1-Gly-NH), 8.39 (br, 1H, 2-NH), 8.23 (d, *J* = 8 Hz, 1 H, 3-Phe-NH), 7.89 (d, *J* = 8.5 Hz, 1 H, 2-H6), 7.64 (d, *J* = 8.5 Hz, 1 H, 4-H6), 7.54 (s, 1 H, 2-H3), 7.24 (d, *J* = 7.5 Hz, 2 H, 3-Phe-HAr2), 7.19 (m, *J* = 7.5 Hz, 3 H, 3-Phe-HAr3, 3-Phe-HAr4), 7.14 (d, *J* = 8.5 Hz, 1 H, 2-H5), 6.22 (s, 1 H, 4-H3), 6.18 (d, *J* = 8.5 Hz, 1 H, 4-H5), 5.76 (br, 2H, 4-

NH_2), 5.03-4.98 (m, *J* = 6.5 Hz, 1 H, 3-Phe-Hα), 4.68-4.63 (apparent quin, *J* = 6 Hz, 1 H, 2-Hα), 3.77 (d, *J* = 5 Hz, 2 H, 1-Gly-H1), 3.60 (d, *J* = 6.5 Hz, 2 H, 4-Hα), 3.16-3.14 (dd, *J* = 14, 6.5 Hz, 1 H, 3-Phe-Hβ), 2.99-2.96 (dd, *J* = 14, 6.5 Hz, 1 H, 3-Phe-Hβ'), 2.08-2.03 (m, *J* = 6.5 Hz, 1 H, 4-Hβ), 1.41-1.38 (dd, *J* = 8.5, 6 Hz, 6 H, 2-Hβ), 0.96-0.94 (dd, *J* = 6.5, 16.5 Hz, 6 H, 4-Hγ) ppm; ^{13}C NMR (DMSO-d_6, 126 MHz) δ: 170.5 (1-Gly-CO), 167.8 (3-Phe-CO), 164.3 (2-CO), 158.7 (4-CO), 156.1 (4-C2), 153.6 (4-C1), 153.1 (4-C4), 136.4 (2-C4), 132.8 (4-C6), 131.9 (2-C6), 131.0 (3-Phe-CAr1), 129.0 (3-Phe-CAr2), 128.2 (3-Phe-CAr3), 126.4 (3-Phe-CAr4), 117.7 (2-C1), 115.1 (2-C5), 111.2 (4-C5), 110.5 (2-C3), 106.2 (4-C3), 74.7 (4-Cα), 71.5 (2-Cα), 54.5 (3-Phe-Cα), 40.0 (1-Gly-C1), 38.4 (3-Phe-Cβ), 27.5 (4-Cβ), 21.5 (2-Cβ), 19.1 (4-Cγ) ppm; IR (neat) ν (cm^{-1}): 3255, 3142, 2923, 2806, 1677, 1618, 1584, 1496, 1270, 1200; ESI-MS found: 591 $(M+H)^+$; HRMS *m/z* calculated for $C_{32}H_{38}N_4NaO_7$ $(M+Na)^+$: 613.2633; Found: 613.2635.

H_2N-[*O*-*i*Bu-(2-HABA)]-Leu-[*O*-*i*Pr-(2-HABA)]-Leu-CO_2H (112)

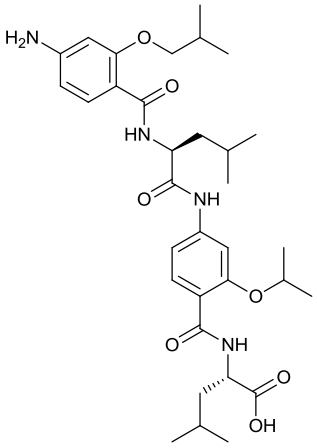

Pale yellow solid, > 90% pure by NMR; isolated yield: 5.2 mg, 9%; R_f 0.16 (SiO_2, 20% methanol in acetonitrile); ^{1}H NMR (DMSO-d_6, 500 MHz) δ: 10.48 (s, 1H,1-Leu-CO_2H), 8.41 (d, *J* = 8 Hz, 2 H, 1-Leu-NH, 2-NH), 8.13 (d, *J* = 8 Hz, 1 H, 3-Leu-NH), 7.87 (d, *J* = 8.5 Hz, 1 H, 2-H6), 7.67 (d, *J* = 8.5 Hz, 1 H, 4-H6), 7.63 (s, 1 H, 2-H3), 7.26 (d, *J* = 8.5 Hz, 1 H, 2-H5), 6.27 (s, 1 H, 4-H3), 6.21 (d, *J* = 8.5 Hz, 1 H, 4-H5), 4.80 - 4.75 (m, *J* = 6.5 Hz, 1 H, 3-Leu-Hα), 4.75-4.70 (apparent quin, *J* = 6 Hz, 1 H, 2- Hα), 4.51 (apparent quin, *J* = 5 Hz, 2 H, 1-Leu- Hα), 3.85 (d, *J* = 6 Hz, 2 H, 4-Hα), 2.19-2.14, (m, *J* = 6 Hz, 1 H, 4-Hβ), 1.72-1.59 (m, 6 H, 1-Leu-Hγ, 1-Leu-Hβ, 3-Leu-Hγ, 3-Leu-Hβ), 1.41-1.39 (dd, *J* = 12.5, 6 Hz, 6 H, 2-Hβ), 1.08 (d, *J* = 6 Hz, 6 H, 4-Hγ), 0.96-0.91 (m, 12 H, 1-Leu-Hδ, 3-Leu-Hδ) ppm; ^{13}C NMR (DMSO-d_6, 126 MHz) δ: 173.9 (1-Leu-CO), 172.0 (3-Leu-CO), 164.5 (4-CO), 163.7 (2-CO), 158.7 (2-C2), 156.0 (4-C4), 153.6 (2-C4), 143.0 (4-C2), 132.8 (4-C6), 131.9 (2-C6), 116.7 (2-C1), 111.3 (2-C5), 107.8 (4-C1), 106.2 (4-C5), 104.5 (2-C3), 96.6 (4-C3), 74.6 (4-Cα), 71.7 (2-Cα), 51.9 (1-Leu-Cα, 3-Leu-

Cα), 41.9 (1-Leu-C1), 40.9 (3-Leu-Cβ), 28.8 (4-Cβ), 27.8 (3-Leu-Cγ), 24.5 (1-Leu-Cδ), 22.9 (1-Leu-Cγ), 22.7 (3-Leu-Cδ), 21.8 (2-Cβ), 19.1 (4-Cγ) ppm; IR (neat) ν(cm^{-1}): 3357, 2978, 2928, 1691, 1628, 1593, 1493, 1258, 1213; ESI-MS found: 613 $(M+H)^+$; HRMS *m/z* calculated for $C_{33}H_{49}N_4O_7$ $(M+H)^+$: 613.3596; Found: 613.3604.

H_2N-[*O*-Bn-(3-HABA)]-Trp-[*O*-*i*Pr-(2-HABA)]-Gly-CO_2H (113)

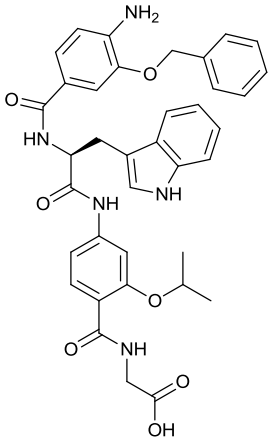

Yellow solid, > 90% pure by NMR; isolated yield: 9.8 mg, 15%; R_f 0.53 (SiO_2, 20% methanol in acetonitrile); $[\alpha]_D^{26.6}$ = + 91.1° (c 0.006 g mL^{-1}, methanol);^{1}H NMR (DMSO-d_6, 500 MHz) δ: 10.83 (s, 1 H, 3-Trp-NH1), 10.46 (s, 1H,1-Gly-CO_2H), 8.51 (t, *J* = 5 Hz, 1 H, 1-Gly-NH), 8.26 (d, *J* = 7.5 Hz, 1 H, 3-Trp-NH), 7.90 (d, *J* = 8.5 Hz, 1 H, 2-H6), 7.75 (d, *J* = 7.5 Hz, 1 H, 3-Trp-HAr4), 7.65 (s, 1 H, 2-H3), 7.51 (d, *J* = 7.5 Hz, 2 H, 4-HAr2), 7.45 (s, 1 H, 4-H2), 7.41 (t, *J* = 7.5 Hz, 3 H, 4-HAr3, 4-HAr4), 7.33-7.31 (m, 3 H, 4-H6, 3-Trp-HAr7, 2-NH), 7.28 (s, 1 H, 3-TrpHAr2), 7.27 (d, *J* = 8.5 Hz, 1 H, 2-H5), 7.07 (t, *J* = 7.5 Hz, 1H, 3-Trp-HAr6), 6.99 (t, *J* = 7.5 Hz, 1H, 3-Trp-HAr5), 6.64 (d, *J* = 8Hz, 1 H, 4-H5), 5.33 (br, 2H, 4-NH_2), 5.17-5.13 (dd, *J* = 12, 4 Hz, 2 H, 4-Hα), 4.89-4.85 (dd, *J* = 9 , 5 Hz, 1 H, 3-Trp-Hα), 4.74-4.69 (apparent quin, *J* = 6 Hz, 1 H, 2-Hα), 4.00 (d, *J* = 5 Hz, 2 H, 1-Gly-H1), 3.27-3.24 (dd, *J* = 11 , 5 Hz, 2 H, 3-Trp-Hβ), 1.43-1.41 (dd, *J* = 9.5, 6 Hz, 6 H, 2-Hβ) ppm; ^{13}C NMR (DMSO-d_6, 126 MHz) δ: 171.2 (1-Gly-CO), 166.3 (4-CO), 163.8 (2-CO), 156.2 (3-Trp-CO), 144.1 (4-C1), 143.1 (2-C2), 141.5 (4-C4), 138.2 (2-C4), 137.2 (4-C3, 3-Trp-CAr7a), 136.0 (3-Trp-CAr3a), 131.9 (2-C6), 128.4 (4-CAr3, 4-CAr4), 127.7 (4-CAr1), 127.5 (4-CAr2, 3-Trp-CAr3), 124.5 (3-Trp-CAr2), 123.7 (4-C6), 121.8 (3-Trp-CAr7), 120.8 (3-Trp-CAr5), 118.6 (3-Trp-CAr4), 118.2 (3-Trp-CAr6), 115.1 (2-C1), 112.3 (4-C5), 111.4 (4-C2), 110.2 (2-C5), 104.8 (2-C3), 71.9 (2-Cα), 69.4 (4-Cα), 55.1 (3-Trp-Cα), 41.0 (1-Gly-C1), 27.5 (3-Trp-Cβ), 21.6 (2-Cβ) ppm; IR (neat) ν(cm^{-1}): 3259, 3143, 2921, 2810, 1686, 1617, 1591, 1494, 1298, 1209; ESI-MS found: 664 $(M+H)^+$; HRMS *m/z* calculated for $C_{37}H_{37}N_5NaO_7$ $(M+Na)^+$: 686.2585; Found: 686.2599.

H_2N-[*O*-Bn-(2-HABA)]-Trp-[*O*-*i*Pr-(2-HABA)]-Gly-CO_2H (114)

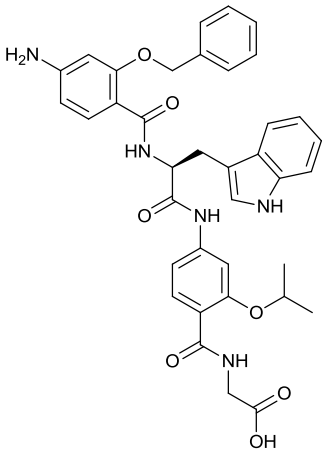

Pale brown solid, > 90% pure by NMR; isolated yield: 10.6 mg, 16%); R_f 0.083 (SiO_2, 20% methanol in acetonitrile); $[\alpha]_D^{27.6}$ = + 50.5° (c 0.008 g mL^{-1}, methanol); ^{1}H NMR (DMSO-d_6, 500 MHz) δ: 10.78 (s, 1 H, 3-Trp-NH1), 10.47 (s, 1H,1-Gly-CO_2H), 8.49 (t, *J* = 5 Hz, 1 H, 1-Gly-NH), 8.19 (d, *J* = 6.5 Hz, 1 H, 3-Trp-NH), 7.90 (d, *J* = 8.5 Hz, 1 H, 2-H6), 7.63 (d, *J* = 8.5 Hz, 1 H, 4-H6), 7.63 (s, 1 H, 2-H3), 7.55 (d, *J* = 8 Hz, 1 H, 3-Trp-HAr4), 7.45 (d, *J* = 7.5 Hz, 2 H, 4-HAr2), 7.36 (t, *J* = 7.5 Hz, 3 H, 4-H-Ar3, 4-HAr4), 7.28 (d, *J* = 8 Hz, 1 H, 3-Trp-HAr7), 7.27 (s, 1 H, 3-TrpHAr2), 7.22 (d, *J* = 8.5 Hz, 1 H, 2-H5), 7.05 (t, *J* = 7.5 Hz, 1H, 3-Trp-HAr6), 6.94 (t, *J* = 7.5 Hz, 1H, 3-Trp-HAr5), 6.72 (s, 1H, 2-NH), 6.32 (s, 1 H, 4H1), 6.19 (d, *J* = 8Hz, 1 H, 4-H2), 5.78 (br, 2H, 4-NH_2), 5.17-5.08 (dd, *J* = 32.5, 11.5 Hz, 2 H, 4-Hα), 4.92-4.88 (dd, *J* = 11.5 , 6.5 Hz, 1 H, 3-Trp-Hα), 4.73-4.68 (apparent quin, *J* = 6.5 Hz, 1 H, 2-Hα), 4.05 (d, *J* = 5 Hz, 2 H, 1-Gly-H1), 3.19-3.15 (dd, *J* = 11.5 , 6.5 Hz, 2 H, 3-Trp-Hβ), 2.99-2.88 (dd, *J* = 11.5 , 6.5 Hz, 2 H, 3-Trp-Hβ'),1.43-1.40 (dd, *J* = 9.5, 6.5 Hz, 6 H, 2-Hβ) ppm; ^{13}C NMR (DMSO-d_6, 126 MHz) δ: 171.2 (1-Gly-CO), 166.6 (4-CO), 163.9 (2-CO), 158.2 (3-Trp-CO), 156.2 (4-C2), 153.5 (4-C4), 143.1 (2-C2), 136.2 (2-C4), 137.1 (3-Trp-CAr3a), 132.7 (4-C6), 131.8 (2-C6), 128.5 (4-CAr2, 3-Trp-CAr3), 128.1 (4-CAr1), 128.0 (4-CAr3, 4-CAr4), 127.1 (3-Trp-CAr2), 123.3 (3-Trp-CAr7), 120.9 (3-Trp-CAr6), 118.5 (3-Trp-CAr4), 118.2 (3-Trp-CAr5), 116.5 (3-Trp-CAr7a), 111.3 (2-C5), 109.4 (2-C1), 108.2 (4-C1), 106.5 (4-C5), 104.8 (2-C3), 97.2 (4-C3), 71.9 (2-Cα), 69.8 (4-Cα), 54.5 (3-Trp-Cα), 41.6 (1-Gly-C1), 28.0 (3-Trp-Cβ), 21.6 (2-Cβ) ppm; IR (neat) ν (cm^{-1}): 3358, 3064, 2980, 2928, 1692, 1628, 1593, 1494, 1258, 1213; ESI-MS found: 664 $(M+H)^+$; HRMS *m/z* calculated for $C_{37}H_{37}N_5NaO_7$ $(M+Na)^+$: 686.2585; Found: 686.2592.

H_2N-[*O*- *i*Bu-(2-HABA)]-Trp-[*O*-*i*Pr-(2-HABA)]-Gly-CO_2H (115)

Yellow solid, > 90% pure by NMR; isolated yield: 9.3 mg, 15%; R_f 0.59 (SiO_2, 20% methanol in acetonitrile); ^{1}H NMR (DMSO-d_6, 500 MHz) δ: 10.83 (s, 1 H, 3-Trp-NH1), 10.45 (s, 1H,1-Gly-CO_2H), 8.48 (t, *J* = 4 Hz, 1 H, 1-Gly-NH), 8.30 (d, *J* = 7.5

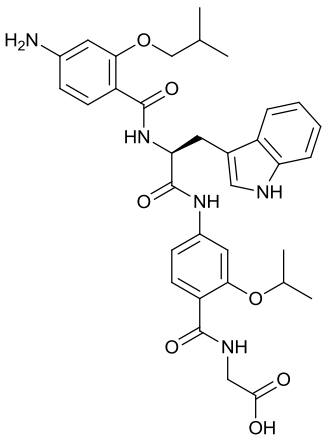

Hz, 1 H, 3-Trp-NH), 7.88 (d, *J* = 8.5 Hz, 1 H, 2-H6), 7.68 (d, *J* = 8.5 Hz, 1 H, 4-H6), 7.60 (d, *J* = 7 Hz, 1 H, 3-Trp-HAr4), 7.53 (s, 1 H, 2-H3), 7.31 (d, *J* = 7 Hz, 1 H, 3-Trp-HAr7), 7.19 (d, *J* = 8.5 Hz, 1 H, 2-H5), 7.10 (s, 1 H, 3-TrpHAr8), 7.05 (t, *J* = 7.5 Hz, 1H, 3-Trp-HAr6), 6.95 (t, *J* = 7.5 Hz, 1H, 3-Trp-HAr5), 6.59 (s, 1H, 2-NH), 6.22 (d, *J* = 8Hz, 1 H, 4-H5), 6.20 (s, 1 H, 4-H3), 5.75 (br, 2H, 4-NH_2), 5.07-5.03 (dd, *J* = 13.5 , 6.5 Hz, 1 H, 3-Trp-Hα), 4.70-4.65 (apparent quin, *J* = 5.5 Hz, 1 H, 2-Hα), 4.02 (d, *J* = 4 Hz, 2 H, 1-Gly-H1), 3.73-3.70 (apparent quin, *J* = 6 Hz, 2 H, 4-Hα), 3.31-3.28 (dd, *J* = 14.5 , 7 Hz, 2 H, 3-Trp-Hβ), 1.94-1.90 (dd, *J* = 13.5 , 6.5 Hz, 1 H, 4-Hβ),1.42-1.39 (dd, *J* = 9.5, 5.5 Hz, 6 H, 2-Hβ), 0.94-0.88 (dd, *J* = 13.5 , 6.5 Hz, 6 H, 4-Hγ), ppm; ^{13}C NMR (DMSO-d_6, 126 MHz) δ: 171.2 (1-Gly-CO), 164.4 (3-Trp-CO), 163.9 (2-CO), 158.27 (4-CO), 156.2 (2-C4), 153.6 (4-C4), 142.9 (2-C2), 136.1 (4-C2), 132.7 (4-C6), 131.8 (2-C6), 129.2 (3-Trp-CAr3a), 127.4 (3-Trp-CAr7), 123.2 (3-Trp-CAr3), 120.9 (3-Trp-CAr6), 118.4 (3-Trp-CAr2), 118.2 (3-Trp-CAr4), 116.6 (3-Trp-CAr7a), 115.0 (3-Trp-CAr5), 111.4 (2-C5), 109.3 (2-C1), 108.0 (4-C5), 106.2 (4-C1), 104.8 (2-C3), 96.7 (4-C3), 74.6 (4-Cα), 71.8 (2-Cα), 54.1 (3-Trp-Cα), 41.7 (1-Gly-C1), 28.5 (3-Trp-Cβ), 27.4 (4-Cβ), 21.6 (2-Cβ), 19.1 (2-Cγ) ppm; IR (neat) ν (cm^{-1}): 3357, 3134, 2967, 2933, 1689, 1619, 1587, 1494, 1258, 1199; ESI-MS found: 630 $(M+H)^+$; HRMS *m/z* calculated for $C_{34}H_{39}N_5NaO_7$ $(M+Na)^+$: 652.2742; Found: 652.2747.

H_2N-[*O*-Bn-(3-HABA)]-4-F-Phe-[*O*-*i*Pr-(2-HABA)]-Gly-CO_2H (116)

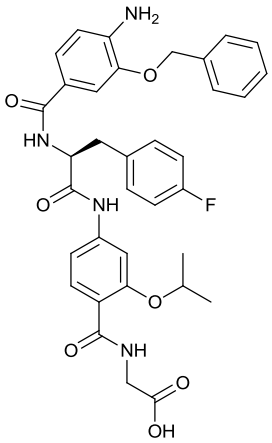

Colourless solid, > 95% pure by NMR; isolated yield: 12.5 mg, 19%; R_f 0.10 (SiO_2, 20% methanol in acetonitrile); $[\alpha]_D^{27.1}$ = + 140.6° (c 0.005 g mL^{-1}, methanol); ^{1}H NMR DMSO-d_6, 500 MHz) δ: 10.44 (s, 1H,1-Gly-CO_2H), 8.47 (t, *J* = 5 Hz, 1 H, 1-Gly-NH), 8.34 (d, *J* = 8 Hz, 1 H, 3-Phe-NH), 7.90 (d, *J* = 9 Hz, 1 H, 2-H6), 7.62 (s, 1 H, 2-H3), 7.51 (d, *J* = 7 Hz, 2 H, 4-HAr2), 7.44 (s, 1 H, 4-H2), 7.43-7.39 (m, 5 H, 3-Phe-HAr2, 4-HAr3, 4-HAr4), 7.35 (s, 1H, 2-NH), 7.33 (d, *J* = 8.5 Hz, 1 H, 4-H5), 7.25 (d, *J* = 9 Hz, 1 H, 2-H5), 7.10 (t, *J* = 9 Hz, 2H, 3-Phe-HAr3),

6.66 (d, *J* = 9 Hz, 1 H, 4-H5), 5.34 (br, 2H, 4-NH_2), 5.16 (s, 2 H, 4-Hα), 4.81-4.76 (dd, *J* = 9.5 , 5 Hz, 1 H, 3-Phe-Hα), 4.74-4.70 (apparent quin, *J* = 6 Hz, 1 H, 2-Hα), 4.06 (d, *J* = 5 Hz, 2 H, 1-Gly-H1), 3.14-3.07 (dd, *J* = 9.5, 5 Hz, 2 H, 3-Phe-Hβ), 1.43-1.41 (dd, *J* = 12, 6 Hz, 6 H, 2-Hβ) ppm; ^{13}C NMR (DMSO-d_6, 126 MHz) δ: 171.2 (1-Gly-CO), 166.4 (4-CO), 163.9 (2-CO), 161.9-160.0 (d, *J* = 242 Hz, 3-Phe-CAr4), 156.2 (3-Phe-CO), 144.1 (4-C3), 143.0 (2-C2), 141.6 (4-C4), 137.2 (2-C4), 134.3 (3-Phe-CAr1), 131.9 (2-C6), 131.0 (4-CAr1), 128.3 (4-CAr3, 4-CAr4), 127.7 (4-C2), 127.4 (3-Phe-CAr2, 4-CAr2), 121.7 (4-C6), 120.8 (4-C1), 116.6 (2-C1), 114.8-114.7 (d, *J* = 20 Hz, 3-Phe-CAr3), 112.3 (4-C5), 111.3 (2-C5), 104.7 (2-C3), 71.9 (2-Cα), 69.4 (4-Cα), 55.9 (3-Phe-Cα), 41.6 (1-Gly-C1), 36.2 (3-Phe-Cβ), 21.6 (2-Cβ) ppm; IR (neat) ν (cm^{-1}): 3358, 2975, 2931, 1690, 1596, 1496, 1260, 1216, 754; ESI-MS found: 643 $(M+H)^+$; HRMS *m/z* calculated for $C_{35}H_{35}FN_4NaO_7$ $(M+Na)^+$: 665.2382; Found: 665.2386.

H_2N-[*O*-Bn-(3-HABA)]-4-Br-Phe-[*O*-*i*Pr-(2-HABA)]-Gly-CO_2H (117)

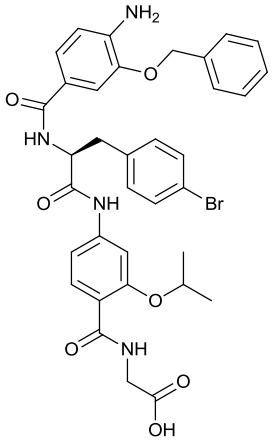

Colourless solid, > 95% pure by NMR; isolated yield: 3.7 mg, 5%; R_f 0.14 (SiO_2, 20% methanol in acetonitrile); $[\alpha]_D^{27.0}$ = + 243.6° (c 0.003 g mL^{-1}, methanol); ^{1}H NMR DMSO-d_6, 500 MHz) δ: 10.45 (s, 1H,1-Gly-CO_2H), 8.47 (t, *J* = 5 Hz, 1 H, 1-Gly-NH), 8.35 (d, *J* = 8 Hz, 1 H, 3-Phe-NH), 7.91 (d, *J* = 8.5 Hz, 1 H, 2-H6), 7.61 (s, 1 H, 2-H3), 7.51 (d, *J* = 8.5 Hz, 2 H, 4-HAr2), 7.47 (d, *J* = 8.5 Hz, 2 H, 4-HAr3), 7.42 (s, 1 H, 4-H2), 7.41 (d, *J* = 8.5 Hz, 2 H, 3-Phe-HAr2), 7.39 (s, 1H, 2-NH), 7.36 (t, *J* = 8.5 Hz, 3H, 3-Phe-HAr3, 4-HAr4), 7.32 (d, *J* = 8.5 Hz, 1 H, 4-H6), 7.25 (d, *J* = 8.5 Hz, 1 H, 2-H5), 6.64 (d, *J* = 8.5 Hz, 1 H, 4-H5), 5.35 (br, 2H, 4-NH_2), 5.16 (s, 2 H, 4-Hα), 4.82-4.79 (dd, *J* = 9.5 , 5 Hz, 1 H, 3-Phe-Hα), 4.72-4.71 (apparent quin, *J* = 6 Hz, 1 H, 2-Hα), 4.05 (d, *J* = 5 Hz, 2 H, 1-Gly-H1), 3.10-3.07 (dd, *J* = 9.5 , 5 Hz, 2 H, 3-Phe-Hβ), 1.43-1.41 (dd, *J* = 12, 6 Hz, 6 H, 2-Hβ) ppm; ^{13}C NMR (DMSO-d_6, 126 MHz) δ: 171.2 (1-Gly-CO), 166.4 (4-CO), 163.9 (2-CO), 156.2 (3-Phe-CO), 144.0 (4-C3), 143.0 (2-C2), 141.6 (4-C4), 137.7 (3-Phe-CAr1),137.2 (2-C4), 131.9 (2-C6), 131.4 (3-Phe-CAr2), 131.0 (4-CAr1, 4-CAr4), 128.3 (4-CAr3), 127.7 (4-C2), 127.4 (3-Phe-CAr3, 4-CAr2), 121.7 (4-C6), 120.8 (4-C1), 119.5 (3-Phe-

CAr4),116.6 (2-C1), 112.3 (4-C5), 111.3 (2-C5), 104.7 (2-C3), 71.9 (2-Cα), 69.4 (4-Cα), 55.6 (3-Phe-Cα), 41.6 (1-Gly-C1), 36.4 (3-Phe-Cβ), 21.6 (2-Cβ) ppm; ESI-MS found: 705 $(M+H)^+$; IR (neat) ν (cm^{-1}): 3355, 2919, 2850, 1677, 1596, 1494, 1260, 1215, 754; HRMS *m/z* calculated for $C_{35}H_{35}BrN_4NaO_7$ $(M+Na)^+$: 725.1581; Found: 725.1585.

H_2N-[*O*-Bn-(3-HABA)]-4-Cl-Phe-[*O*-*i*Pr-(2-HABA)]-Gly-CO_2H (118)

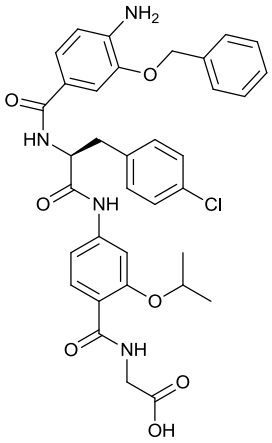

Colourless solid, > 95% pure by NMR; isolated yield: 20.1 mg, 30%; R_f 0.16 (SiO_2, 20% methanol in acetonitrile); $[\alpha]_D^{26.9}$ = + 239.7° (c 0.005 g mL^{-1}, methanol); ^{1}H NMR DMSO-d_6, 500 MHz) δ: 10.45 (s, 1H,1-Gly-CO_2H), 8.48 (t, *J* = 5 Hz, 1 H, 1-Gly-NH), 8.35 (d, *J* = 8 Hz, 1 H, 3-Phe-NH), 7.91 (d, *J* = 8.5 Hz, 1 H, 2-H6), 7.61 (s, 1 H, 2-H3), 7.51 (d, *J* = 8.5 Hz, 2 H, 4-HAr2), 7.43 (s, 1 H, 4-H2), 7.42-7.39 (m, 4 H, 3-Phe-HAr2, 4-HAr3), 7.36-7.34 (m, 3H, 4-HAr4, 3-Phe-HAr2,), 7.33 (d, *J* = 8.5 Hz, 1 H, 4-H6), 7.32 (s, 1H, 2-NH), 7.25 (d, *J* = 8.5 Hz, 1 H, 2-H5), 6.65 (d, *J* = 8.5 Hz, 1 H, 4-H5), 5.35 (br, 2H, 4-NH_2), 5.16 (s, 2 H, 4-Hα), 4.83-4.78 (dd, *J* = 9.5 , 5 Hz, 1 H, 3-Phe-Hα), 4.74-4.70 (apparent quin, *J* = 6 Hz, 1 H, 2-Hα), 4.05 (d, *J* = 5 Hz, 2 H, 1-Gly-H1), 3.15-3.07 (dd, *J* = 9.5 , 5 Hz, 2 H, 3-Phe-Hβ), 1.43-1.41 (dd, *J* = 12, 6 Hz, 6 H, 2-Hβ) ppm; ^{13}C NMR (DMSO-d_6, 126 MHz) δ: 171.2 (1-Gly-CO), 166.4 (4-CO), 163.9 (2-CO), 156.2 (3-Phe-CO), 144.1 (4-C3), 143.0 (2-C2), 141.6 (4-C4), 137.2 (2-C4), 131.9 (2-C6), 131.1 (3-Phe-CAr1, 3-Phe-CAr3), 131.0 (3-Phe-CAr4), 128.3 (4-CAr1, 4-CAr3), 128.0 (4-C2), 127.7 (4-CAr4), 127.4 (3-Phe-CAr2, 4-CAr2), 121.7 (4-C6), 120.7 (4-C1), 116.6 (2-C1), 112.3 (4-C5), 111.3 (2-C5), 104.7 (2-C3), 71.9 (2-Cα), 69.4 (4-Cα), 55.6 (3-Phe-Cα), 41.6 (1-Gly-C1), 36.4 (3-Phe-Cβ), 21.6 (2-Cβ) ppm; IR (neat) ν (cm^{-1}): 3358, 3034, 2979, 2931, 1726, 1688, 1594, 1493, 1260, 1214, 754; ESI-MS found: 659 $(M+H)^+$; HRMS *m/z* calculated for $C_{35}H_{35}ClN_4NaO_7$ $(M+Na)^+$: 681.2086; Found: 681.2092.

H_2N-[*O*-Bn-(3-HABA)]-Tyr-[*O*-*i*Pr-(2-HABA)]-Gly-CO_2H (119)

Colourless solid, > 95% pure by NMR; isolated yield: 12.6 mg, 20%; R_f 0.092 (SiO_2, 20% methanol in acetonitrile); $[\alpha]_D^{26.9}$ = + 16.4° (c 0.004 g mL^{-1}, methanol); ^{1}H NMR

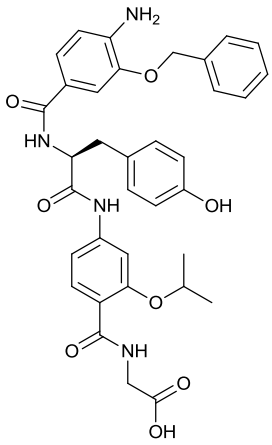

DMSO-d_6, 500 MHz) δ: 10.38 (s, 1H,1-Gly-CO_2H), 9.17 (s, 1 H, 3-Tyr-OH), 8.47 (t, *J* = 5 Hz, 1 H, 1-Gly-NH), 8.25 (d, *J* = 8 Hz, 1 H, 3-Tyr-NH), 7.90 (d, *J* = 8.5 Hz, 1 H, 2-H6), 7.62 (s, 1 H, 2-H3), 7.52 (d, *J* = 7.5 Hz, 2 H, 4-HAr2), 7.43 (s, 1 H, 4-H2), 7.41 (t, *J* = 7.5 Hz, 2 H, 4-HAr3), 7.39 (s, 1H, 2-NH), 7.34 (d, *J* = 8.5 Hz, 1 H, 4-H6), 7.33 (t, *J* = 7.5 Hz, 1H, 4-HAr4), 7.25 (d, *J* = 8.5 Hz, 1 H, 2-H5), 7.18 (d, *J* = 8.5 Hz, 2 H, 3-Tyr-HAr2), 6.65 (d, *J* = 8.5 Hz, 3 H, 4-H5, 3-Tyr-HAr3), 5.34 (br, 2H, 4-NH_2), 5.16 (s, 2 H, 4-Hα), 4.74-4.70 (apparent quin, *J* = 6, 5 Hz, 2 H, 3-Tyr-Hα, 2-Hα), 4.06 (d, *J* = 5 Hz, 2 H, 1-Gly-H1), 3.03-2.98 (dd, *J* = 13, 5 Hz, 2 H, 3-Tyr-Hβ), 1.43-1.41 (dd, *J* = 12, 6 Hz, 6 H, 2-Hβ) ppm; ^{13}C NMR (DMSO-d_6, 126 MHz) δ: 171.2 (1-Gly-CO), 166.4 (4-CO), 163.9 (2-CO), 156.2 (3-Tyr-CO), 155.8 (3-Tyr-CAr4), 144.1 (4-C3), 143.1 (2-C2), 141.5 (4-C4), 137.2 (2-C4), 131.9 (2-C6), 130.1 (3-Tyr-CAr1, 3-Tyr-CAr2), 128.4 (4-CAr2), 128.1 (4-CAr1), 127.7 (4-C2), 127.4 (4-CAr3, 4-CAr4), 121.7 (4-C6), 120.9 (4-C1), 116.5 (2-C1), 114.9 (3-Tyr-CAr3), 112.4 (4-C5), 111.3 (2-C5), 104.6 (2-C3), 71.9 (2-Cα), 69.4 (4-Cα), 56.2 (3-Tyr-Cα), 41.6 (1-Gly-C1), 36.4 (3-Tyr-Cβ), 21.6 (2-Cβ) ppm; IR (neat) ν (cm^{-1}): 3457, 3327, 2977, 2932, 1727, 1680, 1594, 1493, 1257, 1216; ESI-MS found: 641 $(M+H)^+$; HRMS *m/z* calculated for $C_{35}H_{36}N_4NaO_8$ $(M+Na)^+$: 663.2425; Found: 663.2430.

H_2N-[*O*-Bn-(3-HABA)]-His-[*O*-*i*Pr-(2-HABA)]-Gly-CO_2H (120)

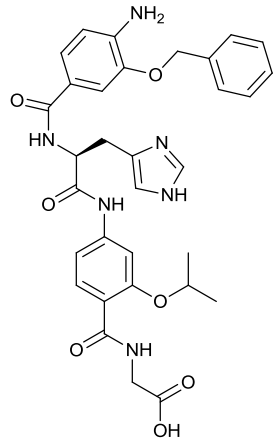

Colourless solid, > 95% pure by NMR; isolated yield: 2.6 mg, 4%; R_f 0.01 (SiO_2, 20% methanol in acetonitrile); $[\alpha]_D^{27.0}$ = + 32.5° (c 0.002 g mL^{-1}, methanol); ^{1}H NMR DMSO-d_6, 500 MHz) δ: 10.36 (s, 1H,1-Gly-CO_2H), 8.47 (t, *J* = 5 Hz, 1 H, 1-Gly-NH), 8.40 (d, *J* = 8 Hz, 1 H, 3-His-NH), 7.89 (d, *J* = 8.5 Hz, 1 H, 2-H6), 7.86 (s, 1 H, 3-His-HAr5), 7.63 (s, 1 H, 2-H3), 7.52 (d, *J* = 7.5 Hz, 2 H, 4-HAr2), 7.46 (s, 1 H, 4-H2), 7.41 (t, *J* = 7.5 Hz, 3 H, 4-HAr3, 4-HAr4), 7.35 (s, 1H, 2-NH), 7.34 (d, *J* = 8 Hz, 1 H, 4-H6), 7.25 (d, *J* = 8.5 Hz, 1 H, 2-H5), 6.99 (s, 1 H, 3-His-HAr2), 6.67 (d, *J* = 8 Hz, 1 H, 4-H5), 5.34 (br, 2H, 4-NH_2), 5.16 (s, 2 H, 4-Hα), 4.80-4.76

(dd, *J* = 8, 6 Hz, 1 H, 3-His-Hα), 4.73-4.68 (apparent quin, *J* = 5.5 Hz, 1 H, 2-Hα), 4.5 (d, *J* = 5 Hz, 2 H, 1-Gly-H1), 3.14-3.07 (dd, *J* = 9, 6 Hz, 2 H, 3-His-Hβ), 1.42-1.40 (dd, *J* = 10.5, 5.5 Hz, 6 H, 2-Hβ) ppm; ^{13}C NMR (DMSO-d_6, 126 MHz) δ: 171.2 (1-Gly-CO), 166.2 (4-CO), 163.9 (2-CO), 156.2 (3-His-CO), 144.2 (4-C3), 143.1 (2-C2), 141.6 (4-C4), 137.2 (2-C4), 134.5 (4-CAr4), 131.8 (2-C6), 129.6 (3-HisCAr4), 128.4 (4-CAr2), 128.1 (4-CAr1, 4-CAr3), 127.7 (4-C2), 127.4 (3-His-CAr2), 121.6 (4-C6), 120.8 (4-C1), 116.5 (2-C1), 115.3 (3-His-CAr5), 112.4 (4-C5), 111.4 (2-C5), 104.7 (2-C3), 71.9 (2-Cα), 69.5 (4-Cα), 54.3 (3-His-Cα), 41.6 (1-Gly-C1), 28.8 (3-His-Cβ), 21.6 (2-Cβ) ppm; IR (neat) ν(cm^{-1}): 3456, 3356, 2980, 2931, 1728, 1688, 1614, 1493, 1259, 1213; ESI-MS found: 615 $(M+H)^+$; HRMS *m/z* calculated for $C_{32}H_{35}N_6O_7$ $(M+H)^+$: 615.2562; Found: 615.2573.

H_2N-[*O*-*i*Bu-(2-HABA)]-Phe-[*O*-*i*Pr-(2-HABA)]-Glu-CO_2H (121)

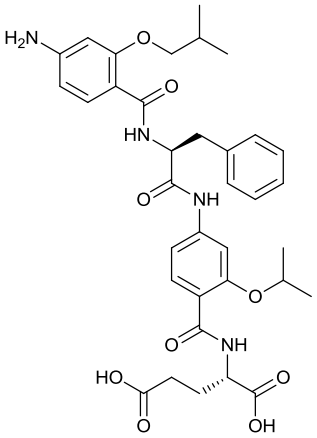

Colourless solid, > 90% pure by NMR; isolated yield: 16.5 mg, 25%; R_f 0.14 (SiO_2, 20% methanol in acetonitrile); ^{1}H NMR (DMSO-d_6, 500 MHz) δ: 10.46 (s, 1H,1-Glu-CO_2H), 8.49 (d, *J* = 7 Hz, 1 H, 1-Glu-NH), 8.25 (d, *J* = 8 Hz, 1 H, 3-Phe-NH), 7.85 (d, *J* = 8.5 Hz, 1 H, 2-H6), 7.65 (d, *J* = 8.5 Hz, 1 H, 4-H6), 7.58 (s, 1 H, 2-H3), 7.29 (s, 1H, 2-NH), 7.26 (d, *J* = 7 Hz, 2 H, 3-Phe-HAr3), 7.23-7.20 (m, 3 H, 3-Phe-HAr2, 3-Phe-HAr4), 7.16(d, *J* = 8.5 Hz, 1 H, 2-H5), 6.25 (s, 1 H, 4-H3), 6.19 (d, *J* = 8.5 Hz, 1 H, 4-H5), 5.78 (br, 2H, 4-NH_2), 5.05-5.00 (dd, *J* = 13.5, 7.5 Hz, 1 H, 3-Phe-Hα), 4.72-4.68 (apparent quin, *J* = 6 Hz, 1 H, 2-Hα), 4.54-4.51 (dd, *J* = 11.5, 5 Hz, 1 H, 1-Glu-Hα), 3.78 (d, *J* = 6.5 Hz, 2 H, 4-Hα), 3.19-3.14 (dd, *J* = 13.5, 6 Hz, 1 H, 3-Phe-Hβ), 3.02-2.99 (dd, *J* = 13.5, 7.5 Hz, 1 H, 3-Phe-Hβ'), 2.32-2.27 (dd, *J* = 12, 5 Hz, 2 H, 1-Glu-Hγ), 2.1-2.06 (m, *2*H, 1-Glu-Hβ, 4-Hβ), 2.05-1.93 (apparent quin, *J* = 5 Hz, 1 H, 1-Glu-Hβ'), 1.43-1.39 (dd, *J* = 9.5, 6 Hz, 6 H, 2-Hβ), 1.00-0.97 (dd, *J* = 11, 6.5 Hz, 6 H, 4-Hγ) ppm; ^{13}C NMR (DMSO-d_6, 126 MHz) δ: 173.6 (1-Glu-COδ), 173.0 (1-Glu-CO), 170.6 (3-Phe-CO), 164.4 (4-CO), 163.7 (2-CO), 158.7 (4-C2), 156.0 (2-C2), 153.6 (4-C4), 142.8 (2-C4), 136.9 (3-Phe-CAr1), 132.7 (4-C6), 131.8 (2-C6), 129.0 (3-Phe-CAr3), 128.2 (3-Phe-CAr2), 126.5 (3-Phe-CAr4), 116.8 (2-C1), 111.3 (2-C5), 107.8 (4-C5), 106.2 (2-C3), 104.6 (4-C1),

96.7 (4-C3), 74.7 (4-Cα), 71.7 (2-Cα), 54.5 (3-Phe-Cα), 51.6 (1-Glu-Cα), 38.4 (3-Phe-Cβ), 29.8 (1-Glu-Cγ), 27.5 (4-Cβ), 27.1 (1-Glu-Cβ), 21.6 (2-Cβ), 19.2 (4-Cγ) ppm; IR (neat) ν(cm^{-1}): 3473, 3357, 3088, 2962, 2930, 1702, 1626, 1592, 1494, 1257, 1198; ESI-MS found: 663 $(M+H)^+$; HRMS *m/z* calculated for $C_{35}H_{42}N_4NaO_9$ $(M+Na)^+$: 685.2844; Found: 685.2849.

H_2N-Glu-[*O-i*Bu-(2-HABA)]-Phe-[*O-i*Pr-(2-HABA)]-Glu-CO_2H (122)

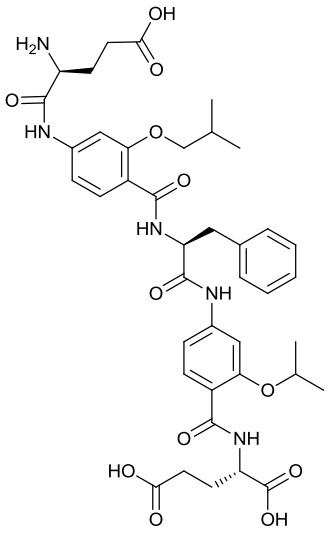

Pale yellow solid, > 90% pure by NMR; isolated yield: 4.1 mg, 5%; R_f 0.02 (SiO_2, 20% methanol in acetonitrile); ^{1}H NMR (DMSO-d_6, 500 MHz) δ: 10.48 (s, 1H,1-Glu-CO_2H), 8.57 (d, *J* = 6.5 Hz, 1 H, 1-Glu-NH), 8.41 (d, *J* = 8 Hz, 1 H, 3-Phe-NH), 7.87 (d, *J* = 8.5 Hz, 1 H, 2-H6), 7.84 (d, *J* = 8.5 Hz, 1 H, 4-H6), 7.55 (s, 2 H, 2-H3, 4-H3), 7.28 (s, 1H, 2-NH), 7.24 (d, *J* = 7 Hz, 2 H, 3-Phe-HAr3), 7.25 (d, *J* = 8.5 Hz, 1 H, 4-H5),7.19-7.18 (m, 3 H, 3-Phe-HAr2, 3-Phe-HAr4), 7.16 (d, *J* = 8.5 Hz, 1 H, 2-H5), 7.14 (s, 1 H, 4-NH), 5.31 (br, 2H, 4-NH_2), 5.05-5.00 (dd, *J* = 13.5, 7.5 Hz, 1 H, 3-Phe-Hα), 4.69-4.64 (apparent quin, *J* = 6 Hz, 1 H, 2-Hα), 4.45-4.41 (dd, *J* = 13, 6.5 Hz, 1 H, 1-Glu-Hα), 3.84 (d, *J* = 6.5 Hz, 2 H, 4-Hα), 3.64 (t, *J* = 6.5 Hz, 1 H, 5-Glu-Hα), 3.21-3.17 (dd, *J* = 13.5, 7.5 Hz, 1 H, 3-Phe-Hβ), 3.06-3.01 (dd, *J* = 13.5, 7.5 Hz, 1 H, 3-Phe-Hβ'), 2.35 (t, *J* = 7 Hz, 2 H, 5-Glu-Hγ), 2.27 (t, *J* = 7.5 Hz, 2 H, 1-Glu-Hγ), 2.10-2.06 (apparent quin, *J* = 6.5 Hz, 1 H, 4-Hβ), 2.01-1.95 (m, 3H, 1-Glu-Hβ, 5-Glu-Hβ), 1.87-1.81 (apparent quin, *J* = 6.5 Hz, 1 H, 5-Glu-Hβ'), 1.41-1.36 (dd, *J* = 9.5, 6 Hz, 6 H, 2-Hβ), 0.98-0.94 (dd, *J* = 11.5, 6.5 Hz, 6 H, 4-Hγ) ppm; ^{13}C NMR (DMSO-d_6, 126 MHz) δ: 173.8 (5-Glu-COδ, 5-Glu-CO), 173.1 (1-Glu-COδ), 171.9 (1-Glu-CO), 170.2 (3-Phe-CO), 163.5 (4-CO), 163.4 (2-CO), 157.4 (4-C2), 156.1 (2-C2), 142.7 (4-C4), 142.6 (2-C4), 136.7 (3-Phe-CAr1), 131.9 (2-C6), 129.6 (4-C6), 129.0 (3-Phe-CAr3), 128.2 (3-Phe-CAr2), 126.5 (3-Phe-CAr4), 117.1 (2-C1, 4-C1), 111.3 (4-C5), 111.2 (2-C5), 104.7 (2-C3), 103.3 (4-C3), 75.2 (4-Cα), 71.7 (2-Cα), 56.5 (3-Phe-Cα), 54.7 (5-Glu-Cα), 52.0 (1-Glu-Cα), 35.1 (3-Phe-Cβ), 30.3 (1-Glu-Cγ), 28.7 (5-Glu-Cγ), 27.5 (4-Cβ), 26.6 (1-Glu-Cβ), 25.1 (5-Glu-Cβ),

21.5 (2-Cβ), 19.0 (4-Cγ) ppm; IR (neat) ν(cm^{-1}): 3359, 2931, 1692, 1632, 1595, 1495, 1261, 1199; HRMS *m/z* calculated for $C_{40}H_{50}N_5O_{12}$ $(M+H)^+$: 792.3450; Found: 792.3451.

H_2N-Arg-[*O-i*Bu-(2-HABA)]-Phe-[*O-i*Pr-(2-HABA)]-Glu-CO_2H (123)

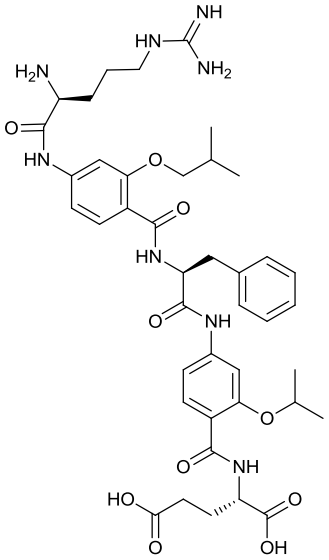

Orange solid, > 90% pure by NMR; isolated yield: 7 mg, 9%; R_f 0.042 (SiO_2, 20% methanol in acetonitrile); ^{1}H NMR (DMSO-d_6, 500 MHz) δ: 10.54 (s, 1H,1-Glu-CO_2H), 8.62 (br, 2 H, 1-Glu-NH, 5-Arg-NHε), 8.41 (d, *J* = 8 Hz, 1 H, 3-Phe-NH), 7.88 (d, *J* = 8.5 Hz, 1 H, 4-H6), 7.86 (s, 1 H, 4-H3), 7.85 (d, *J* = 8.5 Hz, 1 H, 2-H6), 7.60 (s, 1 H, 2-H5), 7.54 (d, *J* = 7 Hz, 2 H, 3-Phe-HAr2), 7.39 (d, *J* = 8.5 Hz, 1 H, 4-H3),7.34 (br, 1 H, 5-Arg-NHη), 7.31 (t, *J* = 7 Hz, 1 H, 3-Phe-HAr4), 7.25 (s, 1H, 2-NH), 7.23 (t, *J* = 7 Hz, 1 H, 3-Phe-HAr3), 7.17 (d, *J* = 8.5 Hz, 1 H, 2-H5), 7.15 (s, 1H, 4-NH), 5.31 (t, *J* = 5 Hz, 2H, 5-Arg-NH_2), 5.05-5.02 (dd, *J* = 13.5, 7.5 Hz, 1 H, 3-Phe-Hα), 4.72-4.62 (m, *J* = 6 Hz, 2 H, 2-Hα, 5-Arg-Hα), 4.39-4.35 (m, 2 H, 1-Glu-Hα, 5-Arg-NHθ), 3.83 (d, *J* = 6.5 Hz, 2 H, 4-Hα), 3.16-3.11 (m, 2 H, 3-Phe-Hβ, 5-Arg-Hβ), 3.01-2.97 (m, 2 H, 3-Phe-Hβ', 5-Arg-Hβ'), 2.27-2.24 (m, 4 H, 1-Glu-Hγ, 5-Arg-Hδ), 2.11-2.05 (apparent quin, *J* = 6.5 Hz, 1 H, 4-Hβ), 2.00-1.96 (m, 3 H, 5-Arg-Hγ, 1-Glu-Hβ), 1.82-1.76 (quin, *J* = 6 Hz, 1 H, 5-Arg-Hγ'), 1.41-1.38 (dd, *J* = 11.5, 6 Hz, 6 H, 2-Hβ), 0.98-0.94 (dd, *J* = 14.5, 6.5 Hz, 6 H, 4-Hγ) ppm; ^{13}C NMR (DMSO-d_6, 126 MHz) δ: 174.8 (5-Arg-CO), 174.0 (1-Glu-COδ), 173.5 (1-Glu-CO), 170.2 (3-Phe-CO), 163.5 (4-CO), 160.8 (2-CO), 157.4 (5-Arg-CNε), 156.9 (4-C2), 156.1 (2-C2), 142.8 (4-C4), 142.6 (2-C4), 136.8 (3-Phe-CAr1), 132.0 (2-C6), 129.3 (4-C6), 129.1 (3-Phe-CAr3), 128.2 (3-Phe-CAr2), 126.5 (3-Phe-CAr4), 117.2 (4-C1), 115.9 (2-C1), 111.3 (4-C5, 2-C5), 104.7 (2-C3), 103.3 (2-C3), 75.2 (4-Cα), 71.7 (2-Cα), 59.8 (5-Arg-Cα), 54.7 (3-Phe-Cα), 52.4 (1-Glu-Cα), 45.5 (5-Arg-Cβ), 38.2 (3-Phe-Cβ), 29.0 (1-Glu-Cγ), 27.7 (1-Glu-Cβ), 27.4 (4-Cβ), 24.6 (5-Arg-Cδ), 22.0 (5-Arg-Cγ), 21.5 (2-Cγ), 19.1 (4-Cγ) ppm; IR (neat) ν(cm^{-1}): 3358, 3172, 2966,

2929, 1671, 1597, 1496, 1262, 1199; HRMS *m/z* calculated for $C_{41}H_{56}N_8O_{10}$ $(M+2H)^{2+}$: 410.2054; Found: 410.2063.

H_2N-[*O-i*Bu-(2-HABA)]-Phe-[*O-i*Pr-(2-HABA)]-Pro-CO_2H (124)

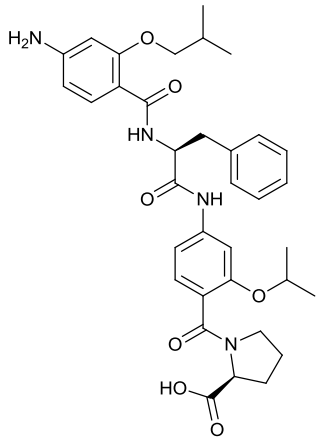

Pale brown solid, > 90% pure by NMR; isolated yield: 25.5 mg, 41%; R_f 0.5 (SiO_2, 20% methanol in acetonitrile); ^{1}H NMR (DMSO-d_6, 500 MHz) δ: 10.36 (s, 1H,1-Pro-CO_2H), 8.41 (d, *J* = 7 Hz, 1 H, 3-Phe-NH), 7.87 (d, *J* = 8.5 Hz, 1 H, 2-H6), 7.86 (d, *J* = 8.5 Hz, 1 H, 4-H6), 7.55 (s, 1 H, 2-H3), 7.38 (s, 1 H, 4-H3), 7.28 (s, 1H, 2-NH), 7.25 (d, *J* = 7 Hz, 1 H, 3-Phe-HAr4), 7.23 (d, *J* = 8.5 Hz, 1 H, 4-H5), 7.20-7.18 (m, 4 H, 3-Phe-HAr2, 3-Phe-HAr3), 7.11 (s, 1H, 4-NH), 7.08 (d, *J* = 8.5 Hz, 1 H, 2-H5), 5.05-5.01 (dd, *J* = 13.5, 7.5 Hz, 1 H, 3-Phe-Hα), 4.49-4.44 (apparent quin, *J* = 6 Hz, 1 H, 2-Hα), 4.34-4.31 (dd, *J* = 9.5, 5 Hz, 1 H, 1-Pro-Hα), 3.84 (d, *J* = 6.5 Hz, 2 H, 4-Hα), 3.21-3.17 (dd, *J* = 13.5, 6 Hz, 1 H, 3-Phe-Hβ), 3.05-3.00 (m, 3 H, 3-Phe-Hβ', 1-Pro-Hδ), 2.23-2.19 (dd, *J* = 9.5, 5 Hz, 1 H, 1-Pro-Hβ), 2.10-2.05 (apparent quin, *J* = 6.5 Hz, 1H, 4-Hβ), 2.01-1.97 (dd, *J* = 9.5, 5 Hz, 1 H, 1-Pro-Hβ'), 1.26-1.23 (dd, *J* = 9.5, 6 Hz, 6 H, 2-Hβ), 1.16-1.13 (t, *J* = 9.5, 2 H, 1-Pro-Hγ), 0.99-0.94 (dd, *J* = 13.5, 6.5 Hz, 6 H, 4-Hγ) ppm; ^{13}C NMR (DMSO-d_6, 126 MHz) δ: 173.3 (1-Pro-CO), 169.8 (3-Phe-CO), 166.5 (2-CO), 163.5 (4-CO), 157.4 (4-C2, 2-C2), 142.6 (4-C4), 140.5 (2-C4), 136.8 (3-Phe-CAr1), 132.0 (4-C6, 2-C6), 129.1 (3-Phe-CAr3), 128.2 (3-Phe-CAr2), 126.5 (3-Phe-CAr4), 123.1 (4-C1), 116.0 (2-C1), 111.4 (4-C5), 111.2 (2-C5), 105.3 (4-C3), 103.4 (2-C3), 75.2 (4-Cα), 70.5 (2-Cα), 58.2 (1-Pro-Cα), 54.6 (3-Phe-Cα), 45.6 (1-Pro-Cδ), 38.3 (3-Phe-Cβ), 29.2 (1-Pro-Cγ), 27.8 (1-Pro-Cβ), 27.5 (4-Cβ), 21.6 (2-Cβ), 19.1 (4-Cγ) ppm; IR (neat) ν (cm^{-1}): 3367, 3031, 2958, 2927, 1725, 1596, 1498, 1268, 1199; ESI-MS found: 631 $(M+H)^+$; HRMS *m/z* calculated for $C_{35}H_{43}N_4O_7$ $(M+H)^+$: 631.3126; Found: 631.3136.

H_2N-Glu-[*O-i*Bu-(2-HABA)]-Phe-[*O-i*Pr-(2-HABA)]-Pro-CO_2H (125)

Pale yellow solid, > 90% pure by NMR; isolated yield: 19.4 mg, 26%; R_f 0.03 (SiO_2, 20% methanol in acetonitrile); ^{1}H NMR (DMSO-d_6, 500 MHz) δ: 10.36 (s, 1H,1-Pro-

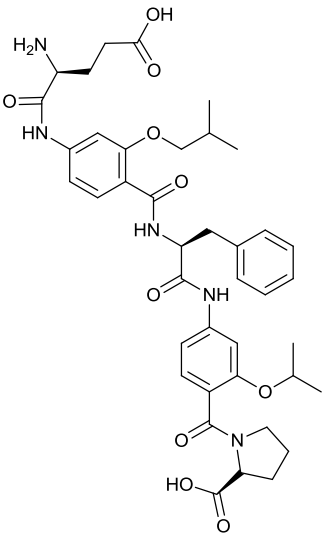

CO_2H), 8.41 (d, *J* = 7 Hz, 1 H, 3-Phe-NH), 7.87 (d, *J* = 8.5 Hz, 1 H, 2-H6), 7.86 (d, *J* = 8.5 Hz, 1 H, 4-H6), 7.55 (s, 1 H, 2-H3), 7.38 (s, 1 H, 4-H3), 7.28 (s, 1H, 2-NH), 7.25 (d, *J* = 7 Hz, 1 H, 3-Phe-HAr4), 7.23 (d, *J* = 8.5 Hz, 1 H, 4-H5), 7.20-7.18 (m, 4 H, 3-Phe-HAr2, 3-Phe-HAr3), 7.11 (s, 1H, 4-NH), 7.08 (d, *J* = 8.5 Hz, 1 H, 2-H5), 5.05-5.01 (dd, *J* = 13.5, 7.5 Hz, 1 H, 3-Phe-Hα), 4.49-4.44 (apparent quin, *J* = 6 Hz, 1 H, 2-Hα), 4.34-4.31 (dd, *J* = 9.5, 5 Hz, 1 H, 1-Pro-Hα), 3.84 (d, *J* = 6.5 Hz, 2 H, 4-Hα), 3.73-3.71 (t, *J* = 7 Hz, 1 H, 5-Glu-Hα), 3.21-3.17 (dd, *J* = 13.5, 6 Hz, 1 H, 3-Phe-Hβ), 3.05-3.00 (m, 3 H, 3-Phe-Hβ', 1-Pro-Hδ), 2.37-2.34 (dd, *J* = 14.5, 7 Hz, 2 H, 5-Glu-Hγ), 2.23-2.19 (dd, *J* = 9.5, 5 Hz, 1 H, 1-Pro-Hβ), 2.10-2.05 (apparent quin, *J* = 6.5 Hz, 1H, 4-Hβ), 2.01-1.97 (dd, *J* = 9.5, 5 Hz, 1 H, 1-Pro-Hβ'), 1.90-1.85 (m, 2H, 5-Glu-Hβ), 1.26-1.23 (dd, *J* = 9.5, 6 Hz, 6 H, 2-Hβ), 1.16-1.13 (t, *J* = 9.5, 2 H, 1-Pro-Hγ), 0.99-0.94 (dd, *J* = 13.5, 6.5 Hz, 6 H, 4-Hγ) ppm; ^{13}C NMR (DMSO-d_6, 126 MHz) δ: 177.4 (5-Glu-COδ), 173.6 (5-Glu-CO), 173.3 (1-Pro-CO), 169.8 (3-Phe-CO), 166.5 (2-CO), 163.5 (4-CO), 157.4 (4-C2, 2-C2), 142.6 (4-C4), 140.5 (2-C4), 136.8 (3-Phe-CAr1), 132.0 (4-C6, 2-C6), 129.1 (3-Phe-CAr3), 128.2 (3-Phe-CAr2), 126.5 (3-Phe-CAr4), 123.1 (4-C1), 116.0 (2-C1), 111.4 (4-C5), 111.2 (2-C5), 105.3 (4-C3), 103.4 (2-C3), 75.2 (4-Cα), 70.5 (2-Cα), 58.2 (1-Pro-Cα), 54.6 (3-Phe-Cα), 53.7 (5-Glu-Cα), 45.6 (1-Pro-Cδ), 38.3 (3-Phe-Cβ), 30.1 (5-Glu-Cγ), 29.2 (1-Pro-Cγ), 27.8 (1-Pro-Cβ), 27.5 (4-Cβ), 24.3 (5-Glu-Cβ), 21.7 (2-Cβ), 19.1 (4-Cγ) ppm; IR (neat) ν(cm^{-1}): 3356, 3190, 2930, 1692, 1595, 1495, 1261, 1199; ESI-MS found: 760 $(M+H)^+$; HRMS *m/z* calculated for $C_{40}H_{50}N_5O_{10}$ $(M+H)^+$: 760.3552; Found: 760.3561.

H_2N-Arg-[*O*-*i*Bu-(2-HABA)]-Phe-[*O*-*i*Pr-(2-HABA)]-Pro-CO_2H (126)

Pale yellow solid, > 90% pure by NMR; isolated yield: 25.8 mg, 33%; R_f 0.021 (SiO_2, 20% methanol in acetonitrile); ^{1}H NMR (DMSO-d_6, 500 MHz) δ: 10.40 (s, 1H,1-Pro-CO_2H), 8.40 (d, *J* = 7 Hz, 1 H, 3-Phe-NH), 7.89 (d, *J* = 8.5 Hz, 1 H, 4-H6), 7.53 (s, 1 H, 4-H3), 7.37 (s, 1 H, 1-H3), 7.30 (s, 1 H, 5-Arg-Hη), 7.31 (s, 1H, 2-NH), 7.29 (d,

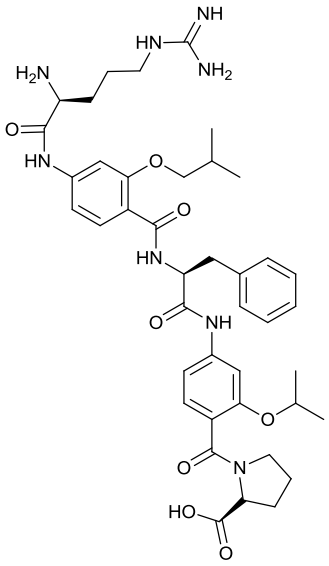

J = 7 Hz, 2 H, 3-Phe-HAr2), 7.24 (d, *J* = 8.5 Hz, 1 H, 4-H5), 7.25 (d, *J* = 7 Hz, 2 H, 3-Phe-HAr3), 7.20 (d, *J* = 8.5 Hz, 1 H, 2-H6), 7.20 (t, *J* = 7 Hz, 1 H, 3-Phe-HAr4), 7.12 (s, 1H, 4-NH), 7.08 (d, *J* = 8.5 Hz, 1 H, 2-H5), 5.04-5.00 (dd, *J* = 13.5, 7.5 Hz, 1 H, 3-Phe-Hα), 4.50-4.44 (apparent quin, *J* = 6 Hz, 2 H, 2-Hα, 5-Arg-Hα), 4.34-4.31 (dd, *J* = 9.5, 5 Hz, 1 H, 1-Pro-Hα), 3.83 (d, *J* = 6.5 Hz, 4 H, 4-Hα, 5-Arg-Hθ), 3.21-3.18 (dd, *J* = 13.5, 6 Hz, 1 H, 3-Phe-Hβ), 3.13 (t, *J* = 7 Hz, 2 H, 1-Pro-Hδ), 3.09-3.05 (dd, *J* = 14, 7.5 Hz, 2 H, 5-Arg-Hδ), 2.68-2.66 (m, 1 H, 3-Phe-Hβ'), 2.23-2.19 (dd, *J* = 9.5, 5 Hz, 1 H, 1-Pro-Hβ), 2.11-2.06 (apparent quin, *J* = 6.5 Hz, 1H, 4-Hβ), 2.01-1.97 (dd, *J* = 9.5, 5 Hz, 1 H, 1-Pro-Hβ'), 1.89-1.83 (m, 3H, 5-Arg-Hβ, 5-Arg-Hγ), 1.56-1.51 (dd, *J* = 9.5, 6 Hz, 1H, 5-Arg-Hβ'), 1.26-1.24 (dd, *J* = 9.5, 6 Hz, 6 H, 2-Hβ), 1.18-1.15 (t, *J* = 9.5, 2 H, 1-Pro-Hγ), 0.99-0.94 (dd, *J* = 13.5, 6.5 Hz, 6 H, 4-Hγ) ppm; ^{13}C NMR (DMSO-d_6, 126 MHz) δ: 173.3 (5-Arg-CO), 169.9 (1-Pro-CO), 166.4 (3-Phe-CO), 163.4 (4-CO), 157.9 (2-CO), 157.4 (5-Arg-CNζ), 156.7 (4-C2), 153.5 (2-C2), 142.4 (4-C4), 140.5 (2-C4), 136.8 (3-Phe-CAr1), 131.1 (2-C6), 129.9(4-C6), 129.1 (3-Phe-CAr3), 128.4 (3-Phe-CAr2), 126.5 (3-Phe-CAr4), 123.1 (4-C1), 116.2 (2-C1), 111.4 (4-C5), 111.2 (2-C5), 105.3 (4-C3), 103.3 (2-C3), 75.2 (4-Cα), 70.6 (2-Cα), 58.2 (1-Pro-Cα), 54.6 (3-Phe-Cα), 47.5 (5-Arg-Cα), 45.7 (1-Pro-Cδ), 38.3 (3-Phe-Cβ), 30.6 (5-Arg-Cγ), 29.2 (1-Pro-Cγ), 29.0 (1-Pro-Cβ), 27.4 (4-Cβ), 24.3 (5-Arg-Cδ), 22.5 (5-Arg-Cβ), 21.7 (2-Cβ), 19.0 (4-Cγ) ppm; IR (neat) ν (cm^{-1}): 3359, 3183, 2959, 2930, 1672, 1596, 1496, 1262, 1199; HRMS *m/z* calculated for $C_{41}H_{56}N_8O_8$ $(M+2H)^{2+}$: 394.2105; Found: 394.2114.

H_2N-Glu-[*O-i*Bu-(2-HABA)]-Phe-[*O-i*Pr-(2-HABA)]-Gly-CO_2H (127)

Pale yellow solid, > 90% pure by NMR; isolated yield: 8.9 mg, 12%; R_f 0.61 (SiO_2, 20% methanol in acetonitrile); ^{1}H NMR (DMSO-d_6, 500 MHz) δ: 10.49 (s, 1H,1-Gly-CO_2H), 10.49 (s, 1H,1-Glu-CO_2H), 8.47 (t, *J* = 5 Hz, 1 H, 1-Gly-NH), 8.41 (d, *J* = 8 Hz, 1 H, 3-Phe-NH), 7.87 (d, *J* = 8.5 Hz, 1 H, 2-H6), 7.86 (d, *J* = 8.5 Hz, 1 H, 4-H6), 7.56 (s, 1 H, 4-H3), 7.55 (s, 1 H, 2-H3), 7.28 (s, 1H, 2-NH), 7.25 (t, *J* = 7 Hz, 1 H, 3-

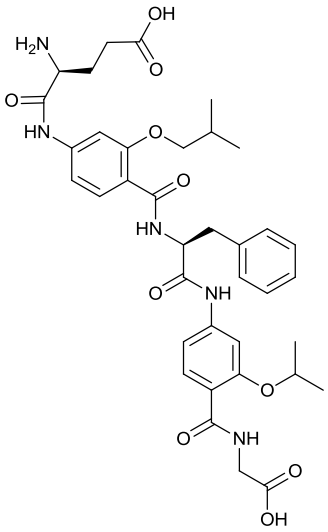

Phe-HAr4), 7.23 (d, *J* = 8.5 Hz, 1 H, 4-H5), 7.21 (s, 1H, 4-NH), 7.20-7.18 (m, 4 H, 3-Phe-HAr2, 3-Phe-HAr3), 7.16 (d, *J* = 8.5 Hz, 1 H, 2-H5), 5.30 (br, 2H, 5-Glu-NH_2), 5.05-5.01 (dd, *J* = 13.5, 7.5 Hz, 1 H, 3-Phe-Hα), 4.69-4.64 (apparent quin, *J* = 6 Hz, 1 H, 2-Hα), 3.97 (d, *J* = 5 Hz, 2 H, 1-Gly-H1), 3.84 (d, *J* = 6.5 Hz, 2 H, 4-Hα), 3.21-3.17 (dd, *J* = 13.5, 6 Hz, 1 H, 3-Phe-Hβ), 3.05-3.01 (dd, *J* = 13.5, 7.5 Hz, 1 H, 3-Phe-Hβ'), 2.99-2.97 (dd, *J* = 13, 7 Hz, 1 H, 5-Glu-Hα), 2.36-2.3 (dd, *J* = 14, 7 Hz, 2 H, 5-Glu-Hγ), 2.1-2.06 (apparent quin, *J* = 6.5 Hz, 1H, 4-Hβ), 2.01-1.95 (m, 2H, 5-Glu-Hβ), 1.41-1.38 (dd, *J* = 9.5, 6 Hz, 6 H, 2-Hβ), 0.98-0.94 (dd, *J* = 11, 6.5 Hz, 6 H, 4-Hγ) ppm; ^{13}C NMR (DMSO-d_6, 126 MHz) δ: 173.9 (5-Glu-COδ), 173.0 (5-Glu-CO), 171.3 (1-Gly-CO), 170.2 (3-Phe-CO), 163.7 (4-CO), 163.5 (2-CO), 157.4 (4-C2), 156.2 (2-C2), 153.6 (4-C4, 2-C4), 136.7 (3-Phe-CAr1), 132.9 (4-C6, 2-C6), 129.0 (3-Phe-CAr3), 128.2 (3-Phe-CAr2), 126.5 (3-Phe-CAr4), 116.9 (2-C1, 4-C1), 111.4 (4-C5), 111.1 (2-C5), 104.8 (4-C3), 103.3 (2-C3), 75.1 (4-Cα), 71.9 (2-Cα), 54.7 (3-Phe-Cα), 40.1 (1-Gly-C1), 38.2 (5-Glu-Cα), 35.1 (3-Phe-Cβ), 31.2 (5-Glu-Cγ), 28.7 (4-Cβ), 27.5 (5-Glu-Cβ), 21.6 (2-Cβ), 19.1 (4-Cγ) ppm; IR (neat) ν (cm^{-1}): 3358, 3270, 3168, 2958, 2925, 1691, 1594, 1494, 1259, 1200; ESI-MS found: 720 $(M+H)^+$; HRMS *m/z* calculated for $C_{37}H_{46}N_5O_{10}$ $(M+H)^+$: 720.3239; Found: 720.3249.

H_2N-Arg-[*O-i*Bu-(2-HABA)]-Phe-[*O-i*Pr-(2-HABA)]-Gly-CO_2H (128)

Orange solid, > 90% pure by NMR; isolated yield: 12.8 mg, 18%; R_f 0.01 (SiO_2, 20% methanol in acetonitrile); ^{1}H NMR (DMSO-d_6, 500 MHz) δ: 10.48 (s, 1H,1-Gly-CO_2H), 8.53 (t, *J* = 5 Hz, 2 H, 1-Gly-NH, 5-Arg-NHε), 8.40 (d, *J* = 7 Hz, 1 H, 3-Phe-NH), 7.93 (s, 1 H, 4-H3), 7.91 (d, *J* = 8.5 Hz, 1 H, 4-H6), 7.90 (s, 1 H, 2-H3), 7.85 (d, *J* = 8.5 Hz, 1 H, 2-H6), 7.54 (d, *J* = 7 Hz, 2 H, 3-Phe-HAr2), 7.46 (s, 1H, 4-NH), 7.42 (br, 2 H, 5-Arg-NHη), 7.35 (d, *J* = 8.5 Hz, 1 H, 4-H5), 7.31 (t, *J* = 7 Hz, 1 H, 3-Phe-HAr4), 7.25 (s, 1H, 2-NH), 7.24 (t, *J* = 7 Hz, 1 H, 3-Phe-HAr3),7.19 (d, *J* = 8.5 Hz, 1 H, 2-H5), 5.31 (t, *J* = 5 Hz, 2H, 5-Arg-NH_2), 5.05-5.01 (dd, *J* = 13.5, 7.5 Hz, 1

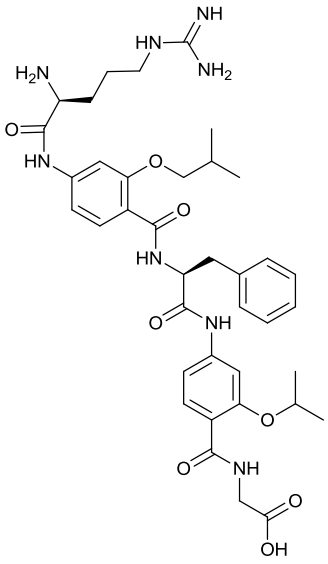

H, 3-Phe-Hα), 4.70-4.63 (m, *J* = 6 Hz, 2 H, 2-Hα, 5-Arg-Hα), 3.88-3.82 (m, 6 H, 1-Gly-H1, 4-Hα, 5-Arg-NH_2θ), 3.12-3.09 (m, 3 H, 3-Phe-Hβ, 5-Arg-Hδ), 2.65-2.62 (dd, *J* = 13.5, 7.5 Hz, 1 H, 3-Phe-Hβ'), 2.07-2.04 (quin, *J* = 6.5 Hz, 1 H, 5-Arg-Hβ), 2.01-1.96 (m, 4 H, 5-Arg-Hγ, 5-Arg-Hβ', 4-Hβ), 1.39-1.36 (dd, *J* = 11.5, 6 Hz, 12 H, 2-Hβ, 4-Hγ) ppm; ^{13}C NMR (DMSO-d_6, 126 MHz) δ: 174.2 (5-Arg-CO), 171.6 (1-Gly-CO), 170.2 (3-Phe-CO), 169.6 (4-CO), 163.4 (2-CO), 160.8 (5-Arg-CNζ), 157.0 (4-C2), 156.1 (2-C2), 143.0 (4-C4), 142.2 (2-C4), 136.8 (3-Phe-CAr1), 131.9 (2-C6), 129.6 (4-C6), 129.0 (3-Phe-CAr3), 128.2 (3-Phe-CAr2), 127.6 (3-Phe-CAr4), 117.5 (4-C1), 117.1 (2-C1), 111.6 (4-C5), 111.3 (2-C5), 105.1 (2-C3), 104.8 (2-C3), 75.2 (4-Cα), 71.8 (2-Cα), 59.9 (3-Phe-Cα), 42.9 (1-Gly-C1), 35.1 (5-Arg-Cα), 34.3 (3-Phe-Cβ), 31.2 (5-Arg-Cγ), 29.0 (4-Cβ), 27.5 (5-Arg-Cβ), 25.1 (5-Arg-Cδ), 21.5 (2-Cγ), 19.0 (4-Cγ) ppm; IR (neat) ν(cm^{-1}): 3359, 3181, 2921, 2851, 1630, 1595, 1492, 1258, 1200; HRMS *m/z* calculated for $C_{38}H_{52}N_8O_8$ $(M+2H)^{2+}$: 374.1949; Found: 374.1953.

H_2N-[*O*-Bn-(3-HABA)]-D-Phe-[*O*-*i*Pr-(2-HABA)]-Gly-CO_2H (129)

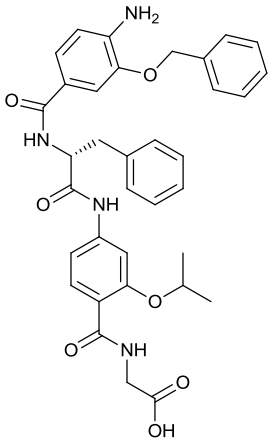

Colourless solid, > 95% pure by NMR; isolated yield: 10.3 mg, 17%; R_f 0.82 (SiO_2, 20% methanol in acetonitrile); $[\alpha]_D^{27.5}$ = -23.4° (c 0.008 g mL^{-1}, methanol); ^{1}H NMR (DMSO-d_6, 500 MHz) δ: 10.46 (s, 1H,1-Gly-CO_2H), 8.47 (t, *J* = 5 Hz, 1 H, 1-Gly-NH), 8.35 (d, *J* = 8 Hz, 1 H, 3-D-Phe-NH), 7.89 (d, *J* = 8.5 Hz, 1 H, 2-H6), 7.64 (s, 1 H, 2-H3), 7.50 (d, *J* = 8.5 Hz, 2 H, 3- D-Phe-HAr2), 7.42 (s, 1 H, 4-H2), 7.40-7.37 (m, 5 H, 4-HAr2, 4-H-Ar3, 4-HAr4), 7.32 (t, *J* = 8.5 Hz, 2 H, 3- D-Phe-HAr3), 7.26 (d, *J* = 8.5 Hz, 2 H, 4-H6, 2-H5), 7.25 (s, 1H, 2-NH), 7.17 (t, *J* = 8.5 Hz, 1H, 3- D-Phe-HAr4), 6.62 (d, *J* = 8.5 Hz, 1 H, 4-H5), 5.32 (br, 2H, 4-NH_2), 5.15 (s, 2 H, 4-Hα), 4.82-4.77 (dd, *J* = 8.5 , 5.5 Hz, 1 H, 3-D-Phe-Hα), 4.73-4.68 (quin, *J* = 6 Hz, 1 H, 2-Hα), 4.01 (d, *J* = 5 Hz, 2 H, 1-Gly-H1), 3.13-3.09 (dd, *J* = 8.5 , 5.5

Hz, 2 H, 3- D-Phe-Hβ), 1.45-1.43 (dd, *J* = 8.5, 6 Hz, 6 H, 2-Hβ), ppm; ^{13}C NMR (DMSO-d_6, 126 MHz) δ: 171.5 (1-Gly-CO), 166.4 (4-CO), 163.9 (2-CO), 156.2 (3-D-Phe-CO), 144.0 (4-C3), 143.0 (2-C2), 141.5 (4-C4), 138.2 (2-C4), 137.2 (2-C6), 131.9 (4-CAr1), 129.2 (3- D-Phe-CAr3), 128.4 (4-CAr2, 4-CAr3), 128.1 (4-CAr4), 127.7 (4-C2), 127.4 (3- D-Phe-CAr2, 3- D-Phe-CAr4), 126.3 (3- D-Phe-CAr1), 121.8 (4-C6), 120.8 (4-C1), 116.6 (2-C1), 112.3 (4-C5), 111.4 (2-C5), 104.7 (2-C3), 71.9 (2-Cα), 69.4 (4-Cα), 55.9 (3- D-Phe-Cα), 41.9 (1-Gly-C1), 37.1 (3- D-Phe-Cβ), 21.6 (2-Cβ) ppm; IR (neat) ν (cm^{-1}): 3358, 3032, 2979, 2929, 1682, 1596, 1494, 1258, 1211; ESI-MS found: 625 $(M+H)^+$; HRMS *m/z* calculated for $C_{35}H_{37}N_4O_7$ $(M+H)^+$: 625.2657; Found: 625.2668.

H_2N-[*O*-Bn-(3-HABA)]-D-Trp-[*O*-*i*Pr-(2-HABA)]-Gly-CO_2H (130)

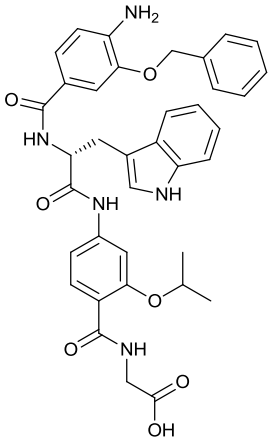

Pale brown solid, > 90% pure by NMR; isolated yield: 5 mg, 8%; R_f 0.083 (SiO_2, 20% methanol in acetonitrile); $[\alpha]_D^{28.3}$ = -137.6° (c 0.007 g mL^{-1}, methanol); ^{1}H NMR (DMSO-d_6, 500 MHz) δ: 10.83 (s, 1 H, 3-D-Trp-NH'), 10.45 (s, 1H,1-Gly-CO_2H), 8.48 (t, *J* = 5 Hz, 1 H, 1-Gly-NH), 8.24 (d, *J* = 7.5 Hz, 1 H, 3-D -Trp-NH), 7.90 (d, *J* = 8.5 Hz, 1 H, 2-H6), 7.75 (d, *J* = 7.5 Hz, 1 H, 3-D-Trp-HAr4), 7.65 (s, 1 H, 2-H3), 7.51 (d, *J* = 7.5 Hz, 2 H, 4-HAr2), 7.45 (s, 1 H, 4-H2), 7.41 (t, *J* = 7.5 Hz, 3 H, 4-HAr3, 4-HAr4), 7.35-7.32 (m, 3 H, 4-H6, 3-D-Trp-HAr7, 2-NH), 7.28 (s, 1 H, 3-D-Trp-HAr2), 7.26 (d, *J* = 8.5 Hz, 1 H, 2-H5), 7.07 (t, *J* = 7.5 Hz, 1H, 3-D-Trp-HAr6), 6.99 (t, *J* = 7.5 Hz, 1H, 3-D-Trp-HAr5), 6.64 (d, *J* = 8Hz, 1 H, 4-H5), 5.33 (br, 2H, 4-NH_2), 5.18-5.11 (dd, *J* = 12, 4 Hz, 2 H, 4-Hα), 4.89-4.84 (dd, *J* = 9, 5 Hz, 1 H, 3-D-Trp-Hα), 4.74-4.69 (apparent quin, *J* = 6 Hz, 1 H, 2-Hα), 4.04 (d, *J* = 5 Hz, 2 H, 1-Gly-H1), 3.28-3.24 (dd, *J* = 11 , 5 Hz, 2 H, 3-D-Trp-Hβ), 1.43-1.41 (dd, *J* = 9.5, 6 Hz, 6 H, 2-Hβ) ppm; ^{13}C NMR (DMSO-d_6, 126 MHz) δ: 171.2 (1-Gly-CO), 164.5 (4-CO), 163.9 (2-CO), 158.2 (3-D-Trp-CO), 156.2 (4-C1), 155.9 (2-C2), 153.5 (4-C4), 143.1 (2-C4), 136.1 (4-C3), 132.7 (3-D-Trp-CAr7a), 131.8 (2-C6), 129.6 (3-D-Trp-CAr3a), 128.5 (4-CAr3, 4-CAr4), 128.1 (4-CAr1), 128.0 (4-CAr2, 3-D-Trp-CAr3), 127.1 (3-D-Trp-CAr2), 125.2 (4-C6), 123.3 (3-D-Trp-CAr7), 120.9 (3-D-Trp-CAr5), 118.2 (3-D-Trp-CAr4), 116.5 (3-D-Trp-CAr6), 111.3 (2-C1), 109.4 (4-C5),

108.2 (4-C2), 106.5 (2-C5), 97.2 (2-C3), 71.9 (2-Cα), 69.8 (4-Cα), 48.6 (3-D-Trp-Cα), 41.6 (1-Gly-C1), 28.0 (3-D -Trp-Cβ), 21.6 (2-Cβ) ppm; IR (neat) ν(cm^{-1}): 3384, 2922, 1634, 1597, 1494, 1259, 1216; ESI-MS found: 664 $(M+H)^+$; HRMS *m/z* calculated for $C_{37}H_{37}N_5NaO_7$ $(M+Na)^+$: 686.2585; Found: 686.2590.

H_2N-[*O*-Bn-(2-HABA)]-D-Trp-[*O*-*i*Pr-(2-HABA)]-Gly-CO_2H (131)

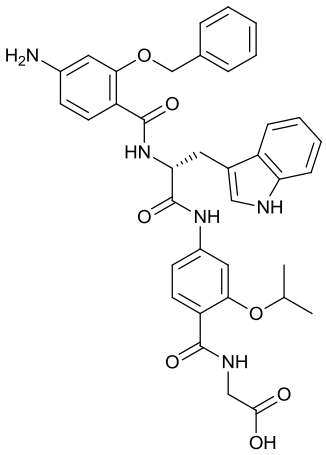

Brown solid, > 90% pure by NMR; isolated yield: 5.3 mg, 8%; R_f 0.083 (SiO_2, 20% methanol in acetonitrile); $[\alpha]_D^{28.3}$ = - 32.1° (c 0.003 g mL^{-1}, methanol); ^{1}H NMR (DMSO-d_6, 500 MHz) δ: 10.78 (s, 1 H, 3-D-Trp-NH'), 10.47 (s, 1H,1-Gly-CO_2H), 8.49 (t, *J* = 5 Hz, 1 H, 1-Gly-NH), 8.19 (d, *J* = 6.5 Hz, 1 H, 3- D-Trp-NH), 7.90 (d, *J* = 8.5 Hz, 1 H, 2-H6), 7.64 (d, *J* = 8.5 Hz, 1 H, 4-H6), 7.63 (s, 1 H, 2-H3), 7.55 (d, *J* = 8 Hz, 1 H, 3- D-Trp-HAr4), 7.45 (d, *J* = 7.5 Hz, 2 H, 4-HAr2), 7.36 (t, *J* = 7.5 Hz, 3 H, 4-H-Ar3, 4-HAr4), 7.28 (d, *J* = 8 Hz, 1 H, 3- D-Trp-HAr7), 7.28 (s, 1 H, 3- D-TrpHAr2), 7.22 (d, *J* = 8.5 Hz, 1 H, 2-H5), 7.05 (t, *J* = 7.5 Hz, 1H, 3- D-Trp-HAr6), 6.94 (t, *J* = 7.5 Hz, 1H, 3- D-Trp-HAr5), 6.72 (s, 1H, 2-NH), 6.32 (s, 1 H, 4-H3), 6.19 (d, *J* = 8Hz, 1 H, 4-H5), 5.78 (br, 2H, 4-NH_2), 5.17-5.08 (dd, *J* = 32.5, 11.5 Hz, 2 H, 4-Hα), 4.92-4.88 (dd, *J* = 11.5 , 6.5 Hz, 1 H, 3- D-Trp-Hα), 4.73-4.68 (apparent quin, *J* = 6.5 Hz, 1 H, 2-Hα), 4.05 (d, *J* = 5 Hz, 2 H, 1-Gly-H1), 3.17-3.15 (dd, *J* = 11.5 , 6.5 Hz, 2 H, 3- D-Trp-Hβ), 2.93-2.88 (dd, *J* = 11.5 , 6.5 Hz, 2 H, 3- D-Trp-Hβ'),1.43-1.40 (dd, *J* = 9.5, 6.5 Hz, 6 H, 2-Hβ) ppm; ^{13}C NMR (DMSO-d_6, 126 MHz) δ: 171.2 (1-Gly-CO), 166.3 (4-CO), 163.9 (2-CO), 156.2 (3- D-Trp-CO), 144.1 (4-C2), 143.2 (4-C4), 141.5 (2-C2), 137.22 (2-C4, 3- D-Trp-CAr3a), 136.0 (4-C6), 131.8 (2-C6), 128.4 (4-CAr3, 4-CAr4), 127.7 (4-CAr1), 127.4 (4-CAr2, 3- D-Trp-CAr3), 127.3 (3- D-Trp-CAr2), 123.7 (3- D-Trp-CAr7), 121.7 (3- D-Trp-CAr6), 120.9 (3- D-Trp-CAr4), 118.2 (3- D-Trp-CAr5), 116.5 (3- D-Trp-CAr7a), 112.3 (2-C5), 111.4 (2-C1, 4-C1), 110.2 (4-C5), 104.8 (2-C3), 92.7 (4-C3), 71.9 (2-Cα), 69.8 (4-Cα), 55.1 (3- D-Trp-Cα), 41.6 (1-Gly-C1), 28.8 (3- D-Trp-Cβ), 21.6 (2-Cβ) ppm; IR (neat) ν(cm^{-1}): 3357, 3191, 2923, 2851, 1692, 1631, 1594, 1493, 1258, 1213; ESI-MS found: 664 $(M+H)^+$; HRMS *m/z* calculated for $C_{37}H_{37}N_5NaO_7$ $(M+Na)^+$: 686.2585; Found: 686.2591.

H_2N-[*O*-Bn-(3-HABA)]-Phe-[*O*-*i*Pr-(2-HABA)]-[1-biotin-3-triazol-propyl-Gly]-CO_2H (132)

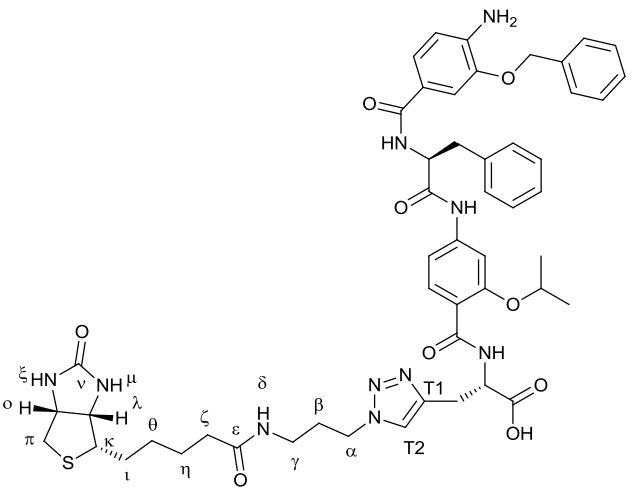

Fmoc-propargyl-Gly (168 mg, 5 equiv.) was dissolved in anhydrous DMF (5 mL), preactivated with HATU (380.29 mg, 10 equiv.) and DIPEA (328 μL, 20 equiv.) for 1 h at room temperature and loaded onto 119 mg of Wang resin (0.84 mmol g^{-1}, 100-200 mesh) using the CEM Liberty® automated microwave assisted peptide synthesiser (double coupling of 30 minutes, microwave heating at 60 °C). The following three units were coupled by employing the standard solid phase procedure described before. The loaded resin was then treated manually and suspended in 1 mL of anhydrous tetrahydrofuran. Azido biotin (32.6 mg, 1 equiv., synthesised by Dr A. Barnard), copper (II) sulphate pentahydrate (2.5 mg, 0.1 equiv.) and sodium ascorbate (3.96 mg, 0.2 equiv.) were added and the resin was allowed to spin at room temperature for 46 h. The resin was then dried and washed with water (3 mL, 5 min), dichloromethane (3 mL, 5 min) and diethyl ether (3 mL, 5 min). Cleavage of the resin and purification were carried out as described in the general solid phase procedure. Pale yellow solid, > 95% pure by NMR; isolated yield: 8.6 mg, 9%); R_f 0.55 (SiO_2, 20% methanol in acetonitrile); ^{1}H NMR (DMSO-d_6, 500 MHz) δ: 10.44 (s, 1 H,1-Prop-Gly-CO_2H), 8.65 (d, *J* = 6.5 Hz, 1 H, 1-Prop-Gly-NH), 8.34 (d, *J* = 8 Hz, 1 H, 3-Phe-NH), 7.91 (d, *J* = 8.5 Hz, 1 H, 2-H6), 7.87 (t, *J* = 5 Hz, 1 H, 1-Biotin-NHδ), 7.84 (s, 1H, 1-Triazol-H2), 7.58 (s, 1 H, 2-H3), 7.51 (d, *J* = 8.5 Hz, 2 H, 3-Phe-HAr2), 7.43 (s, 1 H, 4-H2), 7.42-7.39 (m, 5 H, 4-HAr2, 4-H-Ar4, 3-Phe-HAr3), 7.35 (br, 1H, 2-NH), 7.32 (d, *J* = 8.5 Hz, 1 H, 4-H6), 7.29-7.24 (m, 3 H, 4-HAr3, 2-H5), 7.19 (t, *J* = 7.5 Hz, 1H, 3-Phe-HAr4), 6.66 (d, *J* = 8.5 Hz, 1 H, 4-H5), 6.44 (br, 1H, 1-Biotin-NHξ), 6.37 (br, 1H, 1-Biotin-NHμ), 5.33 (br, 2H, 4-NH_2), 5.16 (s, 2 H, 4-Hα), 4.84-4.78 (dd, *J* = 8 , 5.5 Hz, 1 H, 3-Phe-Hα), 4.75 (br, 1 H, 1-Prop-Gly-Hα), 4.69-4.64 (apparent quin, *J* = 6 Hz, 1 H, 2-Hα), 4.32-

4.29 (m, 3H, 1-Biotin-Hα, 1-Biotin-Hλ), 4.32-4.29 (dd, *J* = 12.5 , 6.5 Hz, 1H, 1-Biotin-Ho), 3.22-3.19 (dd, *J* = 8 , 5.5 Hz, 2 H, 3-Phe-Hβ), 3.13-3.09 (dd, *J* = 12.5 , 6.5 Hz, 2 H, 1-Biotin-Hπ), 3.04-3.01 (dd, *J* = 13.5 , 6.5 Hz, 2 H, 1-Biotin-Hγ), 2.84-2.80 (dd, *J* = 13.5 , 7 Hz, 1H, 1-Prop-Gly-Hβ), 2.59-2.56 (dd, *J* = 13.5 , 7 Hz, 1H, 1-Prop-Gly-Hβ'), 2.07 (t, *J* = 5 Hz, 2 H, 1-Biotin-Hζ), 2.02-1.99 (dd, *J* = 12.5 , 6 Hz, 2 H, 1-Biotin-Hβ), 1.91-1.87 (m, 3 H, 1-Biotin-Hι, 1-Biotin-Hκ), 1.52-1.46 (m, 4 H, 1-Biotin-Hθ, 1-Biotin-Hη),1.33-1.29 (dd, *J* = 8.5, 6 Hz, 6 H, 2-Hβ) ppm; ^{13}C NMR (DMSO-d_6, 126 MHz) δ: 172.1 (1-Biotin-COν), 171.4 (1-Gly-CO), 169.6 (4-CO), 166.4 (2-CO), 162.9 (1-Biotin-COε), 156.2 (3-Phe-CO), 144.0 (4-C3), 143.1 (2-C2), 141.5 (4-C4), 138.2 (2-C4), 137.2 (2-C6), 132.0 (1-Triazol-C1), 129.6 (4-CAr1), 129.2 (3-Phe-CAr3), 128.4 (4-CAr2, 4-CAr3), 128.1 (4-CAr4), 127.7 (4-C2), 127.4 (3-Phe-CAr2, 3-Phe-CAr4), 126.3 (3-Phe-CAr1), 121.8 (4-C6), 120.8 (4-C1), 119.8 (1-Triazol-C2), 116.5 (2-C1), 112.3 (4-C5), 111.2 (2-C5), 104.5 (2-C3), 71.7 (2-Cα), 69.4 (4-Cα), 61.0 (1-Biotin-Co), 59.2 (1-Biotin-Cλ), 55.8 (3-Phe-Cα), 55.4 (1-Prop-Gly-Cα), 47.0 (1-Biotin-Cα), 40.5 (1-Prop-Gly-Cβ), 37.1 (3-Phe-Cβ), 35.6 (1-Biotin-Cπ), 35.1 (1-Biotin-Cγ, 1-Biotin-Cζ), 30.1 (1-Biotin-Cι), 29.0 (1-Biotin-Cκ), 28.2 (1-Biotin-Cβ), 25.2 (1-Biotin-Cη, 1-Biotin-Cθ), 21.4 (2-Cβ) ppm; IR (neat) ν (cm^{-1}): 3356, 2924, 2852, 1683, 1631, 1594, 1494, 1259, 1215; ESI-MS found: 989 $(M+H)^+$; HRMS *m/z* calculated for $C_{51}H_{60}N_{10}NaO_9S$ $(M+Na)^+$: 1011.4158; Found: 1011.4167.

6.2.3 Proteolytic studies

α-Chymotrypsin Type II from bovine pancreas (lyophilized powder, MW = 25 kDa, ≥ 40 units/mg protein), Proteinase K from *Tritirachium album* (lyophilized powder, MW = 28.93 kDa, ≥ 30 units/mg protein) and Trypsin IV-O from chicken egg white (lyophilized powder, MW = 20 kDa, ≥ 20 units/mg protein) were purchased from Sigma-Aldrich and used without further purification.

Hybrid **75** (Figure 6.6 b-d) and WT-p53(Figure 6.7 b-d) (200 μM stock in PBS buffer pH 7.50, 2% DMSO) were treated with the chosen enzyme (0.02 μM stock solutions in PBS buffer pH 7.50) in a 1:10000 enzyme/substrate ratio. Hybrid **75** was further

treated with α-Chymotrypsin increasing the ratio enzyme/substrate to 1:1000 and 1:100 (α-chymotripsin 0.2 μM and 2 μM stock solutions in PBS buffer pH 7.50). The degradation was followed with analytical HPLC (Ascentis® Express Peptide Column, injection volume: 20 μL, acetonitrile/water (0.1% TFA) 5-95% gradient) and the data was analysed to extract kinetic values. To minimize variability, the area of the peak corresponding to DMSO was used as internal reference for correction. A control was also run treating hybrid **75** and WT-p53 with no enzyme (Figure 6.6 a, Figure 6.7 a).

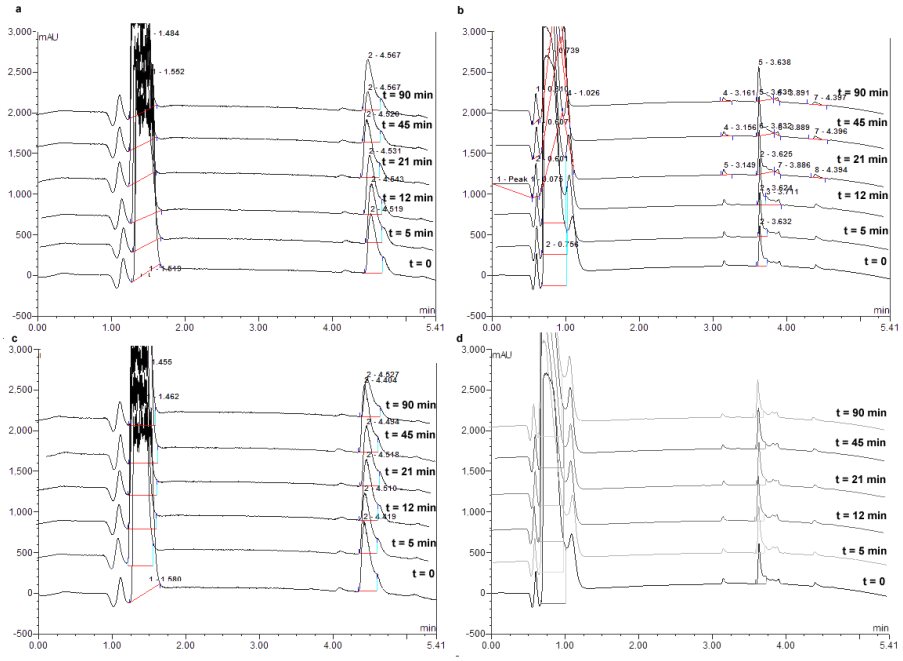

Figure 6.6 Proteolytic study on hybrid 75 a Analytical HPLC trace for **75** treated with no enzyme; **b** Analytical HPLC trace for **75** treated with Trypsin; **c** Analytical HPLC trace for **75** treated with Proteinase K; **d** Analytical HPLC trace for **75** treated with α-Chymotrypsin.

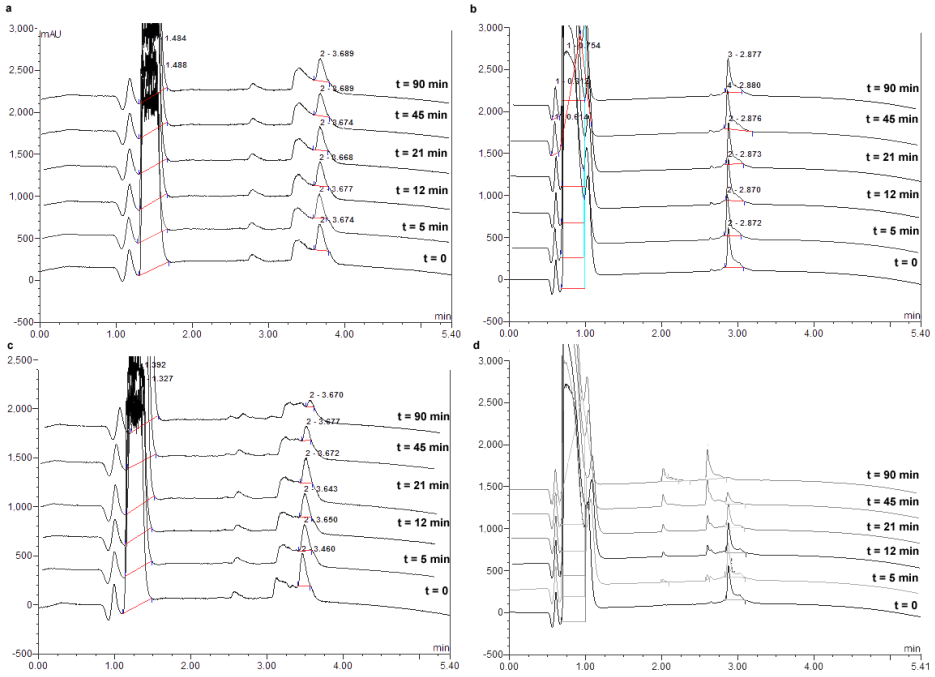

Figure 6.7 Proteolytic study on WT-p53 a Analytical HPLC trace for WT-p53 treated with no enzyme; **b** Analytical HPLC trace for WT-p53 treated with Trypsin; **c** Analytical HPLC trace for WT-p53 treated with Proteinase K; **d** Analytical HPLC trace for WT-p53 treated with α-Chymotrypsin.

6.3 Biophysical assessment of proteomimetics (Chapters 3 and 4, Appendix I)

6.3.1 Proteins expression and purification

The pET14b vector containing *h*DM2 (17-126) L33E was kindly provided by John Robinson (University of Zurich). The protein was expressed in *E.coli* BL21 (DE3) GOLD and purified by Dr J. Miles, Dr K. Long or Dr A. Bartlett following previously published methods.[99,105] The purified *h*DM2 (17-126) L33E was concentrated (typically to ~ 100 μM) and stored at – 80 °C.

The pet28a His-SUMO Mcl-1 (172-327) construct was over-expressed in the *E.coli* strain Rosetta and purified by Dr J. Miles or Dr A. Bartlett. The purified Mcl-1 (172-327) was concentrated (typically to ~ 200 μM) and stored at – 80 °C.

6.3.2 Fluorescence anisotropy assays

WT-p53(15-31) transactivation domain peptide and its fluorescein-labelled analogue p53 (15-31) Flu were purchased from Peptide Protein Research Ltd and used without further purification. WT-NOXA B (68-87) and its fluorescein-labelled analogue FITC-NOXA B (68-87) were synthesised and purified by Dr P. Prabhakaran and D.J. Yeo. Fluorescence anisotropy assays were performed in 96- or 384-well plates (Greiner Bio-one). Each experiment was run in triplicate and the fluorescence anisotropy measured using a Perkin Elmer EnVision^{TM} 2103 MultiLabel plate reader, with excitation at 480 nm (30 nM bandwidth), polarised dichroic mirror at 505 nm and emission at 535 nm (40 nM bandwidth, *S* and *P* polarised).

All experiments were performed in assay buffer: 40 mM phosphate buffer at pH 7.50, containing 200 mM NaCl and 0.02 mg mL^{-1} *bovine serum albumin* (BSA) and data analysed following previously published methods.[99,105]

Determining the binding of p53 to *h*DM2

A stock of *h*DM2 was prepared by diluting the concentrated protein into assay buffer and used to prepare a serial dilution of *h*DM2 (starting point: 10 μM) across the plate (24-points, 2/3 serial dilution). Tracer peptide (p53 (15-31) Flu) was then added to each well to give a final concentration of 54.5 nM. For control wells, the tracer peptide was replaced with an identical volume of assay buffer. The experiments were performed in 96-well plates and the total volume in each well was 150 μL. The data for both the *P* (perpendicular intensity) and *S* (parallel (same) intensity) channels were corrected by subtracting the corresponding control wells and plotted using Origin 7.5.

Determining the binding of NOXA B to Mcl-1

A stock of Mcl-1 was prepared by diluting the concentrated protein into assay buffer and used to prepare a serial dilution of Mcl-1 (starting point: 5 μM) across the plate (24-points, 2/3 serial dilution). Tracer peptide (FITC-NOXA B) was then added to each well to give a final concentration of 50 nM. For control wells, the tracer peptide was replaced with an identical volume of assay buffer. The experiments were performed in 96-well plates and the total volume in each well was 150 μL. The data

for both the *P* and *S* channels were corrected by subtracting the corresponding control wells and plotted using Origin Pro 9.0.

Competition assays

Stocks of ligand (450 μM for 2-*O*-alkylated oligobenzamides and 400 μM for hybrid α-helix mimetics in 90:10 (v/v) assay buffer: DMSO) were used to prepare serial dilution across the plate (starting point: 100 μM; 2-*O*-alkylated oligobenzamides: 24-points, 2/3 serial dilution; hybrid α-helix mimetics: 18-points, 3/4 serial dilution).

For the p53/*h*DM2 FA competition assay, p53 (15-31) Flu and *h*DM217-126 L33E were then added to each well to give a final concentration of 54.5 nM and 154.2 nM, respectively. For the Mcl-1/NOXAB FA competition assay, FITC-NOXAB (68-87) and Mcl-1 (172-327) were added to each well to give a final concentration of 50 nM and 150 nM, respectively. For control wells the tracer peptide was replaced with an identical volume of assay buffer. The total volume in each well was 150 μL for 96-well plates and 60 μL for 384-well plates. The data for both the *P* and *S* channel were corrected by subtracting the corresponding control wells and plotted using Origin Pro 9.0.

References

1 V. Azzarito, K. Long, N. S. Murphy, A. J. Wilson, *Nat Chem* **2013**, *5*, 161-173.

2 S. K. Sia, P. A. Carr, A. G. Cochran, V. N. Malashkevich, P. S. Kim, *Proc. Natl. Acad. Sci. U. S. A.* **2002**, *99*, 14664-14669.

3 M. Sattler, H. Liang, D. Nettesheim, R. P. Meadows, J. E. Harlan, M. Eberstadt, H. S. Yoon, S. B. Shuker, B. S. Chang, A. J. Minn, C. B. Thompson, S. W. Fesik, *Science* **1997**, *275*, 983-986.

4 P. H. Kussie, S. Gorina, V. Marechal, B. Elenbaas, J. Moreau, A. J. Levine, N. P. Pavletich, *Science* **1996**, *274*, 948-953.

5 H. Yin, A. D. Hamilton, *Angew. Chem. Int. Ed.* **2005**, *44*, 4130-4163.

6 S. Jones, J. M. Thornton, *Proc. Natl. Acad. Sci. U. S. A.* **1996**, *93*, 13-20.

7 B. Y. Ma, M. Shatsky, H. J. Wolfson, R. Nussinov, *Prot. Sci.* **2002**, *11*, 184-197.

8 W. E. Stites, *Chem. Rev.* **1997**, *97*, 1233-1250.

9 O. Keskin, A. Gursoy, B. Ma, R. Nussinov, *Chem. Rev.* **2008**, *108*, 1225-1244.

10 L. T. Vassilev, B. T. Vu, B. Graves, D. Carvajal, F. Podlaski, Z. Filipovic, N. Kong, U. Kammlott, C. Lukacs, C. Klein, N. Fotouhi, E. A. Liu, *Science* **2004**, *303*, 844-848.

11 D. J. Parks, L. V. LaFrance, R. R. Calvo, K. L. Milkiewicz, V. Gupta, J. Lattanze, K. Ramachandren, T. E. Carver, E. C. Petrella, M. D. Cummings, D. Maguire, B. L. Grasberger, T. B. Lu, *Bioorg. Med. Chem.* **2005**, *15*, 765-770.

12 A. M. Petros, J. Dinges, D. J. Augeri, S. A. Baumeister, D. A. Betebenner, M. G. Bures, S. W. Elmore, P. J. Hajduk, M. K. Joseph, S. K. Landis, D. G. Nettesheim, S. H. Rosenberg, W. Shen, S. Thomas, X. L. Wang, I. Zanze, H. C. Zhang, S. W. Fesik, *J. Med. Chem.* **2006**, *49*, 656-663.

13 M. Bruncko, T. K. Oost, B. A. Belli, H. Ding, M. K. Joseph, A. Kunzer, D. Martineau, W. J. McClellan, M. Mitten, S. C. Ng, P. M. Nimmer, T. Oltersdorf, C. M. Park, A. M. Petros, A. R. Shoemaker, X. H. Song, X. L. Wang, M. D. Wendt, H. C. Zhang, S. W. Fesik, S. H. Rosenberg, S. W. Elmore, *J. Med. Chem.* **2007**, *50*, 641-662.

14 T. Clackson, J. A. Wells, *Science* **1995**, *267*, 383-386.

15 B. N. Bullock, A. L. Jochim, P. S. Arora, *J. Am. Chem. Soc.* **2011**, *133*, 14220-14223.

16 D. Voet, Voet, J. G., *Biochemistry*. 3rd ed., Editor, Wiley, **2004**.

17 T. Edwards, A. Wilson, *Amino Acids* **2011**, 1-12.

18 B. P. Orner, J. T. Ernst, A. D. Hamilton, *J. Am. Chem. Soc.* **2001**, *123*, 5382-5383.

19 A. J. Wilson, *Chem. Soc. Rev.* **2009**, *38*, 3289-3300.

20 M. P. H. Stumpf, T. Thorne, E. de Silva, R. Stewart, H. J. An, M. Lappe, C. Wiuf, *Proc. Natl. Acad. Sci.* **2008**, *105*, 6959-6964.

21 C. M. Croce, *N. Eng. J. Med.* **2008**, *358*, 502-511.

22 M. Oren, *Cell Death Differ.* **2003**, *10*, 431-442.

23 A. J. Levine, W. Hu, Z. Feng, *Cell Death Differ.* **2006**, *13*, 1027-1036.

24 S. M. Picksley, B. Vojtesek, A. Sparks, D. P. Lane, *Oncogene* **1994**, *9*, 2523-2529.

25 A. M. Petros, E. T. Olejniczak, S. W. Fesik, *Biochimica et Biophysica Acta (BBA) - Molecular Cell Research* **2004**, *1644*, 83-94.

26 L. Chen, S. N. Willis, A. Wei, B. J. Smith, J. I. Fletcher, M. G. Hinds, P. M. Colman, C. L. Day, J. M. Adams, D. C. S. Huang, *Mol. Cell.* **2005**, *17*, 393-403.

27 P. E. Czabotar, E. F. Lee, M. F. van Delft, C. L. Day, B. J. Smith, D. C. S. Huang, W. D. Fairlie, M. G. Hinds, P. M. Colman, *Proc. Natl. Acad. Sci.* **2007**, *104*, 6217-6222.

28 E. Oda, R. Ohki, H. Murasawa, J. Nemoto, T. Shibue, T. Yamashita, T. Tokino, T. Taniguchi, N. Tanaka, *Science* **2000**, *288*, 1053-1058.

29 I. Huc, *Eur. J. Org. Chem.* **2004**, *1*, 17-29.

30 A. S. Ripka, D. H. Rich, *Curr. Opin. Chem. Biol.* **1998**, *2*, 441-452.

31 S. H. Gellman, *Acc. Chem. Res.* **1998**, *31*, 173-180.

32 E. A. Harker, D. S. Daniels, D. A. Guarracino, A. Schepartz, *Bioorg. Med. Chem.* **2009**, *17*, 2038-2046.

33 L. D. Walensky, A. L. Kung, I. Escher, T. J. Malia, S. Barbuto, R. D. Wright, G. Wagner, G. L. Verdine, S. J. Korsmeyer, *Science* **2004**, *305*, 1466-1470.

34 B. L. Grasberger, T. B. Lu, C. Schubert, D. J. Parks, T. E. Carver, H. K. Koblish, M. D. Cummings, L. V. LaFrance, K. L. Milkiewicz, R. R. Calvo, D. Maguire, J. Lattanze, C. F. Franks, S. Y. Zhao, K. Ramachandren, G. R. Bylebyl, M. Zhang, C. L. Manthey, E. C. Petrella, M. W. Pantoliano, I. C. Deckman, J. C. Spurlino, A. C.

Maroney, B. E. Tomczuk, C. J. Molloy, R. F. Bone, *J. Med. Chem.* **2005**, *48*, 909-912.

35 C. Tse, A. R. Shoemaker, J. Adickes, M. G. Anderson, J. Chen, S. Jin, E. F. Johnson, K. C. Marsh, M. J. Mitten, P. Nimmer, L. Roberts, S. K. Tahir, Y. Xiao, X. Yang, H. Zhang, S. Fesik, S. H. Rosenberg, S. W. Elmore, *Cancer Res.* **2008**, *68*, 3421-3428.

36 H. Zhou, J. Chen, J. L. Meagher, C.-Y. Yang, A. Aguilar, L. Liu, L. Bai, X. Cong, Q. Cai, X. Fang, J. A. Stuckey, S. Wang, *J. Med. Chem.* **2012**, *55*, 4664-4682.

37 H. Zhou, A. Aguilar, J. Chen, L. Bai, L. Liu, J. L. Meagher, C.-Y. Yang, D. McEachern, X. Cong, J. A. Stuckey, S. Wang, *J. Med. Chem.* **2012**, *55*, 6149-6161.

38 G. Wang, Z. Nikolovska-Coleska, C.-Y. Yang, R. Wang, G. Tang, J. Guo, S. Shangary, S. Qiu, W. Gao, D. Yang, J. Meagher, J. Stuckey, K. Krajewski, S. Jiang, P. P. Roller, H. O. Abaan, Y. Tomita, S. Wang, *J. Med. Chem.* **2006**, *49*, 6139-6142.

39 R. M. Mohammad, A. S. Goustin, A. Aboukameel, B. Chen, S. Banerjee, G. Wang, Z. Nikolovska-Coleska, S. Wang, A. Al-Katib, *Clin. Cancer Res.* **2007**, *13*, 2226-2235.

40 Z. Wang, A. S. Azmi, A. Ahmad, S. Banerjee, S. Wang, F. H. Sarkar, R. M. Mohammad, *Cancer Res.* **2009**, *69*, 2757-2765.

41 S. Shangary, D. Qin, D. McEachern, M. Liu, R. S. Miller, S. Qiu, Z. Nikolovska-Coleska, K. Ding, G. Wang, J. Chen, D. Bernard, J. Zhang, Y. Lu, Q. Gu, R. B. Shah, K. J. Pienta, X. Ling, S. Kang, M. Guo, Y. Sun, D. Yang, S. Wang, *Proc. Natl. Acad. Sci.* **2008**, *105*, 3933-3938.

42 B. Leader, Q. J. Baca, D. E. Golan, *Nat Rev Drug Discov* **2008**, *7*, 21-39.

43 J. M. Scholtz, R. L. Baldwin, *Annu. Rev. Biophys. Biomol. Structure* **1992**, *21*, 95-118.

44 S. A. Marshall, G. A. Lazar, A. J. Chirino, J. R. Desjarlais, *Drug Discov. Today* **2003**, *8*, 212-221.

45 D. Seebach, S. Abele, J. V. Schreiber, B. Martinoni, A. K. Nussbaum, H. Schild, H. Schulz, H. Hennecke, R. Woessner, F. Bitsch, *Chimia* **1998**, *52*, 734-739.

46 J. D. Glickson, Applequi.J, *J. Am. Chem. Soc.* **1971**, *93*, 3276-3281.

47 R. P. Cheng, S. H. Gellman, W. F. DeGrado, *Chem. Rev.* **2001**, *101*, 3219-3232.

48 D. Seebach, M. Overhand, F. N. M. Kuhnle, B. Martinoni, L. Oberer, U. Hommel, H. Widmer, *Helv. Chim. Acta* **1996**, *79*, 913-941.

49 E. P. English, R. S. Chumanov, S. H. Gellman, T. Compton, *J. Biol. Chem.* **2006**, *281*, 2661-2667.

50 J. D. Sadowsky, W. D. Fairlie, E. B. Hadley, H. S. Lee, N. Umezawa, Z. Nikolovska-Coleska, S. M. Wang, D. C. S. Huang, Y. Tomita, S. H. Gellman, *J. Am. Chem. Soc.* **2007**, *129*, 139-154.

51 D. H. Appella, L. A. Christianson, I. L. Karle, D. R. Powell, S. H. Gellman, *J. Am. Chem. Soc.* **1996**, *118*, 13071-13072.

52 J. D. Sadowsky, J. K. Murray, Y. Tomita, S. H. Gellman, *ChemBioChem* **2007**, *8*, 903-916.

53 D. H. Appella, L. A. Christianson, D. A. Klein, D. R. Powell, X. L. Huang, J. J. Barchi, S. H. Gellman, *Nature* **1997**, *387*, 381-384.

54 E. F. Lee, J. D. Sadowsky, B. J. Smith, P. E. Czabotar, K. J. Peterson-Kaufman, P. M. Colman, S. H. Gellman, W. D. Fairlie, *Angew. Chem. Int. Ed.* **2009**, *48*, 4318-4322.

55 W. S. Horne, M. D. Boersma, M. A. Windsor, S. H. Gellman, *Angew. Chem. Int. Ed.* **2008**, *47*, 2853-2856.

56 E. F. Lee, B. J. Smith, W. S. Horne, K. N. Mayer, M. Evangelista, P. M. Colman, S. H. Gellman, W. D. Fairlie, *ChemBioChem* **2011**, *12*, 2025-2032.

57 W. S. Horne, L. M. Johnson, T. J. Ketas, P. J. Klasse, M. Lu, J. P. Moore, S. H. Gellman, *Proc. Natl. Acad. Sci. USA* **2009**, *106*, 14751-14756.

58 H. E. Blackwell, R. H. Grubbs, *Angew. Chem. Int. Ed.* **1998**, *37*, 3281-3284.

59 G. L. Verdine, C. E. Schafmeister, US US8324428 B2, **2012**.

60 M. L. Stewart, E. Fire, A. E. Keating, L. D. Walensky, *Nat. Chem. Biol.* **2010**, *6*, 595-601.

61 S. Baek, P. S. Kutchukian, G. L. Verdine, R. Huber, T. A. Holak, K. W. Lee, G. M. Popowicz, *J. Am. Chem. Soc.* **2011**, *134*, 103-106.

62 C. Phillips, L. R. Roberts, M. Schade, R. Bazin, A. Bent, N. L. Davies, R. Moore, A. D. Pannifer, A. R. Pickford, S. H. Prior, C. M. Read, A. Scott, D. G. Brown, B. Xu, S. L. Irving, *J. Am. Chem. Soc.* **2011**, *133*, 9696-9699.

63 R. E. Moellering, M. Cornejo, T. N. Davis, C. Del Bianco, J. C. Aster, S. C. Blacklow, A. L. Kung, D. G. Gilliland, G. L. Verdine, J. E. Bradner, *Nature* **2009**, *462*, 182-188.

64 G. H. Bird, N. Madani, A. F. Perry, A. M. Princiotto, J. G. Supko, X. He, E. Gavathiotis, J. G. Sodroski, L. D. Walensky, *Proc. Natl. Acad. Sci.* **2010**, *107*, 14093-14098.

65 D. J. Yeo, S. L. Warriner, A. J. Wilson, *Chem. Commun.* **2013**, *49*, 9131-9133.

66 M. Chorev, E. Roubini, R. L. McKee, S. W. Gibbons, M. E. Goldman, M. P. Caulfield, M. Rosenblatt, *Biochemistry* **1991**, *30*, 5968-5974.

67 J. K. Judice, J. Y. K. Tom, W. Huang, T. Wrin, J. Vennari, C. J. Petropoulos, R. S. McDowell, *Proc. Natl. Acad. Sci. U. S. A.* **1997**, *94*, 13426-13430.

68 T. R. Geistlinger, R. K. Guy, *J. Am. Chem. Soc.* **2003**, *125*, 6852-6853.

69 R. S. Harrison, N. E. Shepherd, H. N. Hoang, G. Ruiz-Gomez, T. A. Hill, R. W. Driver, V. S. Desai, P. R. Young, G. Abbenante, D. P. Fairlie, *Proc. Natl. Acad. Sci. U. S. A.* **2010**, *107*, 11686-11691.

70 A. M. Leduc, J. O. Trent, J. L. Wittliff, K. S. Bramlett, S. L. Briggs, N. Y. Chirgadze, Y. Wang, T. P. Burris, A. F. Spatola, *Proc. Natl. Acad. Sci. U. S. A.* **2003**, *100*, 11273-11278.

71 R. N. Chapman, G. Dimartino, P. S. Arora, *J. Am. Chem. Soc.* **2004**, *126*, 12252-12253.

72 D. Y. Wang, W. Liao, P. S. Arora, *Angew. Chem. Int. Ed.* **2005**, *44*, 6525-6529.

73 D. Wang, M. Lu, P. S. Arora, *Angew. Chem. Int. Ed.* **2008**, *47*, 1879-1882.

74 L. K. Henchey, S. Kushal, R. Dubey, R. N. Chapman, B. Z. Olenyuk, P. S. Arora, *J. Am. Chem. Soc.* **2010**, *132*, 941-943.

75 A. Patgiri, K. K. Yadav, P. S. Arora, D. Bar-Sagi, *Nat Chem Biol* **2011**, *7*, 585-587.

76 S. Kneissl, E. J. Loveridge, C. Williams, M. P. Crump, R. K. Allemann, *ChemBioChem* **2008**, *9*, 3046-3054.

77 D. C. Horwell, W. Howson, W. P. Nolan, G. S. Ratcliffe, D. C. Rees, H. M. G. Willems, *Tetrahedron* **1995**, *51*, 203-216.

78 J. T. Ernst, O. Kutzki, A. K. Debnath, S. Jiang, H. Lu, A. D. Hamilton, *Angew. Chem. Int. Ed.* **2002**, *41*, 278-281.

79 O. Kutzki, H. S. Park, J. T. Ernst, B. P. Orner, H. Yin, A. D. Hamilton, *J. Am. Chem. Soc.* **2002**, *124*, 11838-11839.

80 H. Yin, G.-i. Lee, K. A. Sedey, O. Kutzki, H. S. Park, B. P. Orner, J. T. Ernst, H.-G. Wang, S. M. Sebti, A. D. Hamilton, *J. Am. Chem. Soc.* **2005**, *127*, 10191-10196.

81 I. Saraogi, A. D. Hamilton, *Biochem. Soc. Trans.* **2008**, *36*, 1414-1417.

82 H. Oguri, A. Oomura, S. Tanabe, M. Hirama, *Tetrahedron Lett.* **2005**, *46*, 2179-2183.

83 P. Maity, B. Konig, *Org. Lett.* **2008**, *10*, 1473-1476.

84 P. Restorp, J. Rebek Jr, *Bioorg. Med. Chem.* **2008**, *18*, 5909-5911.

85 J. M. Davis, A. Truong, A. D. Hamilton, *Org. Lett.* **2005**, *7*, 5405-5408.

86 H. Yin, G. I. Lee, K. A. Sedey, J. M. Rodriguez, H. G. Wang, S. M. Sebti, A. D. Hamilton, *J. Am. Chem. Soc.* **2005**, *127*, 5463-5468.

87 J. M. Rodriguez, L. Nevola, N. T. Ross, G. I. Lee, A. D. Hamilton, *ChemBioChem* **2009**, *10*, 829-833.

88 J. M. Rodriguez, N. T. Ross, W. P. Katt, D. Dhar, G.-i. Lee, A. D. Hamilton, *ChemMedChem* **2009**, *4*, 649-656.

89 J. M. Rodriguez, A. D. Hamilton, *Angew. Chem. Int. Ed.* **2007**, *46*, 8614-8617.

90 S. M. Biros, L. Moisan, E. Mann, A. Carella, D. Zhai, J. C. Reed, J. Rebek, *Bioorg. Med. Chem.* **2007**, *17*, 4641-4645.

91 C. G. Cummings, N. T. Ross, W. P. Katt, A. D. Hamilton, *Org. Lett.* **2009**, *11*, 25-28.

92 V. Berl, I. Huc, R. G. Khoury, J. M. Lehn, *Chem.Eur. J.* **2001**, *7*, 2798-2809.

93 J. T. Ernst, J. Becerril, H. S. Park, H. Yin, A. D. Hamilton, *Angew. Chem. Int. Ed.* **2003**, *42*, 535-539.

94 I. Saraogi, J. A. Hebda, J. Becerril, L. A. Estroff, A. D. Miranker, A. D. Hamilton, *Angew. Chem. Int. Ed.* **2010**, *49*, 736-739.

95 I. Saraogi, C. D. Incarvito, A. D. Hamilton, *Angew. Chem. Int. Ed.* **2008**, *47*, 9691-9694.

96 J. L. Yap, X. Cao, K. Vanommeslaeghe, K.-Y. Jung, C. Peddaboina, P. T. Wilder, A. Nan, A. D. MacKerell, W. R. Smythe, S. Fletcher, *Org. Biomol. Chem.* **2012**, *10*, 2928-2933.

97 X. Cao, J. Yap, M. Newell-Rogers, C. Peddaboina, W. Jiang, H. Papaconstantinou, D. Jupitor, A. Rai, K.-Y. Jung, R. Tubin, W. Yu, K. Vanommeslaeghe, P. Wilder, A. MacKerell, S. Fletcher, R. Smythe, *Mol. Cancer* **2013**, *12*, 42-58.

98 J. Plante, F. Campbell, B. Malkova, C. Kilner, S. L. Warriner, A. J. Wilson, *Org. Biomol. Chem.* **2008**, *6*, 138-146.

99 J. P. Plante, T. Burnley, B. Malkova, M. E. Webb, S. L. Warriner, T. A. Edwards, A. J. Wilson, *Chem. Commun.* **2009**, 5091-5093.

100 N. S. Murphy, P. Prabhakaran, V. Azzarito, J. P. Plante, M. J. Hardie, C. A. Kilner, S. L. Warriner, A. J. Wilson, *Chem. Eur. J.* **2013**, *19*, 5546-5550.

101 J. M. Ahn, S. Y. Han, *Tetrahedron Lett.* **2007**, *48*, 3543-3547.

102 A. Shaginian, L. R. Whitby, S. Hong, I. Hwang, B. Farooqi, M. Searcey, J. C. Chen, P. K. Vogt, D. L. Boger, *J. Am. Chem. Soc.* **2009**, *131*, 5564-5572.

103 L. R. Whitby, K. E. Boyle, L. Cai, X. Yu, M. Gochin, D. L. Boger, *Bioorg. Med. Chem.* **2012**, *22*, 2861-2865.

104 P. Prabhakaran, A. Barnard, N. S. Murphy, C. A. Kilner, T. A. Edwards, A. J. Wilson, *Eur. J. Org. Chem.* **2013**, *2013*, 3504-3512.

105 F. Campbell, J. P. Plante, T. A. Edwards, S. L. Warriner, A. J. Wilson, *Org. Biomol. Chem.* **2010**, *8*, 2344-2351.

106 K. Long, T. A. Edwards, A. J. Wilson, *Bioorg. Med. Chem.* **2013**, *21*, 4034-4040.

107 F. Lu, S.-W. Chi, D.-H. Kim, K.-H. Han, I. D. Kuntz, R. K. Guy, *J. Comb. Chem.* **2006**, *8*, 315-325.

108 T. Shahian, G. M. Lee, A. Lazic, L. A. Arnold, P. Velusamy, C. M. Roels, R. K. Guy, C. S. Craik, *Nat Chem Biol* **2009**, *5*, 640-646.

109 J. H. Lee, Q. Zhang, S. Jo, S. C. Chai, M. Oh, W. Im, H. Lu, H. S. Lim, *J. Am. Chem. Soc.* **2011**, *133*, 676-679.

110 I. C. Kim, A. D. Hamilton, *Org. Lett.* **2006**, *8*, 1751-1754.

111 S. Marimganti, M. N. Cheemala, J. M. Ahn, *Org. Lett.* **2009**, *11*, 4418-4421.

112 J. A. Wells, C. L. McClendon, *Nature* **2007**, *450*, 1001-1009.

113 J. Becerril, A. D. Hamilton, *Angew. Chem. Int. Ed.* **2007**, *46*, 4471-4473.

114 P. Tosovska, P. S. Arora, *Org. Lett.* **2010**, *12*, 1588-1591.

115 S. Broch, B. Aboab, F. Anizon, P. Moreau, *Eur. Jour. Med. Chem.* **2010**, *45*, 1657-1662.

116 G. A. Jeffrey, Saenger, W. , *Hydrogen Bonding in Biological Structures*. Editor, Springer, Berlin, **1991**.

117 P. Prabhakaran, V. Azzarito, T. Jacobs, M. J. Hardie, C. A. Kilner, T. A. Edwards, S. L. Warriner, A. J. Wilson, *Tetrahedron* **2012**, *68*, 4485-4491.

118 V. Azzarito, P. Prabhakaran, A. I. Bartlett, N. S. Murphy, M. J. Hardie, C. A. Kilner, T. A. Edwards, S. L. Warriner, A. J. Wilson, *Org. Biomol. Chem.* **2012**, *10*, 6469-6472.

119 J. A. Patch, A. E. Barron, *Curr. Opin. Chem. Biol.* **2002**, *6*, 872-877.

120 A. D. Bautista, C. J. Craig, E. A. Harker, A. Schepartz, *Curr. Opin. Chem. Biol.* **2007**, *11*, 685-692.

121 I. Huc, V. Maurizot, H. Gornitzka, J. M. Leger, *Chem. Commun.* **2002**, 578-579.

122 C. M. Goodman, S. Choi, S. Shandler, W. F. DeGrado, *Nat. Chem. Biol.* **2007**, *3*, 252-262.

123 H. Yin, G. I. Lee, H. S. Park, G. A. Payne, J. M. Rodriguez, S. M. Sebti, A. D. Hamilton, *Angew. Chem. Int. Ed.* **2005**, *44*, 2704-2707.

124 M. C. Etter, *Acc. Chem. Res.* **1990**, *23*, 120-126.

125 J. Bernstein, R. E. Davis, L. Shimoni, N.-L. Chang, *Angew. Chem. Int. Ed.* **1995**, *34*, 1555-1573.

126 A. Stanislaus, B. H. Cooper, *Catal. Rev. - Sci. Eng.* **1994**, *36*, 75-123.

127 F. D. Bellamy, K. Ou, *Tetrahedron Lett.* **1984**, *25*, 839-842.

128 I. Azumaya, T. Okamoto, F. Imabeppu, H. Takayanagi, *Tetrahedron* **2003**, *59*, 2325-2331.

129 Y. Hamuro, S. J. Geib, A. D. Hamilton, *J. Am. Chem. Soc.* **1996**, *118*, 7529-7541.

130 C. A. Hunter, J. K. M. Sanders, *J. Am. Chem. Soc.* **1990**, *112*, 5525-5534.

131 Y. Kodama, K. Nishihata, M. Nishio, N. Nakagawa, *Tetrahedron Lett.* **1977**, *18*, 2105-2108.

132 Y. Umezawa, S. Tsuboyama, H. Takahashi, J. Uzawa, M. Nishio, *Tetrahedron* **1999**, *55*, 10047-10056.

133 O. V. Kulikov, C. Incarvito, A. D. Hamilton, *Tetrahedron Lett.* **2011**, *52*, 3705-3709.

134 F. Mohamadi, N. G. J. Richards, W. C. Guida, R. Liskamp, M. Lipton, C. Caufield, G. Chang, T. Hendrickson, W. C. Still, *J. Comput. Chem.* **1990**, *11*, 440-467.

135 B. Kuhn, P. Mohr, M. Stahl, *J. Med. Chem.* **2010**, *53*, 2601-2611.

136 Y. Hamuro, S. J. Geib, A. D. Hamilton, *J. Am. Chem. Soc.* **1997**, *119*, 10587-10593.

137 B. Huang, J. R. Parquette, *J. Am. Chem. Soc.* **2001**, *123*, 2689-2690.

138 L. R. Steffel, T. J. Cashman, M. H. Reutershan, B. R. Linton, *J. Am. Chem. Soc.* **2007**, *129*, 12956-12957.

139 T. Satoh, S. Suzuki, Y. Suzuki, Y. Miyaji, Z. Imai, *Tetrahedron Lett.* **1969**, 4555-4558.

140 S. H. Gellman, G. P. Dado, G. B. Liang, B. R. Adams, *J. Am. Chem. Soc.* **1991**, *113*, 1164-1173.

141 C. Hansch, A. Leo, R. W. Taft, *Chem. Rev.* **1991**, *91*, 165-195.

142 D. Xin, E. Ko, L. M. Perez, T. R. Ioerger, K. Burgess, *Org. Biomol. Chem.* **2013**, *11*, 7789-7801.

143 B. Blankemeyer-Menge, M. Nimtz, R. Frank, *Tetrahedron Lett.* **1990**, *31*, 1701-1704.

144 L. A. Carpino, *J. Am. Chem. Soc.* **1993**, *115*, 4397-4398.

145 A. Devos, J. Remion, A.-M. Frisque-Hesbain, A. Colens, L. Ghosez, *J. Chem. Soc., Chem. Commun.* **1979**, 1180-1181.

146 H. Kessler, *Angew. Chem. Int. Ed.* **1982**, *21*, 512-523.

147 S. Uhrinova, D. Uhrin, H. Powers, K. Watt, D. Zheleva, P. Fischer, C. McInnes, P. N. Barlow, *J. Mol. Biol.* **2005**, *350*, 587-598.

148 B. Anil, C. Riedinger, J. A. Endicott, M. E. M. Noble, *Acta Cryst. Sect. D* **2013**, *69*, 1358-1366.

149 C. Hansch, A. Leo, S. H. Unger, K. H. Kim, D. Nikaitani, E. J. Lien, *J. Med. Chem.* **1973**, *16*, 1207-1216.

150 C. A. Hunter, *Angew. Chem. Int. Ed.* **2004**, *43*, 5310-5324.

151 I. K. Reddy, R. Mehvar, *Chirality in drug design and development*. Editor, CRC Press, **2004**.

Appendix I

Fluorescence anisotropy competition assay against p53/*h*DM2

A Fluorescence Anisotropy (FA) competition assay to test libraries of compounds against the p53/*h*DM2 PPI, was developed in the group as a result of a joint effort between Dr J. Plante, Prof A. J. Wilson, Dr S. L. Warriner and Dr T. A. Edwards (J. P. Plante *et al.*, *Chem. Commun*. **2009**, 5091-5093).

Upon excitation with plane-polarised light, the anisotropy was measured from the unequal intensities of the light emitted by a fluorophore with different planes of polarisation. A fluorescein-label was chosen as a fluorophore to tag the p53 peptide for this assay (Figure AI.1).

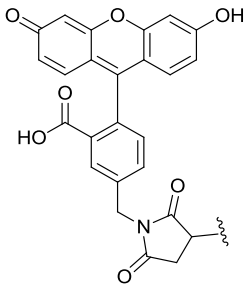

Figure AI.1 Fluorescein-label employed to tag the p53 peptide.

In order to determine the limits of anisotropy that can be observed in the assay, the binding of a fluorescein-labelled p53 (tracer) to *h*DM2 was assessed. Different concentrations were screened and serial dilution of the protein (starting point: 10 μM) into a 54.5 nM stock of tracer afforded optimal conditions.

At low concentrations of protein the p53 tracer is free to tumble in solution and the directionality of the polarised excitation light is not correlated with the emission polarisation. Upon binding to the protein at higher concentrations, the tracer is engaged in a much bigger complex which decreases its rate of tumbling so that it is slow relative to the fluorescence lifetime. The emission polarisation becomes correlated with the excitation polarisation and an increase of the anisotropy is observed (Figure AI.2 a-b).

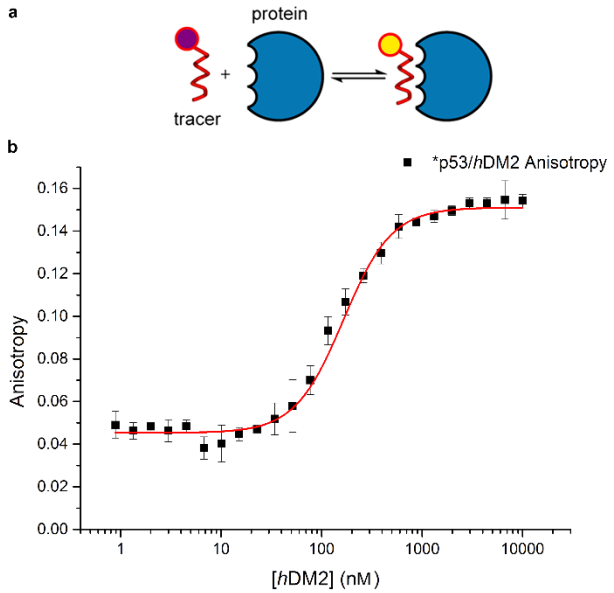

Figure AI.2 FA direct binding assay for p53/*h*DM2 a Cartoon representing the equilibrium of formation of the tracer-protein complex; **b** Fluorescence anisotropy resulting from the direct binding. (40 mM phosphate buffer pH 7.50, 200 mM sodium chloride, 0.02 mg mL^{-1} BSA)

The data for both the *P* (perpendicular intensity) and *S* (parallel (same) intensity) channels, resulting from this measurement and corrected by subtracting the corresponding control wells, were used to calculate the intensity and anisotropy for each well following Equation AI.1 and Equation AI.2:

$$I = (2PG) + S$$

Equation AI.1

$$r = \frac{S - PG}{I}$$

Equation AI.2

Where *I* is the total intensity, *G* is an instrument factor which was set to 1 for all experiments and *r* is the anisotropy.

The average anisotropy (across three replicates) and the standard deviation of these values were then calculated and fit to a sigmoidal logistic model (Equation AI.3, Figure AI.2 b) using Origin 7.5. The maximum (r_{max}) and minimum (r_{min}) anisotropies obtained from this fit were used to calculate the fraction ligand bound (L_b) (Equation AI.4):

$$y = r_{max} + \frac{r_{min} - r_{max}}{1 + \left(x / x_0 \right)^p}$$

Equation AI.3

$$L_b = \frac{r - r_{min}}{(\lambda(r_{max} - r) + (r - r_{min})}$$

Equation AI.4

Where x_0 is the midpoint, p is the power and λ is the ratio of $I_{bound}/I_{unbound}$ and is equal to 1. The fraction ligand bound was multiplied by the concentration of p53 (15-31) Flu and fit to a 1:1 binding model shown in Equation AI.5 to determine the dissociation constant (K_d).

$$y = \frac{K_d + x + [FL] - \sqrt{(K_d + x + [FL])^2 - 4x[FL]}}{2}$$

Equation AI.5

Where [*FL*] is the concentration of p53 (15-31) Flu; y is L_b*[*FL*], and x is the concentration of *h*DM2.

This measurement afforded a K_d of 187.1 ± 24.6 nM for this interaction, in accordance with the value previously published by the group (Figure AI.3).

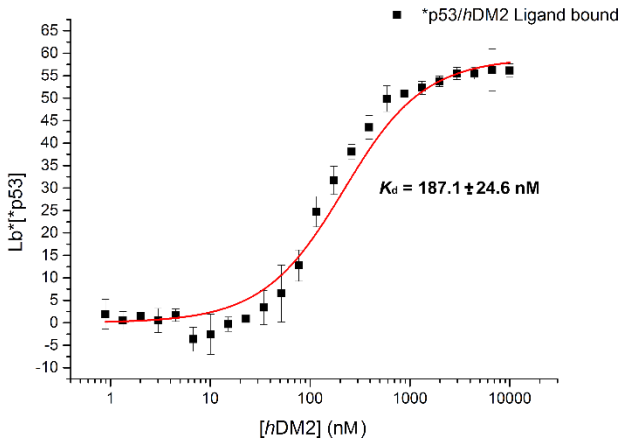

Figure AI.3 Ligand bound plot for determination of the dissociation constant for p53/*h*DM2. (40 mM phosphate buffer pH 7.50, 200 mM sodium chloride, 0.02 mg mL^{-1} BSA)

When the interaction is disrupted by a competitor, the tracer peptide can be displaced and return to tumble faster in solution. This process consequently result in the loss of the directionality of the polarised excitation light and in a decrease of anisotropy (Figure AI.4 a-c).

A FA competition assay was therefore developed in order to assess the ability of designed proteomimetics to inhibit the p53/*h*DM2 PPI. After optimisation, the assay was run through serial dilution of the proteomimetic (starting point: 100 µM) into stocks of tracer and protein, kept at constant concentrations of 54.5 nM and 154.2 nM, respectively. The dose-response titration of the known inhibitor Nutlin-3a (**4**, Chapter 1), obtained after fitting to a sigmoidal logistic model (Equation AI.3) using Origin Pro 9.0, is shown in Figure AI.4 c and provided an IC_{50} of 534.7 ± 23.9 nM, which was in the nanomolar range, as originally reported by Vassilev and co-workers using a surface plasmon resonance assay (IC_{50} = 90 nM, L. T. Vassilev *et al.*, *Science*, **2004**, 303, 844-848).

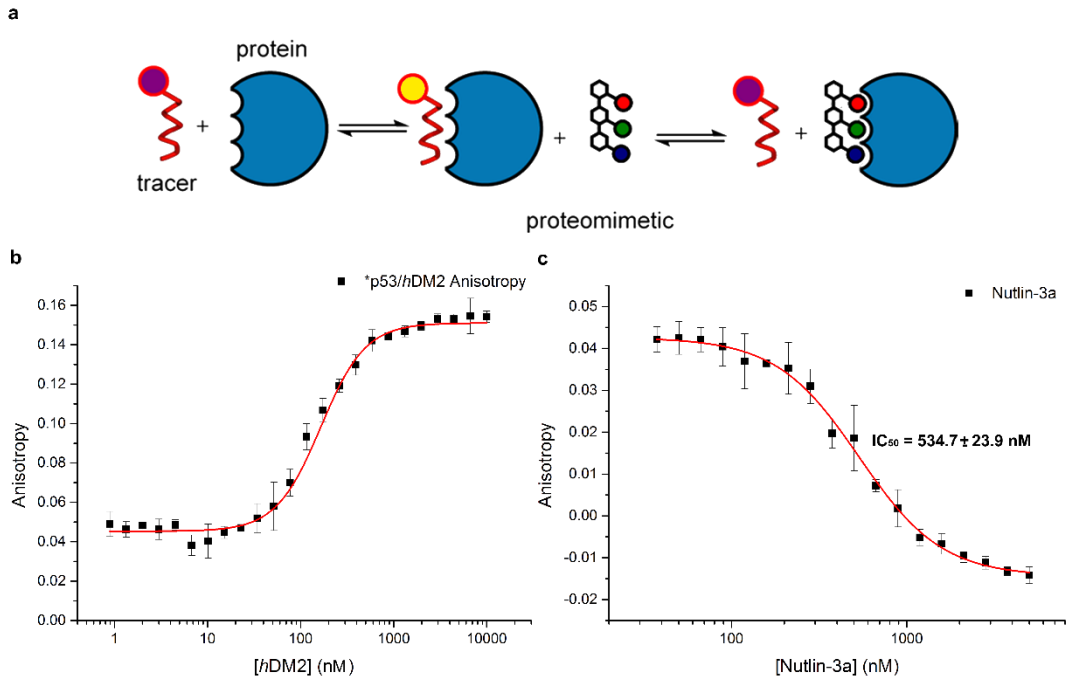

Figure AI.4 FA competition assay against p53/*h*DM2 a Cartoon representing the displacement of the tracer upon binding of a proteomimetic to the protein; **b** Increase of the fluorescence anisotropy resulting from the direct binding of the p53 tracer to the protein; **c** Decrease of the fluorescence anisotropy resulting from the titration of Nutlin-3a. (40 mM phosphate buffer pH 7.50, 200 mM sodium chloride, 0.02 mg mL^{-1} BSA)

Unfortunately, this assay suffers from an intrinsic limitation as an inhibition constant (K_i) cannot be extracted. As shown in Figure AI.5 a, the assay does not occur through a simple two state equilibrium between the free tracer/mimetic or protein and the complex protein-ligand. Further contributions to the anisotropy are instead given by homo-aggregates of the tracer (r_1 in Figure AI.5 a) and hetero tracer-mimetic aggregates (r_2 in Figure AI.5 a).

In the direct binding experiment, the r_1 contribution is added to the theoretical minimum of anisotropy (r_0) provided by the free tracer, resulting in the higher experimental minimum r_{min} (Figure AI.5 b).

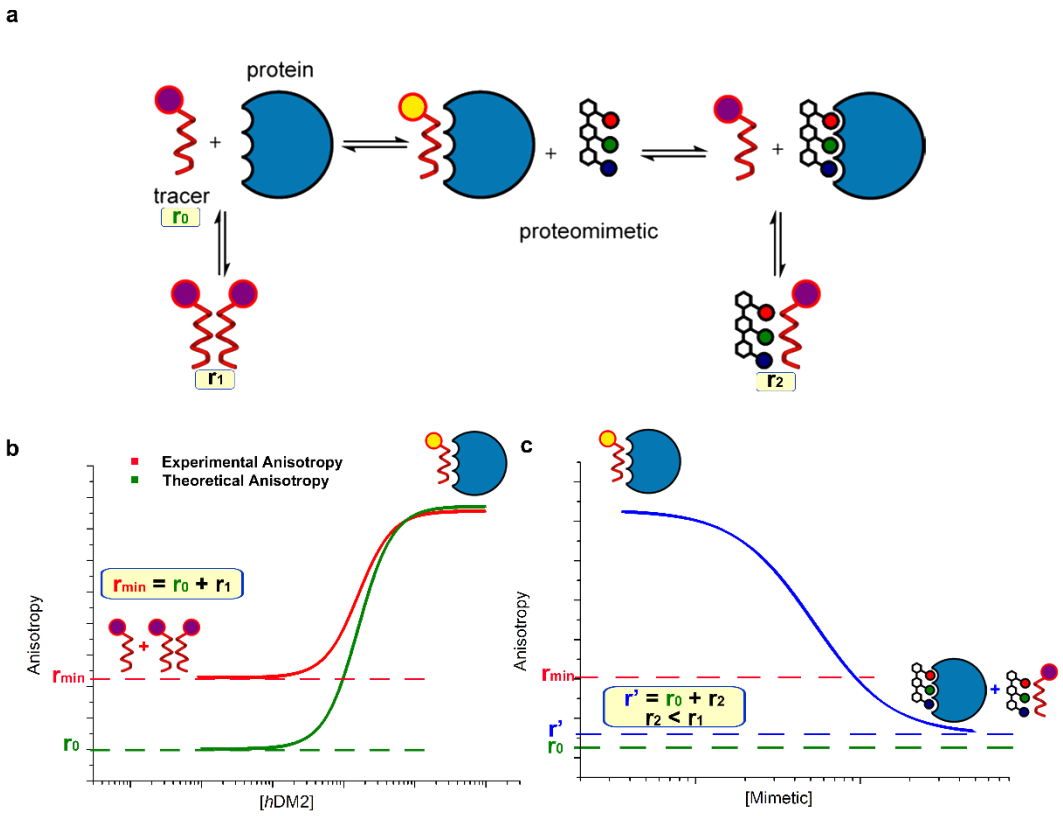

Figure AI.5 Equilibria preventing K_i determination a Cartoon representing the equilibria of complexation/aggregation occurring in the FA competition assay and highlighting r_0, r_1 and r_2 contributions; **b** Experimental (red) and theoretical (green) anisotropies of the direct binding experiment highlighting the difference between the r_0 and r_{min} minima of anisotropy and the additional r_1 contributions to r_{min}; **c** Anisotropy of the competition assay (blue) highlighting the r_0 and r_2 contributions to r' and its difference with r_{min} from direct binding.

Upon competition with a proteomimetic, the anisotropy of the hetero-aggregate (r_2) adds to the overall minimum r'. Since the r_2 contribution is

smaller than the contribution of r_1, the competition minimum r' differs from the binding end-point r_{min}, thus preventing the determination of K_i (Figure AI.5 c).

For this reason, the test was employed only to extract IC_{50} values of inhibition.

Fluorescence anisotropy competition assay against Mcl-1/NOXA B

A FA competition assay to test libraries of compounds against the Mcl-1/NOXA B PPI, was developed in a joint effort with Dr K. Long and D. J. Yeo following the same principles employed in the development of the assay against p53/*h*DM2.

Different concentrations were screened to run a direct binding experiment and serial dilution of Mcl-1 (starting point: 5 μM) into a fluorescein-labelled NOXA B stock at a constant 50 nM concentration, afforded the optimal conditions. Plot of the average anisotropy values (following Equation AI.3, Figure AI.6 a) and conversion to L_b, allowed to extract a K_d of 18.7 ± 0.9 nM for this interaction (Figure AI.6 b, Equation AI.5).

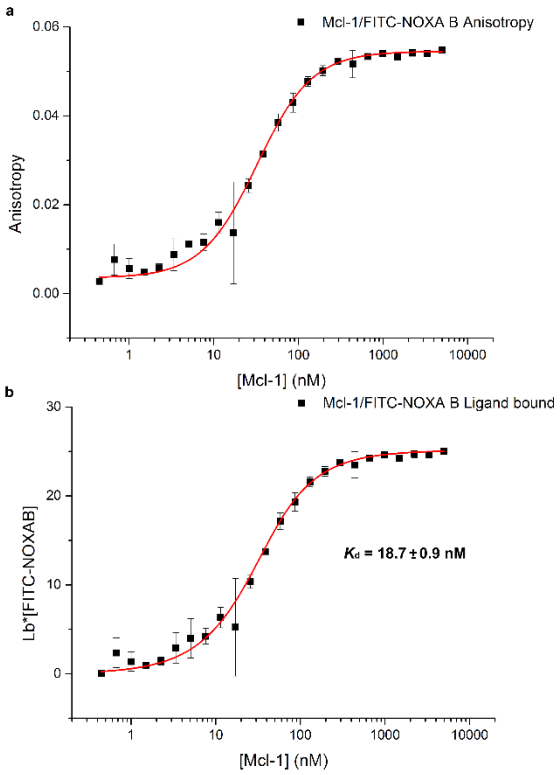

Figure AI.6 FA direct binding assay for Mcl-1/NOXA B a Fluorescence anisotropy resulting from the direct binding; **b** Ligand bound plot for determination of the dissociation constant. (40 mM phosphate buffer pH 7.50, 200 mM sodium chloride, 0.02 mg mL^{-1} BSA)

The competition assay was then developed, using the wild-type (WT) NOXA B as a model substrate to optimise conditions. Serial dilution of WT-NOXA B (starting point: 10 µM) into stocks of tracer and protein at constant concentrations of 50 nM and 150 nM respectively, afforded the best conditions and allowed to obtain the IC_{50} value for the competition (704.3 ± 35.0 nM, Figure AI.7, Equation AI.3).

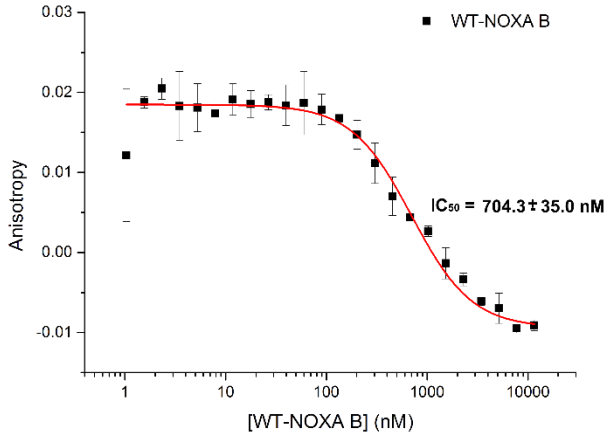

Figure AI.7 FA competition assay of WT-NOXA B against Mcl-1/NOXA B. (40 mM phosphate buffer pH 7.50, 200 mM sodium chloride, 0.02 mg mL^{-1} BSA)

Unfortunately, also for this assay the minimum of anisotropy of the competition was lower than the direct binding minimum, thus implying that further equilibria are involved and preventing the determination of an inhibition constant.

Appendix II

The role of side-chain spacing against p53/*h*DM2

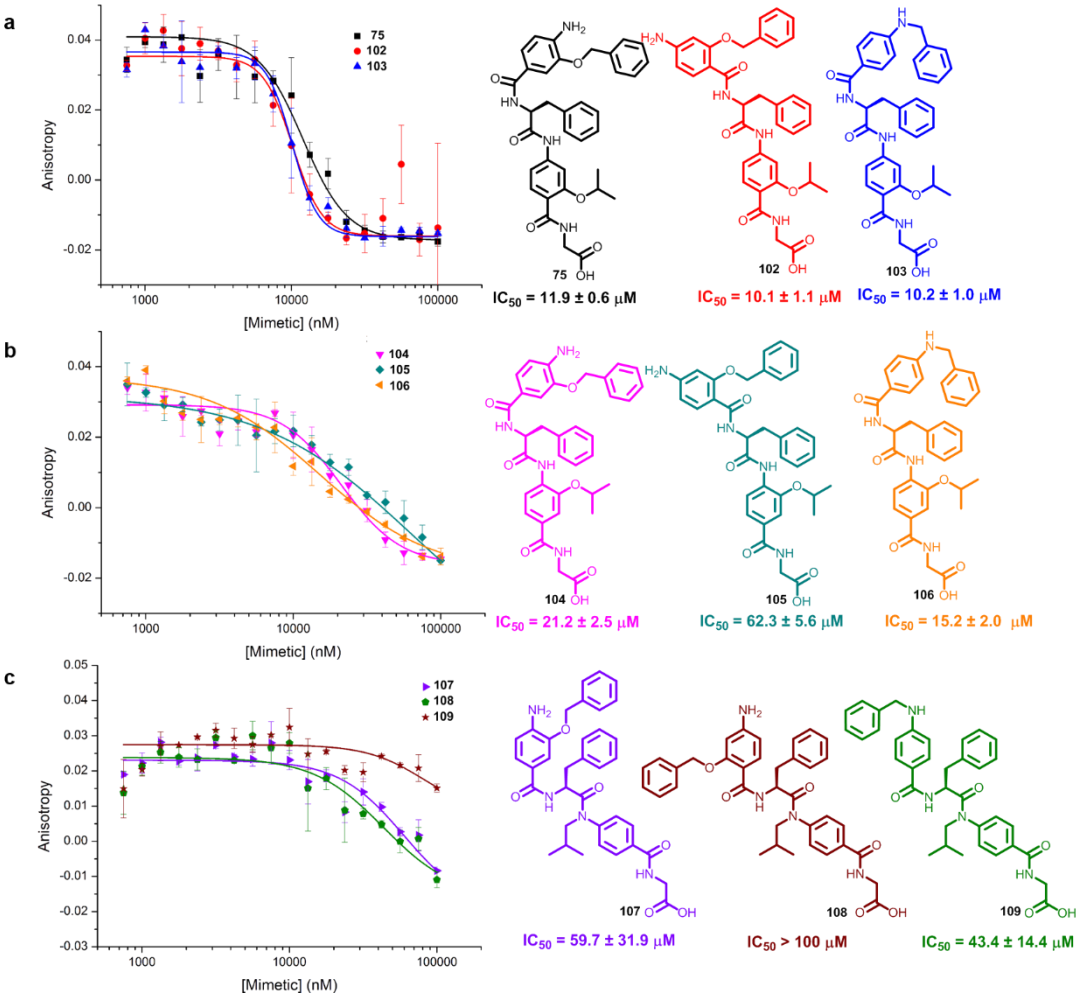

Figure AII.1 Side-chain spacing studies targeting the p53/*h*DM2 PPI: dose-response curves a 2-*O*-alkylated series; **b** 3-*O*-alkylated series; **c** *N*-alkylated series. (40 mM phosphate buffer pH 7.50, 200 mM sodium chloride, 0.02 mg mL^{-1} BSA)

The role of side-chain spacing against Mcl-1/NOXA B

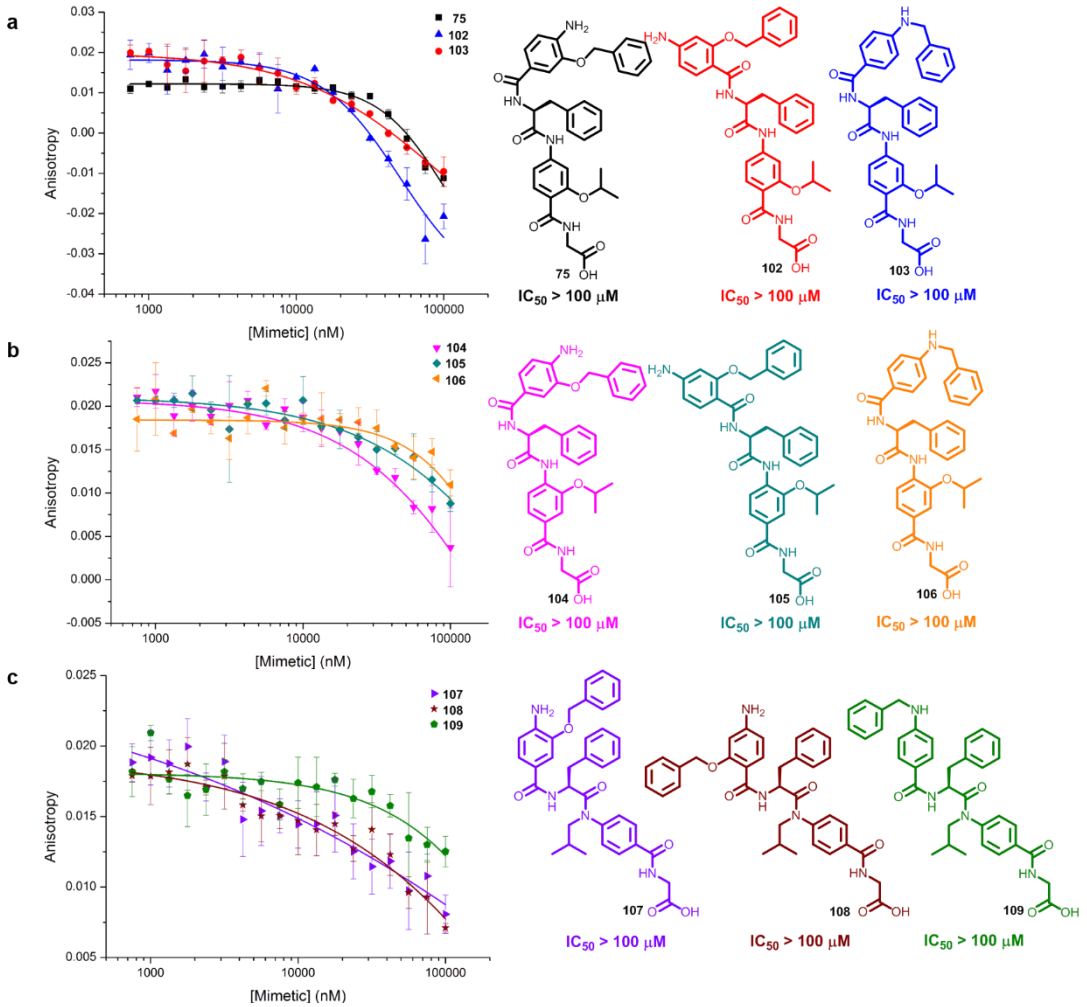

Figure AII.2 Side-chain spacing studies targeting the Mcl-1/NOXA B PPI: dose-response curves a 2-*O*-alkylated series; **b** 3-*O*-alkylated series; **c** *N*-alkylated series. (40 mM phosphate buffer pH 7.50, 200 mM sodium chloride, 0.02 mg mL^{-1} BSA)

Aliphatic hybrid mimetics against p53/*h*DM2

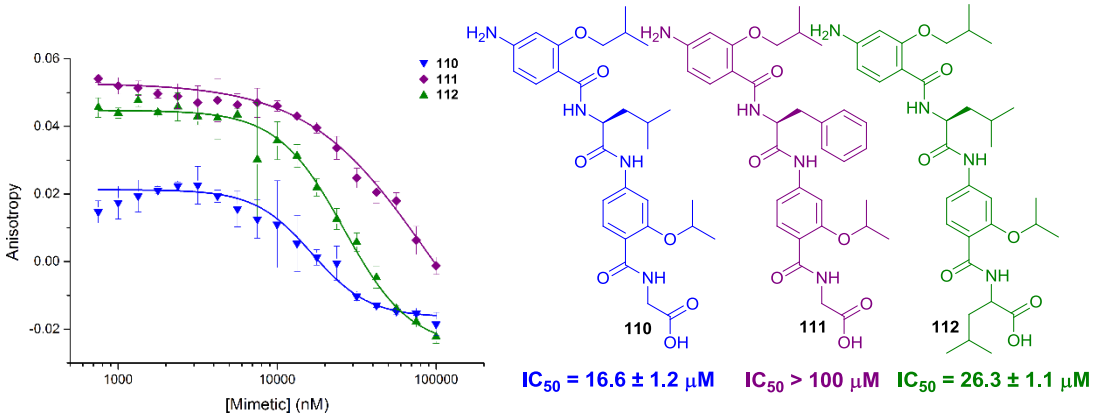

Figure AII.3 Aliphatic hybrid mimetics: Dose-response curves against the p53/*h*DM2 PPI. (40 mM phosphate buffer pH 7.50, 200 mM sodium chloride, 0.02 mg mL^{-1} BSA)

Aliphatic hybrid mimetics against Mcl-1/NOXA B

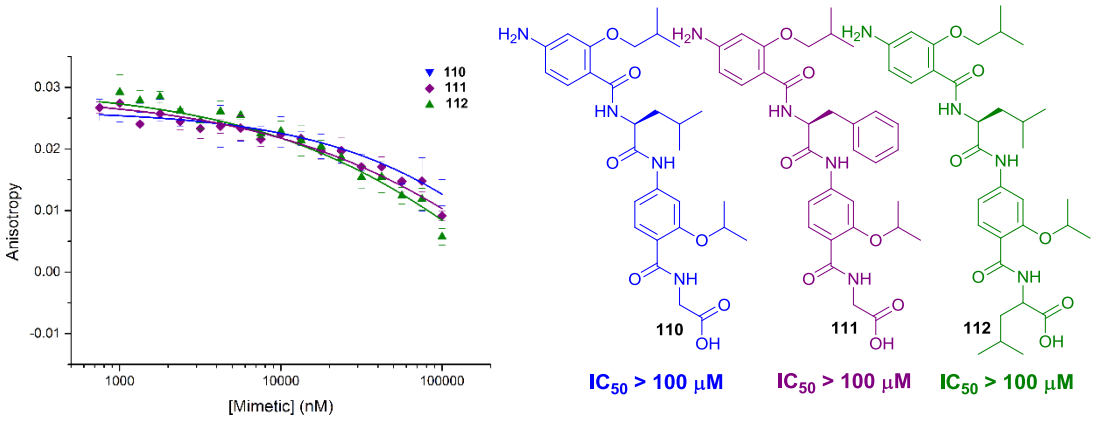

Figure AII.4 Aliphatic hybrid mimetics: Dose-response curves against the Mcl-1/NOXA B PPI. (40 mM phosphate buffer pH 7.50, 200 mM sodium chloride, 0.02 mg mL^{-1} BSA)

AA-functionalised hybrid mimetics against p53/*h*DM2

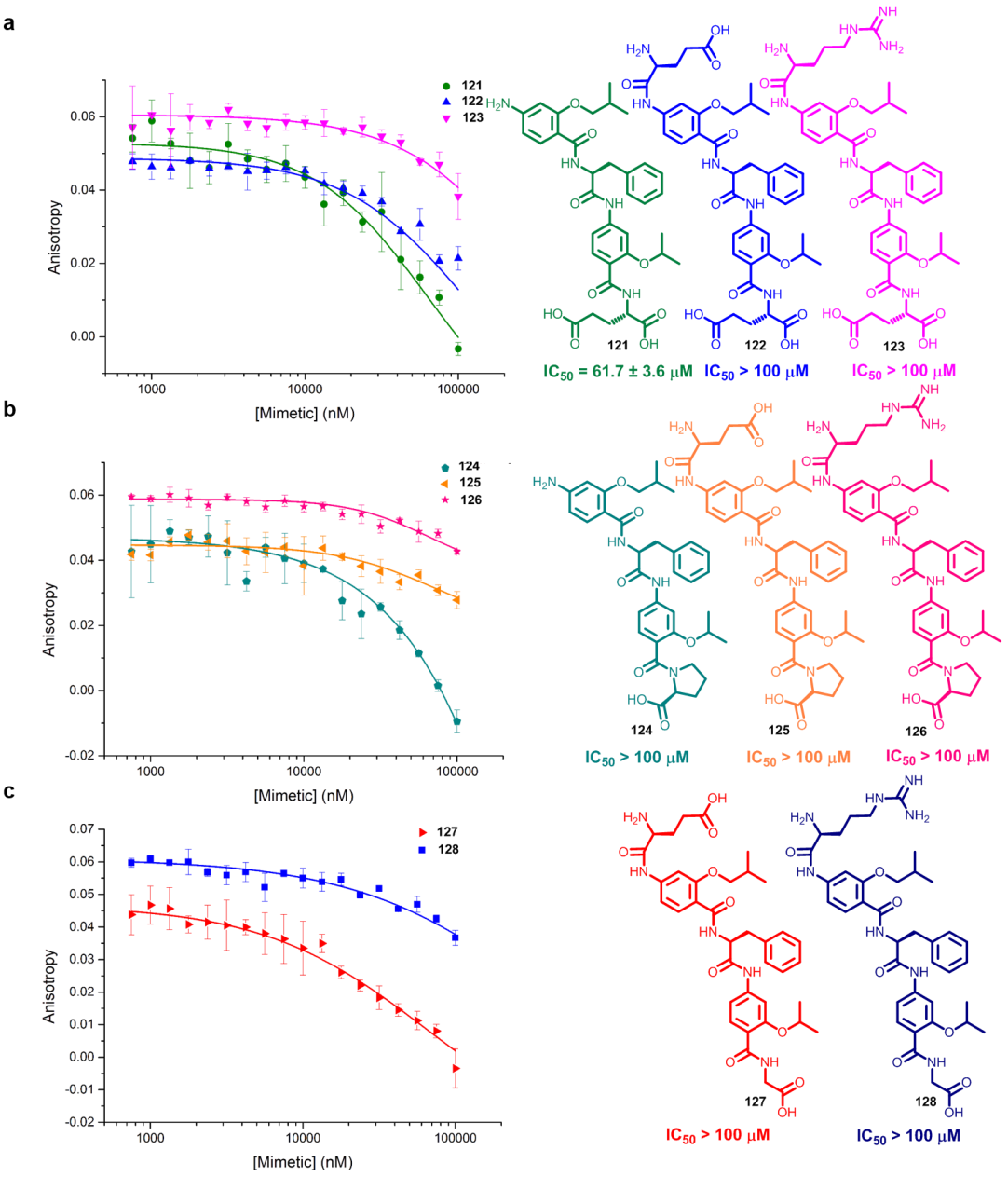

Figure AII.5 AA-functionalised hybrid mimetics: dose-response curves against the p53/*h*DM2 PPI a Bottom Glu series; **b** Bottom Pro series; **c** Top functionalisation. (40 mM phosphate buffer pH 7.50, 200 mM sodium chloride, 0.02 mg mL^{-1} BSA)

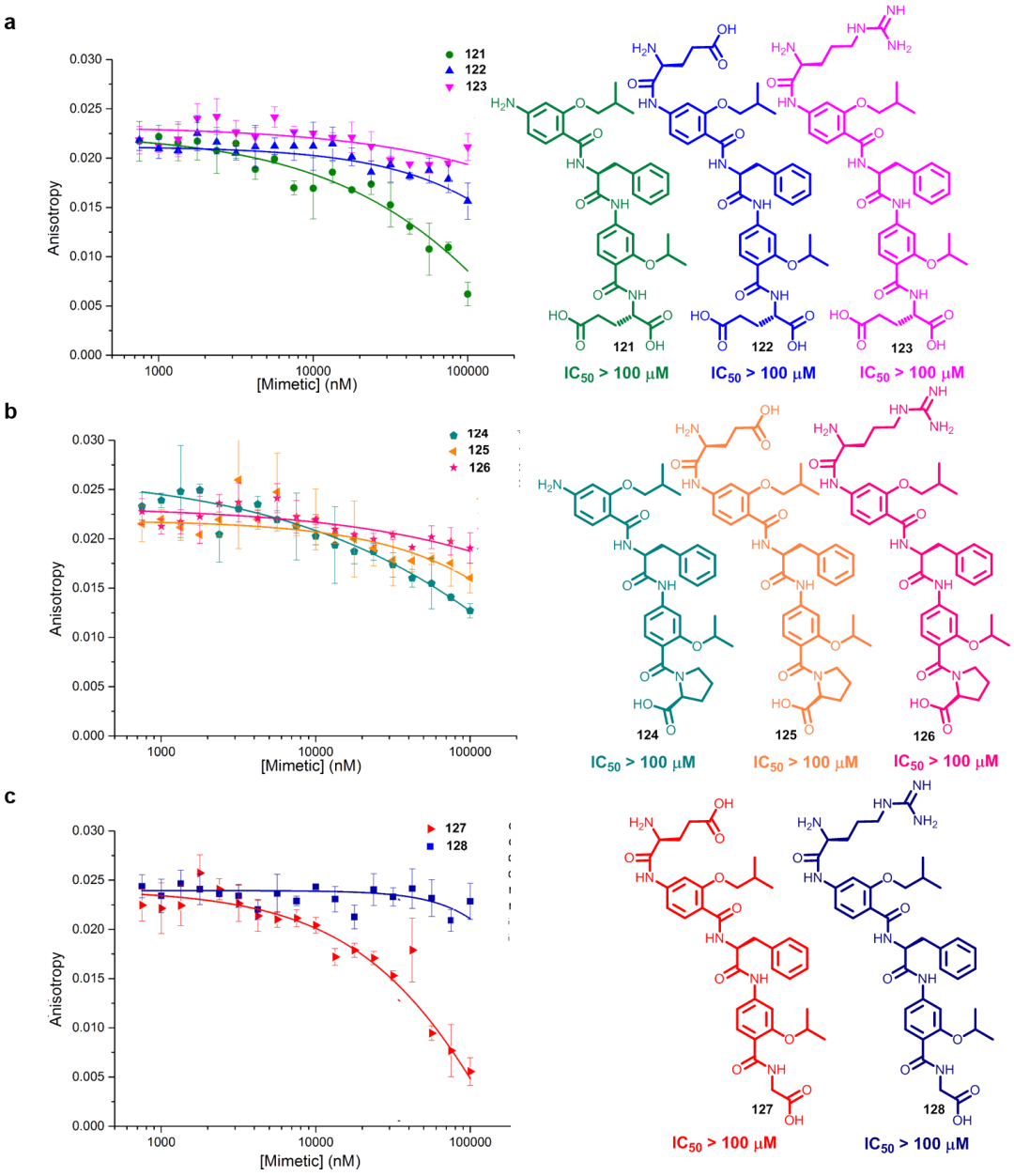

Figure AII.6 AA-functionalised hybrid mimetics: dose-response curves against the Mcl-1/NOXA B PPI a Bottom Glu series; **b** Bottom Pro series; **c** Top functionalisation. (40 mM phosphate buffer pH 7.50, 200 mM sodium chloride, 0.02 mg mL^{-1} BSA)

The effect of the middle unit against Mcl-1/NOXA B

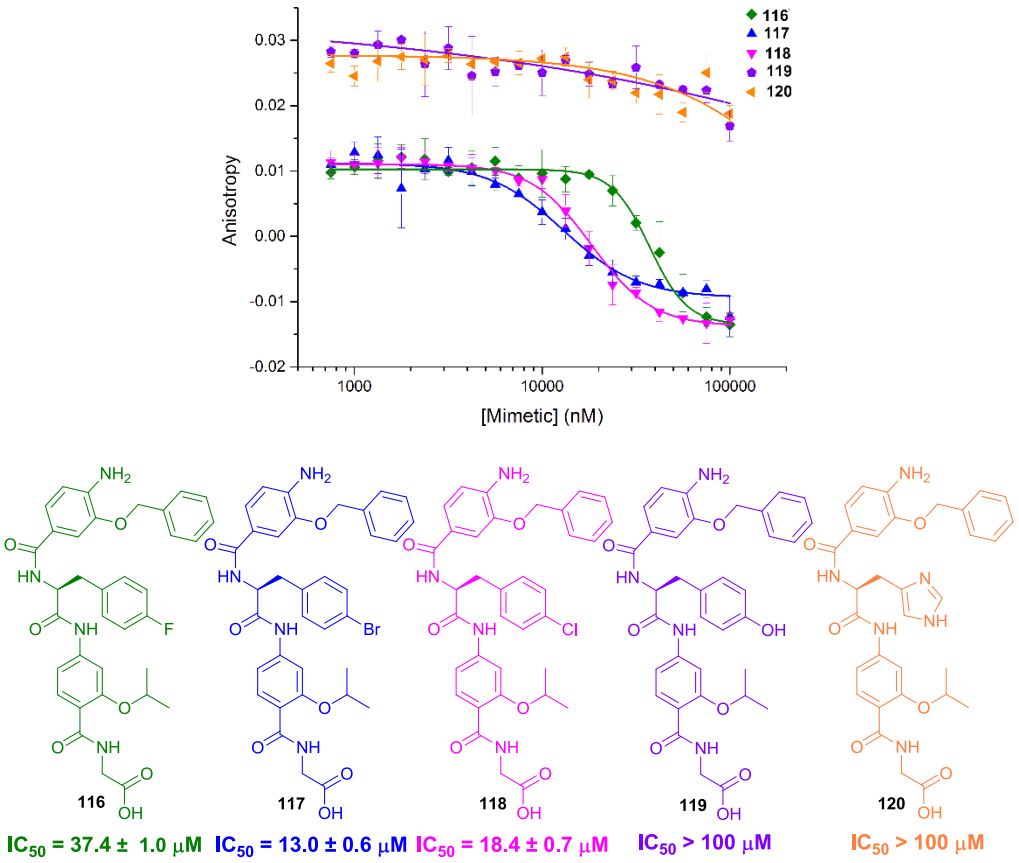

Figure AII.7 Halo-series and polar substituents: Dose-response curves against the Mcl-1/NOXA B PPI. (40 mM phosphate buffer pH 7.50, 200 mM sodium chloride, 0.02 mg mL^{-1} BSA)

Hybrid α-helix mimetics: a selective scaffold

The p53 helix is known to bind to the Mcl-1 cleft (H. Yao *et al.*, *Biochemistry* **2013**, *52*, 6324-6334). Fluorescence Anisotropy direct binding experiments were therefore performed to investigate the affinity of a fluorescently labelled p53 with Mcl-1, leading to a K_d value of 14.4 ± 4.6 µM, in accordance with the value reported in literature (Figure AII.8 a-b).

For comparison with the data obtained on the hybrids, the wild-type p53 peptide was then tested in competition-mode against the Mcl-1/NOXA B PPI. As shown in Figure AII.8 c, no inhibition was observed, revealing that in spite of its

ability to be recognised by Mcl-1, p53 is not able to compete with NOXA B in this PPI.

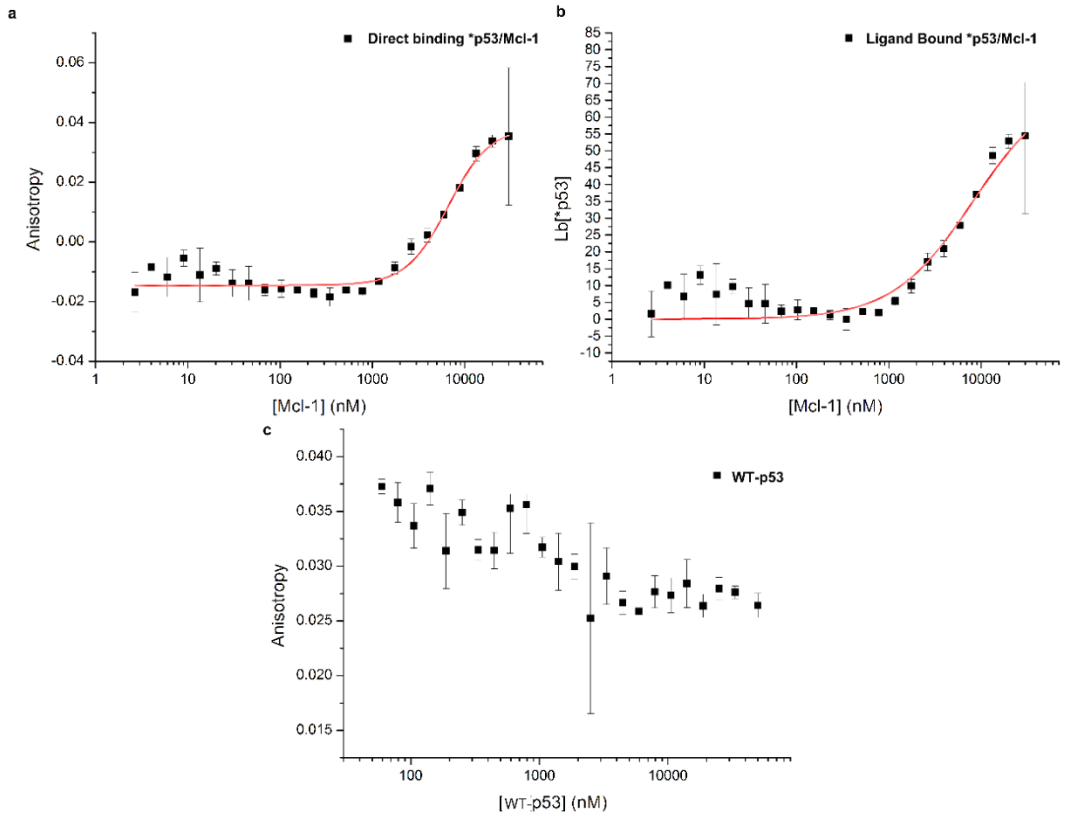

Figure AII.8 Studies on the binding affinity of p53 towards Mcl-1 a Fluorescence Anisotropy direct binding assay of FITC-p53 to Mcl-1; **b** Ligand bound plotting of FITC-p53/Mcl-1; **c** FA competition assay of WT-p53 against Mcl-1/NOXA B. (40 mM phosphate buffer pH 7.50, 200 mM sodium chloride, 0.02 mg mL^{-1} BSA)

This result was noteworthy, as the four identified hybrids inhibitors (**113**, **116-118**), originally designed to be p53-mimetics, were on the other hand able to compete with the native NOXA B peptide and achieve low-micromolar recognition with Mcl-1.

Docking studies on the D-Phe hybrid mimetic 129 in complex with *h*DM2

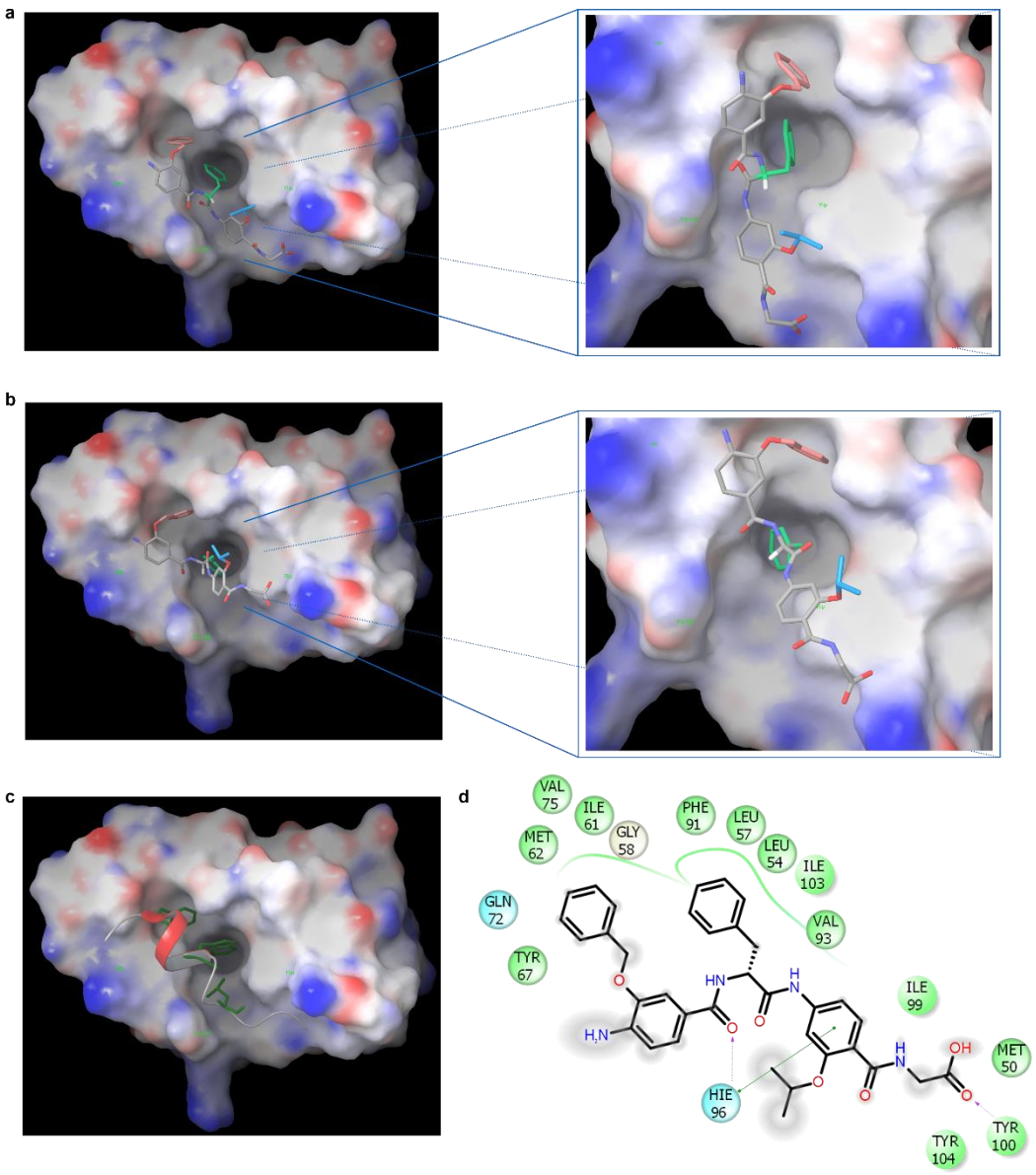

Figure AII.9 Docking studies for the D-Phe (129) hybrid mimetic (PDB ID: 1YCR) a Docked D-Phe functionalised hybrid **129** with protein surface 3D representation and expansion; **b** Docked L-Phe functionalised hybrid **75** with protein surface 3D representation and expansion; **c** p53/*h*DM2 interaction; **d** Docked hybrid **129** in schematic 2D representation highlighting the interacting amino acids (interactions taking place outside the hydrophobic cleft are represented with a grey shade).

Appendix III

Attempted development of an ITC assay for the p53/*h*DM2 PPI

The development of an Isothermal Calorimetry (ITC) assay to monitor the inhibition of the p53/*h*DM2 PPI, was attempted in a joint effort with Dr A. Barnard. Unfortunately the assay was temperamental in our hands and it could not be employed to test the mimetics. Details on the attempts are described below.

The native interaction was initially targeted. After dialysis in a 40 mM sodium phosphate buffer (200 mM sodium chloride, pH = 7.50), the concentration of the protein was determined *via* UV spectroscopy following the Beer-Lambert law, Equation AIII.1 (*h*DM2 Extinction coefficient = 15676 $M^{-1}cm^{-1}$, determined experimentally after protein denaturation with guanidinium chloride following Equation AIII.2). In order to accurately determine the concentration, the solid WT-p53 was then dissolved in the dialysis buffer to obtain a concentration ten fold higher than the protein and used without further dialysis.

$$c = \frac{A_{280}}{\varepsilon_{280}}$$

c = concentration at 280 nm; A_{280} = absorbance at 280 nm; ε_{280} = extinction coefficient at 280 nm.

Equation AIII.1

$$\varepsilon_{nat} = \left(\frac{A_{nat}}{A_{denat}} \right) \times \varepsilon_{denat}$$

ε_{nat} = extinction coefficient at 280 nm; A_{nat} = protein absorbance at 280 nm; A_{denat} = denatured protein absorbance at 280 nm; ε_{denat} = extinction coefficient of the denatured protein at 280 nm, calculated from the number of Trp, Tyr and Cys residues (9080).

Equation AIII.2

Following these conditions, titrations of a 250 μM solution of WT-p53 were performed into buffer for corrections and into a 25 μM *h*DM2 stock using an iTC200 MicroCal calorimeter (GE Healthcare). After an initial 0.5ul injection, 19 subsequent injections of 2 μL ligand were made into 180 μL of the second binding partner with

150 seconds in between injections. The area of each injection was integrated and subtraction of the buffer titration afforded a binding curve (Figure AIII.1).

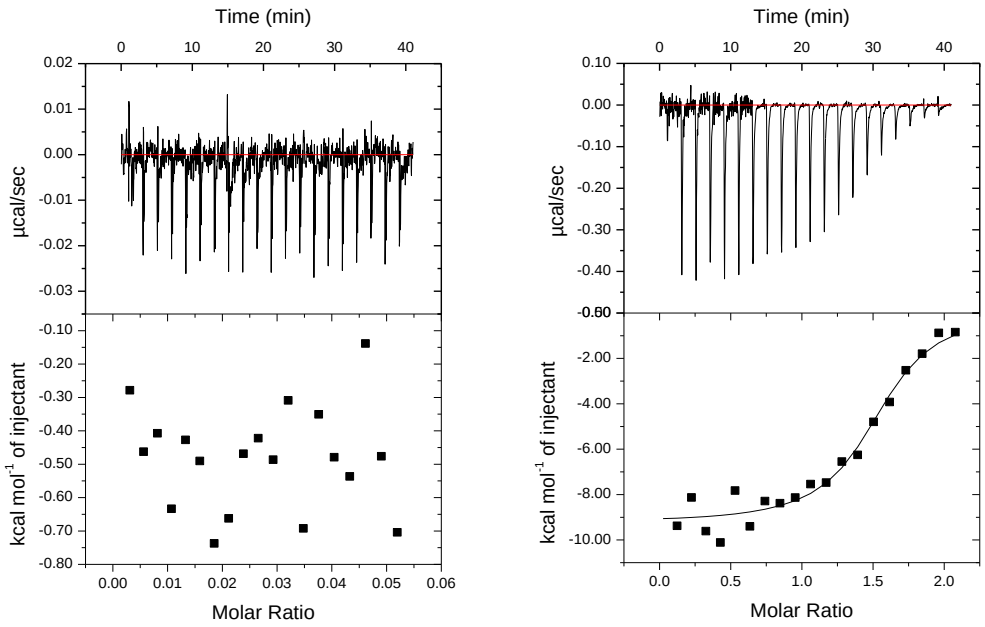

Figure AIII.1 ITC data for the p53/*h*DM2 interaction (right) obtained after correction with the titration of p53 into buffer (left). Reference power 10 µcal/s, 25 °C.

Fitting of the curve using a OneSite model in Origin7, allowed extraction of thermodynamic data (Table AIII.1) and afforded a K_d of 1.47 ± 0.42 µM.

Table AIII.1 Thermodynamic data obtained from ITC of the p53/*h*DM2 interaction.

Model	OneSites
Chi^2/DoF	3.137E5
N	1.51 ± 0.0289 Sites
K	1.47E6 ± 4.20E5 M-1
ΔH	-9224 ± 251.8 cal/mol
ΔS	-2.71 cal/mol/deg

The assay was then attempted using Nutlin-3a. Several attempts at different concentrations and temperatures, revealed that it was not possible to obtain a curve from this titration. A representative example is shown in Figure AIII.2.

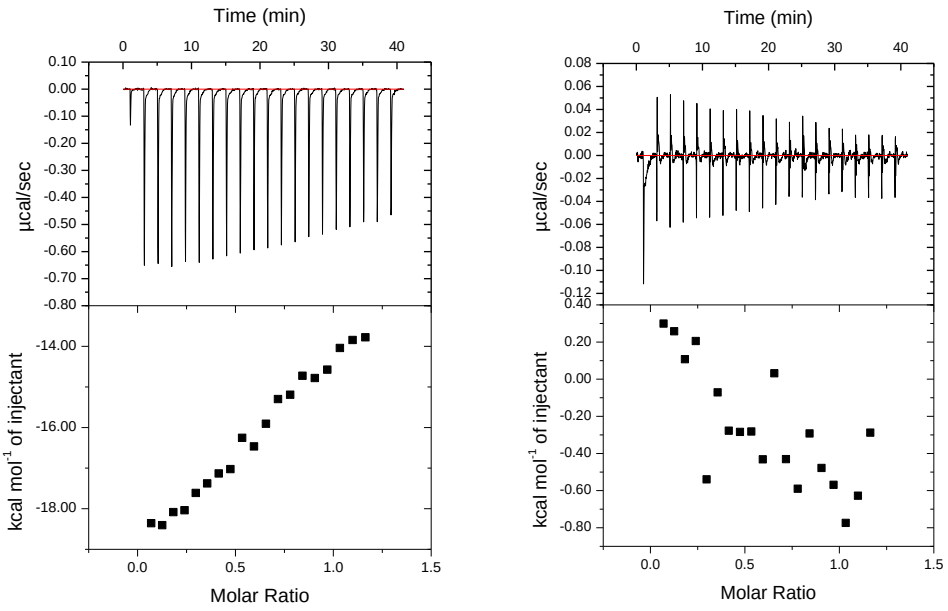

Figure AIII.2 ITC data for the Nutlin-3a/*h*DM2 interaction: titration into buffer (left), titration into *h*DM2 (right). Reference power 10 µcal/s, Nutlin-3a concentration = 140 µM, 25 °C.

The poor solubility of this molecule proved problematic in the preparation of the sample, as precipitation of the compound in the dialysis buffer was observed. Self-aggregation and precipitation could therefore be the reason for the result obtained after titration with the protein.

Attempted CD experiments

Circular dichroism (CD) experiments were attempted in order to assess structural changes in *h*DM2 upon binding of hybrid mimetics. Unfortunately the experiment was not reproducible and it could not be employed for further studies. Details on the attempts are described below.

A CD thermal scan was initially performed on a 25 µM solution of *h*DM2 and on a solution of *h*DM2 incubated with hybrid **98** (Figure AIII.3 c) for 45 minutes (stock concentrations at 25 µM and 30 µM respectively). The experiment was run as a control, since this hybrid was shown to be inactive towards *h*DM2 binding and no structural changes were therefore envisaged in the protein.

Conditions were optimised using 5 mM phosphate buffer (pH = 7.50) and 0.3% acetonitrile (either as an addition to the protein or from a 10 mM compound stock). The thermal scan was run on a Chirascan™ CD Spectrometer (Applied

Photophysics) using a temperature range 20-90 °C on a 1 °C ramp step, held for 120 s before each acquisition.

As expected, the CD traces of the protein and of the solution with **98** (shown in Figure AIII.3 a-b) showed minimal difference.

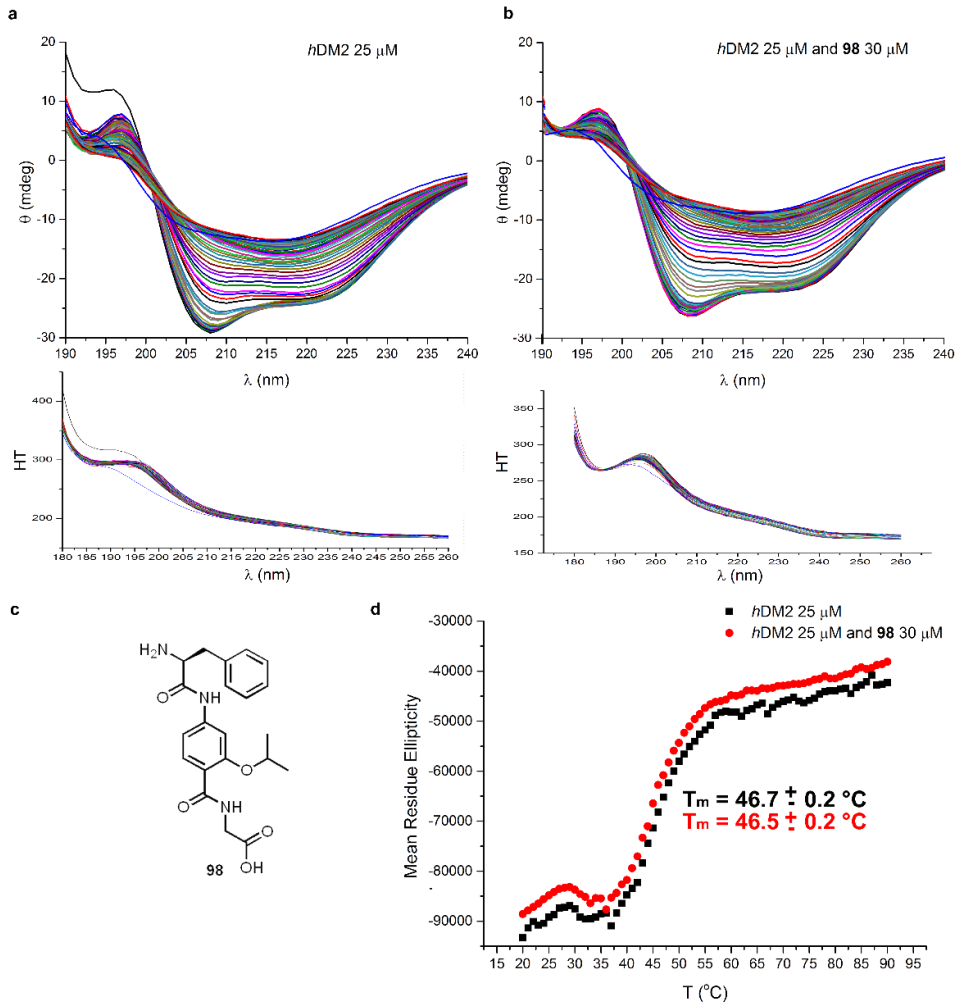

Figure AIII.3 CD thermal scan of the complex hybrid 98/*h*DM2 a CD and high tension (HT) voltage spectra of a 25 μM stock of *h*DM2; **b** CD and HT spectra of the complex hybrid **98**/*h*DM2 (30 μM/25 μM); **c** Structure of hybrid **98**; **d** MRE spectra of *h*DM2 (black) and of the complex hybrid **98**/*h*DM2 (red) showing correspondent melting temperatures.

The mean residue ellipticity (MRE) at 222 nm was then calculated following Equation AIII.3, and the values obtained were plot with a logistic sigmoidal fit in OriginPro 9 to afford the melting temperatures (T_m) resulting from the thermal scan. As shown in Figure AIII.3 d, minimal variation was observed, thus confirming the binding data obtained from the FA full competition curve.

$$\theta_{MRE} = \frac{(\theta \times 10 \times c \times l)}{(N-1)}$$

θ_{MRE} = MRE at 222 nm; θ = observed ellipticity at 222 nm; c = protein concentration (M); l = pathlength (0.1 cm); N = number of peptide bonds.

Equation AIII.3

A CD thermal scan was therefore performed on a 25 µM solution of *h*DM2 and on a solution of *h*DM2 incubated with hybrid **75** (Figure AIII.4 c) for 45 minutes (stock concentrations at 25 µM and 30 µM respectively). Since this hybrid was shown to bind to *h*DM2 in a FA assay, structural changes in the protein might have been envisaged in this experiment.

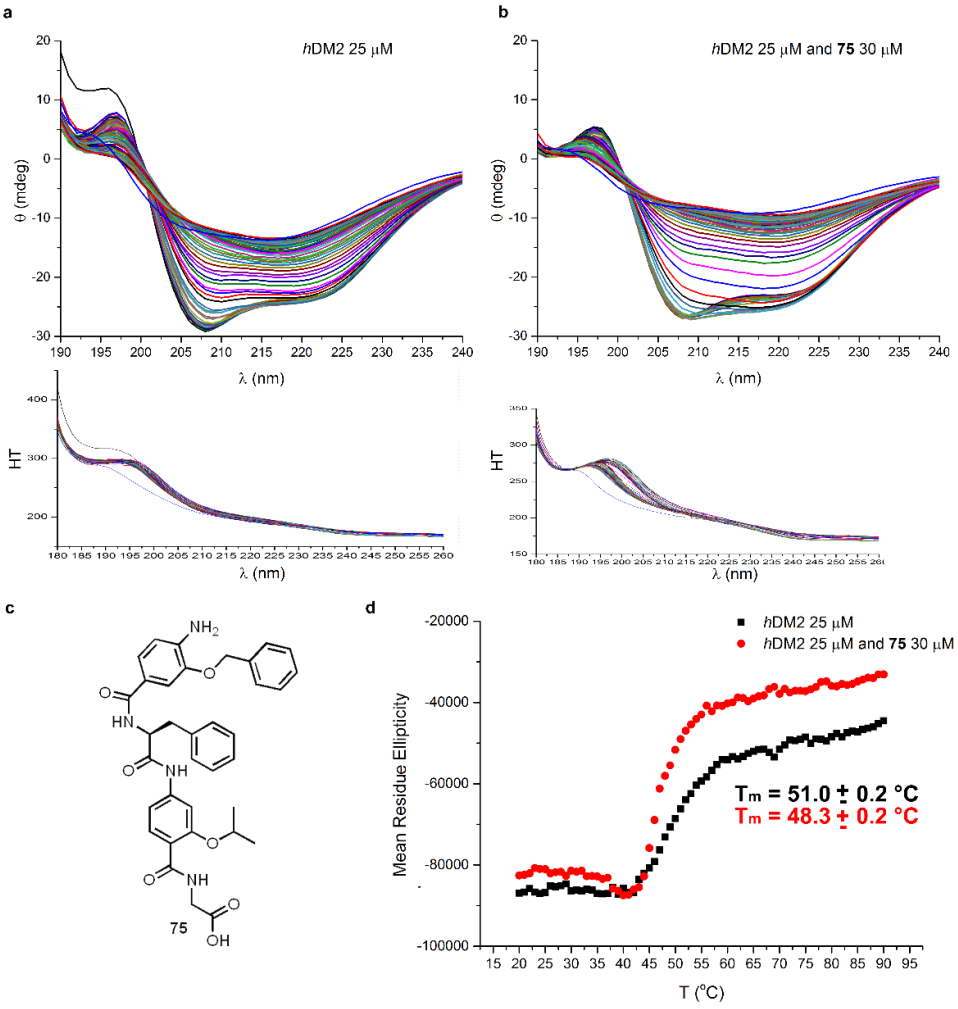

Figure AIII.4 CD thermal scan of the complex hybrid 75/*h*DM2 a CD and HT spectra of a 25 µM stock of *h*DM2; **b** CD and HT spectra of the complex hybrid **75**/*h*DM2 (30 µM/25 µM); **c** Structure of hybrid **75**; **d** MRE spectra of *h*DM2 (black) and of the complex hybrid **75**/*h*DM2 (red) showing correspondent melting temperatures.

As shown in Figure AIII.4 a-b, changes in the CD traces were observed. The MRE plots (Figure AIII.4 d) resulted in a 3 °C difference of the T_m at 222 nm, showing that the protein was stabilised from unfolding in the presence of the mimetic.

The experiment revealed however that the melting temperature of the protein differed from the value obtained in the previous experiment, showing that the data were not reproducible. Unfortunately, repeat attempts confirmed this behaviour. As shown in the representative example in Figure AIII.5, MRE plots could in fact not be accurately replicated.

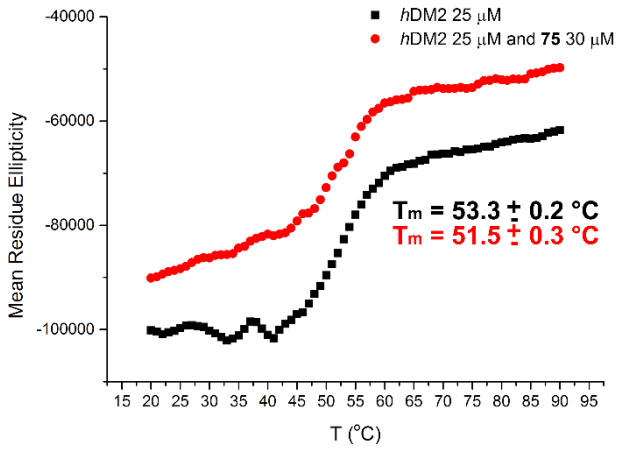

Figure AIII.5 Repeated MRE spectra resulting from the CD thermal scan of *h*DM2 (black) and of the complex hybrid 75/*h*DM2 (red) showing correspondent melting temperatures.

Attempted development of an SPR assay for the p53/*h*DM2 PPI

The development of a surface plasmon resonance (SPR) assay targeting the p53/*h*DM2 PPI, was attempted to access an orthogonal assay to test libraries of mimetics. Unfortunately the only experiment performed, described below, did not work. Further attempts will be needed in future to optimise the conditions to use this assay.

SPR studies were endeavoured to study the interaction between *h*DM2 and a Biotinyl-p53 peptide (synthesised by D. J. Yeo) and a Biotinyl-tagged version of hybrid **75** (**132**).

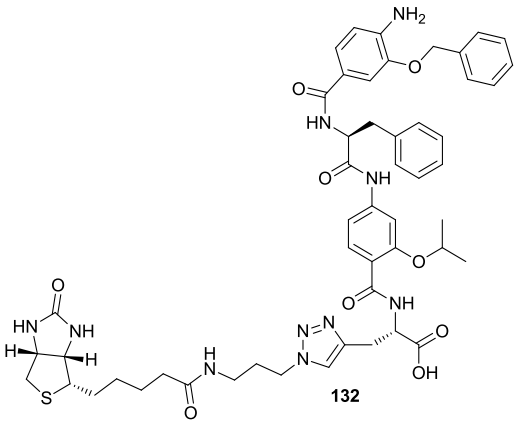

The experiments were run using a Biacore 3000 system (GE Healthcare). Stock solutions of the Biotinylated compounds (0.1 nM in phosphate buffer, pH = 7.50) were immobilised onto a streptavidin functionalised chip (Sensor Chip SA, GE Healthcare) reaching immobilisation densities of 26.7 response units (RUs) for hybrid **132** and 48.1 RUs for the Biotinyl-p53 peptide. One flow cell was left blank for corrections. The *h*DM2 protein was then flushed over the surface at different concentrations (ranging from 19.5 nM to 50 μM) and the response was followed for all the compounds (Figure AIII.6 a-b).

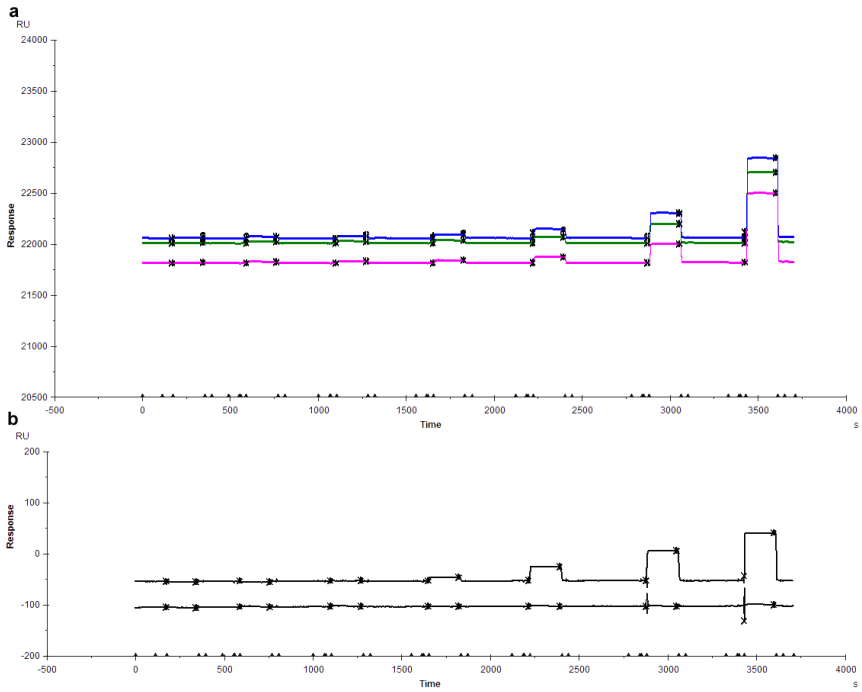

Figure AIII.6 SPR studies a SPR response for the flow cells functionalised with hybrid **132** (green) and Biotinyl-p53 (blue) and the unfunctionalised flow cell (pink); **b** SPR response corrected after blank subtraction.

As shown in Figure AIII.6 b, binding was observed only for the Biotinyl-p53. The shape of the response curves indicated however that the kinetics of the association/dissociation process are really fast and for this reason it was not possible to extract a K_d directly from the response plot. The corrected RU signals obtained were instead plotted against the protein concentrations in OriginPro 9. The data, shown in Figure AIII.7, confirmed that no binding was observed for hybrid **132** and, after analysis with a sigmoidal logistic fit, allowed to extract a K_d of 4.8 ± 0.4 μM for the Biotinyl-p53/*h*DM2 interaction.

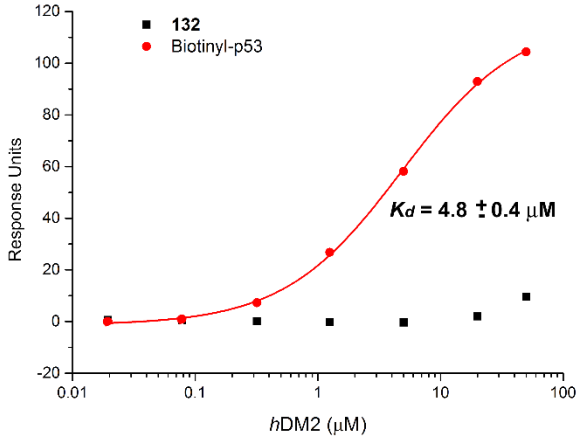

Figure AIII.7 Response units plot for hybrid 132 (black) and Biotinyl-p53 (red) highlighting the K_d obtained from the interaction of the latter with *h*DM2.

The higher value obtained with respect to the native interaction (187.1 ± 24.6 nM in a FA assay, see Appendix I), indicated that the biotinyl-functionality had a negative effect on the binding and suggested that this could be the reason for the inactivity of the other derivative. Further investigation will be needed in order to repeat and confirm this result.